Understanding Along the Channel Phenomena in PEM Water Electrolysis

Zur Erlangung des akademischen Grades eines

DOKTORS DER INGENIEURWISSENSCHAFTEN (Dr.-Ing.)

von der KIT-Fakultät für Elektrotechnik und Informationstechnik
des Karlsruher Instituts für Technologie (KIT)
angenommene

DISSERTATION

von

M.Sc. Niklas Hensle
geboren in Emmendingen

Tag der mündlichen Prüfung:	09.12.2025
Hauptreferent:	PD Dr.-Ing. André Weber
Korreferent:	Prof. Dr. rer. nat. Ulrich Lemmer

Danksagung

Die vorliegende Dissertation entstand während meiner Forschungsaktivität am Fraunhofer ISE in der Arbeitsgruppe *Elektrolyse* im Bereich *Wasserstofftechnologien* innerhalb von 3 Jahren und 9 Monaten.

Zunächst gilt mein Dank meinem Doktorvater PD Dr.-Ing. André Weber vom Institut für Angewandte Materialien - Elektrochemische Technologien (IAM-ET) des Karlsruher Instituts für Technologien (KIT) für die Betreuung meiner Arbeit und die außerordentliche Unterstützung während dieser Zeit. Die Zusammenarbeit und Diskussion zu den einzelnen Veröffentlichungen waren stets sehr inspirierend und hallen bis heute nach.

Des weiteren gilt mein Dank Dr. Tom Smolinka für die Betreuung am Fraunhofer ISE, der mir die Möglichkeit gab mich als Wissenschaftler, aber auch als Projektleiter und persönlich zu entwickeln.

Außerdem möchte ich mich bei all meinen Kollegen am Fraunhofer ISE für die sehr gute Zusammenarbeit bedanken. Ein besonderer Dank gilt Thomas Lickert, Kolja Bromberger, Sebastian Metz, Timo Kurz und Dietmar Gerteisen, welche durch ihre Erfahrung und Kompetenz erheblichen Einfluss auf meine Entwicklung hatten. Bei Jeronimo Horstmann de la Viña möchte ich mich bedanken für die ausgezeichnete Zusammenarbeit bezüglich eigen produzierter CCM-Materialien und bei Stefan Bercher für den Austausch über alle denkbaren Aktivitäten. Zudem möchte ich mich bei all meinen Studierenden bedanken, die extrem gute Arbeit geleistet haben und ohne die, die Vielzahl an Messungen und Veröffentlichungen nicht möglich gewesen wären. Besonders hervorzuheben sind Justin Hoffmann, Nico Winterholler und Stephan Armbruster für ihre ausgezeichneten Arbeiten.

Ein weiterer Dank gilt meinen Kollegen vom KIT IAM-ET, besonders Debora Brinker für die sehr gute Zusammenarbeit und Unterstützung, den Kollegen von Schaeffler Technologies AG & Co. KG für die Zusammenarbeit im Projekt *StacIE* und den Kollegen vom National Renewable Energy Laboratory (NREL), besonders zu erwähnen, Guido Bender, Hunter Simonson und Ken Hansen.

Zuletzt möchte ich mich bei meinen Eltern, Großeltern und der gesamten Familie und all meinen Freunden bedanken, die mich in dieser Zeit stets unterstützt haben.

Zuletzt bleibt nur noch zu sagen: Danke Moggi.

Kurzfassung

In dieser Dissertation wurde eine segmentierte *Along the Channel* Testzelle im Bereich Proton-Austausch-Membran Wasserelektrolyse konzeptioniert und aufgebaut. Der Begriff *Along the Channel* lässt sich hier definieren als eine Testzelle, die entlang der Strömungskanäle ausgerichtet ist und eine industrielle Länge bei labortypischer Breite aufweist. Durch eine Segmentierung können Bereiche entlang der Strömungskanäle unabhängig von einander untersucht werden. Die Testzelle ist für den Hochstrombetrieb bis zu $10\ \mathrm{A} \cdot \mathrm{cm}^{-2}$ ausgelegt, um derzeit noch unerforschte Betriebspunkte, welche in Zukunft Relevanz gewinnen können, zu untersuchen. Dabei werden die Stromdichte- und Temperaturverteilung gemessen, als auch *Elektrochemische Impedanzspektroskopie* in allen Zellsegmenten, sowie der Gesamtzelle entlang der Strömungskanäle simultan durchgeführt.

Zu Beginn der Arbeit werden die Grundlage im Bereich Proton-Austausch-Membran Wasserelektrolyse, die Skalierung zu industrie-relevanten Zellgrößen, sowie die Definition des Begriffs *Along the Channel* erläutert. Anschließend folgt die Erklärung der Auswertemethode für ortsaufgelöste Überpotentialaufschlüsselung und Impedanzanalyse mit den Methoden *Distribution of Relaxation Time* und *Equivalent Circuit Modeling*.

Impedanzspektren weisen im niederfrequenten Messbereich induktive Phänomene auf, die bis dato in der Literatur nicht umfänglich diskutiert wurden. Um diese Wissenschaftslücke zu füllen, wurden Untersuchungen mit unterschiedlichen Testzellen im Labormaßstab, wie der *Fraunhofer ISE Referenzzelle* mit $4\ \mathrm{cm}^2$ aktiver Fläche, durchgeführt. Verschiedene Studien, wie Variation von Betriebs- und Strukturparametern, Messungen mit Referenzelektroden und Vergleiche mit dem Zellbetrieb unter Gleichstrom konnten den Ursprung der so genannten *inductive loops* auf einen Elektrolyteffekt (Membran und Ionomer) an der Anode eingrenzen. Diese Erkenntnisse sind von hoher Relevanz für die Untersuchung von lokalen, niederfrequenten Prozesse, wie beispielsweise Massentransportprozesse in der *Along the Channel* Testzelle.

Das optimale Einsetzen von kohlenstoff-basierten porösen Transportschichten, welche auf der Kathode angewendet werden können, sind ebenfalls in den letzten Jahren nicht intensiv in der Literatur diskutiert worden. Aus diesem Grund wurden Studien zur Zellverpressung, Kontakt zu beschichteten und unbeschichteten Bipolarplatten, das Aufbringen von mikro-porösen Schichten und das Einbringen hydrophobischer Additive durchgeführt. Diese Resultate wurden genutzt für die Materialauswahl und optimale Assemblierung der *Along the Channel* Testzelle.

Die Ergebnisse, die die *Along the Channel* Testzelle betreffen, demonstrieren zunächst die Zellleistung und die Zellfunktionalität unter verschieden Betriebsbedingungen. Relevante Annahmen, wie eine vergleichbare Spannung über die gesamte Zellfläche konnten bewiesen werden. Außerdem wird eine, in dieser Dissertation entwickelte Methode, um hochfrequente Artefakte bei der Bestimmung des Hochfrequenzwiderstands eines Impedanzspektrums zu umgehen aufgezeigt.

Unter industrie-relevantem Zellbetrieb wurden wichtige Erkenntnisse bezüglich Wärmemanagement und Einfluss von inhomogener Zellkontaktierung erzielt. Durch den Einsatz von Katalysatorbeschichteten Membranen zukünftiger Generation mit geringer Katalysatorbeladung, in Kombination mit porösen Transportschichten unterschiedlicher struktureller Eigenschaften, konnte die Bedeutsamkeit und der Einfluss auf kinetische Überpotentiale der optimalen Kontaktierung der Grenzfläche zwischen Katalysatorschicht und porösen Transportschicht gezeigt werden.

Der Betrieb der *Along the Channel* Testzelle nahe des stöichiometrischen Wassergehalts zeigte den Einfluss von Elektrolyt-Austrocknung und Massentransportlimitierungen. Berechnungen des Wassergehalts der Membran und des Verhältnisses von Flüssig- zur Gasphase des Wassers entlang der Strömungskanäle ergaben Erkenntnisse zu relevanten Kipppunkten der Membranbefeuchtung.

Abstract[1]

In this dissertation, a segmented *Along the Channel* test cell for proton exchange membrane water electrolysis with industrially relevant channel length is conceptualized and built. The term *Along the Channel* can be defined as a test cell constructed along the flow field channels using an industrial cell length and a laboratory-scale cell width. By segmenting the cell, specific areas along the flow field channels can be examined independently of each other. The test cell is designed for high current density operation up to $10\ \mathrm{A \cdot cm^{-2}}$ to explore yet untouched, and for the future intended, operation points. Using this test cell, measurements of the current density distribution, temperature distribution, and locally-resolved *Electrochemical Impedance Spectroscopy* are performed along the flow field channels in parallel for all cell segments and the entire cell.

In the first part of this work, the fundamentals of proton exchange membrane water electrolysis and the scaling up to industrial-designed cells including the definition of the term "*Along the Channel*" is elucidated. Furthermore, the methods on locally-resolved voltage breakdown and impedance analysis using *Distribution of Relaxation Time* with subsequent *Equivalent Circuit Modeling* are described.

Impedance spectra in the low-frequency range show inductive features, which have not yet been widely discussed in the literature. Therefore, investigations with different laboratory-scaled test cells, as the $4\ \mathrm{cm}^2$ *Fraunhofer ISE reference cell*, are conducted. Several studies, such as operational and structural parameter variations, reference electrode measurements and the comparison to direct current operation of the cell have circumscribed the origin of the so-called *inductive loops*, attributed to an electrolyte (membrane and ionomer) effect at the anode. These findings are crucial to understand local low-frequency processes, such as mass transport processes, in the *Along the Channel* test cell.

Since the use of carbon-based porous transport layers, which can be employed at the cathode, has not been studied extensively in recent years, a study on laboratory-scale is performed. Therefore, the cell compression, contact resistance to coated and uncoated bipolar plates, the use of micro porous layers, and hydrophobic additives are investigated. With these findings, a proper cell setup and assembly was established for the *Along the Channel* test cell.

The results concerning the *Along the Channel* test cell first demonstrate the performance and

---

[1] Parts of the abstract have been published in [1–6]

functionality of the cell under different operation conditions. Relevant assumptions, as the equality of voltage alongside the active area has been demonstrated. Furthermore, a method, developed within this thesis, to circumvent high-frequency artefacts when determining the high-frequency resistance in an impedance spectrum is shown.

Under industrial-relevant cell operation, important findings regarding heat management and unequal contact alongside the active area have been made. Employing *next-generation* catalyst-coated membranes with low catalyst loading in combination with porous transport layers with different structural parameters demonstrate the importance of proper cell interfaces when reducing catalyst loading.

Operating the cell close to the stoichiometric level showed the severe impact on electrolyte dry-out and mass transport effects. Calculations of the membrane's water content and the liquid-to-gas ratio along the flow field channels indicate that tipping points may exist between liquid and vapor-fed electrolysis operations and significantly influence membrane humidification.

Contents

1 Introduction

1.1 PEM Water Electrolysis and its Development Goals

Anthropogenic global warming is in full progress [7, 8]. Substituting fossil energy carriers with regenerative energy is indispensable. In 2024, the share of renewable energy in the German electricity mix exceeded 60% [9, 10], indicating that progress towards a climate neutral economy has been made in the past years. Moreover, the plan to become "widely greenhouse gas neutral" is targeted for the year 2050 by the German government [11]. Furthermore, utilizing regenerative energy for electricity, heat, and mobility requires employing chemical energy carriers to store energy and ensure compatibility across various applications, such as in the steel, cement and chemical industries; heavy-duty mobility like truck traffic, shipping and aviation; and building heat.

In a carbon dioxide (CO_2)-free world, hydrogen (H_2) is the primary molecule that stores $33.3\ \mathrm{kWh} \cdot \mathrm{kg}^{-1}$ or $1.86\ \mathrm{kWh} \cdot \mathrm{l}^{-1}$ (at $700\ \mathrm{bar}$) of energy [12] without emitting greenhouse gases when burned or oxidized. Hydrogen can be deployed directly to produce electricity, e.g. in fuel cell systems or heat in gas-fired power plants, or to create other chemical energy carriers such as methanol, ammonia, or DME (Dimethylether) [13–18].

Today, hydrogen is regularly produced using fossil energy carriers such as natural gas with a share of greater than 93% in Germany in 2020 [19]. For example, steam reforming produces per mole of methane one mole of carbon dioxide and is classified as *gray hydrogen*. With a subsequent carbon capturing this process is, in principle, CO_2 neutral. However, the challenge remains in storing the large amounts of CO_2, and the reliance on fossil energy carriers persists. This process is classified as *blue hydrogen*. The only way to produce *green hydrogen* is through electrolysis of water using renewables like solar or wind energy.

There are several water electrolysis applications discussed in literature and already used in industry. In general it is distinguished between high and low temperature electrolysis. High temperature applications, such as solid oxide electrolysis, are usually operated at temperatures of $800\ ^{\circ}C$, achieving high cell efficiencies [20, 21] and can be operated in electrolysis and fuel cell mode. Due to the high temperature level, these systems can hardly be operated dynamically, therefore a coupling with the volatile electricity supply from renewables is critical.

For low-temperature electrolysis an established application is the alkaline water electrolysis. Due to the liquid electrolyte (mostly potassium hydroxide) and its high thermal mass, these systems are also not preferred for coupling with renewables [22–24].

Membrane-based low-temperature applications have the advantage that the operation point can dynamically be changed due to the low temperature level and relatively small thermal mass of the thin solid electrolyte which allows coupling to rewenables. Anion exchange membrane water electrolysis (AEMWE) is a promising application since fluorine-free materials and non-noble metals can be employed [25–27]. However, AEM water electrolysis currently falls short of achieving the high current densities and cell efficiencies found in proton exchange membrane water electrolysis (PEMWE) [28–30]. The latter represents the sole water electrolysis application discussed in this dissertation.

PEMWE systems are today ready for series production in the megawatt scale with a standard current density of $\sim$ 2 to 3 $\mathrm{A \cdot cm^{-2}}$ which is very high compared to the other applications mentioned above. Cells are usually stacked together and connected in series circuit forming an PEMWE *stack*. Several hundred compact and modular stacks of $\sim 1\ \mathrm{MW}$ power are intended for the use in building megawatt to gigawatt-scale hydrogen production plants. However, improving cell efficiency and durability, increasing operational current density, and decreasing or substituting the catalyst loading of the platinum group metal (PGM) materials are among others some of the most important areas of research in academia and industry [31–34]. In addition, the scaling up of PEMWE from laboratory-scaled cells of a few square centimeters active area to industry-relevant cell designs of several $1000\ \mathrm{cm^2}$ is challenging regarding performance and long-term stability. Two major issues are the inhomogeneous compression of the cells leading to a current density distribution that partially stresses the components and heterogenous effects due to different water gas ratios alongside the cell area [35–38]. The latter phenomenon is especially pressing along the water supply channels of the cells regarding current density, temperature distribution, and the resulting degradation effects.

The Clean Hydrogen Partnership, European Union and the U.S. Department of Energy, USA announced development targets for different water electrolysis applications [39, 40]. The most relevant targets for PEMWE are summarized in Table 1.1. A drastic reduction of the electricity consumption, capital and operational costs are intended by increasing cell efficiencies. Due to the limited availability of PGM materials, especially iridium, which is used for the oxygen evolution reaction, lowering the catalyst loading is a key target. Coupled with an increase in current density, increased catalyst utilization is intended. However, these cell efficiencies require not only catalyst layer development but also next-generation electrolyte (membrane) materials with significantly lower thickness to reduce the Ohmic cell resistance.

Table 1.1: Summary of the most relevant development targets of the Clean Hydrogen Partnership, European Union and the U.S. Department of Energy [39, 40].

Clean Hydrogen Partnership	Unit	Status 2020	Targets 2024	Targets 2030
Electricity consumption	$\mathrm{kWh \cdot kg^{-1}}$	55	52	48
Capital cost	$€ \cdot \mathrm{kW^{-1}}$	900	700	500
Operation & maintenance cost	$€ \cdot ((\mathrm{kg \cdot d})^{-1} \cdot \mathrm{y}^{-1})$	41	30	21
Current density	$\mathrm{A \cdot cm^{-2}}$	2.2	2.4	3
Degradation	$\% \cdot 1{,}000\mathrm{h}^{-1}$	0.19	0.15	0.12
Use of raw material as catalysts	$\mathrm{mg \cdot W^{-1}}$	2.5	1.25	0.25

U.S. Department of Energy	Unit	Status 2022	Targets 2026	Ultimate targets
Electricity efficiency	$\mathrm{kWh \cdot kg^{-1}}$	55	51	46
Capital cost	$€ \cdot \mathrm{kW^{-1}}$	100	250	150
H_2 production cost	$\$ \cdot \mathrm{kg^{-1}}$	>3.00	2.00	1.00
Cell performance	$\mathrm{A \cdot cm^{-2}}$ @ V	2.0 @ 1.9	3.0 @ 1.8	3.0 @ 1.6
Degradation	$\% \cdot 1{,}000\mathrm{h}^{-1}$	0.25	0.13	0.13
Total PGM content	$\mathrm{mg \cdot cm^{-2}}$	3.0	0.5	0.125

1.2 Fundamentals of PEM Water Electrolysis Cells

PEM water electrolysis cells are electrochemical cells that produce hydrogen and oxygen by splitting water using electrical power. The following sections provide information about the typical cell design and its functionality, thermodynamic fundamentals, and the losses and overpotentials occurring during cell operation.

1.2.1 Cell Design and Functionality

The PEMWE cell, like every electrochemical cell, consists of two electrodes and an electrolyte. The electrolyte is membrane-based and gives the application its name “proton exchange membrane” or “polymer electrolyte membrane” (PEM). The electrodes contain the necessary catalysts and are typically porous to transport fluids, protons, and electrons to the active catalyst particles where the reaction can take place, known as the triple phase boundary (TPB). The porous electrodes are here referred to as catalyst layer (CL). Membrane and electrodes are sandwiched together to form the membrane electrode assembly (MEA). On top of the electrodes, porous transport layers (PTLs) are placed to carry water to the anode. Simultaneously, oxygen at the anode and hydrogen at the cathode need to be carried out through the porous electrodes. At the anode, platinum-coated and titanium-based PTLs are typically employed. Due to the low overpotentials at the cathode, carbon-based materials can be used. Carbon-based PTLs are often and in this dissertation referred to as gas diffusion layers (GDLs). To transport water to and the gases from the PTLs, flow field plates with specific channel designs are implemented. PTLs and flow field plates need to be electrically conductive to carry the current from outer current collectors to the electrodes. Figure 1.1 shows a schematic diagram of a typical PEMWE cell.

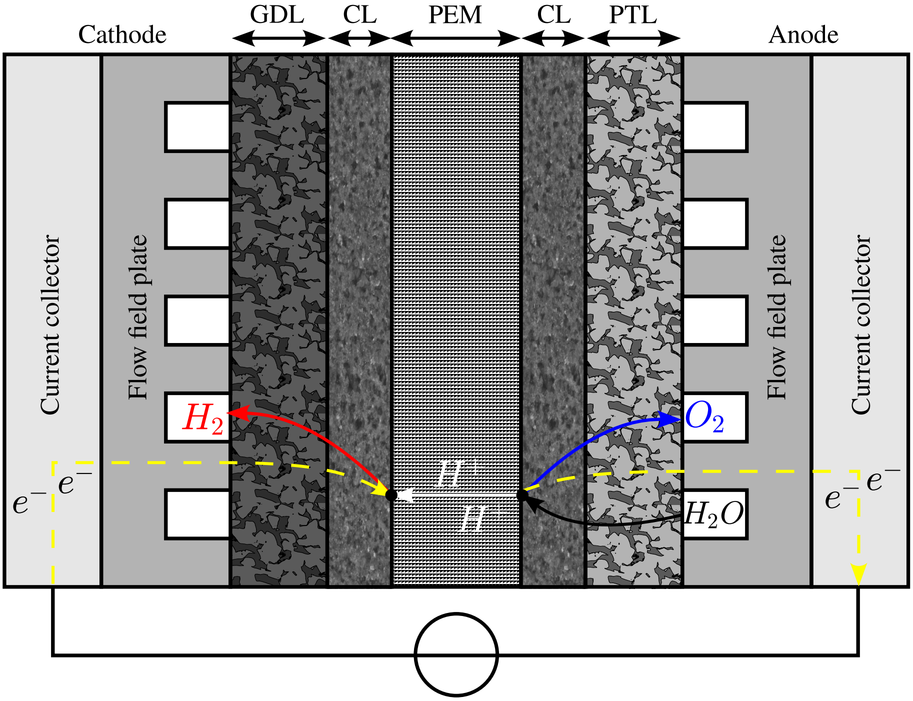

Figure 1.1: Schematic diagram of a PEMWE cell and its functionality.

In this diagram, the anode is shown on the right and the cathode on the left side. Water, as a reactant is supplied through the flow field plates and is drawn by capillary forces through the PTL to the electrode at the anode. At the TPB of the CL the splitting of water molecules into oxygen molecules, protons, and electrons (oxygen evolution reaction, OER) takes place, see Equation (1.1). While the protons travel through the membrane, the electrons follow the electrical circuit towards the cathode. Protons and electrons recombine at the cathode and hydrogen molecules are evolved (hydrogen evolution reaction, HER), see Equation (1.2). Combining Equations (1.1) and (1.2) deliver the overall cell reaction, as shown in Equation (1.3).

$$H_2O \rightarrow \tfrac{1}{2}O_2 + 2H^+ + 2e^- \tag{1.1}$$

$$2H^+ + 2e^- \rightarrow H_2 \tag{1.2}$$

$$H_2O \rightarrow \frac{1}{2}O_2 + H_2 \tag{1.3}$$

The coherence between the flow of the electrical load $\dot{Q}$ (current I) and the molar flow of the reactant $\dot{n}$ (water) is given by Faraday's law [41], see Equation (1.4).

$$\dot{Q} = I = \dot{n} \cdot z \cdot F \tag{1.4}$$

Whereas $z = 2$ describes the number of transferred electrons (see Equation (1.1) and (1.2)) and $F = (96,489.9 \pm 2)$ As $\cdot$ mol^{-1} Faraday's constant. For regular operation of PEMWE cells, a Faraday efficiency of $> 99\%$ is usually present [42]; in this dissertation, a Faraday efficiency of 100% is assumed. This implies that every current applied to the cell is completely converted in the hydrogen and oxygen production neglecting any shunt or corrosion currents.

The state-of-the-art PEMWE components are depicted in Figure 1.2 and explained in the following. At the top, the cathode flow field plate, GDL, and CL are depicted. The membrane separates cathode and anode in the center. The CL and PTL surfaces are highlighted, as shown in the zoom-ins.

Electrolyte

The electrolyte for PEMWE consists of a solid, fluorinated polymer which is proton-conductive due to the sulfonation of the side chains. Typical membrane materials are Nafion® or Fumasep® with a thickness between 50 μm and 200 μm. Due to the announced ban on PFSA (perfluorosulfonic acids), fluorine-free membranes have been developed in the past but are not yet state-of-the-art [43, 44]. The membrane carries the protons from anode to cathode and acts as an electronic insulator. Water is drawn through the membrane as they accompany the protons due to the electro-osmotic drag [45]. In addition, the membrane separates the oxygen at the anode from the hydrogen at the cathode. However, gas crossover (primarily hydrogen from the cathode to the anode) exists and is relevant to industrial operations concerning gas purity and safety issues. Gas crossover is widely discussed in PEMWE literature [46, 47], but is not focused in this thesis.

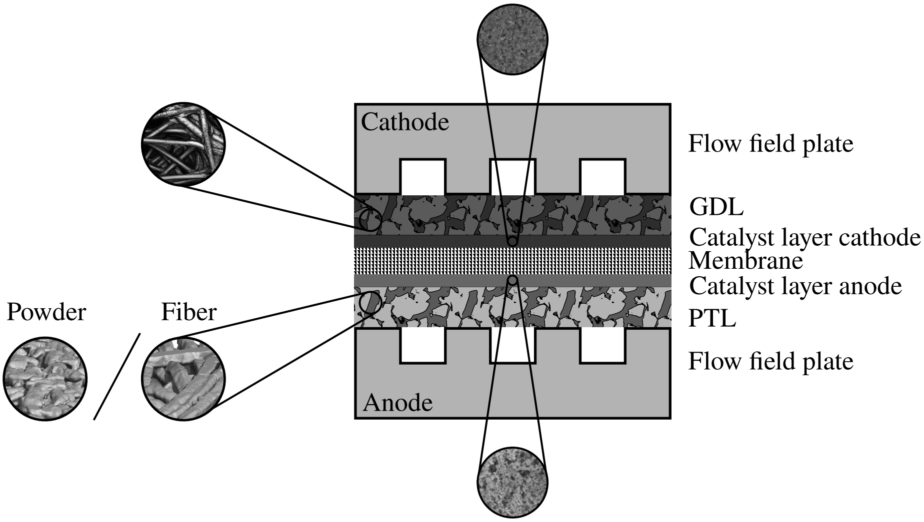

Figure 1.2: Sandwich presentation of a PEMWE cell and its components.

Further requirements are mechanical stability, as the typical industrial operation is under differential pressure of $30\ \mathrm{bar}$ at the cathode and $1\ \mathrm{bar}$ at the anode. Regarding long-term stability over a life time of $80.000\ \mathrm{h}$, the membrane needs to withstand temperatures up to $80\ ^{\circ}\mathrm{C}$, harsh oxidizing conditions at the anode and reducing conditions at the cathode, a pH of ~ 1 and the mechanical stress due to clamping and gas pressure.

Electrodes

Electrodes for PEMWE cells typically consist of porous material that includes catalytically active and electrically conductive catalyst particles and protonic-conductive ionomer. An established way to create a MEA is to coat the electrodes as a CL onto the membrane, which is called catalyst-coated membrane (CCM). This can either be done by direct coating or by decal transfer from a polymer foil onto the membrane [48]. Besides that, coating of a PTL with catalyst is also done and called porous transport electrodes (PTE). This method often shows higher Ohmic resistance due to poorer contact to the membrane as compared to CCMs. In this thesis, only CCMs are considered.

The electrode at the anode typically consists of iridium oxide (IrO_x) as catalyst particles with Nafion® as ionomer. Iridium oxide has proven to be a very active and stable catalyst layer for the OER. A disadvantage is the relatively low electrical conductivity compared to PEM fuel cell electrodes, which can be a limiting factor for the cell performance. The mean pore size and the thickness of a CL are typically a few micrometers. Research is ongoing to use supported iridium oxide particles with titanium oxide as the substrate. Due to the high oxidizing conditions, not many highly conductive materials, such as noble metals can be used. The electrode at the cathode is very similar with a PEM fuel cell electrode for which platinum catalyst supported on carbon particles is used with ionomer as Nafion®.

Porous Transport Layer

Titanium-based materials are used as anode PTLs. There are two relevant types of PTLs, titanium fiber and titanium powder PTLs, which differ in their structural properties, e.g. porosity, pore size distribution, and surface area. PTLs typically range from $100\ \mu\mathrm{m}$ to $1000\ \mu\mathrm{m}$ in thickness and are coated with platinum with a layer of a few hundred nanometers to decrease contact resistance and increase durability. The mean pore size varies from $10\ \mu\mathrm{m}$ to $100\ \mu\mathrm{m}$. At the cathode, carbon-based materials can be used due to the small voltage drop and non-oxidizing conditions. These materials are very similar to those used in PEM fuel cells. Mostly, so-called carbon paper is used, which includes polytetrafluoroethylene (PTFE) for a better gas transport and a micro porous layer (MPL) as an additional layer between PTL and CL to increase contact and catalyst utilization. The use of a MPL at the anode is a highly focused topic in PEMWE research [31, 49] but PTLs with MPL are not yet commercially available.

Flow Field Plates

The flow field plate is used to guarantee a proper electrical transport through its bulk material and to the surrounding components, such as current collector and PTL. In academia, the flow field plates mostly consist of titanium with milled flow field channels. The channel width and depth are usually between $1\ \mathrm{mm}$ to $3\ \mathrm{mm}$, with lands in between the channels of similar width. With the tendency to use thinner PTLs and softer material such as carbon-based PTLs, channel widths tend to decrease to prevent bending between the lands. Different flow field designs are used; typically, a fast throughput of water is intended in academia to prevent excessive increases in water temperature along the active area. Therefore, straight parallel flow fields are used in this thesis. Serpentine flow fields with one or multiple channels, as well as other geometries, have also been reported. Noble metal coatings, such as gold or platinum, are used to prevent corrosion of the titanium material, which is normally done by electroplating with a few micrometers thickness. In industry, milling of flow fields for series production is very cost-intensive. Planar plates with expanded metals or embossed sheet metal on top are a suitable and less expensive alternative.

Current Collector

The current collector serves as the interface between the cell components and the current cables. Therefore, a proper electrical contact with the flow field plate is necessary. The current must be transferred from the current cables through the cross-sectional area of the plate; therefore highly conductive materials, such as copper, are used to minimize Ohmic losses. To prevent degradation, the current collectors are usually coated, e.g. using gold.

1.2.2 Thermodynamics

The equilibrium reversible cell voltage at standard conditions, U^0_{rev}, can be described as being proportional to the change in Gibbs free energy, ΔG, see Equation (1.5).

$$U^0_{\text{rev}} = \frac{\Delta G}{z \cdot F} = \varphi^0_{\text{an,rev}} - \varphi^0_{\text{ca,rev}} \tag{1.5}$$

U^0_{rev} can also be described by the subtraction of the reversible electrode potential φ^0_{rev} of anode (an) and cathode (ca). The reversible cell voltage implies a complete transformation of chemical energy into electrical energy, which is only possible theoretically. The second law of thermodynamics implies that during every energy conversion, the entropy increases which leads to losses in the term of heat dissipation. Therefore, the change in enthalpy ΔH must be considered. This allows for the calculation of the thermoneutral voltage U^0_{th}, which describes the voltage at a certain temperature and pressure at which no thermal energy from the surrounding is needed to maintain the reaction.

$$U^0_{\text{th}} = \frac{\Delta G + T \cdot \Delta S}{z \cdot F} = \frac{\Delta H}{z \cdot F} \tag{1.6}$$

$T \cdot \Delta S$ describes the entropic term (change of entropy multiplied by the operational temperature T), which cannot be used for the actual electrolysis reaction. Therefore, the quotient of the reversible and thermoneutral cell voltages describes the maximum cell efficiency in equilibrium, which is $83\ \%$ for the water electrolysis reaction at standard conditions [12]. As mentioned above, the reversible (and thermoneutral) cell voltage depends on pressure and temperature and can be described by the Nernst equation [50], see Equation (1.7).

$$U_{\text{rev}}(T,p) = U^0_{\text{rev}} - \frac{R \cdot T}{z \cdot F} \cdot ln\left(\frac{a(H_2) \cdot a(O_2)^{1/2}}{a(H_2O)}\right) \tag{1.7}$$

R is the general gas constant and a the activity of the reactants. The exponents of the involved species for the water electrolysis reaction depend on the molar ratio, see Equation (1.3).

1.2.3 Operational Losses and Overpotentials

To produce hydrogen and oxygen, the cell operation needs to be shifted out of equilibrium. This is done by either applying a constant current I (galvanostatic operation) and measuring the cell voltage U, or applying a constant voltage (potentiostatic operation) and measuring the cell current. In this thesis, galvanostatic mode is used as the default cell operation.

To analyze the different loss mechanisms occurring during operation, typically polarization curve (U-I curve) measurements are carried out, during which the cell response (cell voltage) is measured at different operation points (cell current). To compare cells with different active areas, the current is normalized by the active area and the current density i is used. The cell voltage U can be described by the breakdown into the specific overpotentials:

$$U = U_{\text{rev}}(T,p) + \eta_{\text{kin}} + \eta_{\Omega} + \eta_{\text{res}} \tag{1.8}$$

Whereas $U_{\text{rev}}(T,p)$ is the temperature and pressure dependent-reversible cell voltage described by Nernst, see Section 1.2.2, η_{kin} describes kinetic (or activation) losses, η_{Ω} Ohmic losses and η_{res} the residual losses. The residual overpotentials mainly consists of diffusive and convective mass transport, ionic and electronical catalyst resistivity [51–54]. Figure 1.3 shows a schematic diagram of a polarization curve measurement with the different loss overpotentials highlighted and discussed in this section.

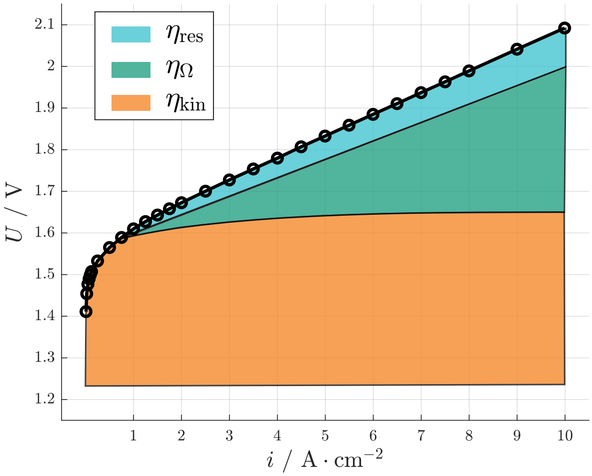

Figure 1.3: Example of a polarization curve measurement with the overpotentials highlighted.

Kinetic Losses

The kinetic losses, also referred to as activation losses, can be quantified using η_{kin} for the anode and cathode separately and describe losses occurring at the electrode and electrolyte interface, the TPB. In every chemical reaction, there is a certain energy barrier for a spontaneous reaction that must be overcome. The necessary activation energy can be covered by either electrical or thermal energy. Therefore, kinetic losses usually decrease with increasing operation temperature. The correlation between the current density and kinetic overpotential is generally described by the Butler-Volmer equation [12]:

$$i = i_0 \cdot \left[\exp(\frac{\alpha \cdot F \cdot \eta_{\mathrm{kin}}}{R \cdot T}) - \exp(-\frac{(1-\alpha) \cdot F \cdot \eta_{\mathrm{kin}}}{R \cdot T}) \right] \tag{1.9}$$

i_0 is the exchange current density, which describes the current at $\eta_{\mathrm{kin}} = 0$ and α the transfer (or symmetry) coefficient for the anodic and cathodic reaction. For high overpotentials, the second exponential term can be neglected and Equation (1.9) can be simplified to the Tafel equation [12] and solved for η_{kin}, see Equation (1.10).

$$\eta_{\mathrm{kin}} = \frac{2.303 \cdot R \cdot T}{\alpha \cdot F} \cdot log_{10}(\frac{i}{i_0}) \tag{1.10}$$

The factor 2.303 describes the conversion between the natural and the decadic logarithm. The latter is used in general for voltage breakdown analysis using the Tafel model, see Section 1.5.

Ohmic Losses

The Ohmic losses contain all electrical and protonic resistances which follow Ohm's law, see Equation (1.11).

$$\eta_{\Omega} = I \cdot (R_{\mathrm{e,bulk}} + R_{\mathrm{p,bulk}} + R_{\mathrm{ICR}}) \tag{1.11}$$

$R_{\mathrm{e,bulk}}$ describes all electrical bulk resistances that occur in the current collector, flow field plate, PTL and catalyst layer due to electron transport. These resistances are sensitive to material properties as conductivity and porosity and can hardly be influenced by operational parameters. $R_{\mathrm{p,bulk}}$ consists of all protonic transport resistances in the membrane and ionomer phase, which are highly sensitive on temperature and water content. Material-wise the membrane thickness is a relevant structural parameter, which can still be optimized by using thinner and more conductive materials. R_{ICR} describe the internal contact resistance (ICR) due to non-optimized compression of the cell. Due to the porous materials and the different surface properties used, mainly given by the different pore sizes and the comparably low conductivity of iridium catalyst particles, the interface between anode PTL and CL contributes significantly to this type of resistance. The sum of all Ohmic resistances can be measured by high frequency resistance (HFR) measurements using electrochemical impedance spectroscopy (EIS), see Section 1.5.

Residual Overpotentials

After subtracting the Nernst potential, Ohmic, and kinetic overpotentials from the cell voltage, the remaining overpotentials, referred to as residual overpotentials, include processes, such as diffusive and convective mass transport and ionic and electronical catalyst layer resistance.
PEM water electrolyzers are typically operated at high water stoichiometries of $\lambda > 50$, in addition, with state-of-the-art porous materials, such as PTLs and CCMs, mass transport related overpotentials are relatively small ($\eta_{\mathrm{MTL}} < 100\mathrm{mV}$) [55]. Furthermore, mass transport limitations resulting in limiting currents are uncommon for PEMWE. However, mass transport related overpotentials in the PTL bulk and catalyst layer can be described by Equation (1.12) [56].

$$\eta_{\mathrm{MTL}} = \frac{2.303 \cdot R \cdot T}{2 \cdot F} \cdot log_{10} \left(\frac{(\frac{p_{\mathrm{O_2,CL}}}{p_{\mathrm{O_2,FF}}})^{0.5} \cdot \frac{p_{\mathrm{H_2,CL}}}{p_{\mathrm{H_2,FF}}}}{\frac{p_{\mathrm{H_2,CL}}}{p_{\mathrm{H_2,FF}}}} \right) \tag{1.12}$$

p_x describes the partial pressure in the CL and the flow field channels (FF), respectively. Since water is incompressible, the activity a is used instead of the partial pressure. Convective mass transport resistance is considered to be negligible in this thesis since a straight parallel flow field channel design with minimal flow resistance is used. Instead, capillary flow must be considered in the porous materials. The capillary flow depends on structural parameters, such as pore size, surface tension, and contact angle.
Ionic and electronical in-plane catalyst layer resistivity is especially for low-loading CCMs a relevant aspect within the residual overpotentials. Padgett et al. presented a method using EIS and subsequent equivalent circuit modeling at cell voltage below the water-splitting voltage to analyze the catalyst layer resistivity [52]. Furthermore, Ernst et al. presented a theoretical method to calculate the ionic in-plane catalyst layer conductivity [49].
Since this thesis focuses on the cell behavior along the channel of industrial-scaled cell designs and not particularly on the processes happening in microstructural scale, the residual overpotentials are not explicitly deconvoluted with the approaches mentioned above. Instead, using EIS with Distribution of Relaxation Time (DRT) and Equivalent Circuit Modeling (ECM), low-frequency processes are analyzed.

1.3 From Laboratory to Industrial-Scaled Cell Designs

In academia, test cells with only a few square centimeters of active area are typically used to assume a homogeneous distribution of structural and operational parameters, which is essential for material characterization. Active areas between $1\ \mathrm{cm}^2$ up to $25\ \mathrm{cm}^2$ are reported and commercially available [57–59]. In this thesis, besides the developed *Along the Channel* (AtC) test cell, the *Fraunhofer ISE reference cell* [59] is used for laboratory-scaled characterization and described as follows, exemplarily for typical academia test cells.
The *Fraunhofer ISE reference cell* has an active area of $3.98\ \mathrm{cm}^2$ with an $2x2\ \mathrm{cm}^2$ area with radii at the edges of $1.5\ \mathrm{mm}$. Figure 1.4 gives an overview of the test cell components.

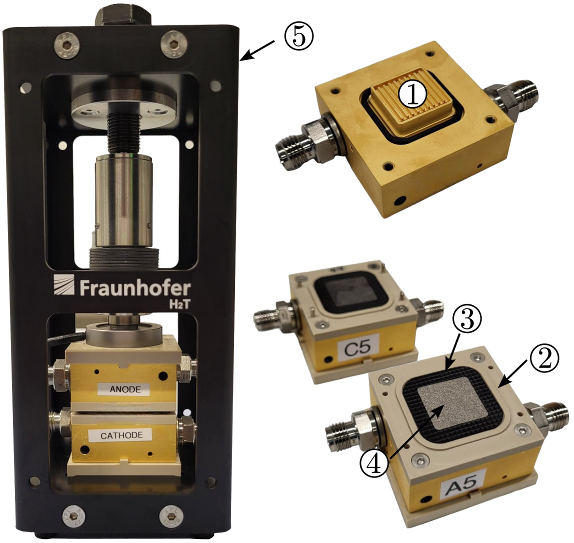

Figure 1.4: Photos of the cell components of the *Fraunhofer ISE reference cell*.

The cell consists of two identical gold-coated titanium cell bodies with a straight parallel flow field (1) consisting of 10 parallel channels with a cross-sectional area of $1\ \mathrm{mm}^2$ and lands of $0.9\ \mathrm{mm}$ width. To use different PTL heights or vary the compression of the cell, a polyether ether ketone (PEEK) based frame (2) is screwed onto the cell body which adjusts the height of the compressed flat sealing used. Therefore,the PTL thickness and height of the compressed sealing allow for adjusting the compression of the active area of the cell. The MEA sample can be placed on the cell body with the screwed-on PEEK frame, the flat sealing (3) and the PTLs (4) on the

flow field. Both cell bodies are stacked together and then compressed by the compression cage (5). The force applied is monitored by a force sensor. The current can be applied to the cell body using 4 mm banana plugs, the potentials is measured at the opposite side. Temperatures can be measured before the cell in the water inlet stream and after the cell in the water-gas outlet stream. Additionally, a 2 mm bore right underneath the flow field can be used to measure the temperature of the cell body close to the active area. More detailed information on the *Fraunhofer ISE reference cell* can be found elsewhere [59].
In industry, the relevant active area is in the range of several 1000 square centimeters. Industrial cell designs usually have cell lengths and widths of 30 cm up to a few meters, depending on the cell design and specific application. Reducing capital expenditure (CAPEX) is key for an economical series production of stack designs. Several factors, e.g. the amount of cost-intensive catalyst materials, such as iridium and platinum, the production of porous material and the manufacturing of the flow field plate are considered regarding costs, performance and long-term stability. A few studies have been published that provide cost overviews of an electrolysis stack [60–63]. Figure 1.5 gives an overview of different fundamental cell designs for industrial applications based on [64].

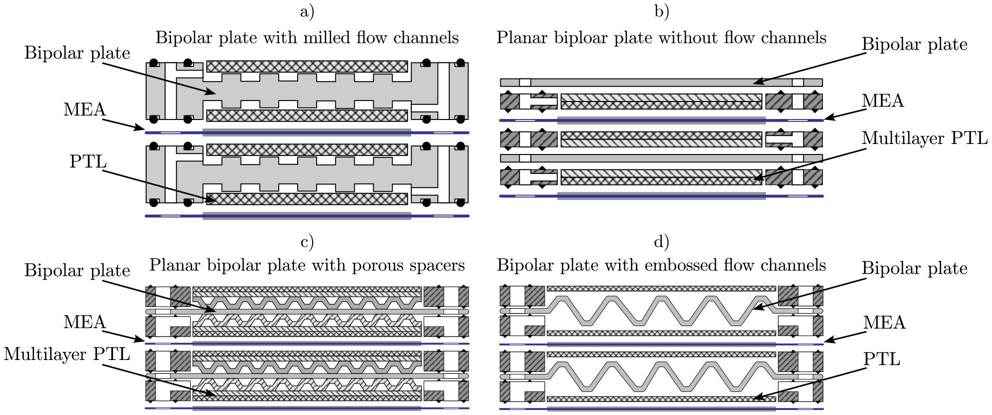

Figure 1.5: Overview of state-of-the-art stack designs. a) Bipolar plate with milled flow fields, b) planar bipolar plate without flow field channels, c) planar bipolar plate with porous spacers, and d) bipolar plate with embossed flow channels - based on [64].

Figure 1.5 a) shows the classical approach with milled flow field channels, which provides low in-plane flow resistance and proper cell compression due to the stiff bipolar plate. However, milling flow field channels into titanium material is cost-intensive. Furthermore, thin PTL materials may bend into the flow channels and reduce active contact area. The use of planar bipolar plates in combination with flow field replacement materials, such as expanded or mesh metals as a multilayer PTL, can be a useful alternative, see Figure 1.5 b). Advantages such as a more uniform contact distribution to PTLs might be given, however, the pressure loss is often significantly increased compared to milled components due to higher in-plane flow resistance. To decrease the in-plane flow resistance, modifications, such as employing porous spacers can be used, see Figure 1.5 c). An even more advanced approach, is to use thin titanium sheets, which are embossed for a certain flow field channel design. This method is often carried out for PEM fuel cell stack designs and is less cost-intensive than milling titanium plates, see Figure 1.5 d). The selection of the flow field and stack designs depend on several key factors, such as operation point, performance, lifetime, degradation, stack and operational costs.

Independent of its actual cell design, in industrial-scaled PEMWE cells, a perfectly homogeneous distribution of structural parameters as porosity, particle distribution, or coated surface area is not realistic. Furthermore, due to the large active area a distribution of operational parameter, as the water-to-gas ratio, current density and temperature can be induced. For example, unequal contact of the cells can lead to significant current density patterns. Structural and operational parameter distribution can lead to thermal hotspots which may increase degradation processes. Inhomogeneities along the water supply channels are especially pressing since reactant water is consumed and gas produced, which accumulates down the channels. With locally resolved investigations, as current density, temperature and impedance distribution measurements, gradients and inhomogeneities along the channel can be analyzed, see section below.

1.4 Along the Channel Analysis

This section provides the definition of the *Along the Channel* approach used within this work. This outcome is based on literature research on locally resolved measurements with a focus along the water supply channels, which is discussed in Section 4.1.

The Along the Channel approach is based on the idea of considering a cell out of an industry PEMWE stack with industrial cell design, from which a thin stripe along its water supply channels is cut out. Figure 1.6 illustrates this approach visually. Therefore, a cell is designed with a laboratory-scaled width of 2 cm and an industry-relevant channel length of 30 cm with a straight parallel flow field design. To be able to analyze phenomena occurring along the water supply channels, the current density, temperature and impedance are measured at different measurement points. To increase the selectivity of the measurement, the cell is segmented, meaning that the transverse current between the measurement points is interrupted.

The analysis within this thesis focuses on locally resolved EIS. On the one hand, EIS is conducted to extract the local HFR and understand the Ohmic loss distribution alongside the active area and to be used for voltage breakdown analysis. On the other hand, the polarization processes are separated by their peak frequencies and analyzed using DRT and subsequent ECM.

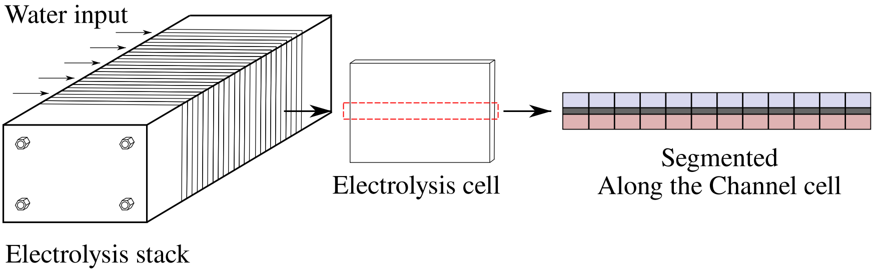

Figure 1.6: Illustration of the Along the Channel approach.

Additionally, the current density distribution (CDD) and temperature distribution are measured. The segmentation, mentioned above, is realized by interrupting (segmenting) the flow field plate and the PTLs at the anode and measuring each segment separated from each other. The measurement of current, temperature, and impedance in each segment is done in parallel using a printed circuit board (PCB). The other active components, such as the membrane and catalyst layer are not segmented since the in-plane resistance of both is assumed to be much higher than the through-plane resistance. The cathode is not segmented since the current collectors of anode and cathode are not segmented, therefore only the electrode with inserted PCB needs to be segmented. With this approach, it is ensured that the current measured in each segment is also flowing through the membrane at the same position. The cell design and employed measurement method are further described in Sections 4.2.1.1 and 4.2.1.2.

1.5 Voltage Breakdown Analysis

Polarization curve measurements are a comparatively simple measurement method to analyze the current-voltage behavior of a PEMWE cell. With voltage breakdown analysis of the polarization curve into the specific overpotentials, as mentioned in Section 1.2.3, Equation (1.8), further information on the cell behavior can be obtained. This analysis method is widely discussed in the literature [35, 56, 65, 66] and is used within this thesis. Figure 1.7 provides an overview of how the voltage breakdown analysis is conducted, which is explained in the following. First, the Ohmic overpotentials are calculated and subtracted from the polarization curve. Therefore, the HFR is measured at every current density step via EIS. Due to high-frequency artifacts caused by wiring, cell housing and test bench equipment, the HFR is often distorted. The, within this thesis, developed method to circumvent high-frequency artifacts and determine the HFR, is discussed in Section 4.3.3. The Ohmic overpotentials are then determined by multiplying the HFR with the

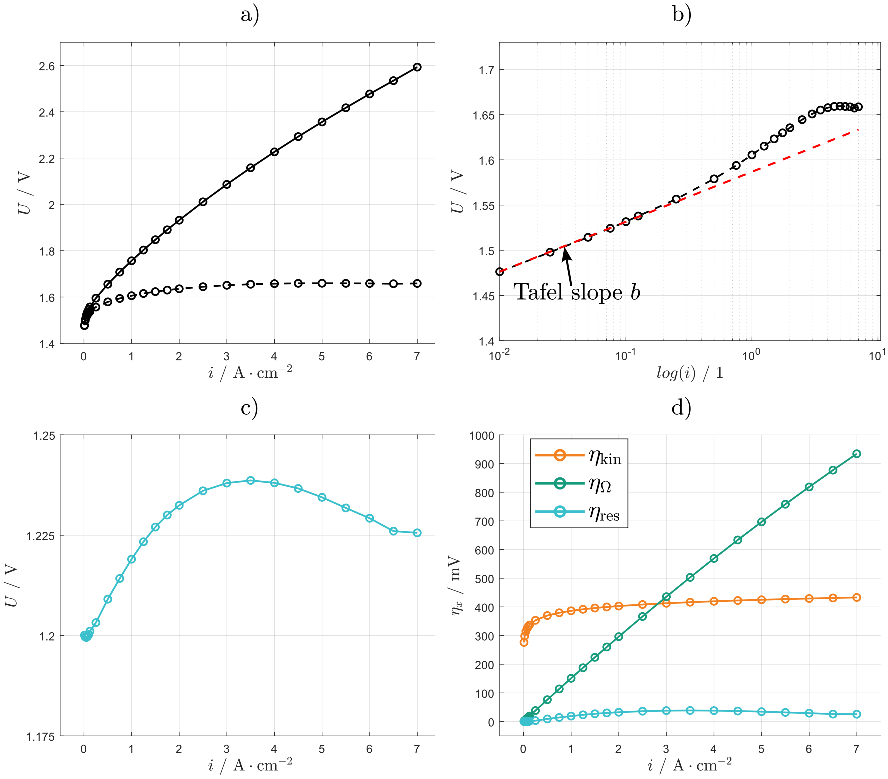

Figure 1.7: Explanation of the voltage breakdown analysis. a) Polarization curve and HFR-free polarization curve (dashed lines at the bottom), b) HFR-free polarization curve over $log(i)$ to extract the Tafel slope b, c) residual overpotentials with Nernst potential, and d) kinetic, Ohmic, and residual overpotentials.

operational current density, see Equation 1.11. To further analyze the Ohmic-free (HFR-free) polarization curve, the Ohmic overpotentials are subtracted from the polarization curve, see Figure 1.7 a), dashed lines at the bottom.

Using the Ohmic-free polarization curve, the kinetic overpotentials are determined by applying the Tafel model, see Equation (1.10). Therefore, the Ohmic-free polarization curve is depicted over the decadic logarithm of the current density i, see Figure 1.7 b). By applying the Tafel model between $0.01\ \mathrm{A} \cdot \mathrm{cm}^{-2}$ and $0.1\ \mathrm{A} \cdot \mathrm{cm}^{-2}$, an influence by mass transport can be neglected and the origin of the overpotentials is only attributed to kinetic losses. Due to the x-axis being on a decadic logarithmic scale, the slope between $0.01\ \mathrm{A} \cdot \mathrm{cm}^{-2}$ and $0.1\ \mathrm{A} \cdot \mathrm{cm}^{-2}$ can be determined, which is referred to as the Tafel slope b, with a typical value between $40\,\mathrm{mV} \cdot \mathrm{dec}^{-1} < b < 70\,\mathrm{mV} \cdot \mathrm{dec}^{-}1$, depending on the operational point and catalyst layer properties. Extrapolating the Tafel slope over the whole current density range, see dashed line in red, shows the additional losses that occur when the HFR-free polarization curve is non-linearly increasing at $0.25\ \mathrm{A} \cdot \mathrm{cm}^{-2}$. The Tafel slope b is then multiplied by the decadic logarithm of the current density i over the entire current density range to calculate the kinetic overpotentials, which are subsequently substracted from the Ohmic-free polarization curve.

The remaining overpotentials consist of the residual overpotential and the Nernst potential, see Figure 1.7 c). The Nernst potential is subtracted and the single overpotentials extracted. The residual overpotentials are typically rather small for PEMWE under standard operational conditions and cell setups. At low current densities, residual overpotentials typically increase due to higher mass transport resistance and decrease at high current densities due to increasing temperature, which may affect the ionic in-plane conductivity of the catalyst layer. Additionally, the low-frequency inductive process typically increases with increasing current density, which lowers the overall cell resistance. The phenomenon of the inductive process is not fully understood in PEMWE and investigated in Chapter 2.

The pressure and temperature dependency of the equilibrium cell voltage $U_0(p, T)$ (Nernst voltage) is calculated by Equation (1.13) and (1.14) according to [67]. It is assumed, that pressure and temperature of the cell is not changing with current density. Figure 1.7 d) shows the Ohmic, kinetic and residual overpotentials without the influence of the Nernst potential.

$$U_0(T) = 1.5184 - 1.5421 \cdot 10^{-3} \cdot T + 9.523 \cdot 10^{-5} \cdot T \cdot \log(T) + 9.84 \cdot 10^{-8} \cdot T^2 \tag{1.13}$$

$$U_0(p, T) = U_0(T) + \frac{3R \cdot T}{4F} \cdot \log(p) \tag{1.14}$$

It should be noted that this analysis method includes two major assumptions. On the one hand, since it is only measured in a two-electrode setup, a separation of the anode and cathode cannot be made. Therefore, it is assumed that the overpotentials due to the HER at cathode are negligible compared with the OER at the anode. On the other hand, measuring the temperature at the electrode is challenging. For this reason, the cell temperature, which is controlled through the water flow at the anode, is assumed to be also present at the electrode. For the locally-resolved voltage breakdown analysis in the AtC cell the inlet water temperature is used for the kinetic overpotential determination.

1.6 Electrochemical Impedance Spectroscopy

Electrochemical impedance spectroscopy (EIS) is a common measurement method in several applications, like batteries, fuel cells, and electrolysis cells [68–71]. With the measurement of the impedance over a frequency spectrum, characteristic resistances such as the series resistance and resistances of polarization processes with different time-constants can be analyzed at different operation points of the cell. This chapter provides an overview about the fundamentals and the used analysis method of DRT and ECM.

1.6.1 Fundamentals

EIS is performed by applying an alternating current (AC) amplitude as a sine wave of either current density or voltage and measuring the respective response signal. In this work mostly galvanostatic EIS is done which is described in the following. The AC amplitude is applied on top of a direct current (DC) bias of a certain operation point, defined by its DC current density, cell temperature, pressure and water flow rate. The AC amplitude is applied at different frequencies usually between $100\ \mathrm{mHz} < f < 100\ \mathrm{kHz}$. Equation (1.15) describes the fundamental correlation between the frequency dependent impedance $Z(j\omega)$ and the current and voltage signal, according to Ohm's law.

$$Z(j\omega) = \frac{U(j\omega)}{i(j\omega)} \tag{1.15}$$

The excitation current $i(j\omega)$ can be described as a function of the AC amplitude i_0 and the sine signal applied:

$$i(j\omega) = i_0 \cdot sin(\omega \cdot t) \tag{1.16}$$

$i(j\omega)$ is chosen as high as possible to reach a proper signal-to-noise ratio and as low as possible to not exceed a linear region around the DC bias. Typically, for $i(j\omega)$ values between 5% and 10% of the DC bias are chosen. To minimize the influence by noise, 10% amplitude is chosen in this thesis. ω is defined as the circular frequency

$$\omega = 2 \cdot \pi \cdot f, \tag{1.17}$$

with f being the applied frequency. The response signal can be described by its amplitude U_0 and the phase shift φ occurring due to processes with certain time constants.

$$U(j\omega) = U_0 \cdot sin(\omega \cdot t + \varphi) \tag{1.18}$$

Figure 1.8 a) shows the perturbation in galvanostatic operation during a polarization curve measurement and Figure 1.8 b) the excitation and response signals during EIS. The impedance $Z(j\omega)$ can be analyzed in polar coordinate representation with $Z_0(j\omega)$ being the magnitude (ratio of voltage and current density amplitude) and φ the phase angle, which is distributed over the frequency typically shown in Bode presentation [72], see Figure 1.8 c). A more common and intuitive presentation is the presentation in complex numbers using Euler's transformation by calculating the real and imaginary part of the impedance.

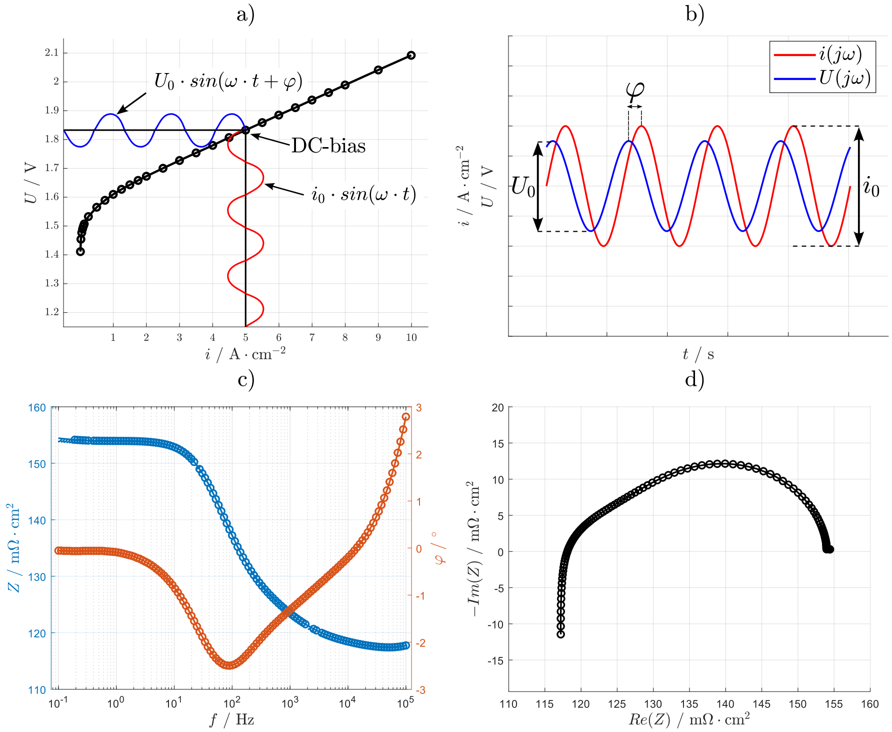

Figure 1.8: Schematic diagrams of EIS fundamentals. a) Excitation signal during polarization curve measurements, b) sine wave of excitation and measurement signal, c) Bode presentation, and d) Nyquist presentation.

This is typically shown in Nyquist presentation, with a negative $Im(Z)$-axis to see capacitive processes (negative phase angle) in the first quadrant, see Figure 1.8 d). With the Nyquist presentation, the essential information about the frequency is missed out. Therefore, it is recommended to indicate characteristic frequency points, e.g. frequency decades, intersection with $Im(Z) = 0$ or the peak of a semicircular shape. In Bode and Nyquist presentations different polarization processes can be detected by the phase angle (Bode) and the imaginary part of the impedance (Nyquist). However, polarization processes often overlay each other due to similar time constants. Therefore, more advanced deconvolution methods such as DRT are senseful to be used, see Section 1.6.3.

1.6.2 Kramers Kronig Test

To conduct a trustable EIS certain quality requirements need to be considered, summed up and described as follows [73]:

Linearity

Since a lot of electrochemical cells tend to behave non-linear only small perturbation amplitudes allow the assumption that the applied and the response signal exhibit the same frequency. With a variation of the amplitude it is relatively easy to detect linearity since it should be independent of the perturbation magnitude.

Causality

The response signal should be causal to the input signal, meaning that the response should totally depend on the perturbation and not be influenced by other sources, like electrical devices or power line frequency.

Stability

The electrochemical cell needs to be stable over the time the EIS is conducted. This can be influenced by small changes of the operational parameters caused by the test bench control or fast degradation effects of the cell itself. It is necessary that the cell shows the same behavior before and after the EIS is done.

Finiteness

The impedance and the phase angle must be finite over $0 < \omega < \infty$, which means that the impedance must incline to constant values towards 0 or infinite values of ω. For experimental data a certain limitation of the frequency range is given. Therefore, using a fitted model to the experimental data can be one solution.

To analyze the quality of the impedance measured, the *Kramers Kronig* test is a well established method [74]. In this thesis, a linear Kramers Kronig validity test is used, developed by Schönleber et al. [75].
The Kramers Kronig test is based on the causality between the measured real and imaginary part of the impedance. Using Equation (1.19) and Equation (1.20) the real part can be calculated out of the imaginary part and vice versa.

$$Re(Z(\omega)) = \frac{2}{\pi} \int_0^\infty \frac{\omega' \cdot Im(Z(\omega'))}{\omega^2 - \omega'^2} \mathrm{d}\omega' \tag{1.19}$$

$$Im(Z(\omega)) = -\frac{2}{\pi} \int_0^\infty \frac{\omega' \cdot Re(Z(\omega'))}{\omega^2 - \omega'^2} \mathrm{d}\omega' \tag{1.20}$$

Using a Kramers Kronig compatible model, such as a series connection of RC-elements (resistor in parallel to a capacitor), which is fitted to the impedance data measured, so-called *Kramers Kronig residuals* can be determined. These residuals describe the relative difference between the compatible model and the impedance data for each frequency. If the measurement data has Kramers Kronig residuals of less than 1%, the measurement data fulfill the Kramers Kronig test.

1.6.3 Distribution of Relaxation Time (DRT)

Distribution of Relaxation Time (DRT) is a method to deconvolute impedance data and therefore separate polarization processes by its characteristic time constant without priori knowledge [76]. With that, the number of relevant processes, their peak frequency, and the area-specific resistance (ASR) of the processes can be detected. Therefore, the distribution function $g(\tau)$ is calculated by Equation (1.21).

$$Z(\omega) = R_0 + Z_{\mathrm{pol}}(\omega) = R_0 + \int_0^\infty g(\tau) \frac{1}{1 + j\omega\tau} \, d\tau \tag{1.21}$$

R_0 is the Ohmic resistance determined by the HFR and $Z_{\text{pol}}(\omega)$ the sum of all polarization resistances.

The DRT function is a mathematically challenging Equation to be solved. One approach is the Tikhonov regularization [77, 78]. Therefore the Tikhonov regularization parameter λ is used. The selection of the optimal value for λ is defying: low values can cause an overestimation of the number of relevant processes; high values may not properly deconvolute the polarization processes. Depending on the cell setup, test bench, and other factors λ is wisely chosen with experience out of former measurements and the literature [79].

Figure 1.9 shows a current density variation in Nyquist (left) and DRT presentation (right). Typically, between $10^4 < f < 10^5$ unclear peaks are detected which is referred to wiring, cell housing, and other artifacts. Else, clear changes of two capacitive processes (positive DRT values) at 10^3 Hz and 10^2 Hz are observed. At < 5 Hz negative DRT values can be seen, which are referred to inductive processes, which is further discussed in Section 1.6.4.

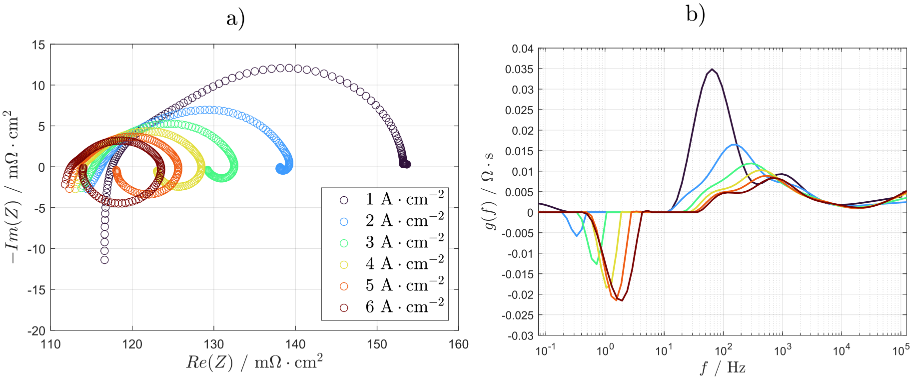

Figure 1.9: Example for DRT analysis under current density variation. a) Nyquist and b) DRT presentation.

1.6.4 Equivalent Circuit Modeling (ECM)

An established method to describe the behavior of polarization processes and quantify their resistance is the analogy to electrical equivalent circuits [12, 80]. Therefore, elements as resistors, capacitors, and inductors can be used in various connections to describe the cell behavior.

The Ohmic cell resistance is usually described by a single resistor as it has no time delay between current/voltage response. Due to inductive high frequency artifacts, the Ohmic resistance is often fitted with additional inductive elements [81]. To describe capacitive cell behavior RC-elements (resistor in parallel to a capacitor) are employed, according to Equation (1.22).

$$Z_{\mathrm{RC}}(\omega) = \frac{R}{1 + j\omega\tau} \tag{1.22}$$

Since a RC-element displays a perfect semicircle in a Nyquist plot and processes are in reality often distorted or consist of more complex processes, a so-called constant phase element (CPE) can replace the capacitor in a RC-element, which is here referred to as a RQ-element. A CPE has an additional exponent which can be changed by fitting the element to the experimental data, typically the exponent ranges between $0.5 < \alpha < 1$, see Equation (1.23).

$$Z_{\mathrm{RC}}(\omega) = \frac{R}{(1 + j\omega\tau)^{\alpha}} \tag{1.23}$$

Other processes, such as mass transport or electrolyte resistance can be modeled by more complex equivalent circuit elements, e.g. transmission line models [82]. To describe mass transport behavior typically a so-called *Warburg Impedance* [83] or a *Finite Diffusion Element* [84] are employed. Generally, in PEMWE very different ECMs are reported to describe mass transport processes, as discussed in [80].

As mentioned in Section 1.6.3, at low frequencies inductive behavior is typically detected at higher current densities. This behavior is known for several applications, such as PEM fuel cells and batteries. In PEMWE less literature is focusing on this topic. In this thesis, these low-frequency inductive processes are modeled using an RQ-element, allowing negative values for the resistance, as discussed in [85]. A detailed analysis of these processes is provided in Chapter 2.

ECM needs prior knowledge about the process to be described. Well known processes, as charge transfer or mass transport can therefore be directly fitted to the impedance data. When information about processes such as the inductive low-frequency process is missing, DRT can provide important information. In this thesis the impedance data measured is always first analyzed by DRT to detect the number of relevant processes and analyze the peak frequency. Out of this information, the ECM is created and fitted to the impedance data. To improve and rate the fitting, the fitted model is again displayed in DRT presentation and compared to the experimental data.

1.7 Scope of the Work

In this dissertation, locally resolved performance-based analyses are performed to gain a deeper understanding of phenomena occurring along the flow field channels of industrially scaled cells. It is focused on local impedance measurements with DRT and subsequent ECM analysis. Current density and temperature distribution measurements support the impedance investigations. Furthermore, voltage breakdown analysis using the Tafel model is performed.

Alongside the investigations using the AtC cell, employing the laboratory-scaled *Fraunhofer ISE reference cell*, not widely discussed low-frequency processes of inductive type, are studied to gain more understanding of the interaction with mass transport processes, which are typically observed at similar frequency regions, see Chapter 2. The appearance of these inductive features in different cell setups is demonstrated, followed by several investigations, including operational and structural parameter variations, reference electrode measurements, and cell setups with purposely provoked mass transport resistance. The knowledge achieved in this study is used to better understand low-frequency processes within the AtC cell.

Since the optimal use of carbon-based PTLs at the cathode is not widely discussed in the literature, studies on the influence of cell compression, contact to coated and uncoated flow fields, the usage of MPLs, and hydrophobic additives are performed, see Chapter 3. These findings are also used to improve the cell setup of the AtC cell.

Within this thesis, a segmented AtC test cell was designed and built. An already existing test bench was modified for high current density operations up to $10\ \mathrm{A} \cdot \mathrm{cm}^{-2}$ and locally-resolved impedance measurements. In Chapter 4 the test bench and test cell design are described and the measurement method presented. The results demonstrate the quality of internal contact distribution and the voltage equality alongside the active area. A method to properly determine the HFR, circumventing high-frequency artifacts, is given and the cell performance and measurement quality discussed under different operational conditions. Finally, the implementation and quality of the reference electrode in the AtC cell are discussed.

Industry-relevant variations of gas pressure, temperature, and water flow rate, with a special focus on high current densities, are carried out with state-of-the-art-materials. PTLs with different structural parameters in combination with state-of-the-art and *next-generation* CCMs with low catalyst loadings are analyzed and the importance of proper cell and interface compression discussed, see Chapter 5.

To gain a better understanding of diffusive processes and membrane dry-out effects along the channel, the cell is measured under water starvation close to the stochiometric level, see Chapter 6. In this study, the origin of inoperable parts of the cell is investigated using EIS and DRT analysis. Presumed tipping points between liquid and vapor-fed electrolysis due to dry-out are studied by calculating the membrane's water content and the liquid-to-gas ratio along the flow field channels.

2 Low-Frequency Inductive Feature in Impedance Spectra [1]

2.1 Introduction

Inductive behavior at low frequencies in EIS is a phenomenon that has already been reported in various electrochemical systems. It is, among others, discussed in the field of lithium-ion batteries [87–89], solid oxide cells [90–94] and PEM fuel cells (PEMFCs) [95–99]. Klotz [100] provides a comprehensive overview, including several other applications.

Electrochemical cells often exhibit an inductive semicircle at low frequencies. In general, inductive behavior is identified based on positive imaginary values in the Nyquist plot. Herein, the real part $Re(Z)$ is decreasing with decreasing frequency and the inductive polarization resistance of the related electrochemical process exhibits a negative value. Thus, the related polarization phenomena decrease the DC resistance and hence improve the cell performance.

In the field of PEMFC there are some hypotheses reported to the cause of inductive loops at low frequencies. These are the formation of platinum oxide at the surface and its dissolution [101], side reactions including adsorbed intermediates (e.g. hydrogen peroxide) [100] or slow water diffusion in the ionomer [101, 102]. Most of those articles describe this inductive behavior using physico-chemical models, ECM or DRT analysis [85, 99, 101, 103, 104]. Göhr and Schiller introduced an ECM to describe a relaxation impedance of interfaces, which typically shows inductive behavior at low frequencies [105]. This model can be applied to describe, for example, the carbon monoxide poisoning of the anode of a PEMFC [106, 107].

Only little work dedicated to the analysis of low-frequency inductive behavior has been reported for PEMWE. Most of the published articles on EIS in this field focus on the series resistance at high frequencies and on the capacitive loop at medium frequencies [37, 68, 81, 108–110]. One of the very few reports at least mentioning low-frequency inductive behavior is provided by Ferriday and Middleton [111]. However, they describe EIS results in PEMWE cells for current densities $< 0.5\ \mathrm{A \cdot cm^{-2}}$ in the low-frequency range only as "highly non-linear, non-reproducible" and provide no further characterization or analysis on what they call a “pseudo-inductive demeanor”.

---

[1] Parts of this chapter have been published in [1, 2, 86]

In PEMWE, the low-frequency inductive loops are observed at frequencies < 20 Hz. At these frequencies capacitive processes mostly related to diffusive and convective mass transport are observable. Various experimental investigations and electrochemical models are reported on mass transport processes in PEM water electrolysis [37, 68, 107–110]. Most of the published studies investigate diffusion processes without the use of EIS and do not explicitly consider the inductive behavior at low frequencies.

In this chapter it is delved deeper into understanding the origins of this inductive loop and how it can be used to enhance performance. The presence of inductive loops using different cell setups and a comparison with DC measurements is shown. Various operational parameter variations and material interventions with the use of on adapted version of the DRT analysis are systematically explored. The superimposing of mass transport processes by inductive cell behavior is essential to discuss diffusion related polarization processes at current densities $> 1\ \mathrm{A} \cdot \mathrm{cm}^{-2}$. Conclusively, developed hypotheses on which physical processes can be related to the inductive loop based on PEM fuel cell and electrolysis knowledge are presented and rated.

In parallel to the work presented in this chapter two works were published recently by Zuo et. al [112] and Franz et al. [113].

Zuo et. al investigated full-frequency impedance spectra including the low-frequency inductive loop employing a $1\ \mathrm{kW}$ stack with 10 cells and an active cell area of $25\ \mathrm{cm}^2$ [112]. To evaluate the impedance measurements DRT and ECM are applied under variations of temperature between $40\ ^\circ\mathrm{C}$ to $80\ ^\circ\mathrm{C}$, cathode gas pressure up to $5\ \mathrm{bar}$, water flow rate between $0.3\ \mathrm{l} \cdot \mathrm{min}^{-1} \cdot \mathrm{cm}^{-2}$ to $1\ \mathrm{l} \cdot \mathrm{min}^{-1} \cdot \mathrm{cm}^{-2}$ and current densities up to $2\ \mathrm{A} \cdot \mathrm{cm}^{-2}$. The analysis of the ASR of the low-frequency inductive feature (in this study referred to as $R_{\mathrm{P_{lf}}}$) shows that the inductive loop is increasing with decreasing temperature, decreasing water flow rate, increasing current density, and increasing cathode pressure. The temperature is found to be most sensitive, low water flow rates increase the inductive loop but show no clear trend on mass transport; the cathode pressure has a rather low influence. The inductive loop is strongly increasing with increasing current density, However, the highest current density of $2\ \mathrm{A} \cdot \mathrm{cm}^{-2}$ is rather low for future relevant operation points.

Franz et. al developed a dynamic electrochemical and thermal model to simulate the low-frequency inductive feature [113]. They postulated that the inductive loop occurs due to transient thermal effects. Therefore, they modelled transient thermal fluxes from the CCM to PTL and the flow field plus the surrounding. They used the experimental data of this chapter. For the whole frequency range, including the inductive loop, they see a proper agreement with the experimental data. They found that the inductive feature consists of three separate processes, the first one (at higher frequencies) is referred to dynamic temperature variation of the CCM. The other two processes are originated from dynamic temperature variation of the flow field or the end plate of the cell. With fixing the flow field temperature (cell housing under isothermal conditions) the second and third inductive loop disappeared in the simulative results as no transient thermal flux is in this case present. Possible methods to experimentally validate this hypothesis is given in the Outlook of this chapter, see Section 2.5.

2.2 Experimental

2.2.1 Test Cells and Test Benches

The measurements discussed in Section 2.3.1 are conducted using different materials for CCMs and PTLs, as well as different test cell housings and test benches. The measurements were conducted at two different laboratories at Fraunhofer ISE and KIT IAM-ET. The investigations at KIT IAM-ET were carried out by Debora Brinker and are also part of [86].
At Fraunhofer ISE, the *ISE reference cell* with an active area of $4\ \mathrm{cm}^2$ [59] and the AtC cell, developed within this thesis, were used at an in-house developed test bench; for a detailed description see Section 4.2.2. At KIT IAM-ET a commercial EL10 cell from Schaeffler Technologies AG & Co. KG, Germany with an active area of $10\ \mathrm{cm}^2$ was used at a commercial E20 test bench from Greenlight Innovation, Canada. State-of-the-art CCMs of three different commercial suppliers are investigated. As PTLs different combinations of coated and uncoated titanium-based fiber materials as well as carbon-based GDLs are used in the different setups. To investigate the electrochemical behavior, the test benches were operated with different electrochemical workstations and power potentiostats from Zahner-Elektrik GmbH & Co. KG, Germany. Table 2.1 provides an overview of the used testing setups, which are compared with each other in Section 2.3.1.

Table 2.1: Overview of different testing setups for the measurements discussed in Section 2.3.1.

Setup	Test cell	CCM	PTL-anode	PTL-cathode	Test bench
1	ISE ref. cell	Commercial 1	Titanium-based fiber	Titanium-based fiber	ISE in-house
2	ISE ref. cell	Commercial 2	Coated titanium-based fiber	Carbon-based GDL	ISE in-house
3	Schaeffler EL10	Commercial 3	Coated titanium-based fiber	Carbon-based GDL	Greenlight Innovation
4	ISE AtC cell	Commercial 1	Titanium-based fiber	Titanium-based fiber	ISE in-house

The measurements of Sections 2.3.3, 2.3.4, 2.3.6, and 2.3.7 are conducted with the Fraunhofer ISE reference cell at the laboratories at Fraunhofer ISE and KIT IAM-ET. Coated titanium-fiber PTLs with a thickness of 250 μm at both anode and cathode and a high-loading commercially available CCM are employed.

The measurements employing reference electrodes are conducted with a test cell developed at Fraunhofer ISE and a test cell developed by Leibniz University of Hannover, Germany, for further details see Section 2.2.2.

2.2.2 Reference Electrode Setups

To separate the anodic and cathodic polarization processes a test cell with implemented reference electrode can be a helpful approach [114–116]. In this study two different types of reference electrodes are employed to identify whether the inductive process occurs at anode, cathode or both electrodes. Therefore, one test cell developed by Fraunhofer ISE and another one by Leibniz University Hannover are used.

The test cell at Fraunhofer ISE presents an active area of 23 cm^2 next to a reference electrode of 1 cm^2 created by laser ablation. The concept was presented by Gerteisen [117] in a case study on fuel cells. The reference electrode employs a concept of a catalyst, which is electrically insulated from the active catalyst layer without harming the membrane. The electrical insulation is enabled by segmented bipolar plates and PTLs. Figure 2.1 shows a schematic diagram of this approach.

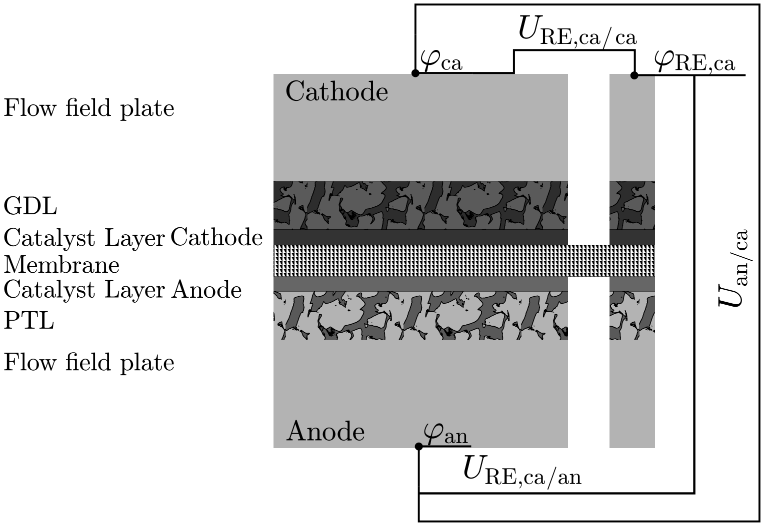

Figure 2.1: Schematic diagram of the laser ablation reference electrode setup - according to [117].

For each reference electrode, the voltage $U_{\mathrm{RE,ca/an}} = \varphi_{\mathrm{RE,ca}} - \varphi_{\mathrm{an}}$, $U_{\mathrm{RE,ca/ca}} = \varphi_{\mathrm{RE,ca}} - \varphi_{\mathrm{ca}}$, and the cell voltage ($U_{an/ca} = \varphi_{\mathrm{an}} - \varphi_{\mathrm{ca}}$) are measured. Herewith, anodic and cathodic contributions can be separated. These measurements can be done for the DC cell operation and EIS. The laser ablation allows for a good alignment of the electrode catalyst layers and, therefore, a homogeneous distribution of the potentials [117, 118]. The impedance spectra are collected applying reference electrodes present on the anode and cathode. This approach should enable a separation of polarization phenomena at anode and cathode, respectively. It should be noted that contributions from a portion of the membrane and from the catalyst layer-membrane interface as well as artifacts according to [119] have to be considered. The test cell is provided with gold-coated flow fields on both sides and $1\ \mathrm{mm}$ thick titanium fiber PTLs. The tested CCM is commercially produced and presents a $120\ \mu\mathrm{m}$ thick membrane with $2.3\ \mathrm{mg} \cdot \mathrm{cm}^{-2}$ of iridium oxide and $0.35\ \mathrm{mg} \cdot \mathrm{cm}^{-2}$ platinum on the anode and cathode electrodes, respectively. The measurements were carried out at an in-house built test bench at Fraunhofer ISE. Further information can be found elsewhere [2]. This type of reference electrodes is also employed in the AtC cell, see Section 4.2.1.

The reference electrode used at Leibniz University Hannover is a salt bridge reference electrode which is incorporated into the $4\ \mathrm{cm}^2$ test cell by Fraunhofer ISE mentioned above. The salt bridge is integrated through one of the end plates, terminating in the flow field. The other end of the salt bridge is immersed in a $0.5\ \mathrm{M}$ sulfuric acid solution. An external reference electrode (Ag/AgCl RE from Bioanalytical Systems, Inc., USA with a $3\ \mathrm{mol} \cdot \mathrm{l}^{-1}$ NaCl solution) is employed in the same solution. The salt bridge requires humidification during operation to maintain protonic conductivity. Refer to [120] for a comprehensive overview. Regarding salt bridge reference electrode preparation, the PTL undergoes a 15-minute ultrasonic bath cleaning, followed by impregnation at the point touched by the salt bridge tip. This impregnation involves applying $1\ \mu\mathrm{l}$ of a 5 wt% Nafion solution. Platinum-coated titanium fiber PTLs are used for both the anode and cathode, along with the standard CCM used in this work. The measurements have been performed at an in-house built test bench at Leibnitz University of Hannover, see Section 2.2.1.

2.2.3 Silicon Impregnation

Since capacitive diffusion processes and the inductive loop appear at similar time constants it is hard to investigate the share of both processes on the total cell resistance. From previous studies it is known that a bad transport of gas in the PTL increases diffusion related resistances since gas molecules block active catalyst parts [35, 65, 121, 122], which can be detected due to additional capacitive processes at low frequencies in impedance spectra. To increase the diffusion resistances, the PTL used in one setup of this study is impregnated with liquid and hardening silicon to impede the gas transport and increase the gas concentration in the catalyst layer on purpose. It is assumed that there is very little impact on water transport by the silicon impregnation compared to the gas transport due to water soaking tests. To ensure electrical contact to the surrounding components (CCM and bipolar plate) the silicon on the PTL surface is grinded and only the inner pores remain blocked. As can be seen in the results, the series resistance of the impregnated PTLs is always higher compared to the measurements with unmodified PTLs. This needs to be attributed to remaining silicon on the PTL surface leading to increased contact resistance. Treating the PTL on the full area was only possible for the cathode. For the anode a drastic increase of mass transport overpotential was observed which exceeded the voltage limit. Therefore, the silicon treatment on the anode PTL was only done for half the area. In all measurements only one PTL is impregnated, the respective other remains unmodified. A commercial CCM is used for these measurements. Pictures of the modified PTLs are given in [2].

2.2.4 CCM Preparation for Structural Parameter Variation

Anode Catalyst Layer Variation

To understand the influence of CCM morphology on the inductive loop, anode catalyst layers with varying iridium oxide particle types and number or printed layers are produced at Fraunhofer ISE using screen printing. The catalyst material is provided by Heraeus Precious Metals GmbH & Co. KG, Germany. The cathode catalyst layers and the membrane (FS-990-PK PEM) provided by Fumatech BWT GmbH, Germany are the same for each produced CCM.
Two different types of anode catalyst powder which are differentiated in “fine” (mean particle size $1.3\ \mu\mathrm{m}$) and “coarse” (mean particle size $4.7\ \mu\mathrm{m}$) are used. The iridium content for both catalyst powders is 83 wt%. All catalyst layers have the same ionomer solid content of 16.67 wt% and comparable ink preparation. The catalyst layers are screen-printed on a PTFE decal foil and later transferred by hot pressing onto the membrane. The catalyst loading per print was varied by using different meshes for screen printing. A summary of the CCMs used in this study is given in Table 2.2.

Membrane Thickness Variation

To investigate the influence of different membrane thicknesses on the inductive loop three different Nafion-based membranes are used and coated with the same anodic and cathodic catalyst layer at Fraunhofer ISE. The anode catalyst powder is provided by Alfa Aesar, USA and the cathode catalyst powder by Umicore AG & Co. KG, Germany. The anode has a loading of $(1.10 \pm 0.01)\ \mathrm{mg_{Ir}} \cdot \mathrm{cm}^{-2}$ with 16.67 wt% ionomer and the cathode $(0.50 \pm 0.03)\ \mathrm{mg_{Pt}} \cdot \mathrm{cm}^{-2}$

with 29.49 wt% ionomer. The iridium content of the anode catalyst particles is 84.5 wt%. The employed membranes are N212 (50 μm), N115 (125 μm) and N117 (178 μm).

Table 2.2: CCM properties of Fraunhofer ISE in-house produced CCMs used for anode catalyst layer variation.

CCM	**Anode loading** / $\mathrm{mg_{Ir} \cdot cm^{-2}}$	**Anode catalyst type**	**Anode number of layers**	**Cathode loading** / $\mathrm{mg_{Pt} \cdot cm^{-2}}$
1	0.83 ± 0.05	Fine	1	0.400 ± 0.007
2	0.736 ± 0.026	Coarse	1	0.396 ± 0.013
3	0.845 ± 0.015	Coarse	2	0.404 ± 0.008

2.2.5 Electrochemical Measurement and Analysis

The impedance measurements are performed in galvanostatic mode at different DC bias current densities ranging from $0.5\ \mathrm{A \cdot cm^{-2}}$ to $6\ \mathrm{A \cdot cm^{-2}}$. The default operation point in this study is at $60\ ^{\circ}\mathrm{C}$ and ambient pressure. At KIT the water was supplied only at the anode with a flow rate of $15\ \mathrm{ml \cdot min^{-1} \cdot cm^{-2}}$ and at Fraunhofer ISE a flow rate of $25\ \mathrm{ml \cdot min^{-1} \cdot cm^{-2}}$ was fed to anode and cathode. An alternating current with a small perturbation of 10% of the DC current is applied. The spectra were measured over a frequency range of $100\ \mathrm{kHz}$ to $100\ \mathrm{mHz}$ with a frequency resolution of 10 steps per decade and an integration time according to 10 periods.

Before the electrochemical characterization a well investigated break-in procedure is performed. For the commercial CCM a voltage of $1.7\ \mathrm{V}$ is applied and held for 12 hours. For the CCMs prepared at Fraunhofer ISE a specific break-in procedure is done mainly consisting of repeated polarization curves and constant voltage mode for several hours. Before each impedance measurement the stability of the cell is checked regarding the voltage response during a holding time of 5 minutes at the current DC-bias.

The quality of the impedance data is analyzed by the Kramers Kronig test, see Section 1.6.2. The data itself is analyzed by DRT with subsequent ECM (see Section 1.6.3 and 1.6.4), the fitting results are discussed in Section 2.3.3. To choose the optimal value for the Tikhonov regularization parameter λ, the impedance data is analyzed using DRT with different values for λ shown in the Appendix Figure A.1 for the measurement of Figure 2.4 at $3\ \mathrm{A \cdot cm^{-2}}$. A value of $\lambda = 0.0001$ clearly shows too many peaks which cannot be attributed to physico-chemical processes, $\lambda = 0.01$ showed a logical number of peaks but cannot properly resolve the charge transfer region. Performing this analysis for a number of impedance spectra measured at varied operating conditions, the optimal value for these measurements was found to be $\lambda = 0.005$. This result is also in good agreement with the values used for PEM fuel cell studies [79] with this approach being slightly more conservative to minimize misinterpretation.

2.3 Results

2.3.1 Presence of Low-Frequency Inductive Features

Low-frequency inductive loops are reproducible phenomena which occur in all PEMWE cells used within this study. Before testing, all CCMs were conditioned in a comparable way. The measurements shown in Figure 2.2 were conducted at a temperature of $80\ ^{\circ}\mathrm{C}$ and pressure of 1 bar at Fraunhofer ISE and at ambient pressure at KIT IAM-ET.

CCMs, testing environments, and current densities are varied. In order to exclude influences by drift and nonlinearities, the Kramers Kronig test [75] was performed for all measurements and is exemplarily shown for the measurement at $7\ \mathrm{A} \cdot \mathrm{cm}^{-2}$. In most cases Kramers Kronig residuals below 1% were observed, only Figure 2.2 c) shows high residuals at high frequencies, which are related to inductive artefacts due to wiring and the test cell housing. For the low-frequency region analyzed in this work, the Kramers Kronig residuals are on an acceptable level.

In all measurements shown in Figure 2.2, a significant inductive loop is visible. Increasing current density leads to a decrease of (positive) capacitive and an increase of (negative) inductive polarization resistance. With these results, it can be demonstrated that this behavior is independent from the CCMs and PTLs, test cell housing and test benches used in this work. Setup 1, 2 and 4 show a quite comparable polarization behavior and tendency with increasing current density. Also, the frequency at which the low-frequency inductive behavior starts is very similar. Setup 3 and 4 show high-frequency inductance due to wiring, it is referred to various publications for detailed understanding [81, 123, 124]. However, there are differences in the low-frequency region in the spectra of setup 3. An additional capacitive process most likely related to diffusion at frequencies of approximately 1 Hz can be seen. Therefore, the inductive behavior is only dominant at lower frequencies.

Additional impedance measurements using setup 1 at the same bias current but with varying current amplitude show no effect on the inductive loop, see Appendix Figure A.2. This also hints that the inductive loop is no measurement artifact but related to a physico-chemical process in the cell affecting its DC performance.

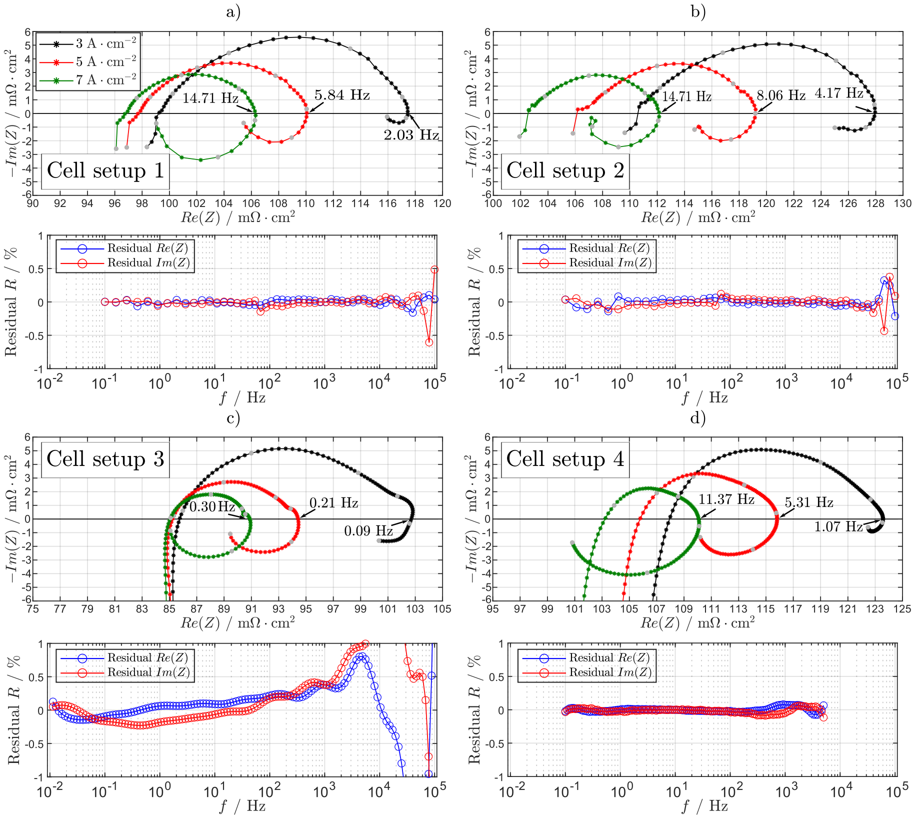

Figure 2.2: Comparison of inductive loops of different test cell setups (1-4). The residual of the Kramers Kronig test is exemplarily shown for each measurement at 7 $\mathrm{A \cdot cm^{-2}}$. The measurements of setup 3 were conducted at KIT IAM-ET and are also part of [86]. Figure reformatted and taken from [1].

2.3.2 Comparison between Impedance and Polarization Curve Measurements

To understand the impact of the inductive behavior on the cell performance, the polarization curve of setup 3 (see Table 2.1) is exemplarily compared with the impedance spectra at different current densities, see Figure 2.3. Therefore, specific resistances, as the HFR, here referred to as the series resistance (R_{Series}), and low-frequency resistance (R_{LFR}) are determined by the intersections with $-Im(Z) = 0$ at high and medium frequencies in the spectra and the resistance at the minimal frequency of 10 mHz (minimal-frequency resistance, R_{MFR}). The resistance of the polarization curve (R_{DC}) was determined by calculating the local slope of the polarization curve at the investigated operation points, see Figure 2.3 a).

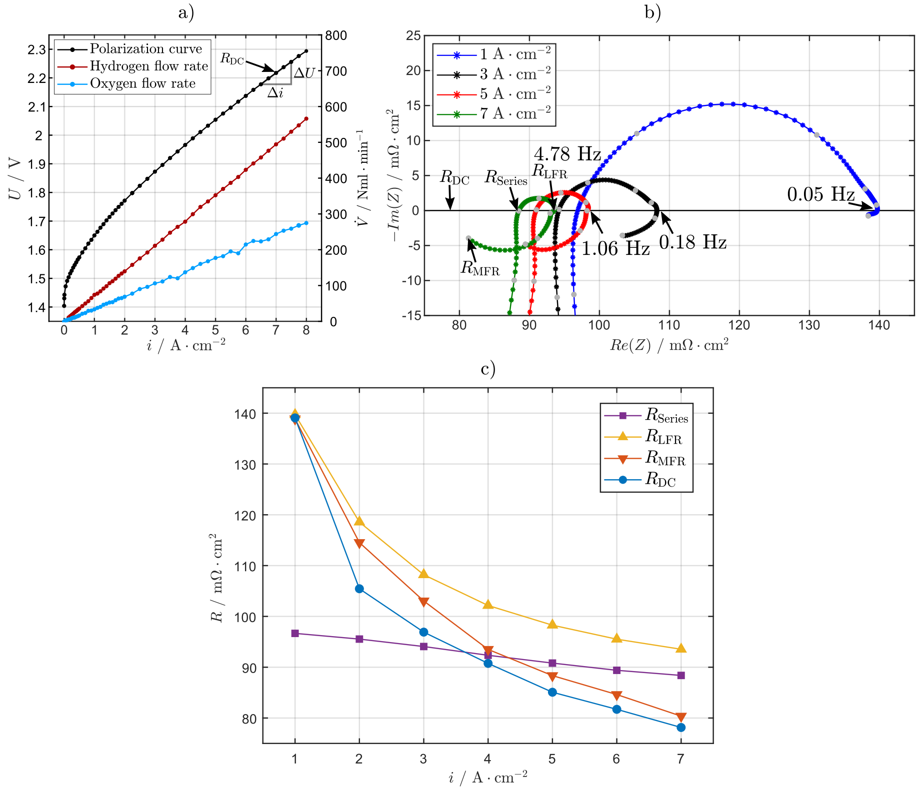

Figure 2.3: a) Polarization curve and produced hydrogen and oxygen standard flow rates of setup 3, b) EIS of setup 3 at different current densities, ambient pressure and 60 °C. The specific resistances (R_{Series}, R_{LFR} and R_{MFR}) and the DC resistance R_{DC}, calculated from the local slope of the polarization curve a), are exemplarily shown for the measurement at 7 $\mathrm{A \cdot cm^{-2}}$. c) Specific resistances of the EIS and the polarization curve over the current density. The measurements were conducted at KIT IAM-ET and are also part of [86]. Figure reformatted and taken from [1].

To be sure that the inductive processes are affecting the gas production, the measured volume flow of produced hydrogen and oxygen during the polarization curve are shown. At low flow rates ($< 20\ \mathrm{Nml \cdot min^{-1}}$) the flow meters are too unprecise to be evaluated. Between 1 $\mathrm{A \cdot cm^{-2}}$ and 8 $\mathrm{A \cdot cm^{-2}}$ a mean ratio between hydrogen and oxygen flow rate of 2.03 ± 0.06 was measured. With the most pessimistic evaluation (lowest value within accuracy of the used mass flow meters)

the Faradaic efficiency was $\eta_{\mathrm{F,H_2}} = (0.99 \pm 0.01)$.
Figure 2.3 b) shows the EIS at different current densities. The specific resistances are marked for the EIS at $7\ \mathrm{A \cdot cm^{-2}}$ to show the evaluation method, which was used for every operation point. The value of R_{DC} taken from the polarization curve is indicated as well. Figure 2.3 c) shows the evaluated resistances for current densities from $1\ \mathrm{A \cdot cm^{-2}}$ to $7\ \mathrm{A \cdot cm^{-2}}$. For a low current density of $1\ \mathrm{A \cdot cm^{-2}}$ the inductive behavior is small and so R_{LFR} and R_{MFR} are approximately similar with R_{DC}. With increasing current density these values start to diverge. R_{LFR} shows at higher current densities a significantly higher value than R_{DC}. Contrary to this, R_{MFR} shows analogous tendency compared with R_{DC}. The difference between R_{DC} and R_{MFR} is due to the fact that R_{MFR} is the resistance measured for the lowest frequency of $f = 10\ \mathrm{mHz}$ corresponding to a time constant $\tau \approx 16\ \mathrm{s}$ whereas the delay time during the polarization curve measurement was $120\ \mathrm{s}$. The extrapolation of the spectra towards lower frequencies indicates a good agreement with R_{DC}. In the field of PEMFC it is already reported that R_{DC} can reach values lower than R_{LFR} [98, 101]. In this case a part of the capacitive polarization losses is compensated by the low-frequency inductive process. It is here shown that in PEMWE at extreme conditions, the R_{DC} has even lower values than the series resistance. The negative resistance of the low-frequency inductive processes not only fully compensates the capacitive polarization resistance but additionally a significant part of the series resistance. It should be noted that the series resistance may not have been accurately determined due to high frequency inductances as mentioned above. These might lead to an overestimation of the series resistance. Other reasons could be that the series resistance is measured too high due to the fact, that there are slow processes decreasing the membrane resistivity which are only recognizable at low frequencies. Examples for this are different states of humidification due to slow water transport and changes of catalyst coverage as suggested for PEMFC [101, 124, 125].

2.3.3 DRT and ECM Analysis

To investigate the inductive effect at low frequencies, a more detailed current density variation was performed at Fraunhofer ISE with the Fraunhofer ISE reference cell, shown in Figure 2.4 a) in the Nyquist and Figure 2.4 b) in the respective DRT representation. Looking at the Nyquist plot, at low current densities no inductive loop is visible, but clearly increasing with increasing current density. At $6\ \mathrm{A \cdot cm^{-2}}$ the capacitive and inductive polarization is very equal in magnitude and so the high frequency series resistance is very comparable with the resistance at $100\ \mathrm{mHz}$ which is close to the direct current resistance detectable from polarization curve measurements. For more information on the comparison to polarization curve measurements see Section 2.3.2. At high frequencies ($> 30\ \mathrm{kHz}$) inductivities are detectable which can be related to wiring issues.

Focusing on the DRT plot it can easily be seen that the inductive loop is increasing with increasing current density with a shift in frequency between 0.2 Hz to 2 Hz.

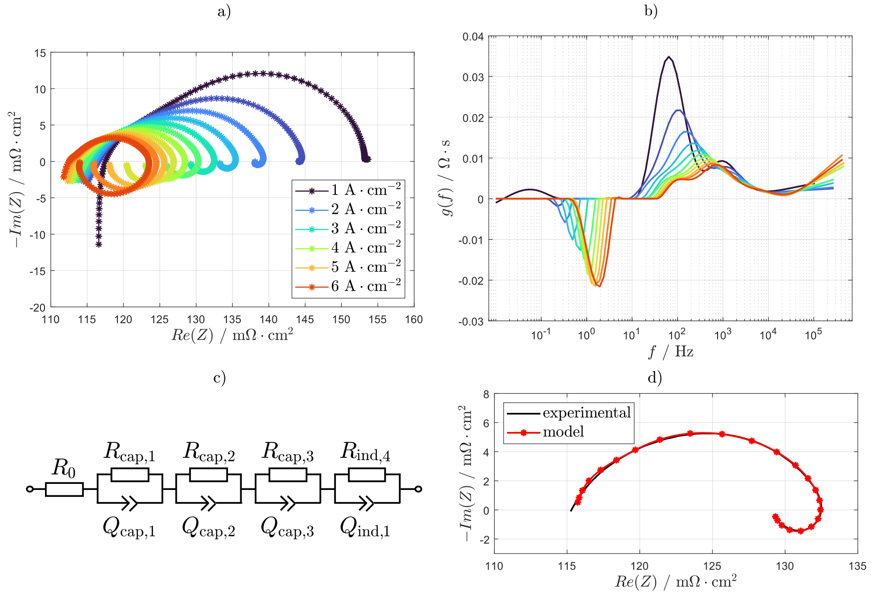

Figure 2.4: a) Nyquist presentation of a current density variation, b) DRT analysis, c) ECM with RQ-elements and d) ECM fit results at 3 $A \cdot cm^{-2}$ for ECM from c). The DRT and ECM analysis were conducted at KIT IAM-ET and are also part of [86]. Figure reformatted and taken from [2].

The large capacitive loop which can be related to the anodic charge transfer resistance is decreasing with a shift towards higher frequencies from 60 Hz to 800 Hz. Between 20 Hz and 100 Hz an additional peak gets visible with increasing current density which might be related to transport processes.

At frequencies around 1 kHz a process which is decreasing with current density is detectable which might be related to the comparably low charge transfer resistance of the cathode. At frequencies $> 10^4$ Hz there are further peaks visible, but the data cannot be analyzed due to cable inductivities.

Additional to this, a fundamental use of ECM with negative RQ-elements is presented to quantify the polarization magnitude of the inductive loop. The number of used RQ-elements are determined by the peaks detected using DRT. Therefore, here and in the following investigations, processes are numbered by descending frequency and it is distinguished between capacitive and inductive processes. Figure 2.4 c) shows the ECM for the RQ-element approach and Figure 2.4 d), the fitting results for a current density of 3 $A \cdot cm^{-2}$. The fit shows a very good agreement with the impedance measurement at low frequencies, which is clearly the focus of this chapter. In the frequency range of charge transfer resistance (100 Hz to 1000 Hz) the fit quality is suitable. For higher frequencies small deviation are occurring which could be related to the influence by wiring on the measurement and the fact that no inductance element is used in the model.

2.3.4 Sensitivity Analysis of Operational Parameters

To get an overview on the effect of different operating parameters on the inductive loop, impedance measurements at different temperatures, pressures, water flow rates (anode side) and current densities are performed. For the flow rate variation, the water flow was decreased in $3.75\,\mathrm{ml}\cdot\mathrm{min}^{-1}\cdot\mathrm{cm}^{-2}$ ($15\,\mathrm{ml}\cdot\mathrm{min}^{-1}$) steps, starting from $18.75\,\mathrm{ml}\cdot\mathrm{min}^{-1}\cdot\mathrm{cm}^{-2}$ ($75\ \mathrm{ml}\cdot\mathrm{min}^{-1}$) and going down to $3.75\ \mathrm{ml}\cdot\mathrm{min}^{-1}\cdot\mathrm{cm}^{-2}$ ($15\ \mathrm{ml}\cdot\mathrm{min}^{-1}$). The results of the last two steps were discarded due to high fluctuations in the temperature.

To compare the size of the inductive loop of each measurement the ASR of the inductive part was determined. This was done by fitting the data with the RQ model, see Figure 2.4 c). The results are shown in Figure 2.5. The total error related to the accuracy of the measurements and the fitting was determined to be $< 6\ \%$. The measurement error is mainly related to small fluctuations in temperature and flow rate.

Figure 2.5 shows the current density variation with a clear trend visible. With increasing current density and therefore increasing voltage (measured voltages marked in the top x-axis) the negative ASR of the inductive part increases. For the temperature variation, shown in Figure 2.5, a clear trend is visible as well. With increasing temperature, the negative ASR decreases. This behavior might also be associated with the higher voltage occurring at the lower temperature for the same current density. A temperature and current density variation were also performed in [1], which show the same tendency. The flow rate variation and the pressure variation show no significant impact on the negative ASR of the inductive loop (Figure 2.5). It should be noted here that the water flow rate is comparably high and could not be lowered further due to arising temperature instability at the test rig, which is attributed to a cooling problem since the test cell is not designed for such low flow rates and has no external heating management implemented. Therefore, the influence of the water flow rate on a stoichiometric level could not be investigated. For PEM fuel cells Meyer and Zhao reported a strong influence of the inlet air flow on the inductive loop. They oscillated the inlet air flow depending on the applied frequency of the AC current density signal during impedance measurements and observed increasing inductive loops [95].

In the measurement shown here it was made sure that the inlet water flow is not affecting the impedance measurements.

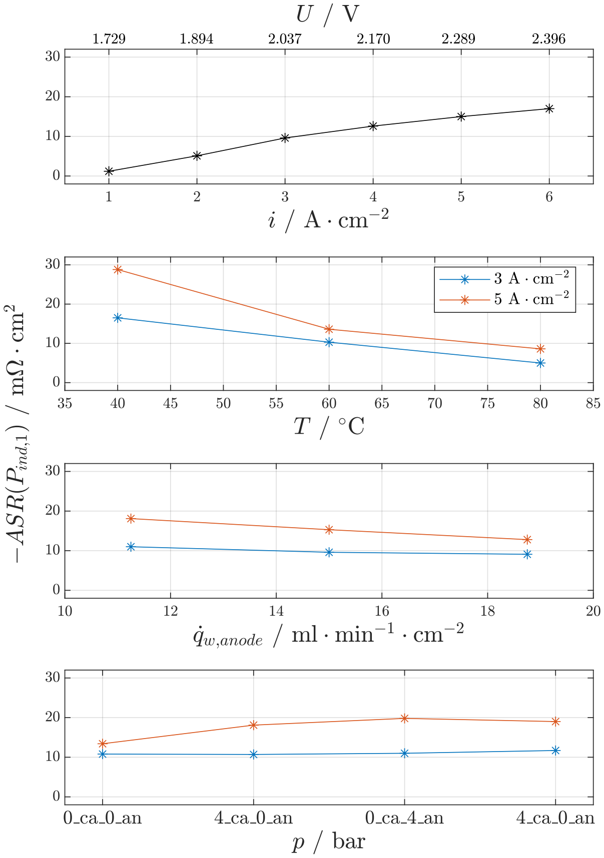

Figure 2.5: ASR values of the inductive feature for the following variations from top to bottom: current density variation from $1\ \mathrm{A \cdot cm^{-2}}$ to $6\ \mathrm{A \cdot cm^{-2}}$, temperature variation from $40\ ^\circ\mathrm{C}$ to $80\ ^\circ\mathrm{C}$, water flow rate variation from $7.5\ \mathrm{ml \cdot min^{-1} \cdot cm^{-2}}$ to $18.75\ \mathrm{ml \cdot min^{-1} \cdot cm^{-2}}$ and pressures of $0\ \mathrm{bar_g}$ to $4\ \mathrm{bar_g}$. The measurement and evaluation were conducted at KIT IAM-ET and are also part of [86]. Figure reformatted and taken from [2].

Only chaotic, non-frequency depending deviations occurred due to the mass flow oscillations $< 1\ \%$. Since the pressure does not show any large and explicit impact on the ASR, it is rather unlikely that the process behind it is related to a process in the gas phase.

2.3.5 Separation of Anodic and Cathodic Low-Frequency Impedance

In Figure 2.6 the results of the two cell setups from Fraunhofer ISE (laser ablation reference electrode) and Leibniz University Hannover (salt bridge reference electrode) are compared. It is important to underline that the two setups are different in their approach. For the laser ablation reference electrode, it is targeted to split the cell voltage in the center of the membrane (through-plane direction), therefore the Ohmic contribution can be seen at anode and cathode and the polarization resistance is divided into anodic and cathodic contributions.

Using the salt bridge reference electrode, the cell voltage is splitted at the catalyst layers protonic potential, therefore most of the Ohmic contribution is only seen at the electrode without implemented reference electrode (anode). The voltage at the electrode with the reference electrode only includes minor Ohmic resistances. The activation overpotential is separated into its contributions from the anodic OER and the cathodic HER.

For both setups it should be noted that they have uncertainties as discussed by Adler at el. [114, 119] and the results have to be regarded with care and are only used to hint in a direction to which side the inductive behavior might be connected. Any quantification by fitting the spectra should be avoided.

Figure 2.6 a) and b) show the Nyquist and DRT presentation at $60\ ^\circ\mathrm{C}$ and a temperature variation between $40\ ^\circ\mathrm{C}$ and $80\ ^\circ\mathrm{C}$ of the laser ablation reference electrodes.

The measurements conducted with the reference electrode at anode and cathode are excellently consistent. The inductive process at low frequencies is only observable at the anode with two significant peaks at > 0.1 Hz and > 1 Hz. In contrast to this, capacitive polarization is only seen at the cathode, which should be related to diffusion processes at these low frequencies.

The temperature dependency of the DRT analysis supports this interpretation since the diffusion polarization resistances (< 100 Hz) are decreasing with increasing temperature. The change in the high frequency inductive part of the spectra of cathode and full cell might be attributed to the effects described in [114]. Thus, a part of the inductive behavior at the anode might be related to an effect induced by the reference electrode.

Figure 2.6 c) and d) show the results of the salt bridge reference electrode by Leibniz University Hannover. In Figure 2.6 c) the Nyquist representation is shown for the mean cell as well as the anode versus reference and the cathode versus reference. For all these measurements the reference was placed at the cathode side. The cathode impedance shows only capacitive polarization behavior and the anode shows also an inductive contribution at low frequencies. It should be noted here that the measurements of the cathode against reference electrode (orange curve) exhibited Kramers Kronig residuals with a mean value of 10% (neglecting the high frequency inductance due to wiring artifacts) most likely due to a bad signal-to-noise ratio.

In Figure 2.6 d) the DRT representation for the measurements is shown. As for the Fraunhofer ISE setup, the cathode shows only a capacitive behavior at low frequencies, which might be connected to diffusion processes. The anode on the other hand shows an inductive peak in the low-frequency region and also capacitive peaks in the high frequency region.

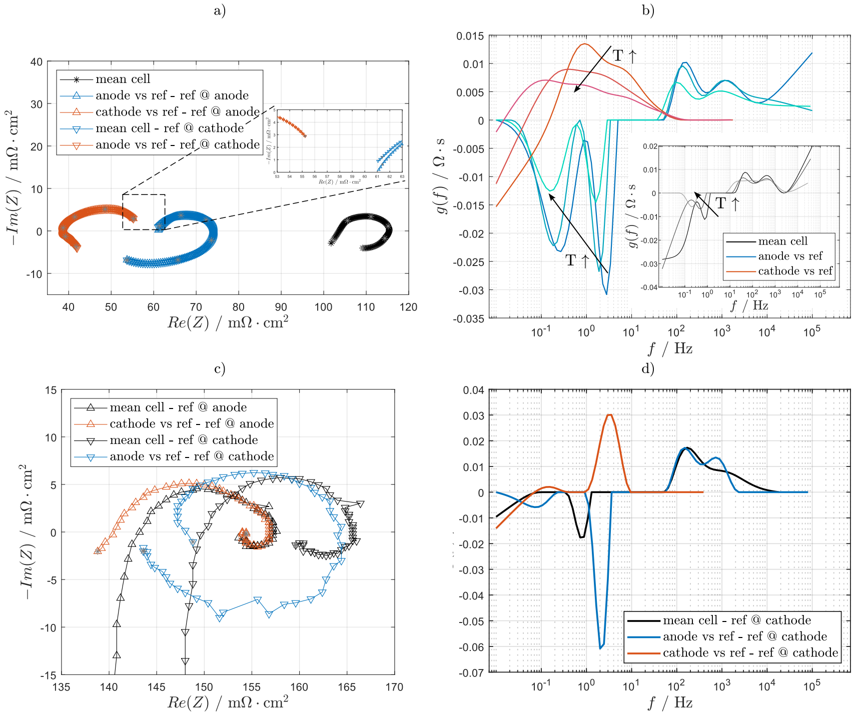

Figure 2.6: Results of impedance measurement with reference electrodes at $4.5\ \mathrm{A \cdot cm^{-2}}$ and ambient pressure. a) Nyquist presentation at 60 °C and b) DRT analysis of impedance measurements at 40 °C, 60 °C and 80 °C with the Fraunhofer ISE reference electrode setup. c) Nyquist presentation and d) DRT analysis of the reference electrode of Leibniz University Hannover at 60 °C. Figure reformatted and taken from [2].

These totally different reference electrode setups both show that the inductive loop only occurs at the anode. No inductive loop contribution from the cathode in all conducted measurements are detected. These results are in consistency with a number of investigations on PEM fuel cells, showing that the low-frequency inductive loop appears at the air electrode [101].

2.3.6 Superimposing Mass Transport Processes

With the silicon impregnation mass transport related polarization resistances are purposely increased at anode and cathode, respectively. This shows the interference between transport related capacitive polarization and the inductive loop. The results of this study are summarized in Figure 2.7. Figure 2.7 a) shows the polarization curve of the untreated measurement (default setup, black) and the silicon impregnated PTLs at anode (blue) and cathode (orange).

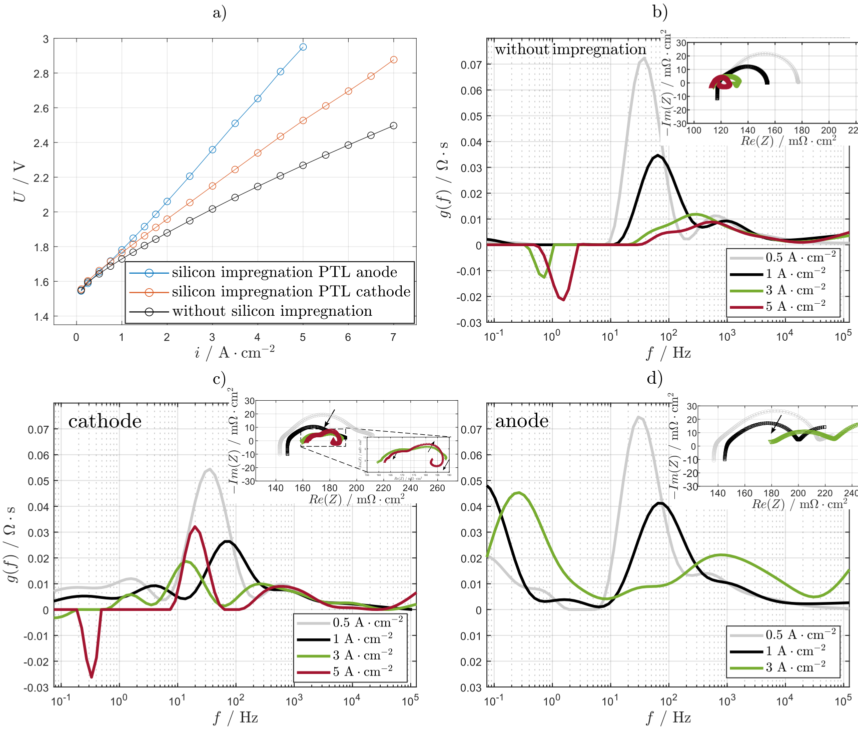

Figure 2.7: Silicon impregnation of PTLs at the default operation point. a) Polarization curve of silicon impregnated setups at anode and cathode and the reference without PTL treatment. DRT and EIS presentation at different current densities b) untreated, c) cathode impregnation and d) anode impregnation. Figure reformatted and taken from [2].

The respective other half cells each remained untreated. Even by focusing on DC measurements only, differences in Ohmic resistance (steeper linear slope at low current densities) and mass transport resistances (order > 1 of the polarization curve at higher current densities) are observable when comparing the not impregnated setup to the impregnated ones, with the anode impregnation showing the strongest impact. To compare the results in more detail, the DRT as well as the Nyquist presentation are given in Figure 2.7 b-d) showing the not impregnated setup, the cathode impregnation and the anode impregnation, respectively.

The Nyquist presentation reveals an increase of Ohmic resistance for the impregnated setups with increasing current density. Usually, with increasing current density the series resistance decreases due to temperature increase of the CCM which can be seen for the setup without impregnation in Figure 2.4 a).

It is assumed that the blocked gas at the interface of the CL and the PTL occupies contact points and therefore increases the contact resistance with increasing amount of gas at higher current densities. For the anode impregnation, see Figure 2.7 d), a second capacitive semicircle as well as an extra peak in the DRT at lower frequencies can be seen which is increasing with current density. The comparison with the Nyquist presentation of the untreated setup, see Figure 2.7 b,) reveals that the inductive loop cannot be seen as it is superimposed by anodic mass transport polarization. Current densities above $3\ \mathrm{A} \cdot \mathrm{cm}^{-2}$ were too unstable to conduct EIS for the impregnation of the anode PTL.

In contrast to this, the impregnation at the cathode, see Figure 2.7 c), shows that the mass transport at the cathode occurs at higher frequencies (between 1 Hz and 20 Hz, shifting to higher frequencies with current density) and is less interfering with the inductive loop, see zoom in at $3\ \mathrm{A} \cdot \mathrm{cm}^{-2}$ and $5\ \mathrm{A} \cdot \mathrm{cm}^{-2}$ in Figure 2.7 c). While the peak at 40 Hz (most-likely related to charge transfer) is decreasing with current density, both the capacitive (mass transport related) and the inductive loop are increasing. The DRT analysis, see Figure 2.7 b-d), shows clearly that the anodic transport polarization is happening at very similar frequencies as the inductive loop (between 0.1 Hz to 0.5 Hz). The cathode diffusion peak appears slightly higher than the inductive loop of the untreated setup between 1 Hz and 2 Hz and is not directly superimposing the inductive loop. The capacitive peak at 10 Hz is also significantly increased compared to the untreated setup, which might also be related to a cathodic transport process. It should be noted that at higher frequencies ($> 10^2$ Hz) also the charge transfer process is influenced by the silicon treatment of the PTLs. It is assumed that this is related to lower electrical and ionic contacting due to silicon, which remains on the PTL surface. This also explains why the silicon treatment at the anode has a higher influence at these frequencies since the kinetic overpotentials are usually more relevant compared with the cathode. Herewith, it is shown that with increasing current density besides the inductive also the mass transport polarization is increasing and that the inductive process is strongly depending on the anode side which is consistent with the reference electrode measurements, see above.

2.3.7 Structural Parameter Variation

2.3.7.1 Anode Catalyst Layer

With a variation of the anode catalyst layer, the influence of structural properties on the low-frequency inductive behavior is discussed. Figure 2.8 shows the DRT analysis of the different CCMs listed in Table 2.2. Figure 2.8 a) and b) compare CCMs with similar iridium oxide loading at a current density variation. The anode catalyst layers in CCM 1 and CCM 2 were printed with one layer, with CCM 1 employing fine particles and CCM 2 coarse particles.

Additionally, in Figure 2.8 c) CCM 3 is shown with coarse particles, comparable loading as CCM 1 and CCM 2, but was produced printing two catalyst layers on top of each other. CCM 1 shows decreasing resistance contributions at frequencies $\sim$ 100 Hz with increasing current density, which can be related to charge transfer. An increasing resistance contribution with increasing current density is visible at frequencies between 5 Hz and 10 Hz which is assigned to anodic mass transport polarization. At frequencies < 1 Hz a second smaller capacitive loop is detectable for CCM 1, which is not increasing with current density, instead seemingly decreasing. Over the whole low-frequency range, no inductive process is detectable at all. CCM 2 on the other hand shows very comparable behavior to the commercial reference cell (see Figure 2.4).

The charge transfer resistance ($\sim$ 100 Hz) is decreasing and the inductive loop ($<$ 3 Hz) is increasing with increasing current density. All CCMs in this study contain the same ionomer to catalyst ratio of 0.2. It is assumed that due to the different particle sizes the ionomer binds differently to the iridium oxide particles surface leading to a significant variation in the ionomer and catalyst distribution within the catalyst layer. The fine particles (CCM 1) show a significant higher surface area than the coarse particles (CCM 2 and 3) which might enable a better binding of the ionomer leading to a denser packed catalyst layer by ionomer. This could result in the pores being more blocked for CCM 1 compared with CCM 2 and 3 and therefore the produced gas requires a higher capillary pressure to get out of the catalyst layer, resulting in increased mass transport resistance.

The seemingly decreasing capacitive behavior of CCM 1 at $<$ 1 Hz shows that the inductive process (increasing with current density and therefore reducing the capacitive polarization) is still existing but superimposed by the capacitive mass transport. Comparing CCM 2 with CCM 3 supports this analysis. Both CCMs have an equal loading but CCM 3 has two printed layers, therefore it is less dense packed resulting in less mass transport polarization and larger inductive loops at the same current density.

Figure 2.8 d) shows the temperature impact for 60 °C and 80 °C at $7\ \mathrm{A \cdot cm^{-2}}$ for CCM 1 and CCM 2. Decreasing temperature leads to increasing inductive behavior (see Figure 2.5), which is in this case clearly visible for CCM 2.

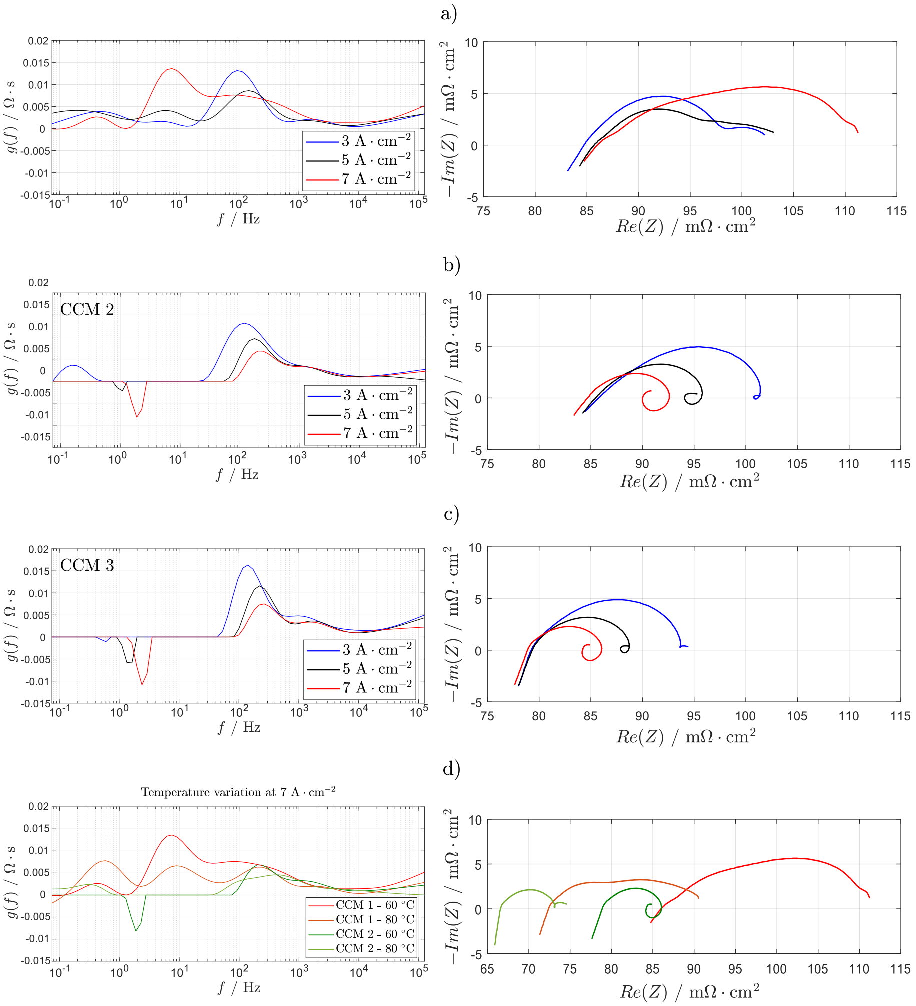

Figure 2.8: Comparison of DRT analysis and Nyquist presentation of the CCMs used for catalyst layer variation study, for an overview of the CCMs see Table 2.2. a) CCM 1, b) CCM 2 and c) CCM 3 during a current density variation. d) Temperature variation of CCM 1 and CCM 2. Figure reformatted and taken from [2].

In contrast to this, CCM 1 shows higher capacitive polarization at ~ 100 Hz at low temperatures, which is consistent with the higher (cathodic) mass transport related polarization behavior at lower temperature, see Figure 2.6 b). At < 1 Hz lower capacitive polarization is visible at low temperatures. This again proofs the assumption, that the inductive loop is still existing but not detectable in the impedance measurement since it is superimposed by mass transport polarization.

With this study the question, whether a denser packed catalyst layer has an impact on the inductive loop or if it is just superimposed by higher mass transport resistance can not be answered. It is only shown that the superimposing of (capacitive) mass transport polarization and the inductive loop is a relevant fact and highly sensitive on anodic catalyst layer properties.

2.3.7.2 Membrane Thickness

To investigate if the thickness of the membrane has an impact on the inductive loop, tests on cells with three different membrane thicknesses but the same anode and cathode catalyst layer are performed. To analyze the impact of the membrane, current density variations are conducted and compared with the results for the different membranes. At the same current density, different inductive loop sizes are observed, as presented in Figure 2.9 free of HFR, exemplarily shown at $5\ \mathrm{A \cdot cm^{-2}}$ in Nyquist, see Figure 2.9 a), and DRT, see Figure 2.9 b), presentation.

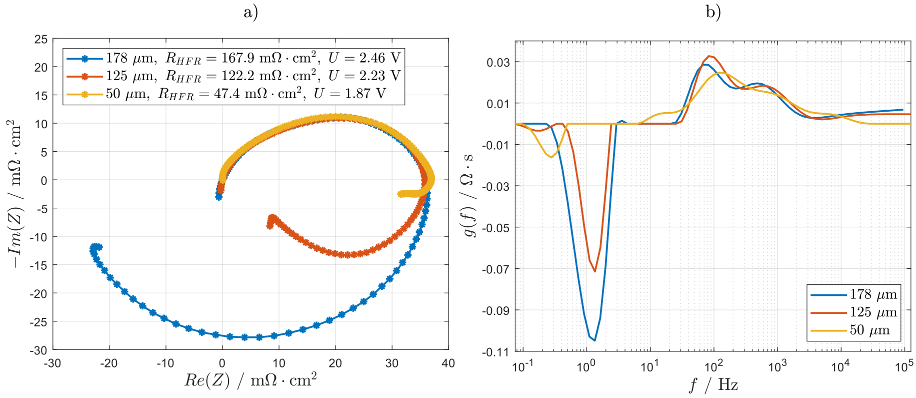

Figure 2.9: Membrane variation measurements shown in a) HFR-free Nyquist and b) DRT presentation for EIS at $5\ \mathrm{A \cdot cm^{-2}}$. The measurements are conducted at KIT IAM-ET and are also part of [86]. Figure reformatted and taken from [2].

Since severe artifacts at high frequencies are present, all impedance data above $30\ \mathrm{kHz}$ are removed. A strong dependency of the inductive loop to the membrane thickness is visible, where the thickest membrane shows the largest loop. As to be expected, the capacitive polarization phenomena at the electrodes are not affected by the membrane and a very good reproducibility of the electrodes regarding charge transfer and mass transport behavior is achieved despite of the different membranes.

What can also be seen from the measurement depicted in Figure 2.9 is that for the thickest membrane the inductive loop compensates the capacitive polarization processes complete and therefore leads to a negative DC resistance while excluding the HFR. The latter finding might suggest that the inductive loop is related to the membrane as otherwise the electrodes in total would exhibit a negative resistance. Anyhow, it has to be considered that the impedance only represents the differential resistance in the working point. As the electrode polarization is strongly nonlinear, the total polarization resistance of the electrodes at higher current densities is significantly larger than the polarization resistance measured by EIS.

2.4 Discussion

With the conducted measurements the origin is encircled and explained by structural and operational parameter dependencies of the inductive loop. In Table 2.3 the variations performed in this study and an overview on their impact on the inductive loop as well as possible explanations are given.

Table 2.3: Parameter variations performed in this study with impact description and possible reasons.

Variation	**Observation**	**Possible Reasons**
Current density	Larger loop at higher current/voltage	• Membrane effect • Anode catalyst
Temperature	Larger loop at lower temperature	• Membrane effect • Anode catalyst
Pressure	No impact	-
Water flow rate	No impact	-
Cathode, anode via reference electrode	Only anode spectra with inductive loop	• Membrane effect • Anode catalyst
PTL impregnation	Strong dependency to anode	• Mass transport overlap
Anode catalyst variation	Larger loop with coarse particles due to less mass transport	• Mass transport overlap
Membrane variation	Larger loop with thicker membrane	• Membrane effect

On the operation parameter side, the current density, temperature, pressure and the water flow rate on the anode side was varied. From these it is seen that the inductive behavior is affected by current/voltage as well as temperature. It should be noted here that the observed temperature effect might also be connected to the changed voltage at different temperatures due to increased membrane resistance. The pressure and water flow rate show no impact on the inductive loop. Furthermore, two setups with different types of reference electrodes were tested from which it is concluded that the inductive loop seems to be located at the anode side. In the reference electrode measurements and as well in some full cell measurements two inductive peaks are detectable in the DRT. This might hint that there is more than one physicochemical process contributing to the low-frequency inductive features. This is consistent with the findings for PEM fuel cell [85].

The PTL impregnation measurements show that there is an overlapping happening between inductive behavior and mass transport losses. If the mass transport losses are increased, the inductive loop is reduced and might even completely vanish. This phenomenon can also be seen in the anode catalyst layer variation with less dense packed catalyst layer due to coarse particles showing less mass transport and therefore a larger inductive loop.

This feature leads to a general problem in applying impedance spectroscopy to PEM water electrolysis cells. If two processes with negative and positive resistance contributions are overlapping in their frequency range, they cannot be properly resolved by impedance spectroscopy or any other kind of dynamic measurement.

The membrane thickness variation showed an increased inductive loop with increasing membrane thickness. These finding suggests that an effect inside the membrane is creating the low-frequency inductive behavior.

These results allow us to present and rate hypotheses, which could explain the inductive processes. Regarding PEM fuel cells three effects are reported: Platinum oxide effects, reaction intermediates and ionomer humidification [101, 126]. It should be noted that PEM fuel cells are significantly different compared with PEM water electrolysis cells. They strongly differ in used cell components and the way of operation (for example reactant stoichiometry). Therefore, a direct transfer of the hypotheses has to be viewed critically. Further investigations on the specific hypotheses are strongly suggested. It is believed that ionomer humidification from product water is hardly transferable to the operation here since a high water to gas ratio in the test cells can be presumed and the water supply to ionomer ensured. Also, no difference was noticed when supplying water to the anode and cathode or the anode only. Local phenomena due to water consumption and gas production at a certain catalyst particle are conceivable but with increasing current density the water amount should decrease at the catalyst and therefore show increasing instead of decreasing resistance. But still, a strong impact from the membrane thickness was observed. One explanation for this could be, that due to the electro-osmotic drag coupled with slow water diffusion the membrane gets internally way more humidified as only by supplying water to it. This could explain, why the inductive process is increasing with increasing current density (increasing proton transfer through the membrane) and with decreasing temperature. Since the lower the temperature the higher the membrane resistance, a better humidification could in this case be more sensitive. Additionally, it should be considered, that at high current densities the local temperature of the anode catalyst layer could be significantly higher due to the heat dissipation of the reaction. It might be the case that the water permeating in and through the membrane and ionomer has a higher temperature as the feed water and therefore amplify the resistance decrease at low frequencies.

The other two effects reported in PEM fuel cells, platinum oxide effects and reaction intermediates, are both related to electrochemical phenomena at the catalyst surface. Both are potential driven and would lead to a larger inductive loop at higher voltages, which would be in consistency with the findings in this chapter. Transferred to the PEM electrolysis case and with keeping the findings in mind, that the inductive loop is coupled with the anode side, a similar hypothesis could be the change of iridium oxidation states with the voltage. Hrbek et al. [126] measured the iridium oxidation state during PEM water electrolysis operation with varying voltages. They show that when changing the operation point between 2 V down to open circuit voltage (OCV) and then up to 2.5 V a reduction of iridium oxide to Ir^0 (iridium black) can occur among the usual states during operation of Ir^{+4} and Ir^{+6}. The change of the iridium oxidation state could lead to a change of the activity and electrical conductivity of the catalyst layer with a certain (comparably slow) time constant which might explain the decreasing resistance at low frequencies. It is hardly believed that a change of the state of iridium due to a voltage change in the mV range can explain that the low-frequency inductive polarization completely compensates the capacitive polarization and leads to a low-frequency resistance being smaller than high frequency series resistance. However, it cannot be excluded that it contributes to the low-frequency inductive features.

Further measurements are suggested to be done, like variation of the water flow rate at the anode on stoichiometric level, high differential pressure and detailed variation of structural membrane and anode catalyst properties. To get a better understanding of the physico-chemical process, electrochemical and fluid dynamic based modeling is suggested.

2.5 Conclusion

From the measurements conducted in this study, the following statements, which should still be considered with caution and not seen as a final answer, can be made:

Inductive effects at low frequencies:

- affect the DC performance of the cell and are visible in DC measurements
- are not affected by the EIS amplitude
- are not affected by water flow rate and pressure change in the regions varied in this study
- are strongly affected by temperature and current density/voltage

- are only observable in the spectra of the anode
- can overlap with low-frequency mass transport processes
- are strongly influenced by membrane thickness

From the investigation and with the knowledge from PEM fuel cells some possible origins of the inductive loop can be provided. One possible explanation is a membrane humidification effect. Another reason might be changing iridium states, but it is not believed that this could be the only reason for the inductive loop. Since two inductive peaks in the DRT of some measurements can be seen, there could also be more than one effect in play. There is also a strong interaction with mass transport losses, especially on the anode side and therefore it is challenging to separate mass transport related polarization and inductive effects in impedance spectra or other dynamic measurements as cyclic voltammetry.

The work of Franz et al. [113] suggests that the inductive loop is caused by transient thermal flux originating from the CCM, see Section 2.1. The simulation results show high agreement with the experimental data of this work. However, the amplitude variation during impedance measurements conducted in this work (see Appendix A.2) does not show any influence on the inductive loop. It is expected that different amplitudes influence the thermal behavior of the cell since the operation point and therefore the losses (heat dissipation of the reaction) are changing with the frequency applied. Since there is no influence on the inductive loop observable, it is likely that more than only thermal effects (e.g. slow water diffusion or change of catalyst oxidation states) need to be considered to understand the origin of the inductive loop.

To validate the thermal influence on the inductive loop described by the model, investigations with temperature measurements close to the anode CL might be a valid option, which can be realized by using micro Pt100 sensors on top of the anode PTL. Furthermore, to validate the second and third inductive loop occuring due to transient heat flux from PTL to flow field plate and the surrounding, using a thermal box can be one solution, as a fixed flow field temperature can thereby be assumed.

3 Usage of Carbon-Based Porous Transport Layers [1]

3.1 Introduction

For cost reduction, carbon-based PTLs, which are often also referred to as GDLs, since the components originate from the development of fuel cells, are an attractive option for use on the cathode side of a PEM water electrolysis cell. Compared to coated titanium-based PTLs, carbon-based materials offer significantly lower material and preparation costs [127, 128]. On the anode side, a high oxygen partial pressure and overpotentials exceeding 1.5 V are expected. Therefore, carbon-based materials are not stable for long-term operation due to corrosion issues [62, 129]. In contrast, the reducing hydrogen atmosphere and low overpotentials at the cathode make carbon-based GDLs a viable option.

In PEMFC, carbon-based GDLs have been extensively investigated over the past 30 years. Studies on interfacial contact [130, 131], compression behavior [132–134], and hydrophobic treatments [135, 136] have been published. Today, carbon-based GDLs are standard in all PEMFC stacks. Furthermore, it is state-of-the-art to use a MPL between the GDL and the catalyst layer to ensure intimate contact and provide gas and water transport paths [137, 138]. Such GDL materials, optimized for PEMFC applications, are often used in PEM water electrolysis without a detailed examination of their advantages or disadvantages [120, 139–144]. There are only a few investigations on the carbon-based material and its influence on the cell behavior [47, 145–147].

To achieve a better understanding on the usage of carbon-based GDLs, this chapter discusses the influence on the cell performance of GDL compression, contact with coated and uncoated flow field plates, MPLs and hydrophobic additives. The knowledge achieved here is used for material selection within the AtC cell, see Chapter 4 - 6.

---

[1] Parts of this chapter have been published in [4]

3.2 Experimental

3.2.1 Experimental Setup

The studies presented in this chapter are conducted using the *Fraunhofer ISE reference cell*, which is described in detail in Section 1.3.

The test bench used within this study was developed and built by Fraunhofer ISE and is comparable with the test bench described in Section 2.2.1.

The CCM used is a state-of-the-art, commercially available E400 Gen.3 by Greenerity GmbH, Germany, consisting of a membrane thickness of $125\ \mu\mathrm{m}$ (Nafion® N115) and Pt/C and IrOx catalyst layers. At the anode, a platinum-coated $250\ \mu\mathrm{m}$ titanium fiber PTL from Bekaert SA, Belgium (2GDL-10-0.25) is employed. The baseline material at the cathode is AvCarb MGL370 from AvCarb Material Solutions, USA, with a nominal uncompressed thickness of $370\ \mu\mathrm{m}$.

For the MPL study, the GDL material was prepared by the University of California, Merced (UCM). A MPL layer was coated on the side of the GDL facing the catalyst layer. One sample has $5\ \mathrm{wt}\%$ PTFE impregnation of the GDL, while the other has no PTFE impregnation.

To evaluate the influence of the MPL on CCMs with low catalyst loading, an additional CCM was produced in-house at Fraunhofer ISE with reduced catalyst loading at the cathode. A Nafion®-based N115 membrane was coated with an anode loading of $(1.88 \pm 0.04)\ \mathrm{mg_{Ir}} \cdot \mathrm{cm}^{-2}$ using catalyst powder supplied by *Alfa Aesar*, USA, to achieve a state-of-the-art anode configuration. In contrast, the cathode was coated with only $(0.054 \pm 0.003)\ \mathrm{mg_{Pt}} \cdot \mathrm{cm}^{-2}$, with catalyst provided by *Umicore AG & Co. KG*, Germany. Both catalyst layers were applied via screen printing onto a decal foil and later hot-pressed onto the membrane.

3.2.2 Post Mortem Microscopy

The polymer frame screwed onto the test cell body features a so-called hard stop that prevents further compression. The nominal compression K_{nom} is defined as the intended compression of the GDL due to the height of the hard stop (h_{hs}) compared to the height of the pristine GDL (h_{GDL}) and given by Equation (3.1):

$$K_{\mathrm{nom}} = \frac{h_{\mathrm{GDL}} - h_{\mathrm{hs}}}{h_{\mathrm{GDL}}} \cdot 100\% \tag{3.1}$$

A schematic diagram is provided in the Appendix Figure A.3. Polymer frames with different hard stop heights were used to achieve 0%, 10%, 20%, 40%, 60%, and 80% compression. To determine the necessary clamping force to reach the hard stop, pressure distribution measurements were performed, using pressure paper by FUJIFILM, Japan. Once the pressure on the hard stop exceeds $2.5\ \mathrm{MPa}$ over the entire hard stop area, the cell is considered to be fully and homogeneously compressed. A similar approach to achieving nominal compression was also employed in [47]. To validate that actual compression matches the nominal compression, compressed GDLs were analyzed using confocal laser scanning microscopy (CLSM) after pressure distribution measurements (to confirm the good manufacturing quality of the polymer frame) and after electrochemical characterization. A microscope by Olympus (LEXT OLS5100), Japan with a $405\ \mathrm{nm}$ diode laser and MPLAPON20xLEXT (0.6 N.A.) objective was used. Image processing and evaluation were conducted using the software provided by Olympus (Analysis Application Version 3.1.1.296). The compression of the GDL is measured by the height difference between compressed (area over flow field lands) and uncompressed (area over flow field channels) carbon fibers on the surface of the sample. The fibers considered for the compression measurement are manually selected. This involves taking a grid of 17x17 images with a 10% overlap, stitched together to achieve high precision in the x-axis and y-axis, covering an area of approximately $1x1\ \mathrm{cm}^2$ at the central part of the GDL. A z-stack of images is captured at each image position with a step size of 1.2 µm, starting at the lowest focus point. The topography is determined by analyzing the variations in the intensity signal of the laser at different focal planes. For post-mortem characterization, samples were dried overnight to remove water content that could affect the measurement data. An example of a compression measurement is presented in the Appendix Figure A.4. All further images of PTFE and MPL presented in this chapter were also recorded using this microscope.

3.2.3 Micromechanical Visualization

To investigate the mechanical properties of the carbon-based GDL, ex situ compression tests were conducted using a custom-built setup for micromechanical testing by Fraunhofer IWM. The setup is based on the work of Kennerknecht [148] and Straub [149]. Similar micromechanical testing setups were utilized in [150, 151].

To simulate compression of the cell setup used in this chapter, a custom-built sample holder and punch with five channels, identical to the land-channel structure of the flow field, are used together with the GDL, CCM, and PTL. A piezo actuator, with a step size of 1.8 nm and a speed of $1\ \mu\mathrm{m} \cdot \mathrm{s}^{-1}$, initially moves to the zero position. The sample is compressed in 5% compression steps until the maximum force of $100\ \mathrm{N}$ is reached. Each compression step is followed by a relaxation phase of 30 seconds to allow the system to stabilize. During the test, imaging through a microscope captured the deformation and intrusion of the GDL into the channel. These images, along with continuous measurements of force and displacement, ensured detailed monitoring throughout the experiment. Displacement data and force at the end of relaxation phases are converted into compression and clamping pressure, respectively. Graphical analysis of the images determines the GDL intrusion. Measurements were conducted at room temperature and under dry conditions. To demonstrate reproducibility, the measurements were performed twice. For the analysis of channel intrusion, compression, and clamping pressure, mean values with error bars from both measurements are shown.

3.2.4 Electrochemical Measurement and Analysis

For the analysis of the cell performance, polarization curves between $0.01\ \mathrm{A} \cdot \mathrm{cm}^{-2}$ and $5\ \mathrm{A} \cdot \mathrm{cm}^{-2}$ at $80\ ^{\circ}\mathrm{C}$ and $60\ ^{\circ}\mathrm{C}$ were conducted with a flow rate at the anode of $150\ \mathrm{ml} \cdot \mathrm{min}^{-1}$ and ambient pressure. The cathode is typically not supplied with water; however, for some measurements, a water flow of $150\ \mathrm{ml} \cdot \mathrm{min}^{-1}$ is also applied to the cathode. Each current step of the polarization curve was held for 300 s, and in the last 30 s, the HFR was measured by recording an impedance spectrum between $100\ \mathrm{kHz}$ and $1000\ \mathrm{Hz}$ and analyzing the impedance at a 0° phase angle. At selected current density steps, EIS was performed between $100\ \mathrm{kHz}$ and $100\ \mathrm{mHz}$ with 10 measurement points per decade and a 10-period integration time.

Before characterization, the dry assembled cell is compressed with a $1\ \mathrm{kN}$ force, and water at $80\ ^{\circ}\mathrm{C}$ is flushed at the anode for one hour. After this, the target compression force is applied, and two galvanostatic steps of $0.2\ \mathrm{A} \cdot \mathrm{cm}^{-2}$ and $1\ \mathrm{A} \cdot \mathrm{cm}^{-2}$ for 30 min each are conducted; afterwards, a voltage of $1.7\ \mathrm{V}$ is held for 12 hours. For the low-loading CCM produced by Fraunhofer ISE, the cell is conditioned with polarization curve measurements in the same current density range as the latter characterization, repeated 5 times. Subsequently, a constant voltage of $1.9\ \mathrm{V}$ is held for 5 hours, followed by 10 hours at $2.1\ \mathrm{V}$. All electrochemical measurements are performed twice to ensure reproducibility.

To analyze the data measured, voltage breakdown and impedance analysis employing the Kramers Kronig test to ensure data quality and using DRT to analyze polarization processes, are performed, according to the methods described in the Sections 1.5, 1.6.2, and 1.6.3.

3.3 Results and Discussion

3.3.1 Compression Behavior of GDL

3.3.1.1 Ex Situ Compression Analysis

The results of the post-mortem CLSM analysis of the GDL material and the ex situ compression analysis by Fraunhofer IWM are presented in Figure 3.1.

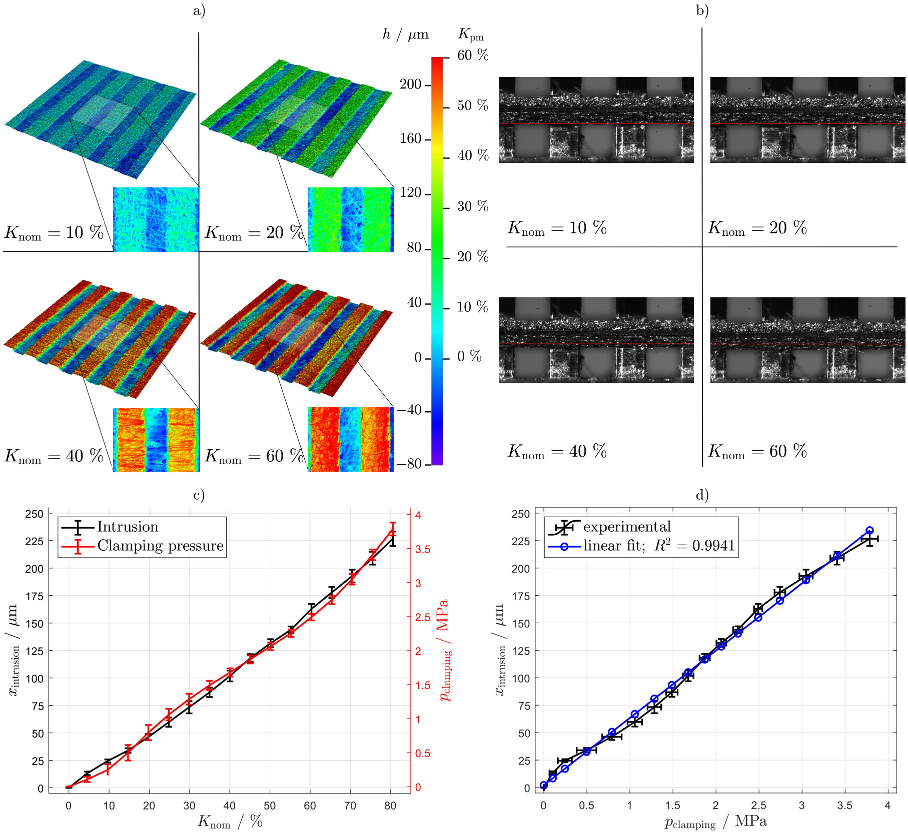

Figure 3.1: Ex situ analysis of different compressions of the GDL. a) Post-mortem CLSM scans of the GDL, b) visualization of the compression analysis, c) analysis of the channel intrusion and clamping pressure over GDL compression, and d) channel intrusion over clamping pressure, measured at Fraunhofer IWM. Figure reformatted and taken from [4].

In Figure 3.1 a) the results of the CLSM scans at 10%, 20%, 40%, and 60% nominal compression are shown, the extracted values for all compression analyses are listed in Table 3.1. The GDL compression is defined by the difference in height between the land and the channel areas, assuming that the GDL does not significantly change in height over the channel compared to the pristine GDL height. The lowest focus point was set within the pores of the compressed fibers, leading to negative values in the CLSM analysis. The top fiber layer of compressed fibers is established as reference level ($h = 0$ μm). Positive values extend up to the surface of the uncompressed fibers, indicating GDL compression. The mean value and standard deviation were calculated from two different samples, which were dried after individual electrochemical characterization.

The samples at 80% compression were destroyed after the electrochemical characterization and could therefore not be analyzed with the microscope, indicating that an excessively high force was applied.

Table 3.1: Compression results of the post-mortem CLSM analysis.

K_{nom} / %	h_{GDL} / μm	K_{pm} / %
0	14.0 ± 0.4	3.8 ± 0.1
10	35.7 ± 1.4	9.6 ± 0.4
20	72.2 ± 21.9	19.5 ± 5.9
40	170.9 ± 20.8	46.2 ± 5.6
60	221.2 ± 10.3	59.8 ± 2.8
80	Not evaluable	Not evaluable

The difference between nominal compression and post-mortem measured compression is in good agreement, indicating that the intended (nominal) compression was present during the electrochemical testing. It should be noted that the GDL sample may exhibit non-negligible elastic compression behavior. Since the microscopy analysis is conducted after the relaxation of the material, the compression during electrochemical characterization may have been even higher. Figure 3.1 b) shows the images taken during the compression analysis conducted at Fraunhofer IWM at the same compression steps as in Figure 3.1 a). The compression is determined by the height change of the displacement sensor relative to the pristine GDL height. The starting point, which corresponds to 0% compression, is determined by the force sensor at the first time point when a force greater than 0 N is measured. Since the GDL sample is slightly pressed forward during compression, the land height is obscured, which can lead to misinterpretations. Therefore, the land height in the uncompressed condition is marked, see the dashed line in red. The GDL material becomes more compressed over the flow field lands and is pressed into the flow field channels. A rearrangement of the fibers is observed as they break, which may significantly change the GDL properties and theoretically lead to better electrical bulk conductivity, smaller porosity, and a more uniform mean pore size distribution over the flow field lands. Based on the images shown, an influence on interfacial contact can be inferred when comparing the different compressions.

Figures 3.1 c) and 3.1 d) show the intrusion into the channel and the clamping pressure during the compression analysis at Fraunhofer IWM. The intrusion into the channel is analyzed by visually determining the height of the GDL over the channels compared to the land height, see the red dashed line in Figure 3.1 b). The clamping pressure is determined by referencing the measured force to the area of the flow field lands. Each measurement was conducted twice; the error bars indicate reproducibility.

The changes in intrusion into the channel and clamping pressure both appear to increase with increasing compression, as shown by the non-linear behavior in Figure 3.1 c). It can be interpreted that the porous GDL is first compressed as fibers break and the bulk material becomes denser. As the force increases further, the compressed material is pressed more into the channels, and more force is required to compress the cell due to the increasing counter force. The channel intrusion and clamping pressure seem to correlate linearly in the applied force range, as shown in Figure 3.1 d). The linear fit ($R^2 > 0.99$) reveals a slope of approximately $61\ \mu\mathrm{m} \cdot \mathrm{MPa}^{-1}$, which may assist future analyses in understanding channel intrusion in relation to the applied clamping pressure. It should be noted that these measurements were carried out at room temperature and dry conditions. The properties of the components may differ during electrochemical characterization.

3.3.1.2 In Situ Compression Analysis

The results of the electrochemical measurements of compression variation are presented in Figure 3.2. The polarization curve and the HFR-free polarization curve (dashed lines at the bottom) are shown in Figure 3.2 a). The best cell performance was achieved at 10%, 20%, and 40% compression, with only marginal differences that fall within the measurement reproducibility, see error bars.

At 0% compression, worse performance is observed in the polarization curve. Since the HFR-free curves agree for 0% to 40% compression, this difference appears to be related solely to Ohmic variations, most likely due to insufficient contact between the layers. At 60% compression, a significantly higher Ohmic resistance, but comparable cell polarization, is detected. At 80% compression, a substantial increase in Ohmic overpotential is observed, and the HFR-free polarization curve shows increased values. As discussed above, the GDL at 80% compression was significantly damaged; therefore, the reproducibility of the measurement is low, see error bars.

Figure 3.2 b) shows the voltage breakdown and the contributions of Ohmic, kinetic, and residual overpotentials at $3\ \mathrm{A} \cdot \mathrm{cm}^{-2}$ for different compressions. The shaded area for 80% compression highlights its low reliability due to broken GDL fibers. The Ohmic overpotentials reach their minima at 20% and 40% compression, with 10% compression being only slightly higher. Insufficient compression at 0% and excessive compression at 60% and 80% are indicated by significantly higher Ohmic overpotentials. The kinetic overpotentials between 10% and 60% compression differ by less than 1.5% from each other, with no observable trend. At 0% compression, an increase in kinetic overpotentials of approximately 4.4% compared to the 20% compression baseline for this study is detected. This is attributed to a loss of active area, as some interfacial contacts are not fully closed, which may be related to the anode and cathode. At 80% compression, the kinetic overpotentials increase by over 9% compared to 20% compression.

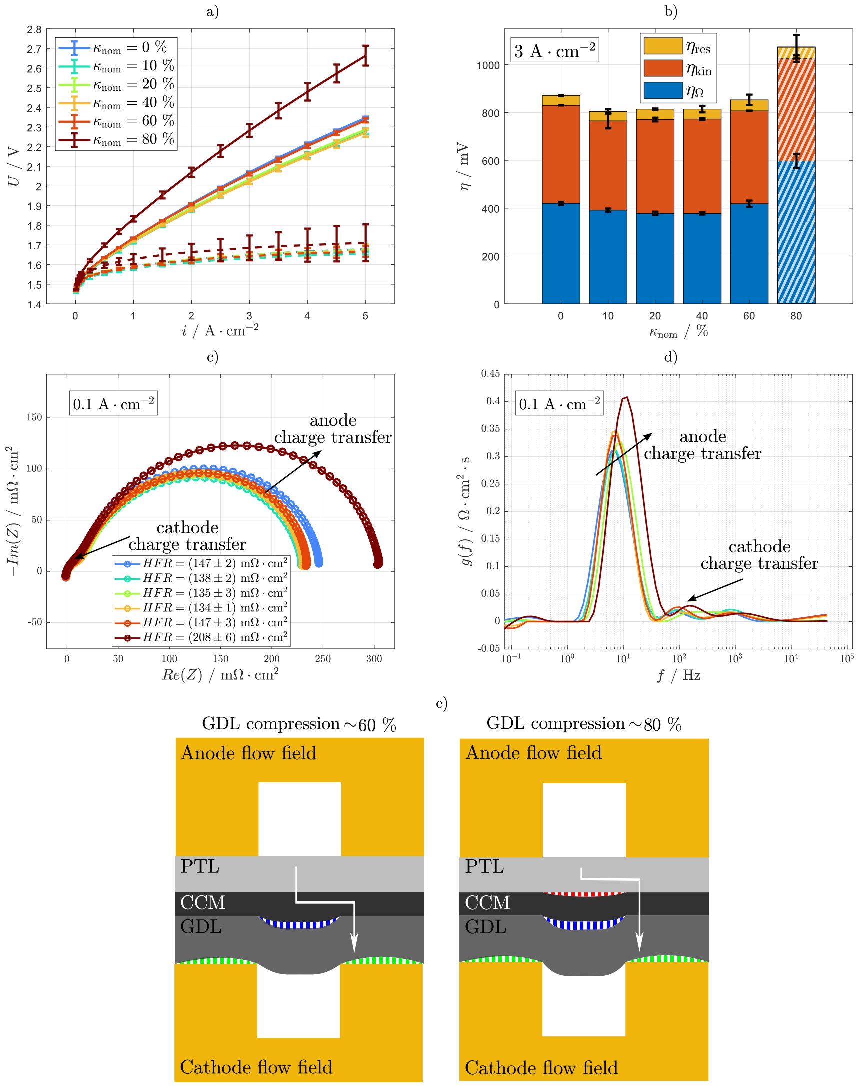

Figure 3.2: Electrochemical analysis of different compression of the GDL. a) Polarization curve and HFR-free polarization curve (dashed lines), b) deconvolution of the overpotentials at 3 A · cm^{-2}, c) HFR-free EIS at 0.1 A · cm^{-2}, and d) schematic diagram of the influence of compression on interfacial contact. The measurements are done at 60 °C, ambient pressure, and 150 ml · min^{-1} anode water flow. Figure reformatted and taken from [4].

The increased kinetic losses are also observable in the impedance spectra and the DRT analysis in Figures 3.2 c) and d). The impedance at 0.1 A · cm^{-2} is presented, where charge transfer resistances are typically dominant. A first peak is detectable in the DRT at around 1 kHz, which is attributed to catalyst layer resistance, appearing insignificant compared to the other processes. At frequencies around 100 Hz, a small capacitive loop is evident, with all spectra being consistent. This loop is associated with the cathode charge transfer process; see the discussion in Figure 3.5 regarding low cathode loading CCMs. For 10% to 60% compression, the spectra across the total frequency range agree with each other, indicating no significant difference in polarization resistance. The 0% compression shows slightly higher resistance, while 80% compression exhibits a much higher expansion of the second capacitive loop, usually associated with anode charge transfer. The DRT peak at around 10 Hz confirms that the compression between 0% and 60% shows similar polarization, which is significantly increased for 80% compression. Mass transport resistances do not seem to be affected by compression variation. This may be explained by the fact that the diffusive transport of hydrogen is not a bottleneck in PEM water electrolysis cells, as demonstrated in [2], where the pathways in the PTL were purposely blocked at the anode and cathode. Furthermore, ionic and electronic in-plane resistivity does not appear to be affected. Low loading CCMs with comparatively low catalyst layer in-plane conductivity may be more sensitive to such compression variations.

Figure 3.2 e) illustrates the interpretation of the interfacial contacts under excessive compression of the cell. Increased Ohmic resistance can occur due to the bending of the GDL into the flow field channels and the bending of the GDL over the flow field lands (see the dashed areas in white and green over the flow field lands labeled "GDL compression 60 %", left). It is believed that this phenomenon can occur even under low over-compression and is highly dependent on the cell components used and their stiffness. As the compression increases, the interfacial contact between the GDL and CCM may decrease (see the dashed area in white and blue). Over the flow field channels, the GDL detaches from the CCM, which can only be partially compensated by the flexibility and swelling of the CCM. If the detachment becomes too significant, the area at the cathode becomes partly inactive, and protons in the membrane and electrons in the cathode catalyst layer travel from and to the anode in-plane direction toward active sites, as illustrated by the white arrows. At this point, a further increase in Ohmic resistance is expected due to increased path lengths for the protons and the relatively high in-plane resistivity of the catalyst layer. However, it is not believed that there is a significant impact on cathode charge transfer resistance since neighboring active sites at the cathode compensate for the inactive ones without a substantial increase in cathode kinetic overpotentials, which is typical for the HER. This implies a high and well-distributed catalyst loading at the cathode. With low catalyst loading at the cathode, this compensation may significantly impact the cathode kinetic overpotentials.

This described scenario applies to the 60% compression in the shown study. Further increases in compression may lead to detachment of the CCM from the PTL at the anode (see the dashed area in white and red labeled "GDL compression 80 %", right) since the CCM is pressed against the flow field toward the cathode channels, while the titanium PTL remains in place due to its comparatively low flexibility. This detachment may explain the increased charge transfer resistance (see Figure 3.2 c)), due to loss of active area at the anode, which cannot be compensated without increased kinetics since the oxygen evolution reaction requires a relatively high amount of activation energy. This scenario may describe cell behavior at 80% compression.

3.3.2 Contact Resistance of GDLs with Coated and Uncoated Flow Fields

To analyze the importance of flow field coating, cell bodies with gold coating and without any coating are examined at the anode and cathode separately. The default cell body consists of titanium grade 2, which is coated with 10 µm of gold by electroplating. Beneath the gold layer, there is a $1\ \mu\mathrm{m}$ thick platinum support layer coated galvanically. This coating is commercially available from Umicore AG & Co. KG, Germany.

For comparison, a titanium grade 2 cell body is employed that had been used several times in previous electrochemical measurements. The flow field lands showed significant bluish discoloration, which is attributed to a titanium oxide layer of several tens of nanometers. Photos of the coated and uncoated cell bodies are provided in the Appendix Figure A.5.

Using these cell bodies, the electrochemical characterization mentioned in Section 3.2 is conducted with a baseline compression of 20%. Measurements were performed with only the anode flow field coated, only the cathode flow field coated, both flow fields coated, and both flow fields uncoated, see Figure 3.3. Figure 3.3 a) shows the polarization curves and the HFR-free polarization curves (dashed lines at the bottom) for all combinations. The measured HFR during the polarization curve is presented in Figure 3.3 b).

As expected, the case of both flow fields coated shows the best performance and the lowest HFR. Interestingly, with an uncoated anode flow field but a coated cathode flow field, very similar performance and HFR are observed. In contrast, when only the anode flow field is coated, a significant increase in HFR and poor performance is noted. As anticipated, the flow field without any coating demonstrates the worst performance. The HFR-free polarization curve, DRT analysis, and HFR-free impedance spectra at $1\ \mathrm{A} \cdot \mathrm{cm}^{-2}$, see Figures 3.3 c) and d), show that the polarization resistance is not affected by the flow field coating, as expected. The differences in the DRT peaks at approximately $200\ \mathrm{mHz}$ are not considered significant and are attributed to measurement reproducibility.

In the case of uncoated flow fields, the titanium-based PTL fibers ($20\ \mu\mathrm{m}$ fiber diameter) may penetrate through the titanium oxide layer, circumventing the low electrical resistance and directly contacting the comparably conductive pure titanium.

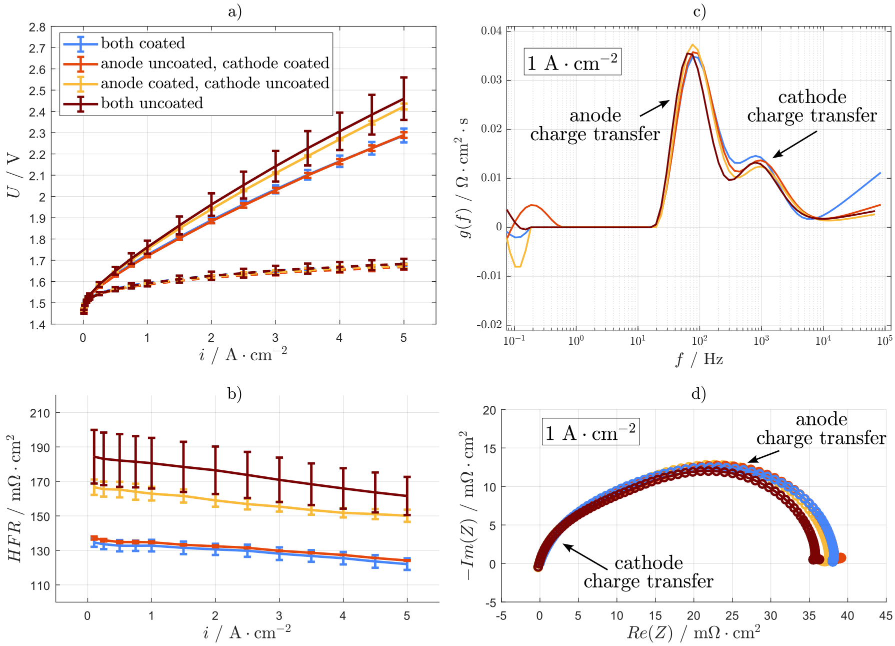

Figure 3.3: Electrochemical analysis of the variation of the coating of the flow field. a) Polarization curve and HFR-free polarization curve (dashed lines), b) HFR over current density, c) DRT analysis, and d) HFR-free EIS at $1\ \mathrm{A \cdot cm^{-2}}$. The measurements are done at $60\ ^\circ\mathrm{C}$, ambient pressure, and $150\ \mathrm{ml \cdot min^{-1}}$ anode water flow. Figure reformatted and taken from [4].

This may be accompanied by "micro-movements" due to temperature and gas pressure effects, which partially remove the oxide layer. Therefore, the Ohmic resistance is comparable to that in the case of both flow fields being coated. The still slightly increased HFR may be explained by a much smaller Ti/Ti contact area compared to the softer gold layer.

In the case of the uncoated cathode flow field, the relatively soft and brittle carbon-based fibers cannot penetrate through the titanium oxide layer and only contact its surface, resulting in a high Ohmic resistance. It is to be mentioned that the used PTLs may not be perfectly coated with platinum, and some fibers or spots may remain uncoated. Consequently, some titanium fibers might be oxidized to titanium oxide, which increases contact resistance and could potentially falsify the results discussed here.

With this study, it is demonstrated that a proper electrical interface to carbon-based GDLs is essential to obtain high cell performance. For industrial designs, such as using milled flow fields or flow field replacement material like perforated or expanded metals, a highly conductive surface with minimal corrosion effects appears necessary. Short-term tests reveal that the anode PTL circumvents oxide layers. It should be noted that the durability of the cell, particularly at the interface of uncoated flow field and PTLs, is not investigated here and higher increase of the Ohmic resistance over time compared to coated flow fields at the anode is expected.

3.3.3 Influence of Micro Porous Layers on GDLs

The produced GDLs with MPLs were analyzed using CLSM. Figure 3.4 shows the CLSM scans of the GDL with and without MPL provided by UCM.

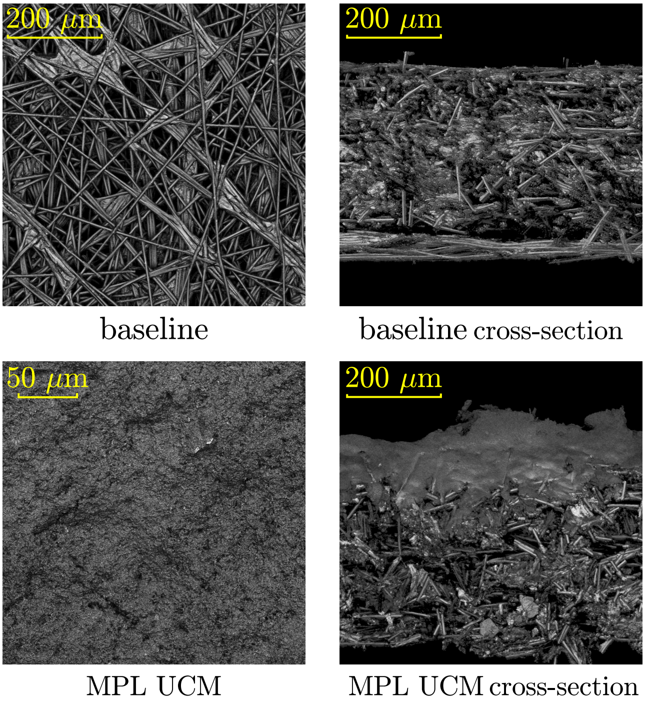

Figure 3.4: CLSM scans of the baseline GDL (top) and baseline GDL with MPL provided by UCM (bottom). Figure reformatted and taken from [4].

The baseline GDL is shown at the top, while the bottom-left panel provides a top view of the MPL. The MPL top view reveals a significant reduction in pore size compared to the GDL without MPL. This reduction in pore size leads to an increased surface area, which is expected to provide a more intimate contact with the catalyst layer and therefore, reduce contact resistances and improve catalyst utilization. The cross-section displaced in the bottom-right panel highlights the structural difference between the bare GDL and GDL with MPL. The MPL layer contains 25 wt% PTFE and

75 wt% acetylene black. In this study, the sample with MPL but without PTFE impregnation is referred to as “UCM MPL”, while the GDL substrate with additional 5 wt% PTFE impregnation and MPL is referred to as “UCM MPL+PTFE”.

Figure 3.5 shows the results of the comparison between baseline GDL and GDL UCM MPL with employed commercial state-of-the-art CCM and low cathode loading CCM produced at Fraunhofer ISE. The polarization curve in Figure 3.5 a) with the commercial CCM shows only slightly improved performance when using the GDL with MPL. The HFR-free curve reveals that beside Ohmic, also kinetic and residual overpotentials marginally differ, see also Appendix Figure A.6. These results indicate the expected positive influence of a MPL. The improved contact and subsequently lowered in plane resistance reduces inactive cell regions and thus also minimizes the activation resistance. The hydrogen diffusion may be as well affected positively as the gas is finely distributed into the GDL. However, it is assumed that due to the high catalyst loading and highly conductive catalyst layer, the commercial CCM does not show huge differences and can be in general used without a MPL on the GDL considering cell performance. However, the cell’s durability may be as well positively influenced, but this aspects are not discussed in this study.

To analyze the positive influence of a MPL, the results of the measurement with in-house produced CCM with $(0.054 \pm 0.003)\ \mathrm{mg_{Pt}} \cdot \mathrm{cm}^{-2}$ cathode catalyst loading are depicted in Figure 3.5 b). A remarkable improvement can be seen in both the polarization and HFR-free polarization curves, with high reproducibility, which can be attributed to the proper coating during the production of the CCM and GDL material. Reduced Ohmic (HFR) and kinetic (Tafel slope in the legend of the residual overpotential graphs) resistances are shown in Figure 3.5 c) and d). Additionally, the residual overpotentials demonstrate improved behavior at high current densities. At current densities below $2\ \mathrm{A} \cdot \mathrm{cm}^{-2}$, the residual overpotentials with MPL are increased compared to the baseline, which may be explained by higher capillary pressure due to the smaller pores of the MPL. This effect may become less significant at higher current densities as the produced gas volume increases significantly.

Figure 3.5 e) shows the HFR-free EIS and the DRT analysis at $0.1\ \mathrm{A} \cdot \mathrm{cm}^{-2}$ indicating the comparably high cathode charge transfer resistance with the low cathode loading (blue curve). For comparison with the commercial CCM, see Figure 3.2 c). With MPL employed, the cathode charge transfer resistance is drastically reduced being comparable with the commercial CCM. As expected, the anode charge transfer resistance seems not to be affected, which is also supported by the consistent DRT peaks.

Since the residual overpotentials as well differ significantly, Figure 3.5 f) provides the HFR-free EIS and the DRT analysis at $3\ \mathrm{A} \cdot \mathrm{cm}^{-2}$, revealing reduced polarization resistances with MPL. The charge transfer decreases with current density, and in both cases, additional capacitive and inductive processes at lower frequencies are detected. The inductive loop has been discussed in Chapter 2 and [1, 2] and is associated with the membrane or an anode effect. In the measurements shown here the differences are not significant and are therefore not discussed. The capacitive

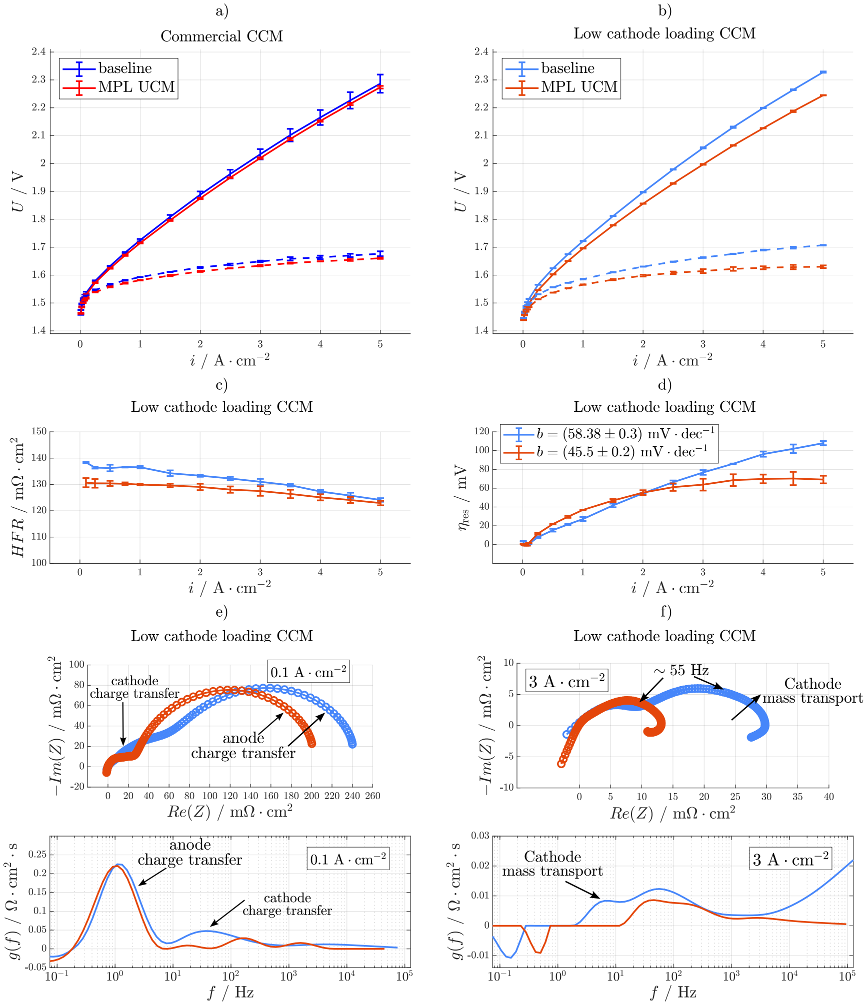

Figure 3.5: Electrochemical analysis of the influence of a MPL on top of the GDL at the cathode compared with the baseline GDL material. Polarization curve and HFR-free polarization curve (dashed lines) with a) commercial CCM and b) low cathode loading CCM, c) HFR and d) residual overpotentials over current density with Tafel slope depicted in the legend and e) EIS analysis in Nyquist (top) and DRT (bottom) presentation at $0.1\ \mathrm{A \cdot cm^{-2}}$ and f) at $3\ \mathrm{A \cdot cm^{-2}}$ with the low loading CCM employed. The measurements are done at $60\ ^\circ\mathrm{C}$, ambient pressure, and $150\ \mathrm{ml \cdot min^{-1}}$ anode water flow. Figure reformatted and taken from [4].

process at $55\ \mathrm{Hz}$ is associated with mass transport resistance at the cathode, as a strong comparison with the previously analysis of blocking PTL pores at the cathode is present, see [2]. For the impeded cathode mass transport, no overlapping of the inductive loop can be seen, which is very comparable to the measurement shown here. As it seems, these resistances could be minimized by employing the MPL, which may be explained by a better distribution of the evolved gas from the catalyst layer into the GDL.

These findings reveal the impact of optimized interfaces to the catalyst layer when using low-loading CCMs, which is widely discussed for the anode [31, 66, 152]. The results clearly demonstrate that the cathode is also of high importance when lowering the overall PGM loading of CCMs. Furthermore, the assumption of “non-polarizable” cathode, e.g. for analysis using the Tafel model seems not to be valid at these low cathode loadings.

3.3.4 Hydrophobic Treatment of GDLs

To analyze the influence of hydrophobic treatment, the measurements with low-loading CCM and MPL by UCM, with and without 5 wt% PTFE, are shown in Figure 3.6.

Figure 3.6 a) provides the voltage breakdown analysis under default conditions with dry cathode operation and $150\ \mathrm{ml} \cdot \mathrm{min}^{-1}$ at the anode. In Figure 3.6 b) both electrodes are flushed with $150\ \mathrm{ml} \cdot \mathrm{min}^{-1}$ water.

During operation with and without water flow at the cathode, no significant difference in cell performance is observed. The HFR analysis over current density reveal increased Ohmic resistance with 5 wt% PTFE amount, which is expected due to the non-conductive properties of PTFE. The HFR-free polarization curves indicate slightly higher overpotentials in both cases with PTFE. The Tafel slope (see legend of residual overpotential graphs) also shows marginally increased values. Since the amount of PTFE of the MPL that contacts the catalyst layer is not affected by the PTFE amount of the GDL, this dependency is not clear at this point. When applying water to the cathode no significant differences to operation with dry cathode are detected in the polarization curve, see Figure 3.6 b). Again, the same trend is observed, as the sample with PTFE shows slightly lower performance, primarily attributed to the increased HFR, as indicated by the HFR-free polarization curve and the HFR over current density.

When comparing Figures 3.6 a) and b), the HFR decreases when applying water to the cathode the decrease is less pronounced with increasing current density. This is attributed to better thermal management of the cell due to the higher heat capacity of the cathode water, which is especially relevant at low current densities and with less reaction heat. This improved thermal management decreases the membrane resistance and helps maintain a more stable temperature as the reaction heat increases with current density.

The Tafel slope does not show significant differences between dry cathode and both electrodes supplied with water, which is atypical due to the differences in temperature as the applied water may remove produced heat of the HER.

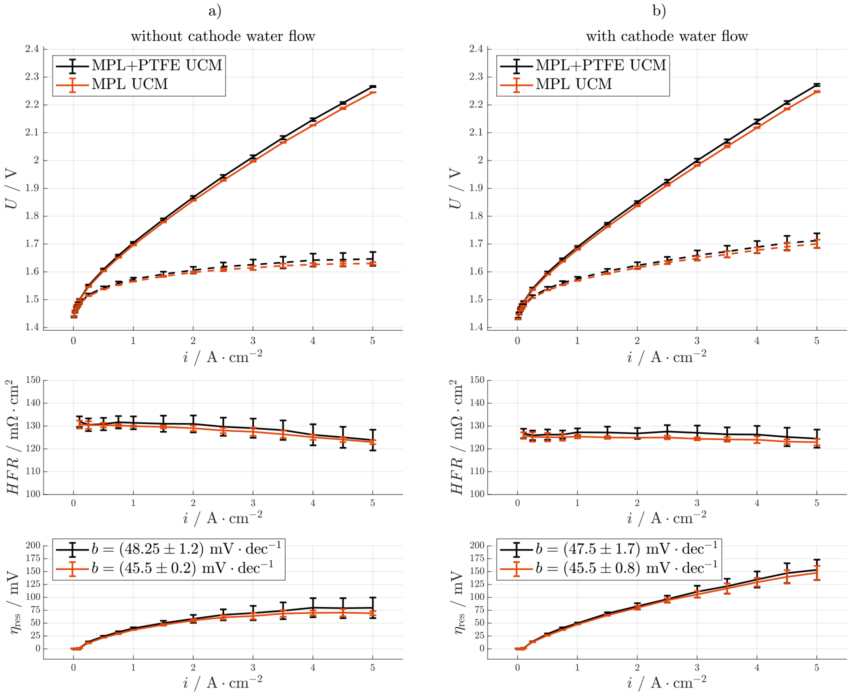

Figure 3.6: Electrochemical analysis of the influence of hydrophobic treatment (PTFE) in the GDL at the cathode using the low-loading CCM and comparing MPL UCM and MPL+PTFE UCM. Polarization curve, HFR-free polarization curve (dashed lines), HFR and residual overpotentials over current density at a) dry cathode and b) with water flow at the cathode. The measurements are done at $60\ ^{\circ}\mathrm{C}$, ambient pressure, and $150\ \mathrm{ml}\cdot\mathrm{min}^{-1}$ water flow. Figure reformatted and taken from [4].

Since the water applied to the cathode mostly affects the cathode itself, this effect may be negligible due to the overall small overpotentials of the HER. The residual overpotentials show clearly increased values with water supply to the cathode, exceeding $70\ \mathrm{mV}$ at $5\ \mathrm{A}\cdot\mathrm{cm}^{-2}$ for the sample with and without PTFE. This increase may be attributed to enhanced cathode mass transport for water-flooded cathode catalyst layers, as described by Bernt et al. [51]. They describe cathode mass transport related overpotentials up to $24\ \mathrm{mV}$ at $3\ \mathrm{A}\cdot\mathrm{cm}^{-2}$ under dry cathode operation, considering electro-osmotic drag of 3 water molecules per proton. At $3\ \mathrm{A}\cdot\mathrm{cm}^{-2}$, a difference of $40\ \mathrm{mV}$ between dry cathode and water flushed cathode operation is observed. The application of water to the cathode may significantly increase capillary pressure within the catalyst and gas diffusion layer, leading to extraordinary increases in hydrogen mass transport losses. Additionally, a reduction in the electronic in-plane conductivity of the cathode catalyst layer may also be plausible. The measurements with commercial CCM are similarly analyzed and presented in the Appendix Figure A.7 but do not reveal different trends compared to those shown for the low-loading CCM.

3.4 Conclusion

This chapter analyzes the usage of carbon-based PTLs and MPLs at the cathode within PEM water electrolysis cells concerning cell performance. The influence of cell compression, contact with coated and uncoated titanium flow fields, the use of a microporous layer, and hydrophobic additives are investigated using a state-of-the-art cell setup.

It is shown that cell compression sensitively effects the overall contact resistance determined by high frequency resistance measurements. Insufficient compression can occur below 10% and excessive compression above 60% GDL compression for the GDL material used in this study. At a cell compression of 80%, an increasing charge transfer resistance was observed at the anode, measured by impedance spectroscopy. Using a confocal laser scanning microscope, the GDL compression was analyzed after electrochemical in situ measurements. Visualization of ex situ compression analysis provides insights into the mechanical behavior of the GDL and the cell at different compressions. Through these analyses, hypotheses regarding cell mechanics, internal contact resistance, and detachment of the CCM from the GDL at the cathode, as well as from the PTL at the anode, are proposed.

Measurements employing gold-coated and uncoated titanium flow fields at anode and cathode shows a significant impact on the contact resistance at the cathode and comparatively less impact at the anode. These phenomena are explained by the titanium fibers of an anode PTL, which penetrate the titanium oxide layer due to their hardness. The comparable soft carbon fibers appear not to be able to penetrate this oxide layer. As intended, no impact on cell polarization could be seen.

The impact of carbon-based micro porous layer on top of the GDL is evaluated in a standard cell setup with a commercial CCM with state-of-the-art loading and a purpose-made CCM produced at Fraunhofer ISE with low cathode loading of $< 0.06\,\mathrm{mg_{Pt}} \cdot \mathrm{cm}^{-2}$. As expected, the commercial CCM demonstrated only slight improvements with the addition of an MPL. The comparatively high state-of-the-art platinum loading, accompanied by a high carbon loading, minimizes the in-plane resistance of the catalyst layer.

In contrast, using the CCM with low cathode catalyst loading, the MPL provides a significant improvement in Ohmic, kinetic, and residual overpotentials. The impedance spectra show a significant reduction in both cathode charge transfer and mass transport resistance, which is attributed to improved contact and reduced inactive catalyst layer surface area.

The influence of PTFE additives was analyzed applying an impregnation of $5\,\mathrm{wt\%}$ PTFE in the GDL with MPL and for the case of a CCM with a low cathode loading. Increased Ohmic resistance is measured for an impregnated GDL, which is referred to the non-conductive properties of PTFE. When applying a water flow to the cathode, increased residual overpotentials are measured for both GDLs (with and without PTFE) which may be explained by increased hydrogen transport resistivity due to the water-flooded catalyst layer at the cathode.

This study demonstrates that a simple transfer of PEM fuel cell materials, such as GDLs with PTFE, does not necessarily justify the associated production efforts or guarantee a positive impact on cell performance. The use of MPLs is highly recommended when employing low catalyst loadings at the cathode; however, the addition of 5 wt% PTFE impregnation did not show an improvement in terms of cell performance. Furthermore, proper electrical contact and compression of carbon-based GDLs are essential for optimal cell performance. Since this chapter focuses solely on cell performance, further measurements and electrochemical modeling regarding cell durability are suggested.

4 Along the Channel Test Cell [1]

4.1 Introduction

To investigate phenomena that occur along the water supply channels, locally resolved measurements can be used to analyze the distribution of current density, temperature and electrochemical impedance [36]. Focusing on the cell behavior in the flow dimension only, an along the channel approach can be used. This analysis method is well-established for PEM fuel cells for which most of the work focus on CDD measurements [153–159]. Also some publications on locally resolved impedance investigations are reported [160–162]. While in PEM water electrolysis this setup has not been used equally much, some studies are published on CDD [37, 108, 163–165], temperature distribution [36, 38] and locally resolved impedance measurements [35, 38].
Immerz et al. presented a $50\ x\ 0.5\ \mathrm{cm}^2$ segmented single-channel PEM water electrolysis test cell with highly resolved current and temperature monitoring [35, 36]. In addition to this, sequential EIS can be conducted at the inlet, the center and the outlet of the cell to gain information about the series resistance as well as charge transfer and mass transport processes. They observed an increase of the HFR, mass transport polarization resistance and therefore decreasing current towards the cell outlet under water starvation of the cell. Furthermore, for the first time, they discussed current density inhomogeneities and their origin in a segmented along the channel cell. However, the cell operation was at rather low current densities of $< 1.5\ \mathrm{A} \cdot \mathrm{cm}^{-2}$.
Parra-Restrepo et al. presented a $30\ x\ 1\ \mathrm{cm}^2$ multi-channel PEM water electrolysis test cell which is divided into 20 segments [165]. This cell is meant to measure the current density and impedance distribution along the channel. Furthermore, a parallel channel fed with hydrogen is added to implement a reference electrode for each segment. The cell was also used for fuel cell operation for which EIS results were published [160]. For the electrolysis mode, only current density distribution results are reported. They analyzed PTLs varying in pore size and saw a significant influence on mass transport up to a current density of $3.5\ \mathrm{A} \cdot \mathrm{cm}^{-2}$.
Sun et al. presented a circular shaped test cell with an active area of $49.5\ \mathrm{cm}^2$ divided into 11 segments and measured the current density and impedance distribution up to $0.8\ \mathrm{A} \cdot \mathrm{cm}^{-2}$. They

---

[1] Parts of this chapter have been published in [3]

have observed that with a water stoichiometry of $\lambda < 5$ the current density is extremely influenced which leads to a decrease of current along the flow channels. For higher water stoichiometry a rather stable current distribution was measured. They correlated the current density behavior at different water stoichiometry with the increasing HFR towards the cell outlet which might be concluded as membrane dry out.

Dedigama et al. provided a $0.3\ x\ 8.5\ \mathrm{cm}^2$ single-channel test cell with the possibility to measure the current density distribution and visualize the bubble behavior due to use of transparent components in the end plate [37]. They showed a significant increase of the current density towards the cell outlet. Compared to the publications mentioned above the water stoichiometry used here is significantly higher ($\lambda > 100$) which might explain the increasing current density towards the end of the cell due to an increasing temperature and a lack of water supply issues. With bubble visualization they observed large bubbles towards the cell outlet most likely related to gas accumulation along the flow channel and the higher gas production due to the increased current density at the cell outlet. However, the current density here was as well very low with a maximum of $< 0.5\ \mathrm{A} \cdot \mathrm{cm}^{-2}$.

Ma et al. recently introduced a test cell with segmented anode flow field with transparent components to visualize the flow behavior [166]. The cell has an active area of $1.8x2.2\ \mathrm{cm}^2$ divided into 8 segments at which current density and temperature was measured in parallel. They found that compression and temperature distribution had a high influence on the current density distribution. Furthermore, overall cell temperature highly affected the cell performance, water flow rate variations far above the stoichiometric level led to differences in cell temperature, which influenced the cell performance. Operating close to the stoichiometric level, water starvation was observed, which led to performance decrease towards the cell outlet and instable cell voltages under galvanostatic mode.

In this chapter the AtC test cell, developed within this thesis, is presented. Firstly, the cell design is described, followed by the measurement method employed, and the test bench, which was adpated for high current density operation and segmented impedance analysis. After that, a detailled proof of concept is discussed in Section 4.3. The internal contact distribution of the segments is demonstrated, the assumption of equal voltage alongside the active area discussed, and a method to analyze the HFR, although high-frequency artefacts are distorting the impedance spectra, is presented. Furthermore, the AtC test cell is compared with a laboratory-scaled cell, its functionality tested under different operation conditions, and the use of reference electrodes shown.

4.2 Experimental

4.2.1 Along the Channel Test Cell Design

4.2.1.1 Cell Setup

An overview of the cell design and its components is given in Figure 4.1. Figure 4.1 a) shows an exploded-view drawing of the default setup with segmented flow field plate at the anode side (bottom) and unsegmented flow field plate at the cathode side (top). Additionally, photos taken during the assembly of the cell and of the assembled cell implemented in the test bench are given in the Appendix A.8.

The cell consists of different cell components which are placed on top of each other and compressed together to ensure gas tightness and a proper electrical contact. For the compression a pneumatic clamping pressure system (1) was designed. Hereby, a moveable stamp at the bottom of the cell compresses all stacked components against the counter plate (2) on top. Spring discs on top of the counter plate are used to equalize the clamping pressure distribution.

To pass the current through the cell, gold coated current collector plates (3) made from copper are implemented at anode and cathode. Each current collector plate is electrically insulated against the clamping pressure system using polymer plates. Two 120 mm^2 copper cables are used per pole to transfer the current (up to 600 A) from the power supply to the cell.

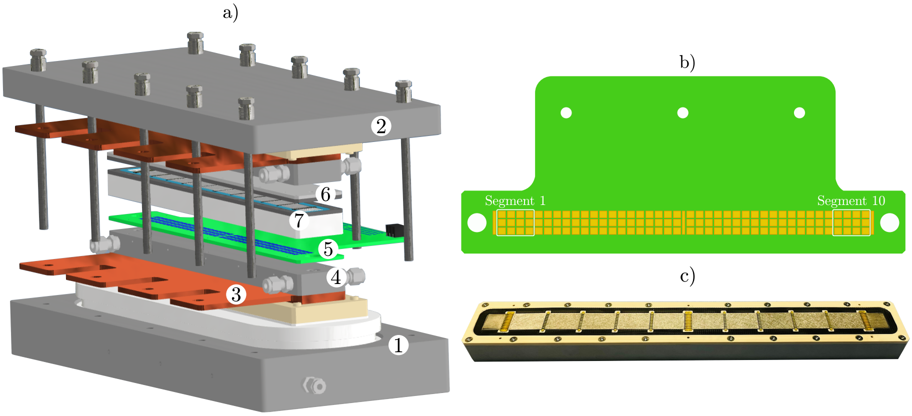

Figure 4.1: a) Exploded-view drawing of the AtC cell (for numbering see description in the text) with default setup (anode segmented, cathode unsegmented), b) top view on the printed-circuit board and c) segmented flow field plate with inserted PTLs. Figure reformatted and taken from [3].

At each side a $20\ \mathrm{mm}$ thick homogenization plate (4) made from titanium is placed at the inner side of the current collector to transfer the current towards the active area of the cell and to homogenize transverse currents and set the boundary cell components onto an equal potential. In addition to this, the water inlets and water-gas outlets are integrated to these titanium plates.

For the locally resolved measurements, a PCB (5) custom-designed by DiLiCo engineering GmbH, Germany is implemented between the homogenization plate and the flow field plate at one of the half cells. The PCB consists of 40 measurement contacts along the channel in three columns resulting in a total of 120 contacts. The cell is divided by the flow field plate and the PTLs in 10 equal segments, per segment 4x3 contacts are available, exemplarily highlighted for segment 1 and 10 in Figure 4.1 b). For each contact the current density is determined via a shunt resistor. The 12 measurement contacts per segment are interconnected using soft conductive material to ensure that very similar current is flowing through the shunts within one segment.

Per segment at the two centered measurement contacts of the 12 shunts per segment, highlighted with white dots in Figure 4.1 b), the AC potential for EIS analysis is measured using a frequency response analyzer (FRA) by Zahner-Elektrik GmbH & Co. KG, Germany before and after the shunt resistor to gain information on the local AC current, see Figure 4.2. With this set up it is possible to measure the impedance at each segment in parallel. In addition to this, in a second layer 120 Pt100 sensors are implemented in the PCB to monitor the temperature distribution. Detailed information about the measurement technique is provided in Section 4.2.1.2.

Upon the PCB at the anode and upon the homogenization plate at the cathode the titanium flow field plate is placed. The flow field plate has 10 milled parallel supply channels, each with a cross sectional width of $1\ \mathrm{mm}$ and a depth of $2\ \mathrm{mm}$. For the unsegmented flow field plate (6) at the cathode, a solid titanium plate was manufactured. For the segmented flow field plate (7) at the anode, 10 titanium inlets with an active contact area of $20x28\ \mathrm{mm}^2$ are pressed into an electrically insulating frame sealed using two radial O-ring gaskets. Figure 4.1 c) shows the assembled segmented flow field plate with inserted PTLs. The flow field plates are gold coated to minimize corrosion and contact resistances, see the channels at inlet, center and outlet. The segmented flow field plate has a height of $23\ \mathrm{mm}$. To be flexible in using PTLs with different thicknesses, polymer frames with different heights are screwed upon the flow field plate. Between the flow field plate and the frame, as well as on top of the frame, a flat sealing by Freudenberg FST GmbH, Germany is used.

On top of the flow field plate, the PTLs are placed. To segment the PTLs, they are shaped into $20x28\mathrm{mm}^2$ pieces and insulating bridges with $2\ \mathrm{mm}$ width are inserted. The insulating bridges are designed to avoid electrical contact between the PTL and to affect the water flow in the flow channels only marginally. Between the two flow field plates with inserted PTLs and flat sealings the CCM is positioned. The active area of the segmented cell setup is determined by the area of all 10 segments resulting in $56\ \mathrm{cm}^2$.

In addition to the locally resolved measurements, to separate anodic and cathodic processes, reference electrodes are implemented at the inlet, center, and outlet of the AtC cell, see strips over the whole width of the PCB in Figure 4.1 b). The reference electrodes are based on the work of Gerteisen [117], which employ laser ablation reference electrodes. For a schematic diagramm and a more detailed description of this approach it is referred to Section 2.2.2. It should be noted that reference electrodes used within the AtC cell require a special cell setup since anode and cathode need to be segmented at the reference electrodes to exclude both sides of the reference electrode from the active cell area. In Section 4.2.1.2 the electrical connection for measurements under cell operation including EIS is explained.

As cell materials, a commercial E400 Gen. 3 CCM by Greenerity GmbH, Germany with a 125 $\mu\mathrm{m}$ thick Nafion®-based membrane is employed in this study. At the anode PTLs with a thickness of 500 $\mu\mathrm{m}$ (2GDL20-0.5) by NV Bekaert SA, Belgium which were in-house sputter-coated with 100 nm platinum on both sides are employed. At the cathode, a carbon-based gas diffusion layer (GDL) with a thickness of 214 $\mu\mathrm{m}$ (SGL 22 BB) by SGL Carbon SE, Germany is used.

4.2.1.2 Measurement Method

A schematic cross-section view of the active parts of the AtC test cell and its technique for current density, temperature and impedance distribution measurements are shown in Figure 4.2. The PCB is positioned between the homogenization plate and the flow field plate at the anode, more detailed information on the used PCB system by the supplier is provided elsewhere [157].

The current density distribution of the DC-bias is determined by measuring the potential difference with a four-wire setup before ($\varphi_{\mathrm{DC,cell}}$) and after ($\varphi_{\mathrm{DC,end}}$) the implemented shunt resistors with $R = 33$ mΩ resistance, see Figure 4.2 c). The measurement accuracy tested by the supplier is for small currents < 50 mA per shunt ± 0.1 mA. For the whole current density range used within this study (up to 5 A per shunt) $\pm 1\%$ measurement accuracy is guaranteed. According to Ohm's law the current is determined by measuring the voltage drop over the known resistance of the shunt resistor.

The temperature distribution is determined by using Pt100 sensors at the same positions as the current density measurement as well with a four-wire setup.

For the locally resolved EIS, one of the two centered shunt resistors per segment is used. Soft conductive GDL material is placed between the PCB and the flow field segment to electrically connect the 12 shunts per segment together. Since the standard deviation of the current within one segment (measured using the 12 shunts) is $< 0.5\%$, one shunt properly represents the EIS for the whole segment. The supporting GDLs between PCB and flow field plate per segment do not have any contact to surrounding segments. The active area for one shunt resistor is calculated by the active area of the whole cell divided by the 120 contacts. The measurement technique is visualized in Figure 4.2 a) for the overall cell voltage and in Figure 4.2 b) and c) for the local current measurement during EIS.

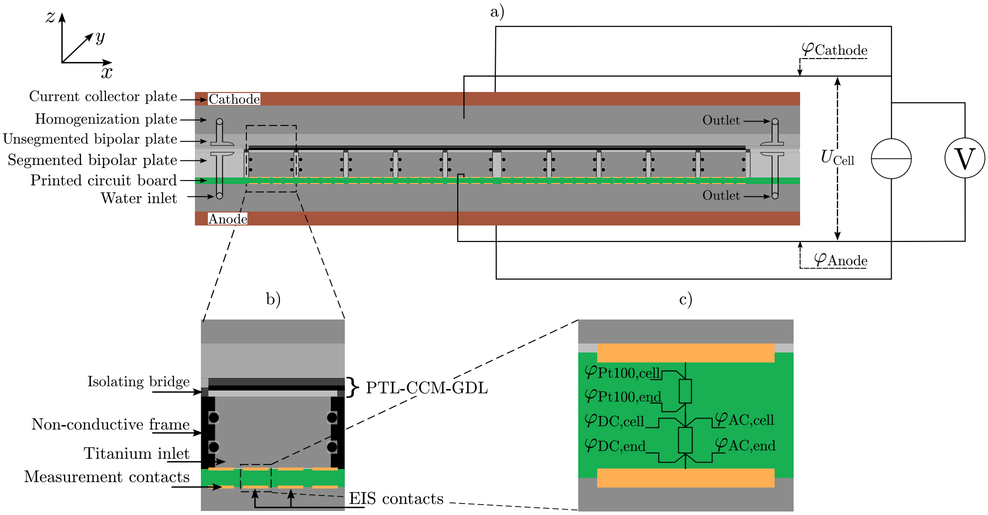

Figure 4.2: a) Schematic cross-section of the AtC test cell, b) detailed presentation of segment 1 and c) explanation of current density, impedance and temperature measurement representative at one of the 120 measurement contacts. Figure reformatted and taken from [3].

For the cell operation a potentiostat and FRA system by Zahner Elektrik GmbH & Co. KG, Germany is used. The potentiostat system consisting of Zahner Zennium X and Zahner EL1000 is implemented into the test bench. With an additional third-party power source by TDK Lambda, Germany DC currents up to 680 A can be reached. Figure 4.3 shows a schematic diagramm of the electrical cell connection.

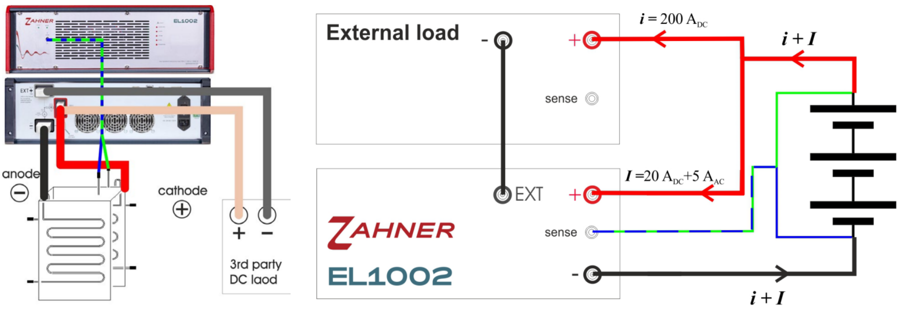

Figure 4.3: Cell connection of Zahner EL1000 with additional third-party power supply, reformatted and taken from [167].

The negative pole of the third-party power source (*External load*) is connected with the EL1000 *EXT* and both positive poles with each other. Within the EL1000 the current ouput of the third-party power source is used to pass through the DC current and modulate an AC amplitude by the Zahner Zennium, which is connected to the EL1000. The EL1000 is then regularly connected to the cell with current and sense cables. For further information is is referred to [167].

To set a DC-bias, the current cables are contacted to the current collector plates at anode and cathode. At the opposite side of the cell, the cell potential (DC and AC) is measured using the main channel of Zahner EL1000. At the non-segmented half-cell, the sense wires are connected to the homogenization plate which is directly contacted to the flow field plate, see Figure 4.1 a). At the half-cell with implemented PCB the potential is measured between the flow field plate and the shunt resistor in segment 5 to exclude the shunt resistance in the cell voltage measurement, see Figure 4.2 a).

The additional sense wires of Zahner Zennium X are connected before ($\varphi_{\mathrm{AC,cell}}$) and after ($\varphi_{\mathrm{AC,end}}$) the shunt resistors in the PCB, analogously to the DC measurement, see Figure 4.2 c). For the data recording, the parallel voltage measurement cards (Zahner PAD 4) with a voltage range of $\pm$ 1 V are employed. With the calibrated resistance of the shunt resistor the local current during the EIS can be determined by measuring the voltage drop, analogously to the DC measurement. This is done at one shunt resistor per segment resulting in a total measurement of 10 segments and the mean cell in parallel. To determine the local impedance, the voltage measurement of the mean cell is then used referring to each segment and the entire cell current measurements. This implies the assumption of very equal voltage along the channel, which is discussed in Section 4.3.2. With this measurement setup, it is possible to operate the cell either in potentiostatic or in galvanostatic mode; all results presented here were obtained in galvanostatic mode.

For the use of the reference electrodes, see Figure 4.12, the PCB is implemented at the cathode for more stable reference electrode conditions. The main channel of the Zahner setup is connected similar to the measurements of the cell segments. To analyze the reference electrodes potential, PAD 4 cards with a voltage range of $\pm$ 4 V are employed and connected to the three reference electrodes at the inlet, center, and outlet of the cell at the cathode.

4.2.2 Test Bench

The test bench, used within this thesis, is an in-house built test bench at Fraunhofer ISE [122], which was modified for the operation at high currents and for parallel impedance measurements. Figure 4.4 provides a simplified flow chart of the test bench. The test bench is designed up to 1000 A (DC) and 10 V, pressure of 50 bar, temperature of 80 $^{\circ}\mathrm{C}$ and a water flow rate of up to 2 $\mathrm{l} \cdot \mathrm{min}^{-1}$. The water flow at anode and cathode can be circulated independently and the water quality is controlled. The two-phase flow coming out of the test cell is fed in a gas water separator, whereby the water is recovered, and the gases leave the test bench through the exhaust. Inline ion exchangers to guarantee a low conductivity of the recirculated water at anode and cathode are employed. A water quality of $< 0.1\ \mu\mathrm{S} \cdot \mathrm{cm}^{-1}$ is assured during measurements independently of the applied temperature and pressure. The test bench is controlled using an in-house developed LabVIEW software environment by National Instruments, USA. This includes pressure and temperature, which are measured and controlled at the cell inlet or outlet, as well as the water inlet flow. The impedance measurements are done with a current amplitude of 10% of the DC-bias between frequencies of 10 kHz and 100 mHz with 10 measurement points per decade and an integration time corresponding to 10 periods. The measurements are proofed on drift and non-linearities using the Kramers Kronig test [75]. The criterion of a valid measurement was set to Kramers Kronig residuals of less than 1% at each frequency point. All impedance spectra shown in this chapter fulfill the Kramers Kronig test.

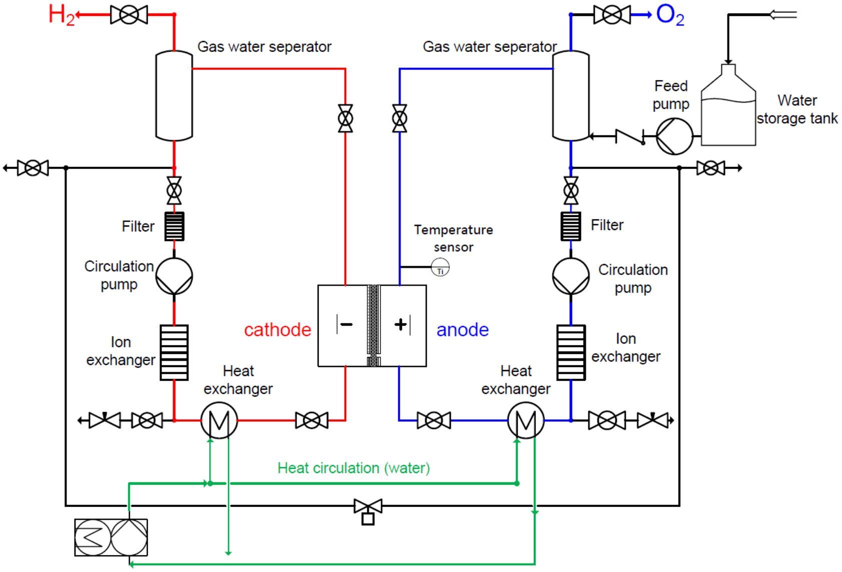

Figure 4.4: Simplified flow chart of the test bench used and modified within this thesis [122].

4.2.3 Electrochemical Measurement and Analysis

To investigate the cell performance polarization curve measurements are conducted between $0.1\ \mathrm{A} \cdot \mathrm{cm}^{-2}$ and $10\ \mathrm{A} \cdot \mathrm{cm}^{-2}$. At selected operation points additionally EIS is performed with a 10% AC amplitude of the DC bias between a frequency of $10\ \mathrm{kHz}$ and $100\ \mathrm{mHz}$. 10 measurement points per decade and a integration time of 10 periods are chosen. The polarization curve and impedance measurements are done at temperatures of $60\ ^{\circ}\mathrm{C}$ and $80\ ^{\circ}\mathrm{C}$, pressure of $1\ \mathrm{bar_g}$ balanced and $10\ \mathrm{bar_g}$ differential prssure, and water flow rates at the anode of $2\ \mathrm{ml} \cdot \mathrm{min}^{-1} \cdot \mathrm{cm}^{-2}$ and $20\ \mathrm{ml} \cdot \mathrm{min}^{-1} \cdot \mathrm{cm}^{-2}$. Before the cell characterization a conditioning including 1 hour of flushing water at $80\ ^{\circ}\mathrm{C}$ followed by 30 minutes at $0.2\ \mathrm{A} \cdot \mathrm{cm}^{-2}$ and $1\ \mathrm{A} \cdot \mathrm{cm}^{-2}$ and an operation 12 hours at $1.7\ \mathrm{V}$. This conditioning is well established for the CCM used in this chapter.

4.3 Results and Discussion

4.3.1 Internal Contact Distribution

An evenly distributed contacting of the segments is essential to analyze along the channel effects in the cell. Without proper contacting an externally induced current distribution can occur which falsifies the measurement results. Unfortunately, a perfect contacting is impossible, therefore the deviations must be considered in the data analysis. C. Immerz et al. reported an influence of PTL and CCM material which led to a current density deviation up to 30% compared to the mean value. With a current density distribution measurement at a low mean current density a reference profile was measured. At different operation points the deviation to the reference profile was calculated and the changes analyzed [36].

In the here presented setup, three main issues can lead to current density inhomogeneities: (1) component tolerance, like PTL and CCM material but also of all milled components and the PCB; (2) global bending of the counter plate and (3) local contacting issues to the measurement contacts of the PCB. To equalize production tolerances, soft conductive material is employed. Small pieces of carbon-based GDL material are used between the flow plate and the PCB to improve the contacting. Influence of global bending of the counter plate has been minimized by supporting the center of the cell between current collector and counter plate with thin stainless-steel sheets with thicknesses in micrometer scale.

To analyze the influence by uneven contacting, tests with pressure paper by Fujifilm, Japan have been performed. Furthermore, before each in-situ measurement the test cell is assembled without CCM but with inserted PTLs to measure the current density distribution in dry condition and at room temperature. Applying all optimizations mentioned above the electrical contact inhomogeneity (without CCM) could be improved from $> 35\%$ standard deviation to $< 5\%$ from the mean current density (5 A absolute) applied, see Figure 4.5 a). As a result, the global bending effects and the contact issues within the segment (reduction of error bar) could be reduced to a minimum.

Furthermore, before and after each electrochemical characterization a CDD reference profile with anodic water flow from segment 1 to 10 and vice-versa is measured with a conditioned cell at begin of test (BoT) and end of test (EoT). Therefore, an operation point at which minimal along the channel effects are expected is chosen (high water flow rate of $10\ \mathrm{ml} \cdot \mathrm{min}^{-1} \cdot \mathrm{cm}^{-2}$ and low current of 5 A absolute at 80 °C). A summary of these pre-tests is given in Figure 4.5 b). Between the pre-testing without CCM and the in-situ operation a clear difference can be seen with randomly changing current density distribution. This might be influenced by the CCM and its swelling and the temperature effect on all components. Also, it is to be mentioned that between the pre-testing and the in-situ measurement the GDL at the cathode is exchanged to first compress a pristine GDL with the CCM which might have a significant influence as well.

Moreover, the current distribution during the measurement is changing, as the difference between BoT and EoT measurements and the switch of the water inlet has a slight leveling effect on the distribution, see Figure 4.5 b). However, all CDD profiles have comparable small overall deviations and no clear trend along the channel. Nevertheless, this behavior of the AtC cell during operation needs to be considered in each analysis as it may superimpose important findings.

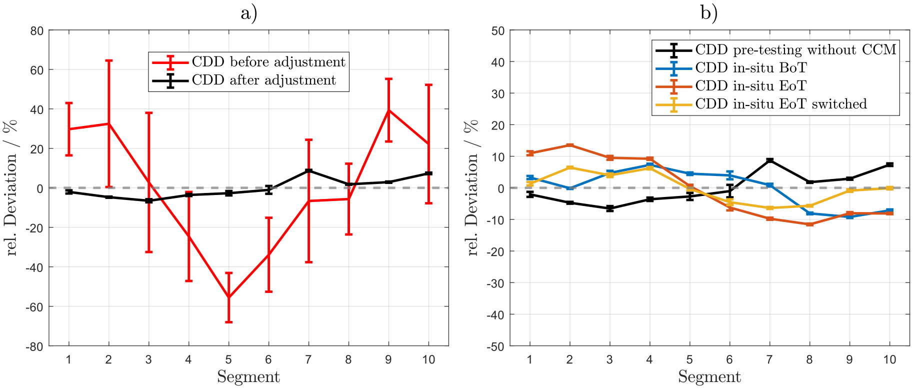

Figure 4.5: Analysis of the internal contact of the segments by measuring the CDD. Relative deviation of pre-testing and in-situ tests at BoT, EoT and with switched water inlet and outlet. The current applied is 5 A in total. In-situ measurements are done at 80 °C and $10\ \mathrm{ml} \cdot \mathrm{min}^{-1} \cdot \mathrm{cm}^{-2}$, pre-testing at dry conditions and room temperature. Figure reformatted and taken from [3].

4.3.2 Voltage Equality

For the locally resolved measurement method used within this thesis, it is assumed that the potential of all segments is approximately equal along the channel. To proof this, the mean cell voltage and the impedance in galvanostatic mode at the same position at the cathode but varied the contacted segment (segment 1 to 10) excluding the shunt resistor at the anode is measured, see Figure 4.6.

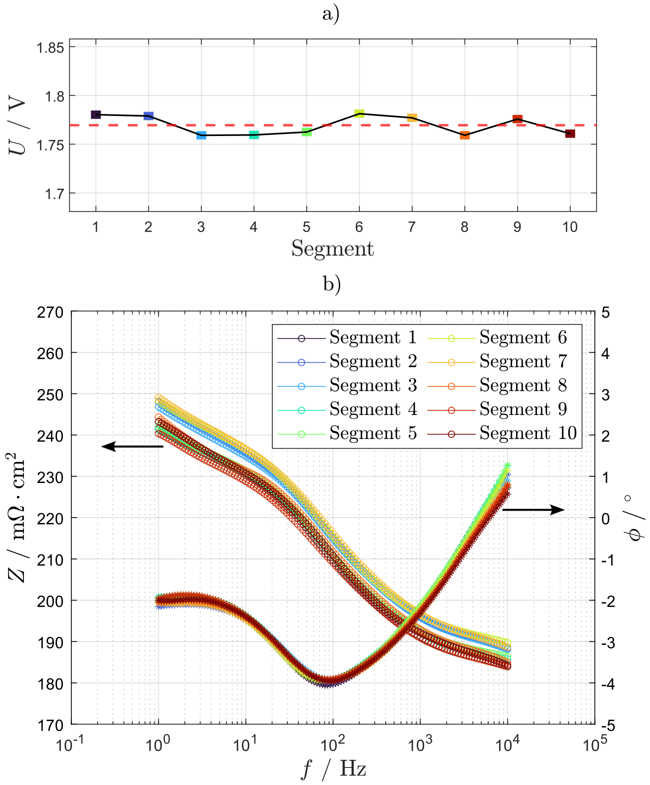

Figure 4.6: a) Galvanostatic mean cell voltage measurement and b) Bode presentation of the mean cell impedance with sense measurement at segment 1 to 10 at the anode. The measurements are done at $1\ \mathrm{A} \cdot \mathrm{cm}^{-2}$, $60\ ^{\circ}\mathrm{C}$, ambient pressure, and a flow rate of $10\ \mathrm{ml} \cdot \mathrm{min}^{-1} \cdot \mathrm{cm}^{-2}$. Figure reformatted and taken from [3].

A voltage deviation of less than $\pm 0.6\%$ was observed when contacting the different segments, see Figure 4.6 a), which is an excellent proof of the potential equalization in the cell. For different used segments very comparable mean cell impedance and phase angle could be measured without any tendency along the channel, see Figure 4.6 b). The mean value of the relative standard deviation of impedance and phase angle over the measured frequency range is $< 1.3\%$ and $< 3.1\%$, respectively. It is demonstrated that the voltage measurement is independent of the segment in the cell at which the voltage measurement is done and that the assumption of equal voltage distribution along the channel is valid. For completeness it should be mentioned that this voltage deviation test was conducted with a slightly different approach to equalize the contacting of the segments compared with the final setup used throughout the rest of this chapter, which led to increased ohmic resistance, detectable at the quite high values for the HFR. Under these conditions and improved cell contact, a HFR of approximately $160\ \mathrm{m\Omega \cdot cm^2}$ is expected, see Figure 4.11.

4.3.3 Determination of the HFR

Impedance measurements at high frequencies are often affected by inductive and capacitive artifacts. These artifacts can often be related to wiring and cell housing issues [81, 102, 168]. Since the test cell presented here has a highly complex measurement setup including four current and two potential wires for the mean cell plus additional 20 wires for the 10 segments the reduction of cable and wire artifacts is crucial. Additionally, the different conducting path lengths in the PCB which are impossible to set perfectly equal for this design might influence the impedance spectra at high frequencies.

Different ways of twisting sense and current cables are investigated, furthermore the cable length and the connection position at the cell is optimized, see Figure 4.7.

In order to see the influence on the HFR and polarization resistances of the mean cell, the cables are purposely positioned in a way to increase high frequency capacitance and inductance and the results compared with the optimized setup, summarized in Figure 4.7. In this case, all setups are measured between the anodic and cathodic end plates and therefore the resistance of the shunt resistor of the PCB is included, which is excluded in the regular measurements by measuring the potential before the shunt resistors. This explains the increased HFR compared with the measurements in the following section.

The measurements show impedance spectra of the mean cell conducted sequentially at the same operation point. The HFR is usually detectable at frequencies $> 1\ \mathrm{kHz}$ and a phase angle of 0° (intersection with $-Im(Z) = 0$ in Nyquist presentation). Since high frequency artifacts influence the determination of the HFR an ECM consisting of a resistor in series connection to one RQ-element (resistor in parallel with a constant phase element) is used and the impedance spectra fitted between 50 Hz and 400 Hz. The fit is extrapolated until the HFR with a phase angle of 0° can be determined.

A fitting of inductive artifacts, which is usually done using an inductance element [81] is in this case not productive, since in the segmented EIS beside inductive also capacitive artifacts are presented, see discussion below in relation to Figure 4.9.

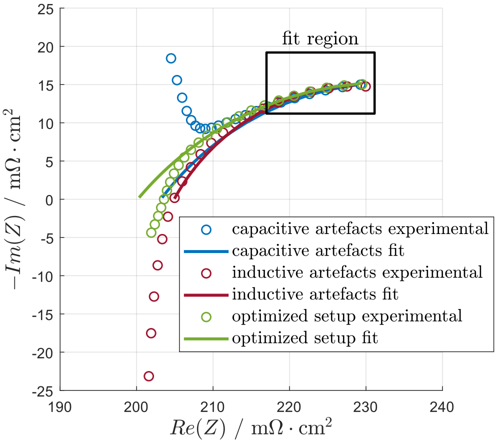

Figure 4.7: Mean cell impedance spectra with purposely induced high-frequency inductive and capacitive artifacts in comparison with the optimized cell setup. Fit results of the ECM to determine the HFR. The measurements are done at $1\ \mathrm{A} \cdot \mathrm{cm}^{-2}$, $60\ ^\circ\mathrm{C}$, ambient pressure, and a flow rate of $10\ \mathrm{ml} \cdot \mathrm{min}^{-1} \cdot \mathrm{cm}^{-2}$. Figure reformatted and taken from [3].

The use of a pseudo-capacitive element (inductance with negative values) to fit a capacitive artifact might be as well a valid option [169].

The HFR is then determined by taken only the series resistor into account. The impedance spectra with different high frequency artifacts show a very comparable HFR value with less than $\pm 1\%$ deviation, see Figure 4.7. As this method is fairly reliable in determining the HFR, it is used for every EIS shown in this chapter using the Zahner Analysis Series Fit tool. This becomes even more important regarding the EIS of the single segments since they are drastically influenced by artifacts due to the complex connection within and to the PCB.

4.3.4 Comparison with a Laboratory-Scaled Cell

The inlet segment of the AtC cell should in priniciple face under high water flow rates homogeneous condition, comparable to the ISE reference cell used in Section 2 and 3. To analyze the quality of the AtC test cell, the cell performance and impedance is compared between segment 1 of the AtC cell and the ISE reference cell. For the latter, measurements from Section 3 are used. The measurements shown are done at ambient pressure for the ISE reference cell

and at $1\ \mathrm{bar_g}$ balanced pressure for the AtC cell, $80\ ^\circ\mathrm{C}$ and a water flow rate at the anode of $37.5\ \mathrm{ml} \cdot \mathrm{min}^{-1} \cdot \mathrm{cm}^{-2}$ for the ISE reference cell and $20\ \mathrm{ml} \cdot \mathrm{min}^{-1} \cdot \mathrm{cm}^{-2}$ for the AtC cell.
As CCM for both setups, a commercial E400 Gen. 3 CCM by Greenerity GmbH, Germany and at the cathode a carbon-based GDL with $370\ \mu\mathrm{m}$ thickness are employed. At the anode, the AtC cell employs a platinum coated titanium fiber PTL with $500\ \mu\mathrm{m}$ thickness and the ISE reference cell the same PTL but with $250\ \mu\mathrm{m}$ thickness.
Figure 4.8 a) provides a comparison of the polarization curve measurements up to $5\ \mathrm{A} \cdot \mathrm{cm}^{-2}$. The measurement of segment 1 of the AtC cell shows a higher slope, which is referred to a higher Ohmic cell resistance. This difference can be explained by a worse compression of the AtC cell due to its complex cell setup. Other than that, the polarization behavior is seemingly comparable. The EIS analysis for $1\ \mathrm{A} \cdot \mathrm{cm}^{-2}$ (top) and $3\ \mathrm{A} \cdot \mathrm{cm}^{-2}$ (bottom), see Figure 4.8 b), supports this, as the polarization resistance is consistent for both cells. The Ohmic resistance is around 5% higher for the AtC cell measurments, see legends.
This analysis shows that segment 1 of the AtC cell behaves as a laboratory-scaled test cell under homogeneous conditions. The increased HFR values lead to higher cell voltages, which can influence the measurements regarding degradation and heat dissipation.

4.3.5 Operation under Different Operational Conditions

To confirm a good technical performance of the AtC cell and demonstrate that it is fit for purpose to be used in further investigations, the overall and local DC performance and impedance under different conditions is analyzed. It is particularly focused on measurements at equal pressure of $1\ \mathrm{bar_g}$ ("$1-1\ \mathrm{bar}$ pressure") and differential pressure of $10\ \mathrm{bar_g}$ ($10\ \mathrm{bar_g}$ cathode, $1\ \mathrm{bar_g}$ anode; "$10-1\ \mathrm{bar}$ pressure") at current densities of up to $10\ \mathrm{A} \cdot \mathrm{cm}^{-2}$, summarized in Figure 4.9.

Figure 4.9 a) shows the mean polarization curve of the cell (segment 1 to 10) for both pressure operations up to $10\ \mathrm{A} \cdot \mathrm{cm}^{-2}$ at $80\ ^\circ\mathrm{C}$. The error bars show the deviation of the mean value of the current density and voltage measurement during the last 30 seconds of each current density step of this measurement. Uncertainties as influences of contacting of the segments (see discussion above), stability issues due to bubble formation and inaccuracies of all control and measurement variables of the test cell and the test bench need to be considered when analyzing these results. Since an exact determination of all possible errors during these measurements is very challenging, reproducibility measurements can deliver a range of expected accuracy.
The reproducibility of the AtC cell was tested by conducting the measurements twice with a new assembly of the cell between the reproducibility measurements. They revealed a voltage deviation of less than $1.4\ \%$ for the whole current density range even in the most critical operation point regarding reproducibility (10 bar differential pressure). This should be representative for all measurements conducted in this study, see Appendix, Figure A.9 a).

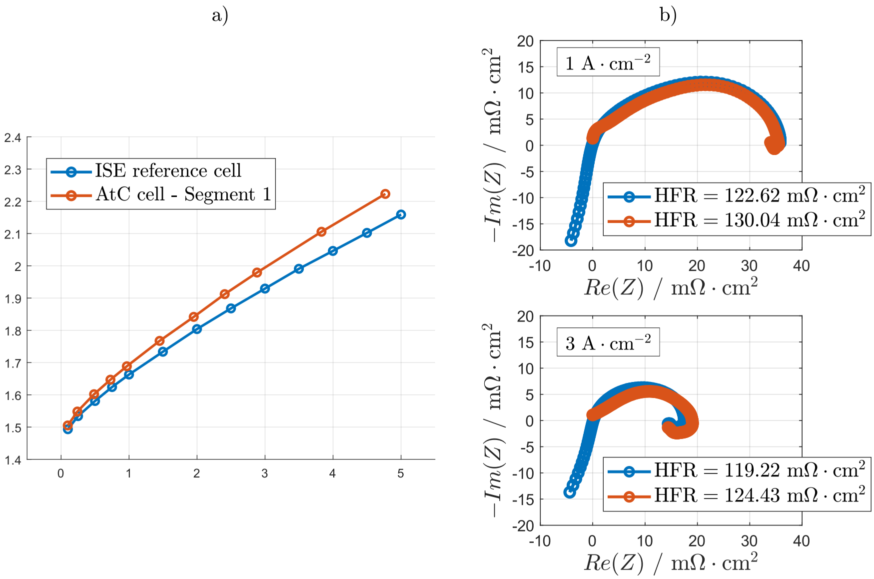

Figure 4.8: Comparison of segment 1 of the AtC cell with the ISE reference cell with comparable cell setup, a) polarization curve measurements and b) HFR-free EIS at $1\ \mathrm{A \cdot cm^{-2}}$ (top) and $3\ \mathrm{A \cdot cm^{-2}}$ (bottom). The measurements are done at ambient pressure for the ISE reference cell and at $1\ \mathrm{bar_g}$ balanced pressure for the AtC cell, $80\ ^\circ\mathrm{C}$ and a water flow rate at the anode of $37.5\ \mathrm{ml \cdot min^{-1} \cdot cm^{-2}}$ for the ISE reference cell and $20\ \mathrm{ml \cdot min^{-1} \cdot cm^{-2}}$ for the AtC cell.

A high anode water flow rate of $20\ \mathrm{ml \cdot min^{-1} \cdot cm^{-2}}$ is chosen to enable minimal temperature gradients along the channel. In both cases, there is no indication for mass transport limitations (exponential trend of the curve towards high current densities). Instead, the curves show a decrease of the slope towards high current densities which is commonly associated to a decrease of the membrane resistance due to a temperature increase [59]. In [1] it is already discussed that temperature effects alone cannot explain this behavior. Instead an increasing inductive loop at low frequencies with increasing current density contributes to a significant decrease in impedance as well.

At low current densities $< 1\ \mathrm{A \cdot cm^{-2}}$ the influence of higher partial pressure of hydrogen resulting in higher voltages can be seen and explained by the pressure dependency of the Nernst equation [170, 171]. In summary, only very small differences are observable for the selected operating conditions, which can also be related to the proper cell design and the implementation of highly reproducible and homogeneously coated commercial materials. Exemplarily, the mean cell impedance at $3\ \mathrm{A \cdot cm^{-2}}$ is shown in the inset of Figure 4.9 a). It is noticeable that the polarization processes are very comparable and at 10 bar differential pressure a lower HFR is

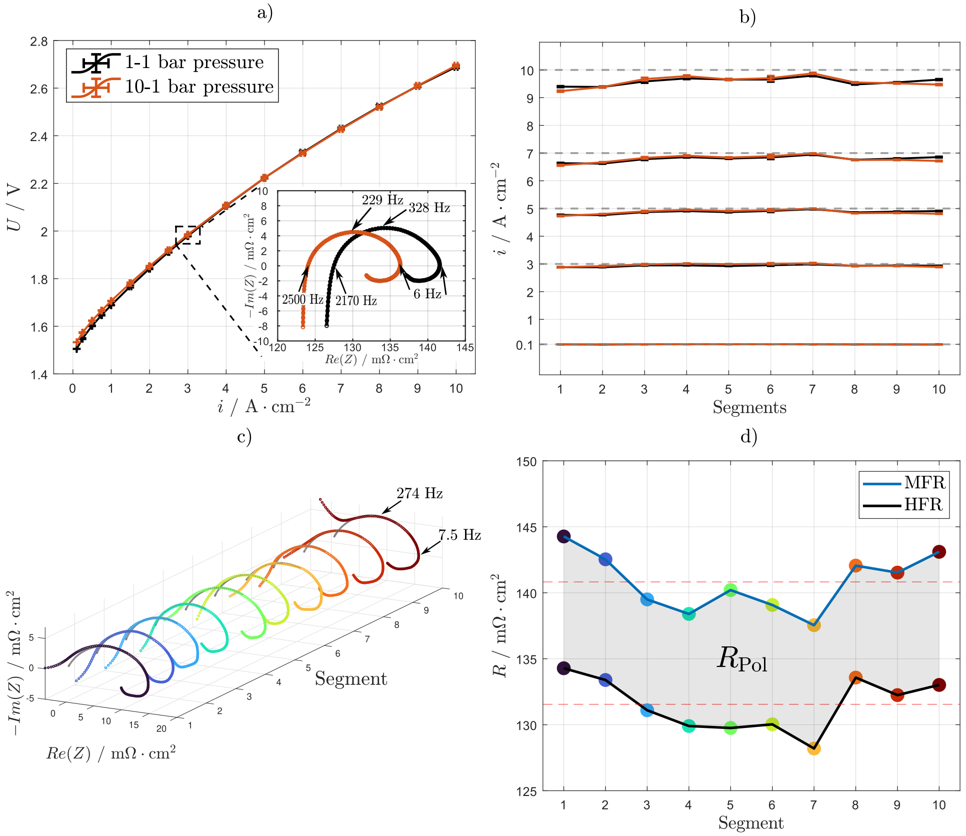

Figure 4.9: a) Polarization curve at $1-1$ bar and $10-1$ bar differential pressure with corresponding impedance spectra at $3\ \mathrm{A \cdot cm^{-2}}$ in the inset, b) CDD along the 10 segments at different mean current densities. c) Locally resolved Ohmic free EIS along the segments at $3\ \mathrm{A \cdot cm^{-2}}$ and $10-1$ bar differential pressure and d) evaluation of the HFR, the polarization resistance and the MFR . The measurements are done at 80 °C, and a water flow rate at the anode of $20\ \mathrm{ml \cdot min^{-1} \cdot cm^{-2}}$ ($1200\ \mathrm{ml \cdot min^{-1}}$). Figure reformatted and taken from [3].

detectable. This might be explained by the better compression of the anode half-cell and therefore better contact between PTL and CCM due to the higher cathode gas pressure.

Figure 4.9 b) shows the current density distribution along the cell segments at several mean current densities during the polarization curve. For all mean current densities, only minor differences between the current density of the 10 segments are noticeable. This demonstrates the very similar contacting of the segments and the small gradient of temperature and gas amount along the channel due to the high water flow rate applied. The error bars show the total measuring error of the time-depending variation of the current density measurement (cell instability) and the mean value of the 12 contacts per segment.

The reproducibility of the current density distribution measurement is given in the Appendix, Figure A.9 for the 10-1 bar measurement. The difference between the conducted measurements is shown for every measured current density during the polarization curve with an error of the mean value of all 10 segments being smaller than $1.6\ \%$. Additionally, the mean error for the parallel temperature measurement is shown in the Appendix Figure A.9 a) with a value less than $1.2\ \%$. Figure A.9 b) depicts the deviation between the two measurements of current density and temperature distribution of the single segments at $1\ \mathrm{A}\cdot\mathrm{cm}^{-2}$, $3\ \mathrm{A}\cdot\mathrm{cm}^{-2}$ and $5\ \mathrm{A}\cdot\mathrm{cm}^{-2}$ representative for all current densities.

When comparing the mean value (gray dotted lines) with the distribution of the current densities, two minor trends can be detected: First, there is a small offset between the nominal output of the potentiostat (DC-bias) and the measured current density of the segments, as can easily be seen for the high current densities$> 5\ \mathrm{A}\cdot\mathrm{cm}^{-2}$ plotted in Figure 4.9 b). This difference might be assigned to small shunt currents through the complex sense wiring above the PCB at the anode half-cell and the given measurement inaccuracy of $\pm 1\ \%$. The different temperatures at the measurement contacts might as well have an influence. The relative difference between the output of the potentiostat and the measured (mean) values using the PCB is linearly increasing with increasing DC-bias. For $0.1\ \mathrm{A}\cdot\mathrm{cm}^{-2} < 1.9\ \%$ and for $10\ \mathrm{A}\cdot\mathrm{cm}^{-2} < 4.2\ \%$ relative offset to the output DC-bias is detected for the differential pressure mode.

Second, although only to a small extend, different segments show slightly different values for the mean current densities measured with the PCB. Throughout the numerous measurements performed, these show a random distribution when comparing measurements with different cell assemblies and are therefore assigned to very minor differences in clamping pressure distributions. In the presented case, slightly lower local current densities are observed for segments 1, 2 and segment 8, 9 and 10 and slightly higher local current for segment 7. The overall relative standard deviation of the measured mean current densities is for currents $\geq 1\ \mathrm{A}\cdot\mathrm{cm}^{-2} < 2\ \%$ and is constant over the applied DC-bias. The relative measured offset to the potentiostat's output and the relative standard deviation of the segments is shown for all mean current densities in the Appendix, Figure A.11.

Figure 4.9 c) and d) show the impedance spectra along the channel at $3\ \mathrm{A}\cdot\mathrm{cm}^{-2}$. The HFR-free locally resolved EIS with the fit for the HFR determination (gray fitting curve at high frequencies, see Section 4.3.3, is shown in Figure 4.9 c). Since the current density shows only minimal, statistical fluctuations along the channel, no significant along the channel effects in the EIS are expected and observed. The influence of minor differences in contacting on the polarization resistance is noticeable. At high frequencies the inductive and capacitive artifacts are present but properly circumvented with the high frequency fit of the HFR, see Figure 4.11. The reproducibility of the impedance measurement is given in the Appendix, Figure A.10 for the mean cell and segment 1, 5 and 10 exemplarily for all segments, as the mean value and standard deviation in Bode presentation of the two measurements conducted with two cell assemblies and identical materials used show. At high frequencies (> 1 kHz) deviations of the phase angle due to wiring artifacts can be seen. At medium to low frequencies (< 1 kHz) the polarization is very similar with a constant difference in the impedance, which is attributed to cell contacting and therefore different values of the HFR. Furthermore, the Kramers Kronig test is done separately for each measurement and shows that both measurements have very low residuals in the low-frequency range but slightly higher errors at high frequencies (> 3 kHz), which is referred to wiring artifacts.

Figure 4.9 d) shows the HFR fitted with the ECM explained in Section 4.3.3 and the MFR (minimal frequency resistance) which is measured at 100 mHz. The MFR is the impedance value measured closest to the DC resistance. The gray area between HFR and MFR can be described by the polarization resistance (R_{Pol}). The contacting issues can herewith be seen with a random distribution along the channel. The behavior of the impedance along the channel is in very good agreement with the current density measurement. Segments 1, 2, 8, 9 and 10 show relatively high and segment 7 very low HFR and MFR values which is consistent with the trend of the local current densities, see paragraph above.

The results so far demonstrate, that the AtC test cell works very reliably under a broad variety of current densities and pressure settings. Smaller differences in the measured values of the segments are negligible, especially as they can easily be understood and analyzed, e.g. the correlation between the current distribution among the segments and the concomitant EIS. However, locally resolved results at very high current densities ($10\ \mathrm{A \cdot cm^{-2}}$) need to be analyzed carefully as the shunt currents circumventing the PCB induce significant deviation from the potentiostat's output.

Figure 4.10 shows the current density (i_{loc}) and temperature (T_{loc}) distribution measured at the 40 contacts of the middle row of the PCB along the channel during a polarization curve measurement up to $6\ \mathrm{A \cdot cm^{-2}}$ at $60\ ^{\circ}\mathrm{C}$ water inlet temperature. The color map indicates the current density applied to the entire cell. Purposely, a constant low anode water flow rate of $2\ \mathrm{ml \cdot min^{-1} \cdot cm^{-2}}$ ($120\ \mathrm{ml \cdot min^{-1}}$) is chosen to see significant gradients along the channel. This flow rate corresponds to a mean cell water stoichiometry of greater than 3800 at $0.1\ \mathrm{A \cdot cm^{-2}}$ and approximately 64 at $6\ \mathrm{A \cdot cm^{-2}}$. According to the ideal gas law ($60\ ^{\circ}\mathrm{C}$, $1\ \mathrm{bar_g}$ pressure), at $6\ \mathrm{A \cdot cm^{-2}}$ an oxygen volume fraction of approximately 12% at the anode outlet can be predicted.

In Figure 4.10 a) the current density distribution over the 10 segments is quite homogeneous for low mean current densities which is expected due to the good homogeneous contacting of the cell, leading to only small differences in Ohmic resistance and the high stoichiometry. Towards higher mean current densities, the local deviations increase. Since the trend of these differences at a given x/L is the same for all current densities but increases in magnitude with increasing mean current density, this is attributed to initial differences in contacting of the segments. For mean current densities $> 4.5\ \mathrm{A \cdot cm^{-2}}$ a clear increase of the local current density along the channel can be seen.

With a 125 μm thick membrane (Nafion$^{\text{TM}}$ N115) that was used for these measurements, voltages up to 2.37 V at 6 $\text{A}\cdot\text{cm}^{-2}$ and 60 °C are observed, which leads to a mean heat dissipation of the reaction of $\approx 5.3\ \text{W}\cdot\text{cm}^{-2}$ (referred to thermoneutral voltage at 60 °C). With the decreasing water content and increasing gas amount, the heat dissipates more through the flow field and the end plates than being removed by the water, which leads to a significant temperature gradient of ≈ 13 K between inlet and outlet measured via the temperature sensors in the PCB. The water temperature along the channel is increasing even more, 17 K temperature difference were observed between water inlet and outlet under these conditions, measured with the inline temperature sensor in the water-gas stream. At the CCM itself even higher temperatures are expected since the temperature sensors of the PCB are > 23 mm (height of flow field plate, see Figure 4.1) away from the CCM and a relevant temperature gradient is expected.

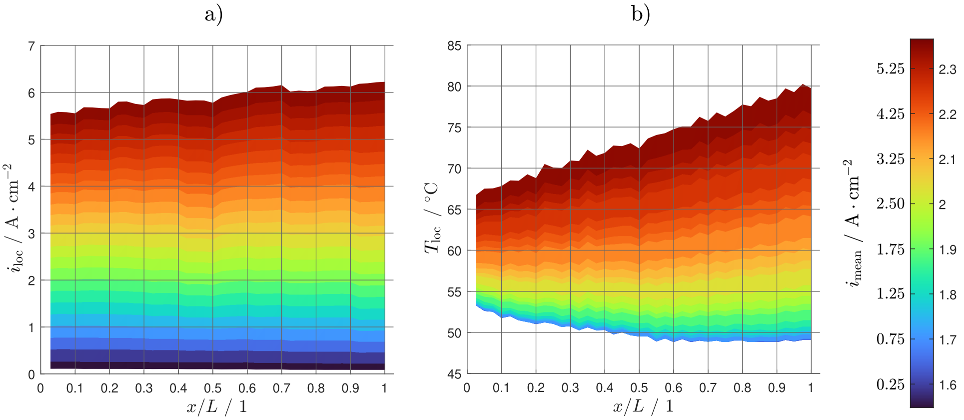

Figure 4.10: a) Current density distribution and b) temperature distribution of the anode flow field plate along the channel during a polarization curve up to 6 $\text{A}\cdot\text{cm}^{-2}$. The measurements are done at 60 °C, balanced pressure of 1 bar, and a water flow rate at the anode of 2 $\text{ml}\cdot\text{min}^{-1}\cdot\text{cm}^{-2}$ (120 $\text{ml}\cdot\text{min}^{-1}$). Figure reformatted and taken from [3].

This explains the increasing current density towards the cell outlet at high current densities.

A membrane dehumidification along the channel would result in an increase of membrane resistance along the channel [35], which seems not to be dominant for the selected conditions here. The low water flow rate and a stoichiometry of ≈ 64 seem to create no significant undersupply of water to the catalyst layer and therefore no increasing mass transport resistance. It is assumed that with today's standard CCM and PTL materials and a proper integration into the cell, undersupply phenomena only occur when operating with extremely low flow rates close to the stoichiometric water amount.

It is to be noted that for low current densities, the heat losses through the end plates are quite high compared to the reaction's heat flux. Therefore, a decreasing temperature is detectable between

the cell inlet and center for low current densities. The temperature of the water increases along the channel, which can be seen at the stabilized temperature profile from center to outlet. Change of the heat capacity due to increasing gas amount is negligible due to the tiny amount of gas produced under these conditions. This also explains the different inlet temperatures measured at the anode flow field plate at $x = 0$. The heat flux into the cell (water controlled at the inlet on $60\ ^\circ\mathrm{C}$) and the heat exchange surface to the surrounding can be assumed as constant but the reaction's heat changes by a factor of > 880 ($\dot{q}_{1.55\mathrm{V}} = 0.006\ \mathrm{W} \cdot \mathrm{cm}^{-2}$, $\dot{q}_{2.37\mathrm{V}} = 5.296\ \mathrm{W} \cdot \mathrm{cm}^{-2}$) during the polarization curve.
Targeting stack like conditions, any heat transport perpendicular to the flow direction should be avoided in a segmented cell, as in a stack the neighboring cell areas and cells produce similar amounts of heat and the cooling is restricted to the water and the in-plane heat conduction of PTLs and the flow field plate. Thermal insulation or external heating of the end plates could improve the thermal cell behavior which will be considered in future studies.
To analyze the membrane resistance along the channel, the HFR at $2\ \mathrm{A} \cdot \mathrm{cm}^{-2}$ and $6\ \mathrm{A} \cdot \mathrm{cm}^{-2}$ along the cell segments is compared, see Figure 4.11 a). At $2\ \mathrm{A} \cdot \mathrm{cm}^{-2}$, a temperature difference between inlet and outlet of $< 1\ \mathrm{K}$ is measured and the HFR shows constant behavior along the channel with only small influences by contacting, compare segment 1 and segment 8. This is in alignment with the stable current density distribution shown in Figure 4.10 a) and can be explained by the homogeneous temperature profile, the quite homogeneous contacting of the segments and the high stoichiometric water supply of ≈ 192 at $2\ \mathrm{A} \cdot \mathrm{cm}^{-2}$.
Contrary to this, at $6\ \mathrm{A} \cdot \mathrm{cm}^{-2}$ a temperature difference between inlet and outlet of $\approx 13\ \mathrm{K}$ was measured and a clear decrease of the HFR along the channel is observed, which is referred to the predominant positive temperature and the comparably smaller negative dehumidification influence on the membrane and its conductivity. This explains as well the current density increase along the channel, see Figure 4.10 a). It is also remarkable that the mean HFR is lowered by around 15% compared to the measurements at $2\ \mathrm{A} \cdot \mathrm{cm}^{-2}$, which can be explained by the increased mean cell temperature. It is here to be mentioned, that with this study extreme conditions are purposely shown, knowing that such conditions are not suitable for industrial long-term applications.
Figure 4.11 b) shows the comparison of the DC cell resistance R_{DC} given by the slope of the polarization curve shown in Figure 4.10 with the locally resolved MFR measured at $100\ \mathrm{mHz}$ of the mean cell and exemplarily for the segments at the inlet, center and outlet (segment 1, 5 and 10) over the current density. Since most polarization processes are faster than $100\ \mathrm{mHz}$ which corresponds to a time constant of $\approx 1.6\ \mathrm{s}$, the MFR should be very comparable to R_{DC} if the EIS and the polarization curve are agreeing. R_{DC} is determined by a polynomial fit of the polarization curve and its derivative with respect to the local current density of the segments and the overall current density, respectively.
For the inlet, center, outlet and the mean cell the trend of the MFR and R_{DC} are in good agreement. The difference in magnitude is assigned to the fact that at $100\ \mathrm{mHz}$ most but not all processes

are included in the impedance measurement. For current densities $> 1\ \mathrm{A \cdot cm^{-2}}$ the MFR shows higher resistance as R_{DC} which is unusual for electrochemical cells but explainable by the inductive loop. Low frequency inductive loops usually lead to an increase in performance and therefore a decreasing resistance which is partially cut off by not measuring towards 0 Hz. This inductive feature can even lead to the fact that R_{DC} shows lower values than the HFR, which can be seen when comparing Figure 4.11 a) and b). This is consistent with the findings on inductive loops, see Chapter 2. For current densities $< 1\ \mathrm{A \cdot cm^{-2}}$ the inductive loop is not present and therefore only capacitive polarization resistance is detectable, which explains the lower MFR compared to R_{DC} since some slow processes with positive contribution to the cell resistance are not included in the MFR.

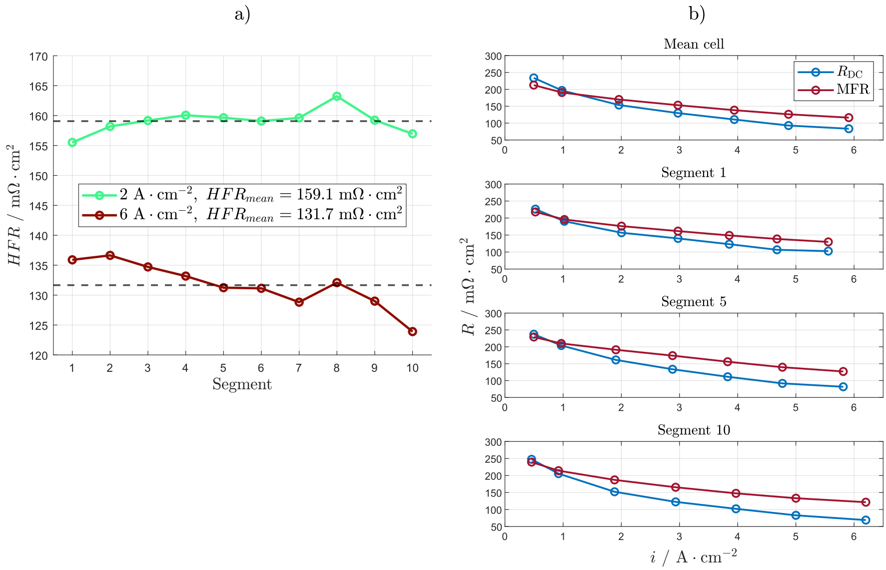
a)

b)

Figure 4.11: a) Analysis of the HFR at $2\ \mathrm{A \cdot cm^{-2}}$ and $6\ \mathrm{A \cdot cm^{-2}}$ along the cell segments and b) comparison of the DC resistance and the MFR over the current density of the mean cell and segment 1, 5 and 10. The measurements are done at 60 °C, balanced pressure of 1 bar, and of $2\ \mathrm{ml \cdot min^{-1} \cdot cm^{-2}}$ ($120\ \mathrm{ml \cdot min^{-1}}$). Figure reformatted and taken from [3].

The temperature influence is visible when comparing the current densities at segment 1, 5 and 10. At lower (mean) current densities ($< 2\ \mathrm{A \cdot cm^{-2}}$) very comparable resistances and local currents are visible. Towards higher current densities a clear shift of decreasing resistance and increasing local current towards the cell outlet is detected, which is consistent with the HFR distribution analysis, see Figure 4.11 a). Also, the difference in magnitude between MFR and R_{DC} diverge more when measuring down the channel. As the tendency still seems to have a logical trend for R_{DC} and MFR, it is concluded that the low frequency inductive feature is becoming more relevant towards the cell outlet. The increasing current density along the channel might explain this since the inductive loop is increasing with increasing current density. However, is mgiht be also possible that the harsh conditions at the cell outlet can lead to a higher through-plane temperature gradient, which might increase this feature. The inductive loop is usually increasing with decreasing input temperature, where higher through-plane temperature gradients are expected, which might drive this effect. To verify this assumption electrochemical and fluidic modeling is suggested.

For a comprehensive understanding of phenomena occurring along the channel, the presented test cell offers a powerful base. However, the cell shows minor limitations. The fact that the (vertical) distance of the local measurement points to the electrode ($> 20\ \mathrm{mm}$) is comparably high, which needs to be considered in the temperature measurements since heat dissipation cannot totally be minimized between these two points. With a channel length of $30\ \mathrm{cm}$ the cell presents the lower limit of industrial relevant designs which makes it still possible to be handled in the laboratory. AtC test cells with longer channel length might reveal higher gradients and are even closer to industrial designs. A higher resolution of the impedance measurement, e.g. a segmentation every $1\ \mathrm{cm}$ might help to understand poisoning or coating defects for large scale materials which is not the focus of this approach.

4.3.6 Reference Electrodes

The results of the study conducted with reference electrodes are provided in the following, the measurement data has been published in [172].

Figure 4.12 show the analysis of a measurement at ambient pressure, temperature of $80\ ^\circ\mathrm{C}$, and a water flow rate at the anode of $1.2\ \mathrm{l} \cdot \mathrm{min}^{-1} \cdot \mathrm{cm}^{-2}$. Figure 4.12 a) provides the polarization curve of the mean cell and the cathodic and anodic contribution at the center of the cell, Figure 4.12 b) shows the HFR-free polarization curve over the decadic logarithm of the current density with the analysis of the Tafel slope b, see legend. Due to misalignment of the laser ablated region of the CCM with the PTL stripe at the reference electrode, the reference electrodes at the inlet and outlet of the cell are not evaluable. The reference electrode at the center indicates that the anode kinetics show 2.5 times higher Tafel slope, which is also in good accordance with the smaller impedance of the cathode at $0.5\ \mathrm{A} \cdot \mathrm{cm}^{-2}$, see Figure 4.12 c) at the top, which is mostly related to charge transfer. However, regarding the polarization curve and HFR-free polarization curve at higher current densities anode and cathode show comparable overpotentials. This is as well in good agreement with the impedance analysis at $4\ \mathrm{A} \cdot \mathrm{cm}^{-2}$ (Figure 4.12 c) at the bottom) at which the cathode show a higher polarization resistance as the anode. The difference in HFR of the anode and cathode spectra may be related with a (through-plane) misalignment of the laser ablated catalyst layers. In theory, with the laser ablation reference electrodes employed, the membrane potential should be measured exactly in the center (in through-plane direction) which should lead to very similar values in the HFR of both spectra.

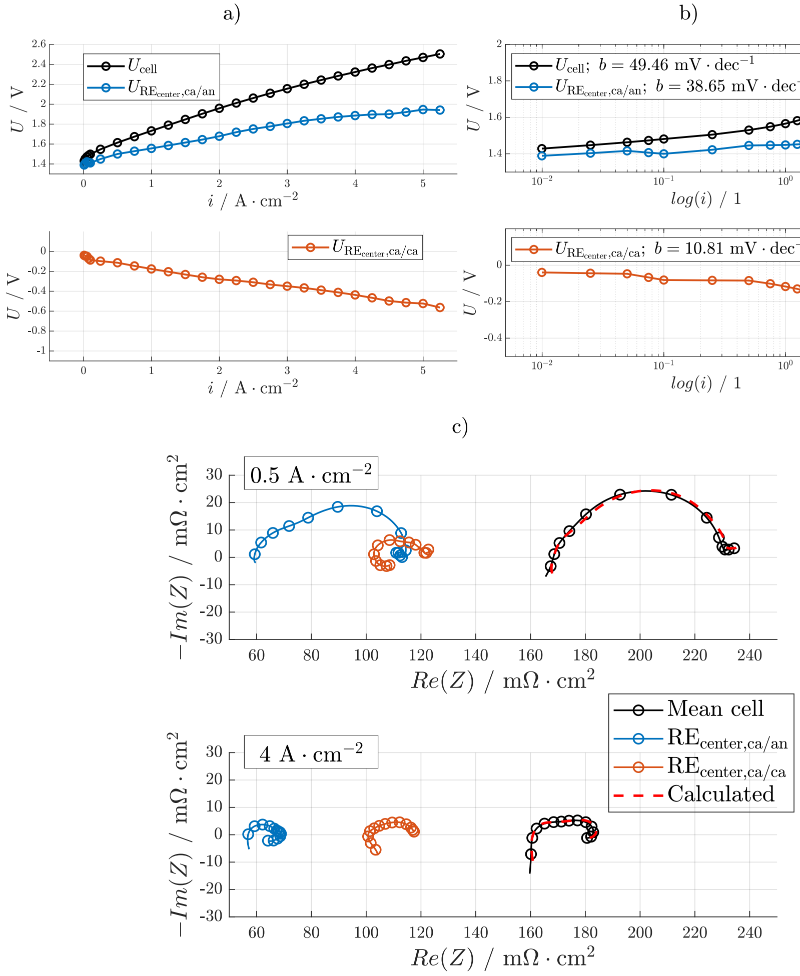

Figure 4.12: Results of the reference electrode setup within the AtC cell. a) Polarization curve of the mean cell and anodic and cathodic contribution at the center of the cell, b) Tafel analysis, and c) EIS analysis.

Alongside the geometry-related artificats, inductive artifacts at high frequencies are likely to occur as discussed in [114, 119] for solid oxide fuel cells and in [173, 174] for lithium ion batteries. These artifacts typically show loops at higher frequencies related to different time constants of the electrochemical polarization processes occuring at the working and reference electrodes, which are seemingly also observable in the measurements shown here, which distort the evaluation of the HFR but also capacitive processes. As discussed in Section 2.3.5, the low-frequency inductive loop is here also only observable at the anode. The sum of the anode and cathode spectra is shown in red dashed lines and show very good agreement with the measured spectrum of the entire cell. It should be noted that this section only discusses the possibility of the use of reference electrodes in the AtC cell. Inaccuracies as the alignment of the in-plane position of the reference electrodes and misalignment of the laser ablated catalyst layers may exist and still need to be optimized. This is especially influencing a proper measurement of the impedance, as discussed in [114, 119]. Furthermore, with the here used cell setup, employing a segmented anode and cathode, the cell performance is much worse than the regular cell operation. However, a proper reference electrode setup has been developed for the AtC cell, which is in good accordance with the other test cells with reference electrode discussed in Section 2.3.5.

4.4 Conclusion

In this chapter, a segmented PEM water electrolysis along the channel test cell for operation at high current densities up to $10\ \mathrm{A} \cdot \mathrm{cm}^{-2}$ is presented. The cell is well suited for operating points up to $80\ \circ\mathrm{C}$ and $10\mathrm{bar}$ differential and balanced pressure. With its 40 contacts along the channel in three rows, highly resolved current density and temperature profiles can be monitored. Due to the possibility of segmenting the flow field plate and the porous transport layer, locally resolved impedance measurements with minimized in-plane crosstalk between the segments can be done in parallel.

Challenges, as the unequal internal contacting of the segments, tightness issues up to 10 bar gas pressure of the segmented bipolar plate and high frequency artifacts in the impedance spectra were faced and have been solved to a suitable level.

It is demonstrated that the locally resolved impedance measurements are in very good agreement with the current density and temperature distribution measurements. Effects of temperature gradients current density, high frequency series resistance and low-frequency impedance response were observable along the channel. Operation up to $10\ \mathrm{A} \cdot \mathrm{cm}^{-2}$ at $10 - 1\ \mathrm{bar}$ differential pressure could be shown without limitations by the test cell and test bench. However, unequal contacting remains a general issue to be solved within segmented test cells but could be minimized considerably in this setup. The contacting of the segments was optimized to an overall standard deviation of the current density distribution of less than $\pm 5\%$ compared with the mean current density applied, which allows us to properly investigate along the channel effects. Furthermore, a method to determine the high frequency series resistance by modeling and extrapolating a specific frequency range in the charge transfer region to circumvent high frequency artifacts due to wiring of the impedance spectra is presented.

For future research, it is recommended to minimizing the distance between the temperature measurement point to the CCM, which is challenging but might provide more precise information on the temperature dependency of loss processes in the cell. Furthermore, test cells with even longer channels might be closer to large scale industrial applications but challenging regarding the required space in laboratories and test benches. For the impedance analysis a higher resolution combined with voltage measurements in each segment could improve the quality of the measurements.

With the present test cell, a measurement application to close the research gap of industrial-relevant spatially resolved measurements in PEM water electrolysis is provided. Practically, the cell can be used to characterize different materials as flow field channels, PTLs and CCMs along the channel at industrial operation. With the combination of current density, temperature and impedance distribution measurements the analysis of the high frequency resistance and polarization processes can properly be done and essential understanding can be provided.

Alongside the regular segmented operation, reference electrodes have been implemented into the AtC cell and tested successfully. Despite of misalignment issues, the reference electrodes of the AtC cell show good agreement with the results of the test cells employing reference electrodes, as discussed in Section 2.3.5.

5 Performance-Based Along the Channel Analysis [1]

5.1 Introduction

Due to its possibility of being operated at high current densities and quickly be switched between different load levels, PEM water electrolysis has high potential to be coupled with renewable electricity from volatile wind and solar energy sources [175–179]. With the development of advanced components, like CCMs with a membrane thickness of less than $100\ \mu\mathrm{m}$, operation at high current densities of $> 5\ \mathrm{A} \cdot \mathrm{cm}^{-2}$ will be feasible in the future [176, 180–183]. Even with low catalyst loading ($< 0.5\ \mathrm{mg}_{\mathrm{PGM}} \cdot \mathrm{cm}^{-2}$), high cell efficiencies are realistic and intended by the Clean Hydrogen Partnership, European Union and the U.S. Department of Energy, USA for future PEM water electrolysis operation [33, 34].

In principle, PEM water electrolyzers can be operated at way higher current densities, as shown in [183]. In this work polarization curve measurements using the *Fraunhofer ISE reference cell* up to $25\ \mathrm{A} \cdot \mathrm{cm}^{-2}$ under high water flow rates, without any indication of mass transport limitations, see Figure 5.1. Whether this phenomenon is also to be seen in industrial scale along the water supply channels is one of the key investigations in this chapter. However, when operating at high current densities and temperature issues must be considered due to the high heat dissipation rate induced by voltage loss (Joule heating). This consideration is important for performance, as well as for degradation-based analyses, which require advanced thermal management within the cell.

To analyze the influence of different water and gas ratios, locally resolved measurements provide a deeper understanding, such as the along the channel approach. Some work employing segmented cells along the flow field are reported in the literature, as discussed in Setion 4.1. However, they all are operated at rather low current densities, providing less relevance for today's and future industrial operation. In this study, the AtC test is employed and the measurement data analyzed by locally resolved voltage breakdown and EIS with subsequent DRT and ECM up to current densities of $7\ \mathrm{A} \cdot \mathrm{cm}^{-2}$.

With parameter variations at industrial-relevant operation points, along the channel and contact

---

[1] Parts of this chapter have been published in [5]

inhomogeneity effects are analyzed. Sintered fiber and powder PTLs are employed to analyze the influence of different structural PTL parameters. For the in situ measurements commercial CCM with state-of-the-art catalyst layer loading and a CCM produced at Fraunhofer ISE with low catalyst loading are used. The latter CCM is in accordance with the US and EU development goals for PEM water electrolysis for the year 2030, see above.

5.2 Experimental

5.2.1 Test Cell and Test Bench

The test cell and test bench used in this chapter are the, in this thesis developed, AtC test cell and the modified test bench. Both are in detail described in Chapter 4.

5.2.2 Cell Materials and Ex Situ Characterization

Porous Transport Layers

The default anode PTL (here referred to as PTL 1) used in this chapter is a platinum-coated sintered titanium fiber PTL with 250 µm thickness. As cathode PTL a carbon-based GDL with a MPL and 215 µm thickness is employed. For the analysis of different structural anodic PTL parameters, a sintered titanium particle PTL with 250 µm which were in-house platinum-coated is used and referred to as PTL 2. The structural parameters of the PTLs were investigated using mercury intrusion porosimetry (MIP) by University of Gießen, Germany [184] and micro-computer tomography (μ-CT) scans by KIT IAM-ET.

For the MIP three samples per PTL are cut out at different positions across the PTL area ($> 20\ \mathrm{cm}^2\ x\ 20\ \mathrm{cm}^2$) to analyze the homogeneity of the materials and the pore size distribution. For μ-CT experiments, samples $< 1\ \mathrm{cm}\ x\ 1\ \mathrm{cm}$ were cut and fixed to a small metal pin. Samples were investigated with a Zeiss Xradia Versa 520 by Carl Zeiss AG, Germany using an accelerating voltage of $60\ \mathrm{kV}$ at $5\ \mathrm{W}$ power and 20x optical magnification resulted in a voxel size of 509 nm. For image processing, segmentation and evaluation the software toolbox GeoDict (Release 2024 from Math2Market GmbH, Germany https://www.geodict.com) is used. Image data was processed by cropping a suitable region of interest, followed by non-local denoising. For segmentation, grey value thresholding based on Otsu [185] proved suitable.

The three-dimensional PTL structure are evaluated for grain and pore size distribution using the modules GrainFind and PoroDict, respectively. Pore space tortuosity was estimated using

DiffuDict. Figure 5.6 a) and b) show the results of the MIP and μ-CT analysis, the parameter that could be extracted from these measurements are summarized in Table 5.1.

Catalyst Coated Membranes

As the default CCM, a commercially available E400 Gen.3 CCM by Greenerity GmbH, Germany, is employed. The catalyst layers are based on IrOx and Pt/C for anode and cathode. The used membrane is a $125\ \mu\mathrm{m}$ Nafion®-based (N115) membrane. More detailed information on the catalyst loading and structure is not available for this commercial CCM but in general it shows a high reproducibility and excellent lifetime and can be taken as an industrial benchmark for state-of-the-art MEA in PEM water electrolysis.
To investigate the impact of low loadings in combination with the variation of structural PTL parameters, an in-house produced CCM based on membrane FS-990-PK ($90\ \mu\mathrm{m}$ thickness, reinforced) by Fumatech BWT GmbH, Germany is employed. Membrane samples were placed on a vacuum table, onto which anodic and cathodic catalyst inks were coated using a 50 mm wide slot-die directly onto the membrane surface. The anodic ink was formulated with unsupported Iridium(IV)-oxide particles (Premion™, 99.99%, 84.5% Iridium) by ThermoFisher Scientific, Germany dispersed in NPA-H20 solution combined with Fumion FSLA-1010 ionomer from Fumatech BWT GmbH at an ionomer-to-solid (I/S) ratio of 16.66 wt%. The total solid content of the ink was 24 wt%. The cathodic ink was prepared using platinum on carbon black particles (Elyst Pt50 0380, 50% Pt) by Umicore AG & Co. KG, Germany. This mixture was also dispersed in a NPA-Water solution combined with Fumion FSLA-1010 ionomer at an ionomer-to-carbon (I/C) ratio of 0.7, yielding a total solid content of 18 wt%. The catalyst layers were dried in a convection drier at $60\ ^{\circ}\mathrm{C}$ for 30 min and additionally hot pressed in a roll-to-roll laminator at $6\ \mathrm{bar}$, $0.07\ \mathrm{m}\cdot\mathrm{min}^{-1}$ and $180\ ^{\circ}\mathrm{C}$. The produced CCMs were in-house investigated using X-ray fluorescence spectroscopy (XRF) to analyze the homogeneity of the catalyst loading over the cell area for both the anode and cathode. Using scanning electron microscope (SEM) the CCM cross-sections were analyzed on catalyst layer thickness homogeneity, as seen Figure 5.6 c) and d).

5.2.3 Electrochemical Measurement and Analysis

The focus of this chapter is the electrochemical characterization using the AtC test cell described above. Therefore, polarization curve measurements are conducted between $0.01\ \mathrm{A}\cdot\mathrm{cm}^{-2}$ and $7\ \mathrm{A}\cdot\mathrm{cm}^{-2}$. The HFR is measured at every current density point. Additionally, at specific operation points ($0.1\ \mathrm{A}\cdot\mathrm{cm}^{-2}$, $0.5\ \mathrm{A}\cdot\mathrm{cm}^{-2}$, $1\ \mathrm{A}\cdot\mathrm{cm}^{-2}$, $3\ \mathrm{A}\cdot\mathrm{cm}^{-2}$, $5\ \mathrm{A}\cdot\mathrm{cm}^{-2}$ and $7\ \mathrm{A}\cdot\mathrm{cm}^{-2}$) EIS is performed for the entire cell and all 10 segments in parallel. At each operation point the current density and the temperature distribution is measured using the integrated PCB. Furthermore, all data of the test bench, such as water temperature, pressure, and flow rate are measured. For detailed description of the measurement methods employed, it is referred to Chapter 4.

Before each characterization a CCM-specific break-in procedure is carried out. For the commercial CCM water is flushed at 80 °C for one hour, followed by current density steps at $0.2\ \mathrm{A \cdot cm^{-2}}$ and $1\ \mathrm{A \cdot cm^{-2}}$ each for 30 minutes. Afterwards constant voltage at $1.7\ \mathrm{V}$ is held for 12 hours. For the Fraunhofer ISE CCMs a protocol is applied consisting of a one-hour water flushing at $80\ ^{\circ}\mathrm{C}$, followed by five polarization curves in the same current density range as the later characterization and two constant voltage phases at $1.9\ \mathrm{V}$ for 5 hours and $2.1\ \mathrm{V}$ for 10 hours. Both break-in protocols have been proven to guarantee sufficient stable cells for performance-based analyses.

The default operation point during characterization is $60\ ^{\circ}\mathrm{C}$, $1\ \mathrm{bar_g}$ balanced pressure and a water flow rate at the anode of $10\ \mathrm{ml \cdot min^{-1} \cdot cm^{-2}}$ without applying water flow to the cathode. The temperature is varied between $40\ ^{\circ}\mathrm{C}$ and $80\ ^{\circ}\mathrm{C}$, the pressure between $1\ \mathrm{bar_g}$ balanced pressure, $5 - 1\ \mathrm{bar_g}$ and $10 - 1\ \mathrm{bar_g}$ differential pressure with the higher pressure at the cathode. The flow rate is varied between $2\ \mathrm{ml \cdot min^{-1} \cdot cm^{-2}}$ $(120\ \mathrm{ml \cdot min^{-1}})$, $10\ \mathrm{ml \cdot min^{-1} \cdot cm^{-2}}$ $(600\ \mathrm{ml \cdot min^{-1}})$ and $20\ \mathrm{ml \cdot min^{-1} \cdot cm^{-2}}$ $(1200\ \mathrm{ml \cdot min^{-1}})$. It is worth noting that today's industrial-operation points are usually driven with high stoichiometry > 100 on which this study is focused on. The stoichiometry range in this study is between > 54 and < 380 000.

To ensure reproducible results and minimize the influence of internal contacting of the segments, every measurement is conducted twice for the studies with commercial CCMs. Meaning that the cell was assembled with the same but pristine CCM and PTLs and the identical measurement pre-testing and protocol was run. Consequently, all figures in this work depict the mean value of both measurements with error bars for the voltage response during a polarization curve. For the current density and temperature distribution also mean value and error bars are displayed. It is important to be noted that each cell assembly's current density profile is (slightly) influenced by the internal contact distribution given by the tolerances of the employed components. By carrying out pressure paper measurements and electrical current density profiles without CCM before each measurement this influence is further minimized. Again, a detailed discussion can be found in Chapter 4. All measurements with low-loading CCMs could not be repeated since not enough material from the same batch were available. Therefore, these results must be considered carefully as reproducibility measurements are not conducted.

5.3 Results and Discussion

5.3.1 High Current Density Operation on Laboratory Scale

Measurements with the $4\ \mathrm{cm}^2$ *Fraunhofer ISE reference* test cell [59] show no mass transport limitations. Even at high current densities of up to $25\ \mathrm{A} \cdot \mathrm{cm}^{-2}$, a linear behavior without any exponential voltage increase due to diffusion or conversion limitations is observable when operating with high water stoichiometries, see Figure 5.1.

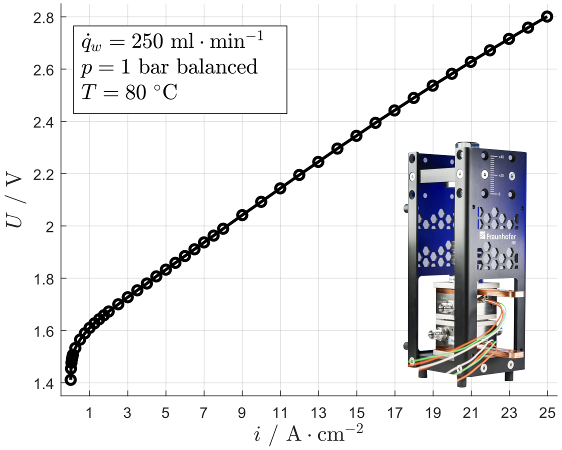

Figure 5.1: Polarization curve measured up to $25\ \mathrm{A} \cdot \mathrm{cm}^{-2}$ and $80\ ^\circ\mathrm{C}$ with the $4\ \mathrm{cm}^2$ ISE reference cell (ambient pressure and a water flow rate of $62.5\ \mathrm{ml} \cdot \mathrm{min}^{-1} \cdot \mathrm{cm}^{-2}$ at anode and cathode). The used CCM is in-house produced at Fraunhofer ISE with a $50\ \mu\mathrm{m}$ thick Nafion N212 membrane and a catalyst loading at the anode and cathode of $(0.20 \pm 0.07)\ \mathrm{mg_{Ir}} \cdot \mathrm{cm}^{-2}$ and $(0.15 \pm 0.03)\ \mathrm{mg_{Pt}} \cdot \mathrm{cm}^{-2}$, respectively.

This is even valid for the here used low-loading CCM produced at Fraunhofer ISE with an iridium loading of $(0.20 \pm 0.07)\ \mathrm{mg} \cdot \mathrm{cm}^{-2}$ for the anode, a platinum loading at the cathode of $(0.15 \pm 0.03)\ \mathrm{mg} \cdot \mathrm{cm}^{-2}$ and a $50\ \mu\mathrm{m}$ thick Nafion® (N212) membrane. As PTLs, $250\ \mu\mathrm{m}$ thick platinum-coated titanium fiber PTLs are used for both sides, which seem to enable a sufficient water supply and gas removal.

At $3\ \mathrm{A} \cdot \mathrm{cm}^{-2}$, a cell efficiency referred to the thermal neutral cell voltage ($1.49\ \mathrm{V}$ at $80\ ^\circ\mathrm{C}$) of more than 86% was measured, meeting the EU and US performance and material development targets for the year 2030 [33, 34]. The cell efficiency might be increased even further by using thinner membranes. However, aspects such as gas crossover and durability need to be considered carefully at these operation points.

Due to the high water flow rate of $62.5\ \mathrm{ml} \cdot \mathrm{min}^{-1} \cdot \mathrm{cm}^{-2}$ applied, corresponding to a stoichiometry of > 445 at $25\ \mathrm{A} \cdot \mathrm{cm}^{-2}$ ($\approx 37\%$ water in volume fraction at the anode under operation condition) an undersupply of water on a macro-scale does not play a significant role. In other words, with the amount of water applied to the cell a maximum hydrogen production of $311\ \mathrm{Nl} \cdot \mathrm{min}^{-1}$ can be realized, which corresponds to $44\ \mathrm{kA}$ current applied to the cell. With the here produced $25\ \mathrm{A} \cdot \mathrm{cm}^{-2}$ (100 A absolute), a water utilization of only 0.22% and an oxygen to liquid volume ratio of 1.39 and hydrogen to liquid volume ratio of 2.79 under normal conditions are present.

This indicates that today's porous materials can properly distribute the water as a reactant to the catalyst particles even though high evolution rates of gas are present. When operating with long water supply channels, accumulation of gas might lead to critical water-to-gas ratio, which is investigated in the following sections.

5.3.2 Performance Analysis Along the Channel

5.3.2.1 Differential Pressure Variation

The results of a differential pressure variation in the AtC test cell are summarized in Figure 5.2. The entire cell polarization curve and the HFR-free polarization curve (dashed lines at the bottom) are shown for $1\ \mathrm{bar_g}$ balanced pressure ("$1 - 1\ \mathrm{bar}$"), 5 to $1\ \mathrm{bar_g}$ ("$5 - 1\ \mathrm{bar}$") and 10 to $1\ \mathrm{bar_g}$ ("$10 - 1\ \mathrm{bar}$") differential pressure at $60\ ^\circ\mathrm{C}$ and $10\ \mathrm{ml} \cdot \mathrm{min}^{-1} \cdot \mathrm{cm}^{-2}$ in Figure 5.2 a). The polarization curves show decreasing performance with increasing differential pressure. The HFR-free polarization curves indicate that the differences are mostly related to different Ohmic resistances, as shown by the Ohmic overpotential in Figure 5.2 b). This behavior is unexpected for the comparably low differential pressures based on the results of Chapter 4, where no influence of differential pressure on the Ohmic resistance was detected. Although the cell setup is comparable in both studies, in this study, a thinner anode PTL is used, with only $250\ \mu\mathrm{m}$ instead of previously used $500\ \mu\mathrm{m}$ thick PTLs, but same GDL and CCM. Therefore, the increased Ohmic resistance at higher differential pressure is attributed to a worse electrical contact at the anode. With higher gas pressure at the cathode, the thin PTL may be pressed more into the channel and bending over the 1 mm channel width, which leads to a decreased electrical contact between PTL and the flow field lands. Furthermore, the increased gas pressure may cause detachment of the GDL at the cathode, resulting in additional increased contact resistance. A better balance of flow field and PTL design should minimize this effect, which is not the focus in this study.

The HFR-free polarization curve exhibits a higher voltage of $\approx 29\ \mathrm{mV}$ between $1\ \mathrm{bar_g}$ and

$10\ \mathrm{bar_g}$ cathode pressure at low current densities, which can be referred to increasing Nernst potential with higher hydrogen pressure.

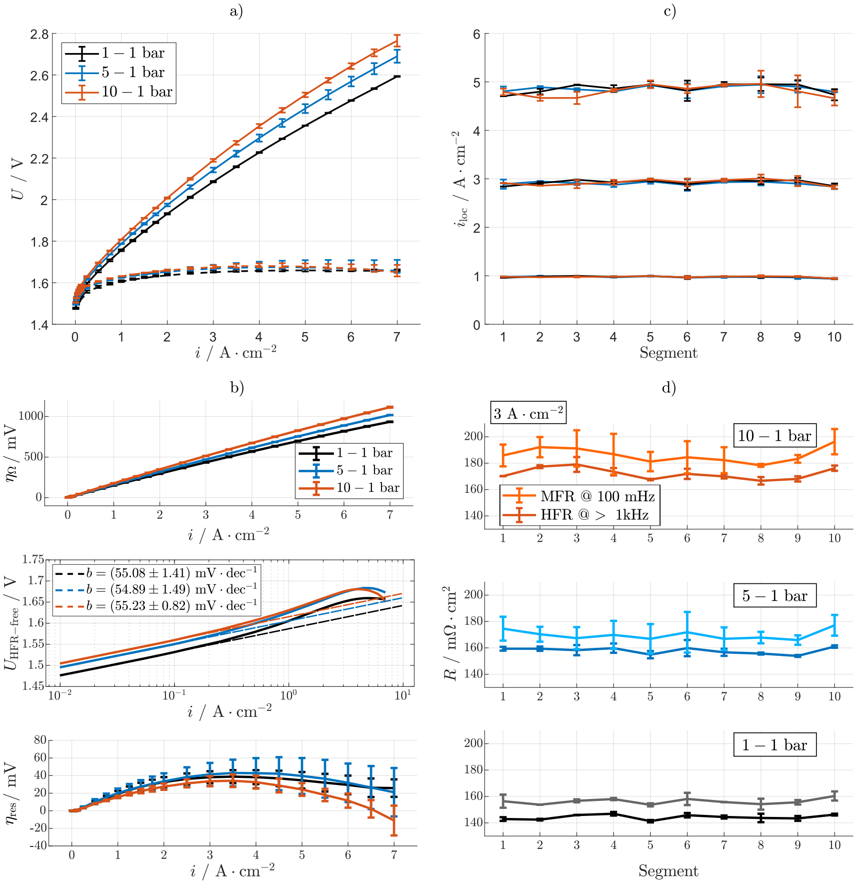

Figure 5.2: Variation of the cathode pressure between 1 bar, 5 bar and 10 bar with always constant anode pressure of 1 bar at 60 °C and an anode flow rate of $10\ \mathrm{ml \cdot min^{-1} \cdot cm^{-2}}$. a) Polarization curve and HFR-free polarization curve of the entire cell, b) voltage breakdown analysis of the entire cell, c) CDD at $1\ \mathrm{A \cdot cm^{-2}}$, $3\ \mathrm{A \cdot cm^{-2}}$ and $5\ \mathrm{A \cdot cm^{-2}}$ mean current density, and d) HFR and MFR distribution along the cell segments at $3\ \mathrm{A \cdot cm^{-2}}$ mean current density. Figure reformatted and taken from [5].

With increasing current density, the three HFR-free curves converge, as kinetic and residual overpotential show smaller contribution at higher gas pressure, see Figure 5.2 b).

The kinetics do not differ significantly, as noted in the legend of $U_{\mathrm{HFR-free}}$ graph in Figure 5.2 b). The decreasing residual overpotentials may be explained by better electronic and ionic conductivity between catalyst particles due to higher compression at the anode of the PTL and the catalyst layer. Additionally, the gas transport at the cathode should be increased since hydrogen needs less volume at higher pressure which may also contribute to this.

Please note that for high current densities, negative values for the residual overpotentials occur. This is a non-electrochemical artifact and related to the increase in cell temperature with increasing current density and inaccuracies of the voltage breakdown calculation. This phenomenon is visualized by the Tafel slope and the intersection with $U_{\mathrm{HFR-free}}$ at current densities above $6\ \mathrm{A} \cdot \mathrm{cm}^{-2}$, see Figure 5.2 b) in the center.

Figure 5.2 c) shows the CDD along the cell segments at different mean current densities. The parallel measured temperature profile is provided in the Appendix Figure A.12. For low current densities, the profiles are in good consistency, and the maximum error due to different contact of the segments is below $80\ \mathrm{mA} \cdot \mathrm{cm}^{-2}$. However, as the mean current density increases, contact issues become more relevant. At $5\ \mathrm{A} \cdot \mathrm{cm}^{-2}$ and 10 to $1\ \mathrm{bar_g}$ pressure operation the segments are better contacted in the center and less at the inlet and outlet of the AtC cell. This is attributed to a slightly better compression in the cell center and an amplifying effect due to the increased gas pressure. As expected, no effect along the channel occurs with increased cathode gas pressure. The temperature profiles show neither a significant temperature gradient influenced by the differential pressure (see Appendix Figure A.12) nor a significant gradient along the channel segments. This is explained by the high water flow rate of $10\ \mathrm{ml} \cdot \mathrm{min}^{-1} \cdot \mathrm{cm}^{-2}$ (non-critical water-to-gas ratio $> 26\ \mathrm{vol\%}$ at the cell outlet at $7\ \mathrm{A} \cdot \mathrm{cm}^{-2}$), which was purposely chosen to realize homogeneous temperature profiles. This is also illustrated by the HFR and MFR (minimal frequency resistance, measured through EIS at $100\ \mathrm{mHz}$) distribution, exemplarily shown for $3\ \mathrm{A} \cdot \mathrm{cm}^{-2}$ in Figure 5.2 d). Both resistances are influenced by the above discussed contact issues and exhibit no converging or diverging effects along the channel, which can be interpreted as a constant polarization resistance. For a cathode pressure of $5\ \mathrm{bar_g}$ and $10\ \mathrm{bar_g}$, the HFR is reproducible, but the MFR shows larger error bars compared to the $1\ \mathrm{bar_g}$ balanced pressure. This is attributed to a more unstable situation of the cell at higher gas pressure.

When comparing the results of this section with results of Figure 5.1 on laboratory scale, severe differences in cell performance are observable, as the AtC cell shows at $1\ \mathrm{bar_g}$ and $7\ \mathrm{A} \cdot \mathrm{cm}^{-2}$ a cell voltage of approximately $2.6\ \mathrm{V}$ while Figure 5.1 reveals only $1.93\ \mathrm{V}$ at $7\ \mathrm{A} \cdot \mathrm{cm}^{-2}$. This is mostly referred to the different thicknesses of the membranes and therefore higher Ohmic cell resistance (Figure 5.2: $125\ \mu\mathrm{m}$ and Figure 5.1: $50\ \mu\mathrm{m}$ membrane thickness). Other aspects as increased contact resistance due to the more complex cell setup of the AtC cell might as well contribute to this. Significant differences in polarization resistance are not likely to be present, as discussed with more comparable cell setups between the AtC cell and the *ISE reference cell* in Section 4.3.4.

5.3.2.2 Temperature Variation

The temperature variation shows, as expected, decreasing performance with decreasing temperature, as summarized in Figure 5.3 a). The temperature is varied between $80\ ^\circ\mathrm{C}$ and $40\ ^\circ\mathrm{C}$ at $1\ \mathrm{bar_g}$ balanced pressure and a water flow rate of $10\ \mathrm{ml} \cdot \mathrm{min}^{-1} \cdot \mathrm{cm}^{-2}$. The polarization curves and the HFR-free polarization curves show at high current densities a cooling effect at $80\ ^\circ\mathrm{C}$ and a heating effect at $40\ ^\circ\mathrm{C}$, which can be seen at the decreasing and increasing slopes, respectively. The $60\ ^\circ\mathrm{C}$ graph remains relatively linear. This effect can also be seen at the temperature differences along the channel. Although the temperature profiles, see Appendix Figure A.13, do not appear to be significantly affected by different cell temperature (temperature difference along the channel even at $5\ \mathrm{A} \cdot \mathrm{cm}^{-2}$ does not exceed $3\ \mathrm{K}$), it clearly shows that at $40\ ^\circ\mathrm{C}$ the cell is heated up, as the temperature gradient to the surrounding $(20\ ^\circ\mathrm{C})$ is compared with $60\ ^\circ\mathrm{C}$ and $80\ ^\circ\mathrm{C}$ operation lower. Figure 5.3 b) indicates that there is no along the channel effect detectable with varying temperature.

The voltage breakdown of the entire cell is shown in Figure 5.3 c) and indicates that, alongside the Ohmic overpotentials, the kinetic overpotentials also increase with decreasing temperature. This is attributed to decreasing membrane conductivity and the higher electrical energy needed to overcome the activation energy of the reaction, as less energy is available from thermal sources. The residual overpotentials are in good agreement with each other for current densities smaller than $4\ \mathrm{A} \cdot \mathrm{cm}^{-2}$ but show slightly increased overpotentials for higher current densities at $80\ ^\circ\mathrm{C}$. Diffusion-related overpotentials usually increase with temperature, as the gas diffusion coefficient decreases. For this high-loading catalyst layer, it is not belied that in-plane resistance of the catalyst layer plays a major role. To facilitate comparison between the voltage breakdown analysis and impedance analysis, Figure 5.3 d) highlights the voltage breakdown for $3\ \mathrm{A} \cdot \mathrm{cm}^{-2}$ in a bar graph format.

Figure 5.3 e) shows the impedance analysis using DRT at $3\ \mathrm{A} \cdot \mathrm{cm}^{-2}$ for the temperature variation. Additionally, the results of the ECM fit are exemplarily shown for the measurement at $60\ ^\circ\mathrm{C}$. The schematic presentation of the used ECM is displayed at the bottom right. Four significant peaks are identified by the DRT analysis for all three measurements at different temperatures. As explained above, each peak can be referred to a single polarization process ($P_{\mathrm{cap},1}$, $P_{\mathrm{cap},2}$, $P_{\mathrm{ind},1}$, and $P_{\mathrm{ind},2}$) and the resulting ECM fit at $60\ ^\circ\mathrm{C}$, is in good agreement with the measurement data for frequencies $< 1\ \mathrm{kHz}$. Due to artifacts induced by wiring and the cell itself, higher frequencies cannot properly be fitted with the ECM used here since no inductive element is used. It should also be noted that this may influence the evaluation of the resistance of $P_{\mathrm{cap},1}$. The corresponding Nyquist plots of the impedance measurement and the ECM fit for $60\ ^\circ\mathrm{C}$ are provided in Figure 5.3 f).

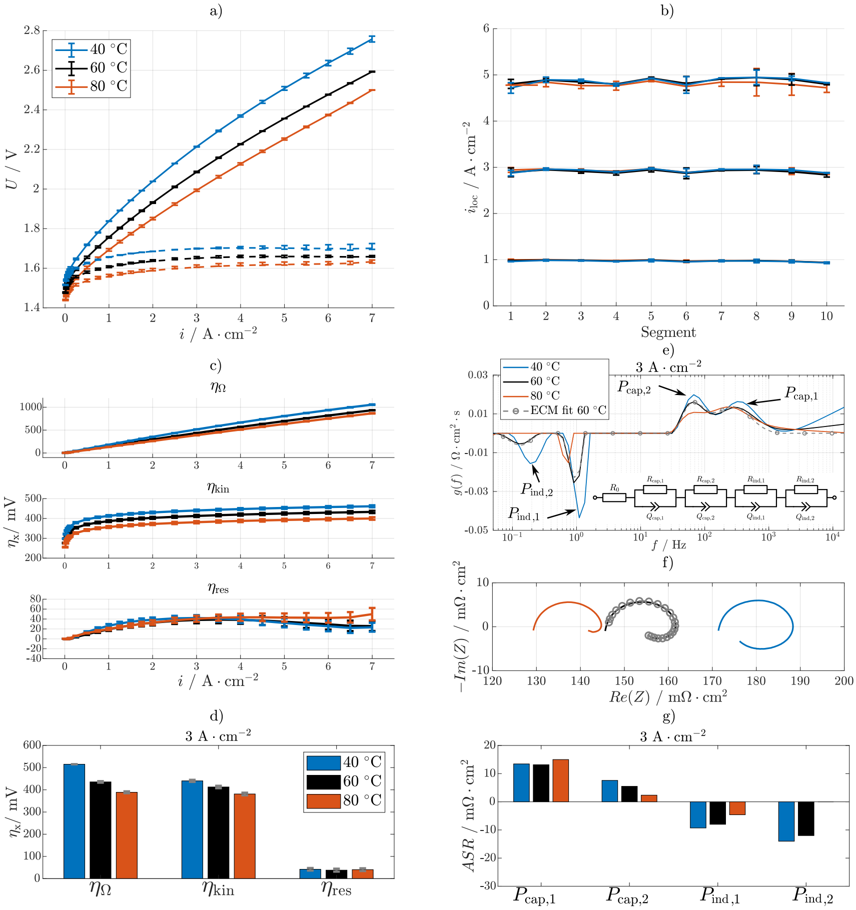

Figure 5.3: Temperature variation between 80 °C, 60 °C and 40 °C at 1 $\mathrm{bar_g}$ balanced pressure and anode flow rate of 10 $\mathrm{ml \cdot min^{-1} \cdot cm^{-2}}$. a) Polarization curve and HFR-free polarization curve of the entire cell, b) CDD at 1 $\mathrm{A \cdot cm^{-2}}$, 3 $\mathrm{A \cdot cm^{-2}}$ and 5 $\mathrm{A \cdot cm^{-2}}$ mean current density, c) voltage breakdown analysis of the entire cell and d) bar graph presentation of voltage breakdown at 3 $\mathrm{A \cdot cm^{-2}}$, e) DRT analysis with ECM fit, f) Nyquist presentation with ECM fit, and g) analysis of the ECM fit at 3 $\mathrm{A \cdot cm^{-2}}$. Figure reformatted and taken from [5].

Figure 5.3 g) shows the bar graph presentation of the ASR extracted from the DRT data for the temperature variation at 3 $\mathrm{A \cdot cm^{-2}}$. $P_{\mathrm{cap},1}$ can be detected between a peak frequency of 250 Hz to 350 Hz. The corresponding ASR shows slightly higher resistance for 80 °C but comparable values for 40 °C and 60 °C. $P_{\mathrm{cap},2}$ is detected between 60 Hz and 80 Hz, the ASR hereby decreases with increasing temperature. It should be noted that the ASR corresponds to the area underneath the DRT peak and not to the peak height. The behavior of $P_{\mathrm{cap},2}$ is characteristic of charge transfer behavior, the behavior of $P_{\mathrm{cap},1}$ is rather atypical. Since low values for the regularization parameter λ are avoided to minimize misinterpretation, the separation of both processes may not be accurately the same for the impedance measured at the different temperatures, which can be observed at the different dilatation of the peaks. Therefore, process $P_{\mathrm{cap},1}$ and $P_{\mathrm{cap},2}$ are summed up and assume that the sum includes the share of anodic and cathodic charge transfer.

$P_{\mathrm{ind},1}$ (between 0.7 Hz and 1.2 Hz) exhibits a typical behavior for the low-frequency inductive feature with an increasing ASR with decreasing temperature. This is consistent with the results in Chapter 2. The inductive process may be related to a membrane effect which is led or at least is accelerated with local temperature, which is more relevant when operating at lower cell temperature. Between 0.1 Hz and 0.25 Hz a second inductive peak is recognizable. $P_{\mathrm{ind},2}$ shows for the $40\ ^\circ\mathrm{C}$ measurement quite high negative values of the ASR. The $60\ ^\circ\mathrm{C}$ measurement also shows a second inductive feature, for $80\ ^\circ\mathrm{C}$ no second inductive feature is detected. There is no clear understanding of the physical significance of one or both inductive features; for further discussion on this, it is referred to Chapter 2. As no low-frequency capacitive process is detectable, mass transport-related processes do not seem to play a dominant role and/or are superimposed by inductive features. This is in good agreement with recent studies showing that mass transport or diffusion related polarization is typically not much relevant when operating at high water stoichiometries [52].

5.3.2.3 Water Flow Rate Variation

Figure 5.4 and Figure 5.5 show the results of the variation of the water flow rate at the anode. The polarization curve and the HFR-free polarization curve of the entire cell are given in Figure 5.4 a), the HFR and residual overpotentials are shown in Figure 5.4 b). For low current densities ($< 3\ \mathrm{A \cdot cm^{-2}}$), only small differences in the polarization curve are detected, with the low flow rate (orange graph) showing the highest overpotentials and the high water flow rate (blue graph) showing the lowest overpotentials, as seen in the zoomed-in section. At higher current densities $> 3\ \mathrm{A \cdot cm^{-2}}$ the behavior changes and the overpotentials are decreasing with decreasing flow rate. This trend is referred to a temperature effect, which is typical when comparing different water flow rates without the use of an external but only an internal heat management of the cell. With the high heat dissipation at high current densities low water flow rates lead to higher temperature at the electrochemically active parts of the CCM. For high water flow rates, the water temperature and thus the CCM temperature are increasing less. Therefore, the cell temperature and hence the performance of the cell is increased with less water applied, compare as well with the temperature profile in Figure 5.4 c). This phenomenon indicates better performance with lower water flow rate. As the performance improvement is related to a higher CCM temperature, this is accompanied by higher stress levels that may affect the durability of the cell.

Figure 5.4 c) shows the current density and temperature profiles along the channel for a mean current density of $5\ \mathrm{A \cdot cm^{-2}}$. The profiles for the mean current densities of $1\ \mathrm{A \cdot cm^{-2}}$ and $3\ \mathrm{A \cdot cm^{-2}}$ are given in the Appendix Figure A.14. At low mean current densities, a stable CDD of the segments along the channel can be observed for all flow rates. The temperature profile is in accordance with the lower performance for low water flow rates at $< 3\ \mathrm{A \cdot cm^{-2}}$ as a difference of approximately 3 K can be seen between $2\ \mathrm{ml \cdot min^{-1} \cdot cm^{-2}}$ and $20\ \mathrm{ml \cdot min^{-1} \cdot cm^{-2}}$. For flow rates of $10\ \mathrm{ml \cdot min^{-1} \cdot cm^{-2}}$ and $20\ \mathrm{ml \cdot min^{-1} \cdot cm^{-2}}$, respectively, still stable temperature profiles and current densities along the cell segments are measured at a mean current density of $5\ \mathrm{A \cdot cm^{-2}}$.

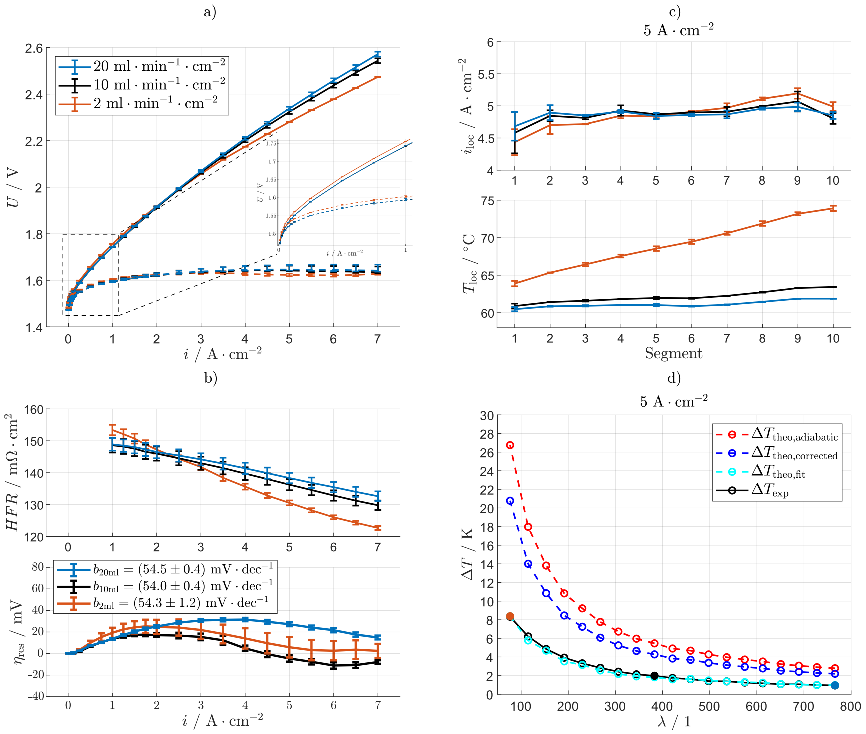

Figure 5.4: Water flow rate variation of $2\ \mathrm{ml \cdot min{-}1 \cdot cm^{-2}}$, $10\ \mathrm{ml \cdot min{-}1 \cdot cm^{-2}}$ and $20\ \mathrm{ml \cdot min{-}1 \cdot cm^{-2}}$ at 1 $\mathrm{bar_g}$ balanced pressure and 60 °C. a) Polarization curve and HFR-free polarization curve of the entire cell, b) mean cell HFR (top) and mean cell residual overpotentials (bottom) over current density, the mean cell Tafel slope is given in the legend at the bottom. c) current density and temperature distribution at $5\ \mathrm{A \cdot cm^{-2}}$ mean cell current density, and d) analysis of temperature difference between inlet and outlet at $5\ \mathrm{A \cdot cm^{-2}}$ under variation of stoichiometry. Figure reformatted and taken from [5].

For the lowest flow rate of $2\ \mathrm{ml} \cdot \mathrm{min}^{-1} \cdot \mathrm{cm}^{-2}$ a temperature gradient of $> 8\ \mathrm{K}$ is measured, which strongly affects the CDD, leading to an increase in current density of $\approx 0.5\ \mathrm{A} \cdot \mathrm{cm}^{-2}$ between inlet and outlet.

These temperature effects can also be seen when analyzing the mean cell HFR at different current densities, see Figure 5.4 b). At low water flow rates, the HFR is decreasing drastically between $1\ \mathrm{A} \cdot \mathrm{cm}^{-2}$ and $7\ \mathrm{A} \cdot \mathrm{cm}^{-2}$, while the HFR at the higher flow rates does not decrease that much. Also, the intersection at $2.5\ \mathrm{A} \cdot \mathrm{cm}^{-2}$ agrees with the intersection of the polarization curves. The calculated Tafel slopes (depicted in the legend of Figure 5.4 b) at the bottom) does not reveal any differences in the measurements and show a similar kinetic behavior at low current densities ($< 0.1\ \mathrm{A} \cdot \mathrm{cm}^{-2}$) for all flow rates. The residual overpotentials do not show a clear trend and do not reveal that there is any mass transport related overpotentials occurring during this water flow rate variation. Figure 5.4 d) shows the measured temperature difference between inlet and outlet for a highly resolved stoichiometry variation at $5\ \mathrm{A} \cdot \mathrm{cm}^{-2}$ mean cell current density (black graph). The three flow rates used in Figure 5.4 a) to 4 c) are marked with the corresponding colors. The measured range corresponds to an outlet water-to-gas ratio of $\approx 9\ \mathrm{vol\%}$ to $\approx 50\ \mathrm{vol\%}$. As assumed, a highly non-linear dependency between the temperature difference and water flow rate is detected. Based on a general rule of thumb, a temperature difference of 3 K between the inlet and outlet is suggested not to be exceeded for proper and long-term stable cell operation. According to the data, this is achieved at a water amount of less than $26\ \mathrm{vol\%}$ corresponding to a stoichiometry of 268 or a water flow rate of $> 6\ \mathrm{ml} \cdot \mathrm{min}^{-1} \cdot \mathrm{cm}^{-2}$.

Since the AtC test cell is neither thermally insulated nor equipped with external heating, the heat dissipation is not negligible. To estimate the heat dissipation, the theoretical temperature difference between the inlet and outlet, under the assumption of an adiabatic system, is calculated (see red graph). By measuring the temperature difference between the inlet and outlet (segments 1 and 10) at negligible reaction heat ($i = 0.01\ \mathrm{A} \cdot \mathrm{cm}^{-2}$ and $U = 1.484\ \mathrm{V}$), the heat loss through the PCB is estimated to be $Q_{\mathrm{loss,PCB}} = 49.41\ \mathrm{W}$, which corrects the adiabatic graph (see blue graph). To analyze the additional heat loss to the surrounding the corrected curve is fitted to the experimental data with an additional heat loss term which represents the residual heat dissipation $Q_{\mathrm{loss,fit}} = 152\ \mathrm{W}$, see cyan graph. The fit shows high agreement with the experimental data and the fitted heat loss term a reasonable value compared with $Q_{\mathrm{loss,PCB}}$ when analyzing the exchange surface area to the PCB and the total to the surrounding. All calculations for Figure 5.4 d) are given in the Appendix A.4. It needs to be stated that temperature differences under adiabatic situations, as in the center of an industrial-scaled stack may be significantly higher and that the results, especially at high current densities and low water flow rates, need to be considered carefully.

For a deeper understanding of the cell behavior along the channel for different water flow rates, EIS analyses for the extreme conditions at $20\ \mathrm{ml} \cdot \mathrm{min}^{-1} \cdot \mathrm{cm}^{-2}$ and $2\ \mathrm{ml} \cdot \mathrm{min}^{-1} \cdot \mathrm{cm}^{-2}$ are conducted at a mean current density of $5\ \mathrm{A} \cdot \mathrm{cm}^{-2}$, see Figure 5.5.

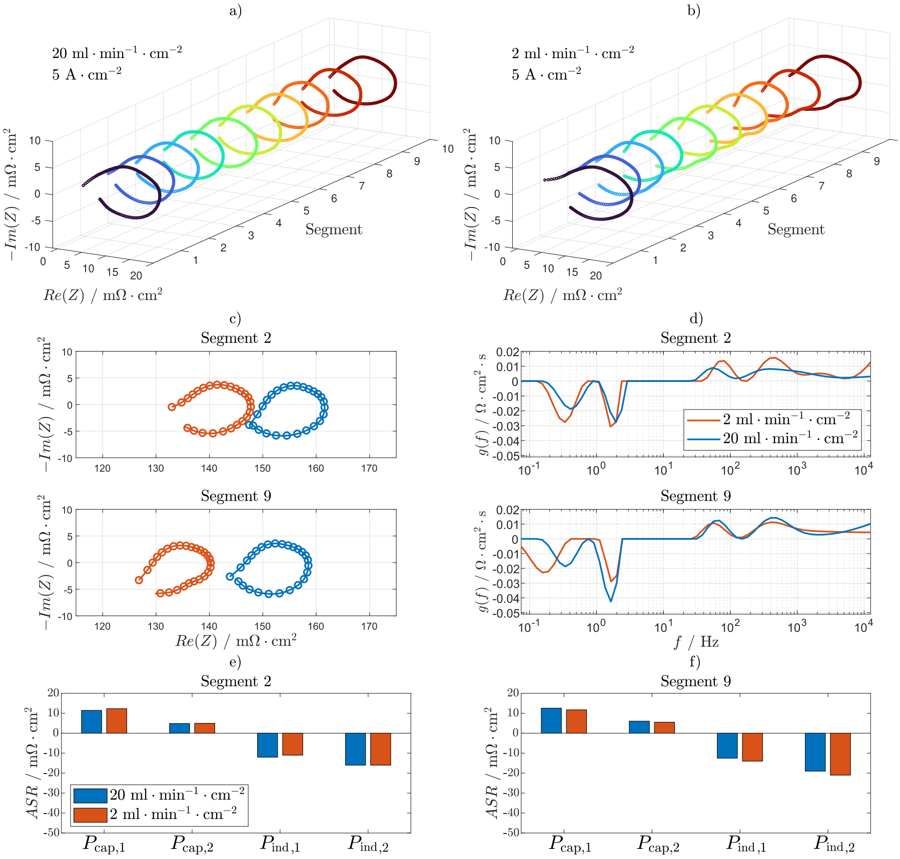

Figure 5.5: Water flow rate variation of 2 ml · min^{-1} · cm^{-2} and 20 ml · min^{-1} · cm^{-2} at 5 A · cm^{-2}, 1 bar balanced pressure and 60 °C. HFR-free Nyquist presentation along the cell segments of a) 20 ml · min^{-1} · cm^{-2} and b) 2 ml · min^{-1} · cm^{-2}. Impedance spectra of segment 2 and segment 9 in c) as Nyquist plot including the HFR, and d) using DRT analysis. Results of ECM fit of segment 2 in e) and segment 9 in f). Figure reformatted and taken from [5].

Figures 5.5 a) and b) show the HFR-free impedance spectra along the cell segments for 20 ml · min^{-1} · cm^{-2} and 2 ml · min^{-1} · cm^{-2}, corresponding to the operating points in Figure 5.4 c). For the high water, flow rate only small temperature or current density gradients exist and a uniform polarization resistance behavior along the channel is detectable. For the low water flow rate, see Figure 5.5 b), a clear change in the low-frequency impedance along the cell segments can be noticed. It appears that the second inductive feature becomes more pronounced toward the outlet of the cell. Figures 5.5 c) and d) show the Nyquist plots and DRT analysis, for segment 2 and segment 9 of the AtC cell for the two flow rates 2 ml · min^{-1} · cm^{-2} (orange graphs) and

$20\ \mathrm{ml} \cdot \mathrm{min}^{-1} \cdot \mathrm{cm}^{-2}$ (blue graphs). To exclude possible boundary effects, the segments 1 and 10 are purposely not chosen for this discussion. The results of the ECM fit for the segment 2 and segment 9 are given in Figures 5.5 e) and f).

For high water flow rates at $20\ \mathrm{ml} \cdot \mathrm{min}^{-1} \cdot \mathrm{cm}^{-2}$, comparable resistances of the four peaks detected by DRT are observed, with only a small decrease of the HFR detected from segment 2 to segment 9. This is expected, as no significant gradient in the water-to-gas ratio and temperature is present.

Contrary to this, the HFR decreases more, and the inductive feature changes significantly at $2\ \mathrm{ml} \cdot \mathrm{min}^{-1} \cdot \mathrm{cm}^{-2}$ between segment 2 and segment 9, as already indicated by the temperature profile in Figure 5.4 c). Figure 5.5 f) shows that the ASR for both inductive processes ($P_{\mathrm{ind},1}$ and $P_{\mathrm{ind},2}$) increases with $P_{\mathrm{ind},2}$ being more affected at low water flow rates. In Figure 5.3 the inductive feature increases with decreasing temperature. Here, an increase in these features with increasing local temperature is observed, as a temperature ≈ 8 K higher at segment 9 compared to segment 2 is measured.

Assuming a constant current distribution, the water-to-gas ratio at segment 2 would be ≈ 50 vol% and at segment 9 < 10 vol%, neglecting water vapor. Since the current density is higher at the outlet compared to the inlet, see Figure 5.4 c), the difference in water-to-gas ratio must be even greater. In 2, the inductive feature is discussed in relation to membrane and ionomer effects. One possible explanation for the inductive loop could be slow water diffusion coupled with local temperature effects, which both should decrease the protonic cell resistance but are only detectable at low frequencies since the processes have a high time constant and therefore are not included in the HFR measurements [2]. It can be assumed that for all measurements shown here, ionomer and membrane are humidified well since liquid water is present. Therefore, water diffusion effects might not be significant to the components but maybe relevant for internal water transport in the ionomer or membrane. Since here a clear increase of the inductive feature with decreasing water amount can be seen, this effect is attributed to be a thermal phenomenon. Dynamic fluidic and thermal modeling is suggested to gain a better understanding of the physico-chemical processes behind the inductive low-frequency feature.

5.3.3 Influence of Porous Transport Layers and Low-Loading Catalyst Layers

5.3.3.1 Ex Situ Analysis

In PEM water electrolysis, typically two different types of titanium-based anode PTLs are commonly used: sintered fiber and sintered particle based PTLs. Their structural parameters differ significantly in porosity, pore size distribution and surface properties. Figure 5.6 shows microstructure analysis results of commercially available PTLs (PTL1 (sintered titanium fiber) and PTL 2 (sintered titanium particle), both with a thickness of 250 μm) and the low-loading CCM produced at Fraunhofer ISE.

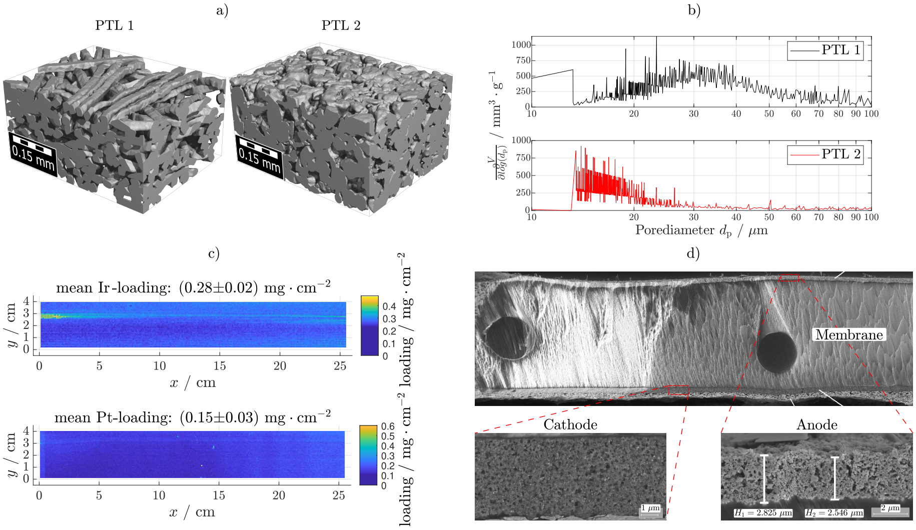

Figure 5.6: Microstructure analysis of commercial PTLs and low-loading CCM produced at Fraunhofer ISE. a) μCT-scans, b) pore size distribution by MIP, c) XRF analysis of the loading and its distribution of the anode (top) and cathode (bottom) catalyst layer, and d) cross-sectional SEM scan of the CCM, the cathode and anode catalyst layer of the low-loading ISE CCM. Figure reformatted and taken from [5].

Figure 5.6 a) shows the 3D µCT-scans, and b) the pore size distribution measured by MIP at the University of Gießen for PTL 1 and PTL 2. The extracted parameters are summarized in Table 1. The pore size distribution measured by the two methods are in very good agreement and show significant microstructural differences of the two types of PTLs, which are justified by the different porosity and through-plane tortuosity evaluated from the $\mu -$ CT-scans. PTL 2 shows a smaller mean pore size, lower porosity and higher through-plane tortuosity which should, in theory, lead to an increased gas transport resistance through the porous material. However, the smaller pore sizes may lead to better water transport through capillary flow. The surface area of PTL 2 is 12% higher than that of PTL 1, see Table 1. The enhanced surface area toward the catalyst layer may significantly improve the catalyst layer and PTL interface, as more contact points are available, which increases catalyst utilization and in-plane conductivity. This is especially relevant when measuring with low-loading CCMs.

Figure 5.6 c) shows the loading distribution of the catalyst layer of the anode (top) and cathode (bottom) measured by XRF for the Fraunhofer ISE CCMs. The XRF measurement is taken at the center $4x25\ \mathrm{cm}^2$ of the catalyst layer; the entire length of the catalyst layer could not be measured due to space limitations of the measurement device. The distribution of the catalyst is very homogeneous over the entire active area with a mean value of $(0.20 \pm 0.07)\ \mathrm{mg_{Ir}} \cdot \mathrm{cm}^{-2}$ at the anode and $(0.15 \pm 0.03)\ \mathrm{mg_{Pt}} \cdot \mathrm{cm}^{-2}$ at the cathode.

Figure 5.6 d) shows the corresponding cross-sectional SEM scan for the CCM. The cathode and anode catalyst layer are zoomed in, revealing a uniform but low catalyst layer thickness of the anode of less than $3\ \mu\mathrm{m}$. Furthermore, both catalyst layers are very homogeneous. With this analysis, the influence by different catalyst layer loadings or significant defects can be neglected. However, as the structural analysis using SEM cannot be performed across the whole active area, inhomogeneities in the ionomer distribution over the entire active area cannot be entirely excluded.

Table 5.1: Pore characteristics of the PTL samples.

Sample	Median pore size / µm (MIP)	Median pore size / µm (µCT)	Porosity / % (µCT)	Through-plane tortuosity / 1 (µCT)	Surface Area / m^{-1} (µCT)
PTL 1	32.7	30.7	54.1	1.80	64023
PTL 2	16.4	17.1	37.0	2.32	71942

5.3.3.2 In Situ Analysis

Figure 5.7 summarizes the results of the electrochemical characterization of PTL 1 and PTL 2. All measurements are performed at $60\ ^\circ\mathrm{C}$, ambient pressure and a water flow rate at the anode of $10\ \mathrm{ml} \cdot \mathrm{min}^{-1} \cdot \mathrm{cm}^{-2}$. To compare the PTLs, measurements with a commercial state-of-the-art CCM and the low-loading CCM produced at Fraunhofer ISE are performed. Figure 5.7 a) shows the polarization curves and the HFR-free polarization curves (dashed lines at the bottom). For the commercial CCM based on a $125\ \mu\mathrm{m}$ Nafion® membrane (square markers) a good performance can be noted deploying a GDL for the cathode, as described in Section 5.2. The polarization curves, as well as the HFR-free polarization curves, do not show significant differences between PTL 1 (black) and PTL 2 (red). Regarding the residual overpotentials see Figure 5.7 b), no significant differences are detectable. The Tafel slope in the legend of Figure 5.7 b) shows slightly lower values for PTL 2. This can be explained by the smaller pore size and the higher surface area for PTL 2 which creates more contact points with the catalyst layer and hence increase catalyst layer utilization. The slightly better performance of PTL 2 regarding the residual overpotentials at high current densities can be attributed to the higher in-plane conductivity of the catalyst and porous transport layer interface. Since the residual overpotentials are decreasing with current density it is assumed that mass transport resistances do not have a relevant contribution to the overall polarization. Additionally, by using PTL 2, for which higher gas transport resistance is expected, no significant mass transport related overpotentials are detected. The decreasing residual overpotential are for both cases interpreted as indicative of increased ionic in-plane conductivity in the catalyst layer, which should be higher with increasing catalyst layer temperature due to greater heat losses from the reaction.

Using the GDL at the cathode in combination with the low-loading CCM based on a $90\ \mu\mathrm{m}$ thick reinforced PFSA membrane (grey graph with round markers) an enormous increase in overpotentials, especially at low current densities is measured.

This is attributed to poor utilization of the catalyst, assuming that contact between the PTL and the thin catalyst layer thickness at the anode ($< 3\ \mu\mathrm{m}$, see Figure 5.6) is difficult to achieve, as already reported in the literature [31]. Even with larger compression of the cell this issue could not be solved. It is assumed that when using a soft GDL with a flow field design, as in this case, consisting of $0.9\ \mathrm{mm}$ land and $1\ \mathrm{mm}$ channel width, the GDL bends into the flow field channel, which decreases the compression or contact between the PTL and catalyst layer at the anode. This behavior must depend on the contact pressure and should result in large kinetic losses (see Tafel slope) and high in-plane resistivities (see residual overpotentials). Since most of the electrons are forced to flow along the catalyst layer close to the land areas of the flow field, resulting in a low catalyst utilization due to the poor contact to the PTL. In the case of the commercial CCM, this effect is not observable, which suggests that there are significant differences in catalyst loading, catalyst layer thickness, and catalyst layer in-plane conductivity between the two CCMs employed. Overall, these results underline the importance of a well-balanced compression of the PTLs in combination with an optimized interface of the flow field and the PTL (e.g. different channel geometry, stiffer GDL material or use of a MPL) to ensure a proper catalyst layer utilization with low loadings.

With the use of titanium PTLs at anode and cathode (see black and red graph with round markers), the contacting issue is minimized, as significantly higher compression of $> 4\ \mathrm{MPa}$ on the active area can be applied. In case of using a GDL at the cathode, the cell is only compressed with less than $2.5\ \mathrm{MPa}$ to minimize a damage of the carbon fibers. The polarization curves of the measurement with either PTL 1 or PTL 2 on both sides of the cell show a similar performance, see Figure 5.7 a). The HFR-free polarization curve for current densities $< 3\ \mathrm{A} \cdot \mathrm{cm}^{-2}$ also yield equal values. However, for higher current densities the HFR-free polarization curve differs from each other. The Tafel slope analysis reveals that the cell setup with PTL 2 results in slightly lower values, following the same trend as in the case of the commercial CCM. The in-house CCM yields larger Tafel slopes for both types of PTLs, which is attributed to the low anode catalyst loading.

The residual overpotentials, as depicted in Figure 5.7 b), differ significantly for current densities $> 3\ \mathrm{A} \cdot \mathrm{cm}^{-2}$. This is attributed to a higher in-plane conductivity at the anode in case of PTL 2 since more contact points of catalyst particles and the PTL are present for this type of PTL. The same trend, albeit less pronounced, can be observed for the commercial CCM.

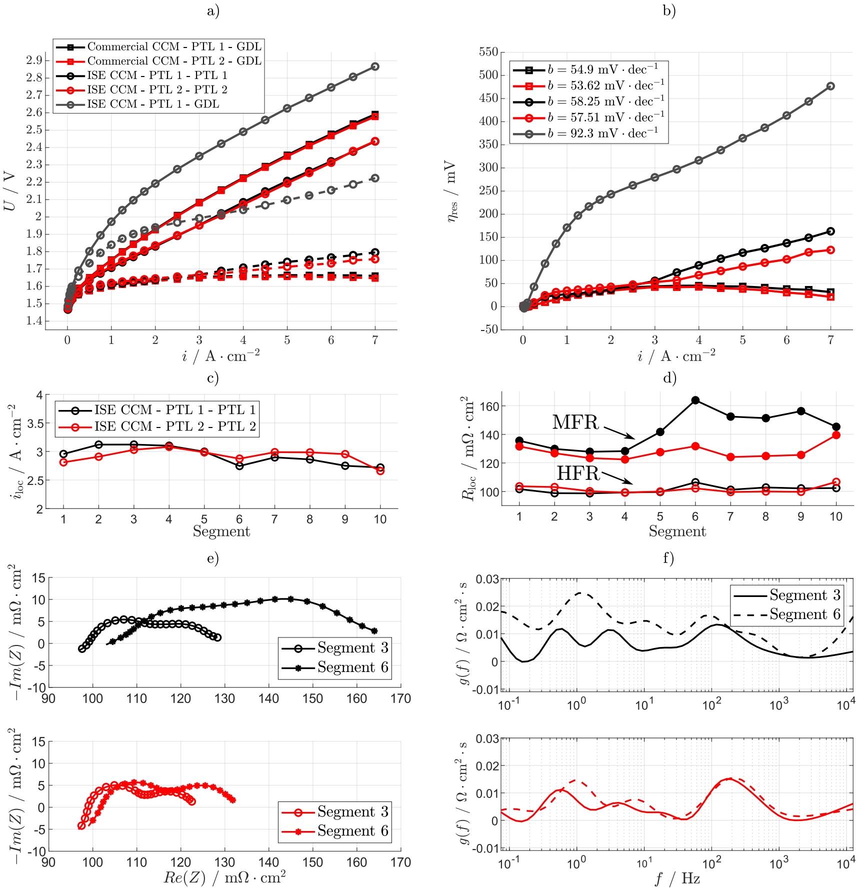

Figure 5.7: In-situ analysis of PTL 1 (black) and PTL 2 (red) measured with the commercial CCM and the low-loading CCM produced at Fraunhofer ISE at 60 °C, ambient pressure and a water flow rate of 10 $\mathrm{ml \cdot min^{-1} \cdot cm^{-2}}$ at the anode. a) Polarization curves and HFR-free polarization curves (dashed lines at the bottom) and b) residual overpotentials. Analysis of the measurement with low-loading CCM and PTL 1 and PTL 2, c) CDD and d) HFR and MFR distribution (bottom) at 3 $\mathrm{A \cdot cm^{-2}}$. Impedance analysis at 3 $\mathrm{A \cdot cm^{-2}}$ of segment 3 and 6 in e) Nyquist and f) DRT presentation. Figure reformatted and taken from [5].

Figure 5.7 c) shows the CDD at a mean current density of 3 $\mathrm{A \cdot cm^{-2}}$ applied for the low-loading CCM. The CDD with the commercial CCM used, and the temperature profiles for both measurements are given in the Appendix Figure A.15. The temperature profiles (see Appendix Figure A.15) are equal and reveal that PTL 2 results in slightly lower temperatures in all segments with the same tendency as PTL 1 for both types of CCM, which might be explained by better thermal conductivity due to the smaller porosity of PTL 2. The temperature increase along the channel is ≈ 1 K for all measurements at a current density of $3\ \mathrm{A} \cdot \mathrm{cm}^{-2}$. Hence, for the measurements with the commercial CCM, no significant gradients of the current density along the channel can be seen, which can again be attributed to the high water flow rate of $10\ \mathrm{ml} \cdot \mathrm{min}^{-1} \cdot \mathrm{cm}^{-2}$ and, thus, appropriate thermal management.

In case of the low-loading CCM, no relevant gradient in the current density can be observed for PTL 2. For the measurement with PTL 1, more current flows at the inlet compared to the outlet. Therefore, the HFR and MFR along the cell segments for the low-loading CCM in combination with PTL 1 and PTL 2 are analyzed in Figure 5.7 d). In both cases the HFR is very constant along the channel and only slightly influenced by cell compression issues. For PTL 1, the HFR appears to be slightly higher between segments 6 and 10 compared to segments 1 to 5. However, the HFR itself clearly cannot explain the gradient in current density for PTL 1, as the difference to PTL 2 is marginal. Regarding the MFR of PTL 2, similar behavior to the HFR is present, which can be interpreted as a constant polarization resistance along the segments. However, for PTL 1, the MFR increases between segments 4 and 6 and remains at this level until segment 9. The CDD can therefore be explained by changing polarization resistances along the channel.

Two characteristic segments for the change in the polarization resistance are segment 3, with the highest, and segment 6 with the lowest performance of all segments for PTL 1. Figure 5.7 e) and f) show the impedance of these two segments in Nyquist and DRT presentation for the measurement using PTL 1 (top, black) and PTL 2 (bottom, red).

As expected from Figure 5.7 d), the impedance spectra using of PTL 2 do not significantly differ between segments 3 and 6, only a slightly increased HFR is detectable. Using PTL 1, a slight increase of the HFR is also observed, but a significant increase in the polarization resistances detected by DRT is noted.

Processes below 10 Hz seem to be the most affected. Contrary to the commercial CCMs used, no low-frequency inductive feature is detected, instead capacitive processes are detectable which are usually associated with mass transport. Since the quality of the produced CCM and the PTLs is analyzed (see discussion on Figure 5.6), the difference between segments 3 and 6 using PTL 1 is not attributed to inhomogeneities in the materials used. Given that the HFR is also slightly affected, contact or compression issues might explain this phenomenon.

To gain a deeper understanding of the effect of different clamping forces for the setup with the low-loading CCM, additional measurements are performed with the Fraunhofer ISE reference cell (active area of $4\ \mathrm{cm}^2$), which was also used in Figure 5.1. The same cell materials as those used for the AtC cell are deployed (low-loading CCM and either PTL 1 or PTL 2 at anode and cathode) but the compression force is varied between $0.5\ \mathrm{kN} \cdot \mathrm{cm}^{-2}$ and $1.125\ \mathrm{kN} \cdot \mathrm{cm}^{-2}$, with the latter force being equal to the compression in the AtC cell, as determined by pressure paper analysis. Figure 5.8 a) shows the impedance spectra for the reference point at $3\ \mathrm{A} \cdot \mathrm{cm}^{-2}$, $60\ ^{\circ}\mathrm{C}$, ambient pressure, and a water flow rate of $100\ \mathrm{ml} \cdot \mathrm{min}^{-1}$ only at the anode for PTL 1 (top) and

PTL 2 (bottom). The setup with PTL 2 was measured at another, but similar, test bench (the same as used for the measurement in Figure 5.1) and with a water flow rate of $150\ \mathrm{ml} \cdot \mathrm{min}^{-1}$; however, both aspects should not significantly influence these findings regarding the clamping force variation.

With less compression force, the HFR is only slightly affected, while the polarization resistance is significantly impacted; see the analysis of the HFR and MFR in Figure 5.8 b) for PTL 1. This perfectly aligns to the phenomenon detected in the AtC cell and allows the conclusion that an unintentionally insufficient compression was given during the AtC measurement with PTL 1. Interestingly, a large impact on the MFR cannot be seen when using PTL 2.

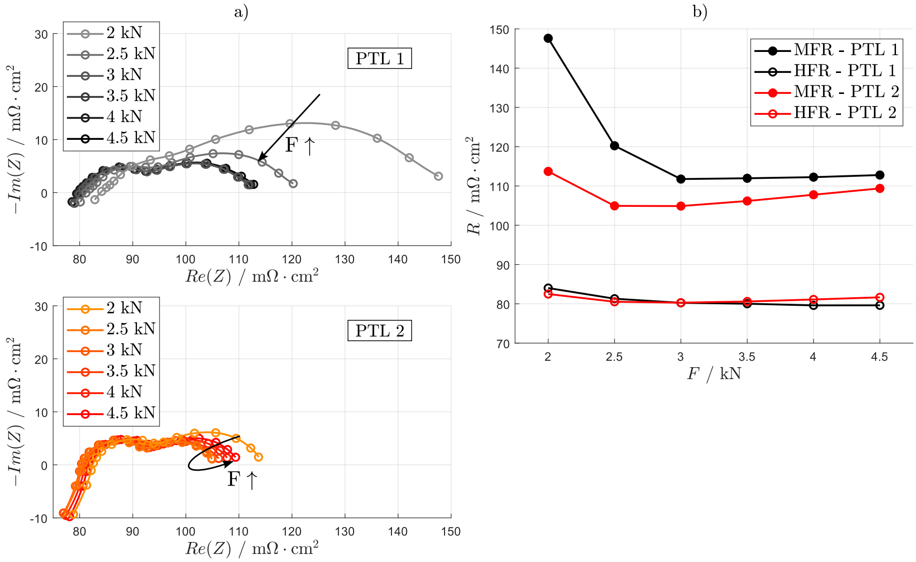

Figure 5.8: Clamping force variation of low-loading CCM with PTL 1 and PTL 2 in the $4\ \mathrm{cm}^2$ Fraunhofer ISE reference cell. a) Nyquist presentation at $3\ \mathrm{A} \cdot \mathrm{cm}^{-2}$ for PTL 1 at the top and PTL 2 at the bottom and b) analysis of the HFR and MFR behavior at different clamping forces. Figure reformatted and taken from [5].

Compared to the setup with PTL 1, the HFR and MFR only slightly decrease between $2\ \mathrm{kN} \cdot \mathrm{cm}^{-2}$ and $2.5\ \mathrm{kN} \cdot \mathrm{cm}^{-2}$ and linearly increase for clamping forces $> 2.5\ \mathrm{kN} \cdot \mathrm{cm}^{-2}$. This leads to the assumption that, for both AtC cell setups measured, comparable but insufficient compressions were realized, which only have a clear impact on the performance using the setup with PTL 1.

It is assumed that polarization resistances, including charge transfer, ionic and electronic in-plane resistivity, and mass transport-related phenomena, become more relevant when using low-loading CCMs with thin catalyst layers and comparatively coarse PTLs. This can be explained by the reduction of active area due to inappropriate contact between the catalyst layer and PTL, which cannot be compensated for due to the low catalyst loading, affecting charge transfer and in-plane catalyst layer resistance. Since low-frequency capacitive processes are even more affected, the gas transport between the catalyst layer and PTL may be inhibited, resulting in higher mass transport resistance, which might also cause local drying of the ionomer. PTL 2 shows a significantly smoother surface; see mean pore size and surface area in Table 1. Therefore, these effects seem to be minimized to a certain extent. A better-aligned catalyst layer-PTL interface (e.g. by using a MPL) seems necessary to circumvent these phenomena.

5.4 Conclusion

In this chapter, a comprehensive voltage breakdown and impedance analysis using DRT with subsequent ECM-fitting for the AtC cell is presented. The cell configurations and operational parameters are varied, considering industrially relevant applications. Up to a current density of $7\ \mathrm{A} \cdot \mathrm{cm}^{-2}$, it is shown that even at rather low water flow rates of $2\ \mathrm{ml} \cdot \mathrm{min}^{-1} \cdot \mathrm{cm}^{-2}$, corresponding to stoichiometries of 54, no undersupply of water and, therefore, no mass transport limitations occur.

Using the Fraunhofer ISE reference cell with an active area of $4\ \mathrm{cm}^2$, it is shown that for high current densities up to $25\ \mathrm{A} \cdot \mathrm{cm}^{-2}$, linear polarization curve behavior is still feasible; hence, no mass transport limitations are observable if a sufficient water supply is ensured.

When operating the AtC cell at high current densities $> 3\ \mathrm{A} \cdot \mathrm{cm}^{-2}$ in combination with low water flow rates significant temperature gradients of over $8\ \mathrm{K}$ can be detected along the channel, resulting in a substantial impact on the HFR and the impedance toward the outlet of the cell. The increase in temperature results in a performance increase despite of lower water stoichiometries, which may increase degradation rates. Theoretical calculations indicate that the temperature gradient would be significantly higher under adiabatic conditions, which may be critical for large scale industrial stack designs.

The influence of PTLs with different structural parameters combined with a commercial state-of-the-art CCM and a low-loading ("next-generation") CCM produced at Fraunhofer ISE was analyzed. It is demonstrated that, on the one hand, PTLs with smaller pore sizes improve catalyst utilization, leading to lower kinetic and residual overpotentials for low-loading CCMs. On the other hand, no significant differences in structural PTL parameters are found with respect to mass transport related polarization resistances, suggesting that this will only play a minor role for industrially relevant operation.

Inappropriate cell compression using low loading CCMs in combination with coarse PTLs surprisingly do not lead to significant differences in the Ohmic resistance. Instead, polarization processes, such as charge transfer, catalyst layer resistivity, and other low-frequency processes as mass transport are affected, which is proven by clamping pressure variations using the $4\ \mathrm{cm}^2$ cell. In summary, today's cell components as CCM and PTLs, distribute the water and gas under industrial-relevant operation points properly, which leads to negligible mass transport related overpotentials along the channels. This implies a low in-plane flow resistance due to the straight parallel channel flow field design used. Even at high current densities, mass transport issues do not limit performance. Instead, the limiting factor for high current density operation is the Ohmic cell resistance, which significantly depends on membrane thickness and may result in low cell efficiencies and uneconomic operation. The influence on polarization resistance due to insufficient cell compression seems relevant only when using low-loading CCMs with thin catalyst layers.

6 Water Starvation Analysis Along the Channel [1]

6.1 Introduction

PEM water electrolyzers are typically operated at high water flow rates to ensure proper water and heat management. The stoichiometric factor λ, defined as the amount of water supplied to the cell relative to the stoichiometric water consumption, typically ranges between 100 and 1000 depending on the water flow applied [5, 59, 186]. Therefore, industrial cell and stack development focuses on proper heat management to minimize temperature gradients and, subsequently, minimize stress for PEM water electrolysis cell components. A properly humidified membrane is also a key factor in cell design regarding performance and durability. Both aspects become more pressing at high current densities, which result in high water consumption and heat dissipation rates due to increased overpotentials. At industrially relevant operation points, mass transport losses or even limitations are not relevant when using state-of-the-art flow components, such as PTLs and flow field designs, as demonstrated in Section 5.3, Figure 5.1 where laboratory-scaled cell designs were operated up to $25\ \mathrm{A} \cdot \mathrm{cm}^{-2}$.

Despite the fact that PEMWE industry is currently not focusing on reducing the amount of water fed to the cell and circulated in the system, investment and operating costs for pumps, ion exchangers and filters can contribute significantly to the overall costs [35, 187–189]. External stack cooling reduces the amount of high purity water needed and may significantly reduce operating costs. Furthermore, large industrial stacks of several $1000\ \mathrm{cm}^2$ active area require a proper distribution of water to and within the electrolysis cells. Otherwise, partial undersupply of the active area may result in local water supply close to the stoichiometric level [36, 38, 165, 190]. These parts might significantly increase the cell's overall overpotential and accelerate degradation.

So far, all works reported on water starvation with industrially relevant cell designs and dimensions have in common that only low current densities of $< 2\ \mathrm{A} \cdot \mathrm{cm}^{-2}$ are investigated [35, 37, 38], which do not represent state-of-the-art or future operation points of up to $5\ \mathrm{A} \cdot \mathrm{cm}^{-2}$.

While standard operation typically involves supplying liquid water exclusively to the anode of the

---

[1] Parts of this chapter have been published in [6]

cell, various unconventional water supply methods have been developed for PEM water electrolysis where water starvation phenomena are more pressing.

One notable approach, patented by Thomassen et al. [191], entails feeding process water to the cathode, requiring water permeation through the membrane for the OER at the anode. This method simplifies the system architecture by maintaining a single-phase flow on the anode side, resulting in a more compact design and reducing system costs while also minimizing risks associated with hydrogen crossover [189]. As a result, thinner membranes ($< 50\ \mu\mathrm{m}$ thickness) can be applied, which drastically decreases Ohmic overpotentials [192]. However, challenges remain, including the necessity for precise water flow control to prevent excess water from accumulating at the anode and to avoid being forced to remove liquid water at the anode outlet. Moreover, cathode-fed cells are often operated at lower current densities compared to anode-fed cells due to potential dry-out conditions arising from mass transport limitations [193]. Another method worth mentioning is PEM steam electrolysis. PEM steam electrolysis involves supplying water vapor instead of liquid water to the cell, which reduces the thermodynamic energy required for the electrolysis process compared to using liquid water [194]. This method benefits from faster reaction kinetics and lower operating voltages [195]. However, little work has yet been reported as there is still a lack of stable membrane ionomers. Water vapor can be introduced to either the cathode or anode of the cell, with the common approach being anode feeding. Cathode feeding results in a significantly lower limiting current density compared to anode feeding and has not yet been extensively investigated [196]. The primary challenge for PEM steam electrolysis is the rapid decay of membrane performance due to elevated temperatures, which limits its investigation primarily to laboratory-scale operations [195].

In this chapter, cell performance analyses of a state-of-the-art PEM water electrolysis up to $5\ \mathrm{A} \cdot \mathrm{cm}^{-2}$ and close to the stoichiometric level are shown. With current density and temperature distribution measurements dry-out effects of the membrane and impeded reactant supply are analyzed, which are confirmed by locally resolved EIS with subsequent focusing on the HFR and low-frequency impedance analyses. The water flow rate is varied between $54\ \mu\mathrm{l} \cdot \mathrm{min}^{-1} \cdot \mathrm{cm}^{-2}$ and $16\ \mu\mathrm{l} \cdot \mathrm{min}^{-1} \cdot \mathrm{cm}^{-2}$, meeting stoichiometries between $3 < \lambda < 50$ depending on the applied current density. The results are compared with industrially relevant flow rates of $10.7\ \mathrm{ml} \cdot \mathrm{min}^{-1} \cdot \mathrm{cm}^{-2}$, with the cell's active area being $56\ \mathrm{cm}^2$. With this study, deeper understanding of dry-out and mass transport effects that may occur in industrial-scaled cells or cells with unconventional cell operation is gained.

6.2 Experimental

6.2.1 Testing Setup

The AtC test cell and test bench used in this chapter is described in detail in Section 4.2.1.1 and 4.2.2. As the CCM, an E400 Gen.3 CCM by Greenerity GmbH, Germany, is used. This CCM is based on an anode IrOx and a cathode Pt/C catalyst layer printed on a Nafion®-based N115 membrane with a dry thickness of $125\ \mu\mathrm{m}$. The catalyst loading and other structural parameters can be considered state-of-the-art for the European market, defined by Clean Hydrogen Partnership, European Union [33]; further information cannot be disclosed. As the anode PTL, a $250\ \mu\mathrm{m}$ PTL (2GDL-10-0.25), electroplated with $200\ \mathrm{nm}$ of platinum on both sides, by NV Bekaert SA, Belgium, is employed. As the cathode PTL, a $215\ \mu\mathrm{m}$ thick SGL22BB by SGL Carbon SE, Germany, is used.

6.2.2 Electrochemical Measurement and Analysis

All electrochemical measurements in this study are conducted at $60\ ^\circ\mathrm{C}$ and controlled on the anode inlet temperature of the water flow. The cell is operated normally at ambient pressure. To analyze the influence of pressure, additional operation at $3\ \mathrm{bar_g}$ and $6\ \mathrm{bar_g}$ balanced pressure is carried out. Water is applied only at the anode; the cathode is operated dry but humidified by the electro-osmotic water drag. The water flow is varied between 54, 107 and $161\ \mu\mathrm{l} \cdot \mathrm{min}^{-1} \cdot \mathrm{cm}^{-2}$ with a referred active cell area of $56\ \mathrm{cm}^2$ to analyze water starvation effects. For comparison a flow rate of $10.7\ \mathrm{ml} \cdot \mathrm{min}^{-1} \cdot \mathrm{cm}^{-2}$ is applied for fully hydrated conditions, as it is known for real operating conditions. Before the characterization, the cell was conditioned with the specific break-in procedure described in Chapter 4.

Polarization curve measurements between $0.01\ \mathrm{A} \cdot \mathrm{cm}^{-2}$ and $5\ \mathrm{A} \cdot \mathrm{cm}^{-2}$ with ten minutes holding time are conducted. At each current density step, the HFR is measured to separate Ohmic and non-Ohmic cell behavior. Therefore, EIS at high frequencies between 10 kHz and 100 Hz is performed. Since high frequency artifacts caused by external and internal wiring in the PCB and the test bench, the impedance at a phase angle of $0\ ^\circ$ is inaccurate for determining the HFR. In Section 4.3.3 a method to extract the HFR by fitting the capacitive semicircle of the anode charge transfer process using an ECM consisting of a resistor in series with a RQ element (resistor with constant phase element in parallel) between $1\ \mathrm{kHz}$ and $100\ \mathrm{Hz}$ is presented. For the analysis of the HFR of the cell segments, the measurement quality is too low to be properly evaluated at current densities $< 1\ \mathrm{A} \cdot \mathrm{cm}^{-2}$, see discussion in Chapter 5. For current densities $< 1\ \mathrm{A} \cdot \mathrm{cm}^{-2}$ the HFR between $1\ \mathrm{A} \cdot \mathrm{cm}^{-2}$ and $2\ \mathrm{A} \cdot \mathrm{cm}^{-2}$ is linearly interpolated and the extrapolated towards lower current densities. At every operation point, the current density and temperature of the cell

segments are measured. To analyze the local cell behavior, the cell is operated at constant current (galvanostatic) mode. Constant voltage (potentiostatic) mode is beneficial at critical operation points to analyze limiting currents, which is therefore conducted as well. Furthermore, at specific current densities (galvanostatic) EIS is conducted between $10\ \mathrm{kHz}$ and $100\ \mathrm{mHz}$ to analyze, in addition to the HFR, the polarization resistance of the mean cell and the cell segments.
The EIS data collected is evaluated by DRT, as described in Section 1.6.3 and tested beforehand using the Kramers Kronig test, see Section 1.6.2.

6.3 Results and Discussion

6.3.1 Polarization Curve Measurements under Water Starvation

At low flow rates, the stoichiometry serves as an important reference value. The stoichiometry λ directly correlates the consumed water ($\dot{n}_{\mathrm{w,stoich}}$) with the amount of water applied ($\dot{n}_{\mathrm{w,app}}$), defined by Equation (2).

$$\lambda = \frac{\dot{n}_{\mathrm{w,app}}}{\dot{n}_{\mathrm{w,stoich}}} = \frac{z \cdot F \cdot \dot{V}_{\mathrm{w,app}} \cdot \rho_{\mathrm{w}}}{i \cdot A \cdot M_{\mathrm{w}}} \tag{6.1}$$

With M_{w} and ρ_{w} being the molar mass and density (at the operational temperature) of water, ($\dot{V}_{\mathrm{w,app}}$), the applied volume flow of water, z the number of transferred electrons, F Faraday's constant, i the mean cell current density, and A the active cell area. As discussed in the Introduction section, PEM water electrolyzers are typically operated under water enrichment ($\lambda > 100$) at which no severe humidification issues of membrane and ionomer are present [37, 186]. At $\lambda < 10$ water deficits are reported in the literature, resulting in increasing Ohmic resistance due to not proper humidified membrane and ionomer [35, 38, 197].
Figure 6.1 shows the performance analysis of the entire AtC cell under water starvation in galvanostatic operation. The polarization curves and HFR-free polarization curves (dashed lines at the bottom) reveal that operation with $107\ \mu\mathrm{l} \cdot \mathrm{m}^{-1} \cdot \mathrm{cm}^{-2}$ (red curve) and $161\ \mu\mathrm{l} \cdot \mathrm{min}^{-1} \cdot \mathrm{cm}^{-2}$ (yellow curve) anode water flow, are consistent with each other but differ from the measurement with high water flow rate of $10.7\ \mathrm{ml} \cdot \mathrm{min}^{-1} \cdot \mathrm{cm}^{-2}$ (black curve) significantly, see Figure 6.1 a). At current densities $< 4\ \mathrm{A} \cdot \mathrm{cm}^{-2}$ and a high water flow rate a significant better performance is measured which can be attributed to a temperature effect. With high water flow rates, the cell is properly heated by the inlet water which results in a low and slightly decreasing HFR with increasing current density, see Figure 6.1 b). The mean cell temperature measured by the 120

temperature sensors within the PCB underneath the anode flow field increases by $9\ \mathrm{K}$ from low to high current densities, see Figure 6.1 c). The error bars describe the standard deviation of all 120 temperature sensors alongside the active area.

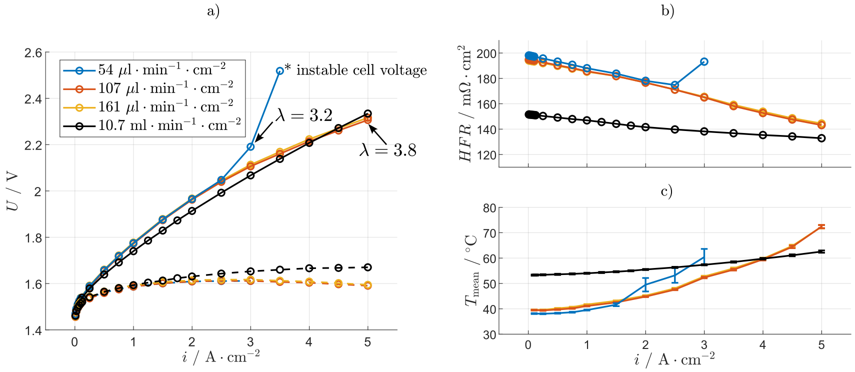

Figure 6.1: Cell behavior of the entire AtC cell under variation of the flow rate. a) Polarization curve and HFR-free polarization curve, b) HFR over current density and c) mean cell temperature measured with the PCB at a flow rate variation between $54\ \mu\mathrm{l} \cdot \mathrm{min}^{-1} \cdot \mathrm{cm}^{-2}$ and $161\ \mu\mathrm{l} \cdot \mathrm{min}^{-1} \cdot \mathrm{cm}^{-2}$ and compared with industrially relevant high flow rates. The measurements are done at 60 °C (inlet water temperature) and ambient pressure. Figure reformatted and taken from [6].

However, at $107\ \mu\mathrm{l} \cdot \mathrm{min}^{-1} \cdot \mathrm{cm}^{-2}$ 2 and $161\ \mu\mathrm{l} \cdot \mathrm{min}^{-1} \cdot \mathrm{cm}^{-2}$ the mean cell temperature, measured with the PCB, changes significantly with current density. At low current densities the cell temperature is around 39 °C, which is explained by the heat loss between CCM and PCB (23 mm distance in height) and the small amount of water (at $60\ ^\circ\mathrm{C}$) supplied to the cell. With increasing current density, the mean cell temperature increases up to $72\ ^\circ\mathrm{C}$, indicating the poor heat management due to the low water flow rate. The intersection of the temperature curves of $107\ \mu\mathrm{l} \cdot \mathrm{min}^{-1} \cdot \mathrm{cm}^{-2}$ and $161\ \mu\mathrm{l} \cdot \mathrm{min}^{-1} \cdot \mathrm{cm}^{-2}$ with $10.7\ \mathrm{ml} \cdot \mathrm{min}^{-1} \cdot \mathrm{cm}^{-2}$ at $4\ \mathrm{A} \cdot \mathrm{cm}^{-2}$ agrees with the intersection of the polarization curves. This temperature effect also explains the lower cell overpotentials, see HFR-free polarization curve. Since the differences for $107\ \mu\mathrm{l} \cdot \mathrm{min}^{-1} \cdot \mathrm{cm}^{-2}$ and $161\ \mu\mathrm{l} \cdot \mathrm{min}^{-1} \cdot \mathrm{cm}^{-2}$ in cell performance and temperature are small ($10\ \mathrm{mV}$), it is assumed that no significant undersupply of water and therefore no pertinent membrane dry-out is present. Even at $5\ \mathrm{A} \cdot \mathrm{cm}^{-2}$ and $107\ \mu\mathrm{l} \cdot \mathrm{min}^{-1} \cdot \mathrm{cm}^{-2}$ with a stoichiometry of $\lambda > 4$, the cell operation seems to be stable. However, the low water flow rates suggest that the membrane conductivity is reduced due to non-optimal membrane humidification, which can be assumed for the high water flow of $10.7\ \mathrm{ml} \cdot \mathrm{min}^{-1} \cdot \mathrm{cm}^{-2}$ applied. It should be noted that the here detected temperature influence is enormous and needs to be considered when analyzing the data. An improved external heat management, e.g. by using a thermal surrounding at operation

temperature (thermal box) may significantly reduce this inaccuracy.
For the measurement with a water flow rate of $54\ \mu\text{l} \cdot \text{min}^{-1} \cdot \text{cm}^{-2}$ comparable cell behavior is measured up to $2\ \text{A} \cdot \text{cm}^{-2}$ with only slightly higher HFR and lower temperature compared with $107\ \mu\text{l} \cdot \text{min}^{-1} \cdot \text{cm}^{-2}$ and $161\ \mu\text{l} \cdot \text{min}^{-1} \cdot \text{cm}^{-2}$. Above a current density of $2\ \text{A} \cdot \text{cm}^{-2}$ ($\lambda \approx 4.8$) the cell performance is decreasing drastically as the HFR but also the cell temperature increase. The error bars of the mean cell temperature indicate an unstable cell behavior during operation, since large temperature differences along the channel occur. When the current density is set from $3\ \text{A} \cdot \text{cm}^{-2}$ to $3.5\ \text{A} \cdot \text{cm}^{-2}$, a linear increase of the cell voltage from $2.3\ \text{V}$ to $2.7\ \text{V}$ was observed for the first $70\ \text{s}$, reaching exponentially within the next $20\ \text{s}$ the voltage limit of $3.5\ \text{V}$ of the test bench, see Appendix Figure A.16. Due to the increasing HFR paired with increasing cell temperature but not affected cell polarization (see HFR-free polarization curve) up to $3\ \text{A} \cdot \text{cm}^{-2}$ the measurement suggests that the cell faced significant membrane dry-out, which is analyzed in the following using impedance spectroscopy.
At $3\ \text{A} \cdot \text{cm}^{-2}$, a stoichiometry of 3.2 can be calculated with significant dry-out effects detected. Since even at higher stoichiometries ($\lambda \approx 4.8$ at $2\ \text{A} \cdot \text{cm}^{-2}$) these effects start to occur and at a flow rate of $107\ \mu\text{l} \cdot \text{min}^{-1} \cdot \text{cm}^{-2}$, stoichiometries of $\lambda \approx 3.8$ seemed not to be effected by dry-out, it is concluded that only considering the stoichiometry cannot provide sufficient information on relevant membrane and ionomer dry-out. Instead, more parameters as local temperature, ratio of liquid and vapor phase of water, membrane-specific electro-osmotic drag and properties of the porous materials need to be considered.

6.3.2 Impedance Analysis of the Entire Cell under Water Starvation

Impedance spectroscopy of the entire cell applied at current densities of $1\ \text{A} \cdot \text{cm}^{-2}$ and $3\ \text{A} \cdot \text{cm}^{-2}$ during the polarization curve reveal significant differences in performance, see Nyquist presentations of Figure 6.2 a) and b). At a current density of $1\ \text{A} \cdot \text{cm}^{-2}$ the polarization resistance seems to be comparable for all flow rates applied, and only differences in the HFR are detected, which fits to the results of Figure 6.1, as all HFR-free polarization curves show equal behavior for $1\ \text{A} \cdot \text{cm}^{-2}$.
At $3\ \text{A} \cdot \text{cm}^{-2}$ beside the change in HFR, which is discussed above, also the polarization resistances change. The capacitive loop at higher frequencies, which is attributed to charge transfer processes, does not significantly differ from each other. The difference between the HFR and the LFR (real part of the impedance at the second intersection with $-Im(Z) = 0$) is for all spectra around $15\ \text{m}\Omega \cdot \text{cm}^2$. This can also be seen at the DRT analysis in Figure 6.2 c) between $25\ \text{Hz}$ and $1\ \text{kHz}$. The processes appear to occur at similar frequencies and show comparable ASR, see

area underneath each peak. This indicates that, although significant differences in water supply are present, the charge transfer resistance is not significantly affected.

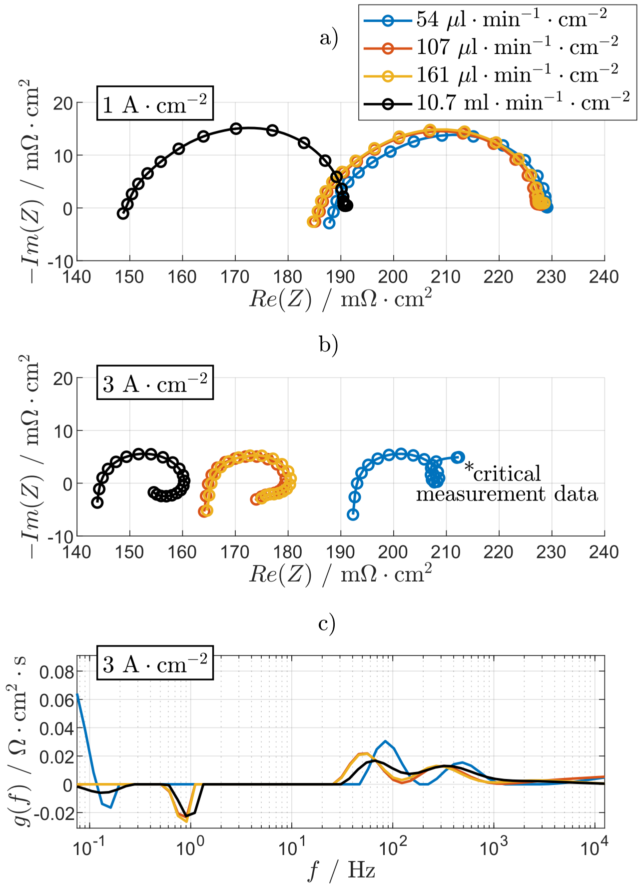

Figure 6.2: Impedance analysis of the mean cell at stoichiometry variation. presentation at a) $1\ \mathrm{A} \cdot \mathrm{cm}^{-2}$ and b) $3\ \mathrm{A} \cdot \mathrm{cm}^{-2}$, c) DRT analysis at $3\ \mathrm{A} \cdot \mathrm{cm}^{-2}$. Figure reformatted and taken from [6].

Contrary to this, the low-frequency impedance below 2 Hz differ from each other, as at high flow rates applied a typical inductive loop is detected, which is in good agreement with the findings in Chapter 2. The physico-chemical processes behind the inductive features are not fully understood yet. In Chapter 2, it is suggested that slow processes which decrease the membrane resistance due to water diffusion or thermal effects might be the origin of this phenomenon. In the DRT analysis two inductive peaks are detected at $1\ \mathrm{Hz}$ and $130\ \mathrm{mHz}$ for $10.7\ \mathrm{ml} \cdot \mathrm{min}^{-1} \cdot \mathrm{cm}^{-2}$ water flow applied. For the $107\ \mu\mathrm{l}\cdot\mathrm{min}^{-1}\cdot\mathrm{cm}^{-2}$ and $161\ \mu\mathrm{l}\cdot\mathrm{min}^{-1}\cdot\mathrm{cm}^{-2}$ the inductive feature at $1\ \mathrm{Hz}$ is as well detectable and comparable with $10.7\ \mu\mathrm{l}\cdot\mathrm{min}^{-1}\cdot\mathrm{cm}^{-2}$. The second inductive process can only be anticipated by the change of the arc in the Nyquist presentation. This process is not detected by the DRT algorithm within the measurement range.

For a water flow rate of $54\ \mu\mathrm{l}\cdot\mathrm{min}^{-1}\cdot\mathrm{cm}^{-2}$, the inductive loop is overlapped by a second capacitive loop which is usually related to mass transport losses or limitations of the reactant, as described in PEM fuel cells and water electrolyzers literature [83, 123, 138, 147, 198]. The small inductive process at around $150\ \mathrm{mHz}$ is superimposed by a comparably large capacitive process according to the DRT analysis, indicating that severe mass transport resistance is present. In general, this impedance measurement at low flow rates needs to be considered carefully as the cell performance behaves unstable, reaching the limits of the Kramers Kronig residuals of $\pm 1\%$ This is especially pressing for the low-frequency range, see dashed lines in the Nyquist presentation. However, with impedance analysis, it is demonstrated that mass transport limitations (second capacitive loop at low frequencies) for water as a reactant occurs simultaneously with increasing membrane resistance (increase of HFR) resulting in a large increase of the mean cell resistance.

6.3.3 Local Impedance Analysis under Water Starvation

Up to this point, only discussed the performance behavior of the entire AtC cell is discussed. The locally resolved impedance spectra at a mean current density of $3\ \mathrm{A}\cdot\mathrm{cm}^{-2}$ and water flow rates of $54\ \mu\mathrm{l}\cdot\mathrm{min}^{-1}\cdot\mathrm{cm}^{-2}$, $107\ \mu\mathrm{l}\cdot\mathrm{min}^{-1}\cdot\mathrm{cm}^{-2}$ and $161\ \mu\mathrm{l}\cdot\mathrm{min}^{-1}\cdot\mathrm{cm}^{-2}$ are depicted in Figure 6.3.

Figure 6.3 a) shows the HFR-free Nyquist presentation at $54\ \mu\mathrm{l}\cdot\mathrm{min}^{-1}\cdot\mathrm{cm}^{-2}$ for all 10 segments, the corresponding spectra at $107\ \mu\mathrm{l}\cdot\mathrm{min}^{-1}\cdot\mathrm{cm}^{-2}$ and $161\ \mu\mathrm{l}\cdot\mathrm{min}^{-1}\cdot\mathrm{cm}^{-2}$ are provided in the Appendix Figure A.17. The HFR distribution along the channel is presented in Figure 6.3 b) at the top. The HFR measured at $161\ \mu\mathrm{l}\cdot\mathrm{min}^{-1}\cdot\mathrm{cm}^{-2}$ water flow shows a homogeneous profile with a maximum spread of $17\ \mathrm{m}\Omega\cdot\mathrm{cm}^2$ which is referred to contact issues of the segments and the temperature gradient of $5\ \mathrm{K}$ along the channel, see Figure 6.3 b) at the bottom. It should be noted that the temperature shown here is measured using the PCB and not the water temperature. Due to heat loss between CCM and the measurement contacts of the PCB temperatures underneath the inlet water temperature are observed. The current density profile (center) also shows a homogeneous distribution. At $107\ \mu\mathrm{l}\cdot\mathrm{min}^{-1}\cdot\mathrm{cm}^{-2}$ equal cell behavior as at $161\ \mu\mathrm{l}\cdot\mathrm{min}^{-1}\cdot\mathrm{cm}^{-2}$ is observed, with a slightly higher HFR for segment 9 and segment 10. At $54\ \mu\mathrm{l}\cdot\mathrm{min}^{-1}\cdot\mathrm{cm}^{-2}$ higher current densities at the inlet and lower at the outlet are detected with increased HFR-values from segment 3 onwards. The temperature profile stays rather constant between segments 1 and 5 and is drastically increasing by $20\ \mathrm{K}$ between segments 6 and 10. These effects can clearly be attributed to undersupply, local dry-out of ionomer and membrane and heating up of the segments. The polarization resistance along the channel supports these findings, see Figure 6.3 a) and the DRT analysis in Figure 6.3 c). For 54 $\mu\mathrm{l} \cdot \mathrm{min}^{-1} \cdot \mathrm{cm}^{-2}$ segment 1 shows an impedance spectrum with a proper water supply, as two capacitive peaks at 400 Hz and 70 Hz, and two inductive features at 1 Hz and below 200 mHz are detectable.

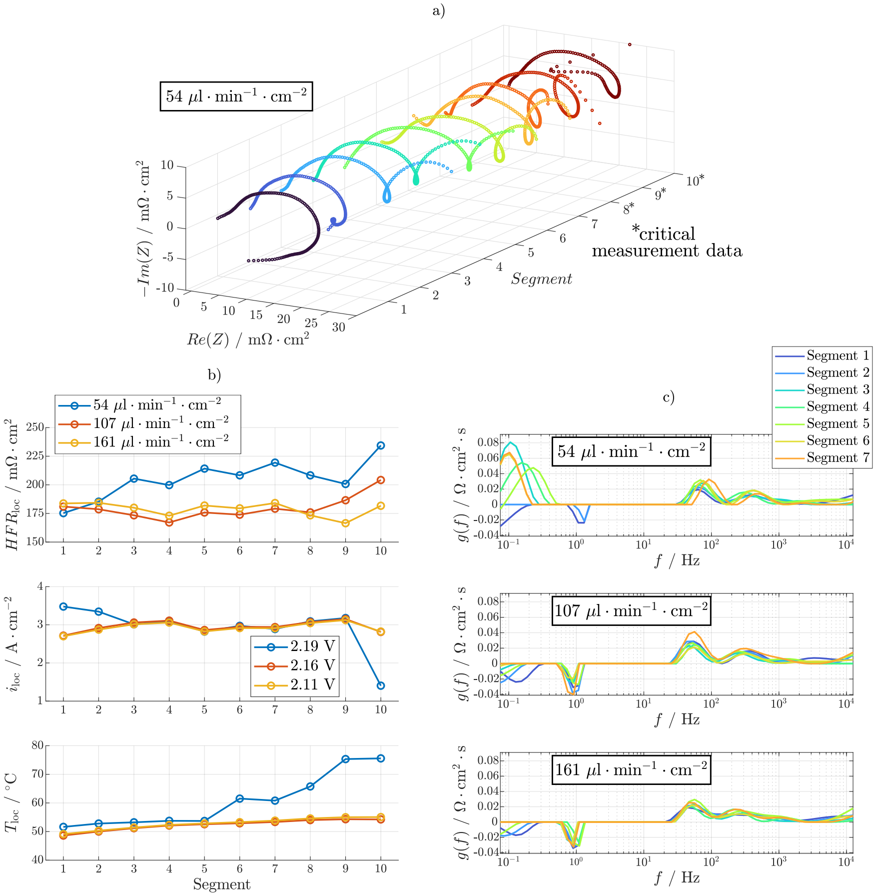

Figure 6.3: Locally resolved performance analysis under flow rate variation. a) HFR-free Nyquist presentation at a water flow rate of 54 $\mu\mathrm{l} \cdot \mathrm{min}^{-1} \cdot \mathrm{cm}^{-2}$, b) current density, HFR, and temperature distribution, and c) DRT analysis of segment 1 to 7 at 54 $\mu\mathrm{l} \cdot \mathrm{min}^{-1} \cdot \mathrm{cm}^{-2}$, 107 $\mu\mathrm{l} \cdot \mathrm{min}^{-1} \cdot \mathrm{cm}^{-2}$, and 161 $\mu\mathrm{l} \cdot \mathrm{min}^{-1} \cdot \mathrm{cm}^{-2}$ anode water flow. The measurements are done at 60 °C (inlet water temperature) and ambient pressure. Figure reformatted and taken from [6].

Segment 2 shows already a slight superimposition of the inductive loop by a low-frequency capacitive loss process; see Figure 6.3 a). For segment 3 to 7 the low-frequency capacitive process is increasing and the negative peak vanishes, indicating that the inductive loop is superimposed by an increasing mass transport resistance. Segment 8 to 10 show highly unstable condition and do not fulfill the Kramers Kronig test at low frequencies, reaching residuals up to $\pm 27\%$. Therefore, these spectra are not further analyzed with DRT and not discussed here. The instability portends the critical situation due to water starvation. The measurements at $107\ \mu\mathrm{l} \cdot \mathrm{min}^{-1} \cdot \mathrm{cm}^{-2}$ and $161\,\mu\mathrm{l} \cdot \mathrm{min}^{-1} \cdot \mathrm{cm}^{-2}$ water flow rate show DRT behavior comparable to $100\,\mathrm{ml} \cdot \mathrm{min}^{-1} \cdot \mathrm{cm}^{-2}$, neither temperature or HFR increase, nor significant mass transport related processes were observable over the entire active area.

6.3.4 Current Density Distribution Analysis under Water Starvation

Since the cell shows highly unstable behavior in galvanostatic mode when operating close to the stoichiometric level, the current density distribution under flow rate variation at potentiostatic mode, at a cell voltage of $2.4\ \mathrm{V}$ is analyzed, see Figure 6.4 a). For an easier comparison of the results, the deviation of the local current density to the mean current density is shown over the cell segments. Each mean current density is given in the legend. At a flow rate of $161\ \mu\mathrm{l} \cdot \mathrm{min}^{-1} \cdot \mathrm{cm}^{-2}$ only marginal deviations of up to 8% are detected. These deviations are related to contact issues of the segments (e.g. see segment 4 and 7) and to a temperature effect. Accumulating gas leads to poorer heat removal along the channel, which results in increased heating of the components, such as the membrane. In turn, increased temperature of the membrane leads to increased membrane conductivity, therefore, (slightly) more current is flowing at the outlet compared to the inlet, see temperature profile in Figure 6.4 b).
At $107\ \mu\mathrm{l} \cdot \mathrm{min}^{-1} \cdot \mathrm{cm}^{-2}$ water flow, a comparable trend is observed between segment 1 and segment 8. However, at segment 9 and 10 a drop in current density compared to the mean current density of -40% and -50%, respectively, is detected. The current density drop may be explained by a beginning of water starvation since a high amount of reactant was consumed by the previous segments. Even lower flow rates of $54\ \mu\mathrm{l} \cdot \mathrm{min}^{-1} \cdot \mathrm{cm}^{-2}$ shows that this current density drop seemingly moves more towards the cell inlet, as the drop occurs already at segment 6 with up to -78% deviation from the mean value. These almost inactive segments lead to a current density increase at the first 5 segments. However, the mean current density is drastically reduced compared with the other measurements, see legend at the bottom left. It should be noted, that the potentiostatic measurements were conducted after the galvanostic measurements as presented in Figure 6.1. Since these harsh measurements clearly harmed the cell components, a significantly reduced overall performance is observed. Several degradation effects need to be

considered, as oxidation of PTL and flow field components, and catalyst layer. However, due to the operation enforcing dry-out most of the degradation effects are assigned to change of ionomer and membrane properties.

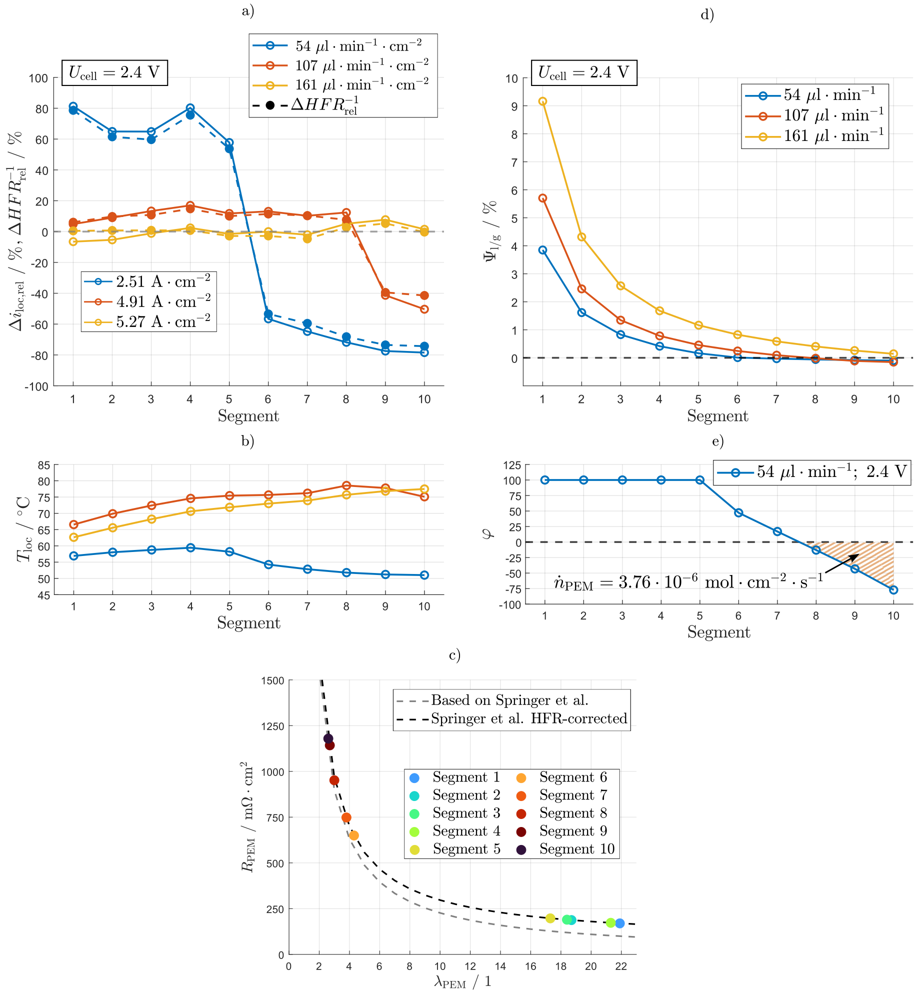

Figure 6.4: Relative deviation of the mean current density ($i_{loc,rel}$) at 2.4 V and water flow rate variation. The relative deviation of the inverse HFR (HFR_{rel}^{-1}) is given in dashed lines, b) corresponding temperature profiles, c) membrane resistance over water content of the membrane according to [199, 200], d) calculation of the liquid-to-gas ratio, and e) calculated relative humidity over the cell segments. The measurements are done at 60 °C (inlet water temperature) and ambient pressure. Figure reformatted and taken from [6].

Investigations of these degradation effects are not focus of this study but is highly recommended to gain more understanding. Characterization methods, such as EIS, cyclic voltammetry, and ex situ analyses as discussed for PEM fuel cell stacks in [201] are expected to be highly valuable.
The Appendix Figure A.18 shows the analysis at 2.0 V and 2.2 V revealing that for all water flow rates no local dry-out occur at 2.0 V. For $54\ \mu\mathrm{l} \cdot \mathrm{min}^{-1} \cdot \mathrm{cm}^{-2}$ and 2.2 V the above discussed current density drop was observed for segment 8 to 10. It also can be seen that the mean cell current density between 2.2 V and 2.4 V is only marginally increasing, which suggests that an operation close to a limiting current is present. The temperature profiles show an increasing trend along the segments whenever a rather constant current profile is present, as the current density drops down (at segment 9 for $107\ \mu\mathrm{l} \cdot \mathrm{min}^{-1} \cdot \mathrm{cm}^{-2}$ and segment 6 for $54\ \mu\mathrm{l} \cdot \mathrm{min}^{-1} \cdot \mathrm{cm}^{-2}$ at 2.4 V) the cell cools down due to less heat dissipation of the reaction, see Figure 6.4 b). This can be interpreted as a critical situation of water supply but no total membrane drying, compare with increasing temperature and increasing HFR for 2.4 V in Figure 6.4.
During these potentiostatic measurements locally resolved impedance measurements were carried out to extract the HFR of each individual segment using the approach mentioned above. Especially at $54\ \mu\mathrm{l} \cdot \mathrm{min}^{-1} \cdot \mathrm{cm}^{-2}$ the impedance data quality and thus the accuracy is low which needs to be carefully considered. The fitting error for the HFR analysis is determined to be $< 12\%$. The HFR measurements discussed here should only be seen in a qualitative way.
According to Ohm's law, the current (density) is at constant voltage inversely proportional to the resistance, see Equation (6.2).

$$\Delta i_{\mathrm{loc,rel}} \propto \Delta R^{-1}_{\mathrm{loc,rel}}, \text{ with } U_{\mathrm{loc,rel}} = U_{\mathrm{cell}} \tag{6.2}$$

With the assumption that a change in HFR is mostly depending on the change of membrane resistance due to humidification (at comparable temperatures) it can be stated that a direct correlation between the inverse HFR and current density distribution explains local membrane dry-out, see Equation (6.3). Therefore, the relative deviation of the inverse HFR is plotted in Figure 6.4 a) with dashed lines, showing high agreement for all measurements. The marginal deviations between current density and inverse HFR are attributed to the poor impedance quality.

$$\Delta i_{\mathrm{loc,rel}} \propto \Delta HFR^{-1}_{\mathrm{loc,rel}}, \text{ with } U_{\mathrm{loc,rel}} = U_{\mathrm{cell}} \tag{6.3}$$

According to Ohm's law, the current (density) is at constant voltage inversely proportional to the resistance. With the assumption, that a change in HFR is mostly depending on the change of membrane resistance due to humidification (at comparable temperatures) it can be stated that a direct correlation between the inverse HFR and current density distribution explains local membrane dry-out. Therefore, the relative deviation of the inverse HFR is plotted in Figure 6.4

a) with dashed lines, showing high agreement for all measurements. The marginal deviations between current density and inverse HFR are referred to the poor impedance quality.
To understand the characteristic drop in current density for 54 and 107 $\mu\mathrm{l} \cdot \mathrm{min}^{-1} \cdot \mathrm{cm}^{-2}$ at segment 6 and segment 9, respectively, an estimation of the water content of the membrane λ_{PEM} is done, see Figure 6.4 c). Springer, Zawodzinski et al. discussed the influence of λ_{PEM} on various membrane parameter of Nafion-based membranes, such as membrane conductivity [199, 200]. They observed a saturation of the water content, which is seen as fully humidified at $\lambda_{\mathrm{PEM}} = 22$. It is assumed that the first segment during the measurement at 2.4150 V and $\mu\mathrm{l} \cdot \mathrm{min}^{-1} \cdot \mathrm{cm}^{-2}$ equals a water content of $\lambda_{\mathrm{PEM}} = 22$. Therefore, the measurement data reported by Springer is corrected by the HFR of the first segment, see black dashed line. Segment 1 to segment 5 range in between $17 < \lambda_{\mathrm{PEM}} < 22$, which is seen as the region between fully vapor-saturated and saturated with liquid water. In contrast, the water content of segment 6 to segment 10 ranges between $2.6 < \lambda_{\mathrm{PEM}} < 4.3$, which indicates the severe membrane drying. Between segment 5 and segment 6 a change in HFR of $> 450\ \mathrm{m}\Omega \cdot \mathrm{cm}^2$ is observed, which leads to the interpretation that in segment 5 all liquid water is consumed and segment 6 to segment 10 is only supplied by water in the vapor phase.
To evaluate this interpretation, a calculation of the liquid-to-gas ratio $\Psi_{\mathrm{l/g}}$ along the cell segments at the anode flow field channel for a flow rate variation of 54 $\mu\mathrm{l} \cdot \mathrm{min}^{-1} \cdot \mathrm{cm}^{-2}$ at 2.4 V cell voltage is presented in Figure 6.4 d). Utilizing the information about the current flowing through each segment and the inlet water, the liquid-to-gas ratio in the flow field channels is calculated for each segment, see Equation (6.4). It is assumed that the amount of liquid water, gaseous water and oxygen at the end of one segment equals the inlet of the next segment. It is presumed that the oxygen produced has a relative humidity of 100% if liquid water is present. The amount of vapor water is calculated by the saturated vapor pressure using Antoine's equation [202], afterwards subtracted from the liquid water amount and added to the gas phase. The electro-osmotic drag is assumed to be constant over the whole active area, independent of membrane humidification, pressure, and temperature. Literature suggests a drag coefficient between $0.9 < \zeta < 7$ (molecules of water per proton) depending on the membrane humidification [45, 200, 203]. If the current density drop between segment 5 and segment 6 is caused by the transition between liquid and vapor-fed electrolysis, a drag coefficient of $\zeta = 3$ can be fitted, which is in good agreement with literature values. The water diffusion and back diffusion through the membrane and the presence of vapor water are not considered here.

$$\Psi_{\mathrm{l/g,j}} = \Psi_{\mathrm{l/g,j-1}} - \frac{\dot{V}_{\mathrm{l,j-1}} - \dot{V}_{\mathrm{l,j}}}{\sum_{1}^{j-1} \dot{V}_{\mathrm{g,prod}} + \dot{V}_{\mathrm{g,j}}} \quad \text{with } 1 \leq j \leq 10 \tag{6.4}$$

$$= \Psi_{\mathrm{l/g,j-1}} - \frac{\overbrace{\dot{V}_{\mathrm{l,j-1}}}^{\text{previous segment}} - \overbrace{\frac{i_{\mathrm{j}} \cdot M_{\mathrm{w}} \cdot (1+\zeta)}{z \cdot F \cdot \rho_{\mathrm{w}}}}^{\text{water consumption by reaction}} - \overbrace{\frac{i_{\mathrm{j}} \cdot M_{\mathrm{w}} \cdot p_{\mathrm{s}}(T)}{z \cdot F \cdot \rho_{\mathrm{w}} \cdot (p_{\mathrm{cell}} - p_{\mathrm{s}}(T))}}^{\text{water evaporation}}}{\underbrace{\sum_{1}^{j-1} \dot{V}_{\mathrm{g,prod}}}_{\text{previous segment}} - \underbrace{\frac{i_{\mathrm{j}} \cdot R \cdot T_{\mathrm{j}}}{z \cdot F \cdot p_{\mathrm{cell}}}}_{\text{water consumption by reaction}} - \underbrace{\frac{i_{\mathrm{j}} \cdot R \cdot T_{\mathrm{j}} \cdot p_{\mathrm{s}}(T)}{z \cdot F \cdot p_{\mathrm{cell}} \cdot (p_{\mathrm{cell}} - p_{\mathrm{s}}(T))}}_{\text{water evaporation}}}$$

i_{j} describes the current in segment j, M_{w} the molar mass and ρ_{w} the density of water, z the number of electrons transferred, F Faraday's constant, and R the universal gas constant. The temperature of each segment T_{j} is measured by the PCB, the temperature in the catalyst layer might be significantly higher since heat dissipation between CCM and PCB is expected, as discussed in Chapter 5. Since the pressure drop along the channel is $< 300\ \mathrm{mbar}$, the pressure in the segments is assumed to be constant and equal to the cell pressure p_{cell}, $p_{\mathrm{s}}(T)$ describes the saturated water pressure. The inlet liquid-to-gas ratio is set as a boundary condition to $\Psi_{\mathrm{l/g}} = 100\%$.

For $161\ \mu\mathrm{l} \cdot \mathrm{min}^{-1} \cdot \mathrm{cm}^{-2}$ a minimum liquid-to-water ratio of 0.13% at segment 10 is observed, which seems to properly feed the electrolysis reaction and humidifies the membrane since no decrease of current density towards the cell outlet is observed, see Figure 6.4 a). For $107\ \mu\mathrm{l} \cdot \mathrm{min}^{-1} \cdot \mathrm{cm}^{-2}$ from segment 8 and for $54\ \mu\mathrm{l} \cdot \mathrm{min}^{-1} \cdot \mathrm{cm}^{-2}$ from segment 6, negative liquid-to-gas ratios are observed. Both values are in good agreement with the characteristic current density drop, which is interpreted as transition between liquid and vapor fed electrolysis. The slight inaccuracy for $107\ \mu\mathrm{l} \cdot \mathrm{min}^{-1} \cdot \mathrm{cm}^{-2}$ (negative values from segment 8 but current density drop at segment 9) is attributed to the neglected water diffusion and homogeneous drag coefficient.

At a negative liquid-to-gas ratio, the reaction is fed by vapor water, which can be calculated by the relative humidity φ as the vapor-water uptake of the produced oxygen. Figure 6.4 e) shows the relative humidity for 2.4 V and $54\ \mu\mathrm{l} \cdot \mathrm{min}^{-1} \cdot \mathrm{cm}^{-2}$. If liquid water is present (segment 1 to segment 5) a relative humidity of 100% is assumed. As the vapor-fed electrolysis is present from segment 6 on, the water amount in vapor phase accumulated between segment 1 and segment 5 supplies the reaction. Therefore, the relative humidity decreases along the channel. At segment 8 to segment 10 negative values for the relative humidity are observed, which is non-physical. One interpretation may be that these cell regions are fed by back diffusion water through the membrane from accumulated drag water at the cathode, which is not considered in this calculations. The stoichiometric water flux which cannot be covered by the calculation (segment 8 to segment 10, see orange dashed area) is $\dot{n}_{\mathrm{stoich,8-10}} = 3.76 \cdot 10^{-6}\ \mathrm{mol} \cdot cm^{-2} \cdot s^{-1}$, which needs to be provided by the back diffusion flux $\dot{n}_{\mathrm{PEM}}$, see Figure 6.4 e). This value for the here used Nafion® N115 membrane is in the same order of magnitude as the values determined in the experimental permeation studies in the literature [204, 205].

6.3.5 Influence of Gas Pressure under Water Starvation

Water transport to the catalyst layer competes with the opposing oxygen removal through PTL and flow field. Since water can be assumed to be incompressible but gas transport is significantly affected by pressure, the cell pressure at both sides (balanced pressure) was set to $0\ \mathrm{bar_g}$, $3\ \mathrm{bar_g}$ and $6\ \mathrm{bar_g}$ in potentiostatic operation, see Figure 6.5.

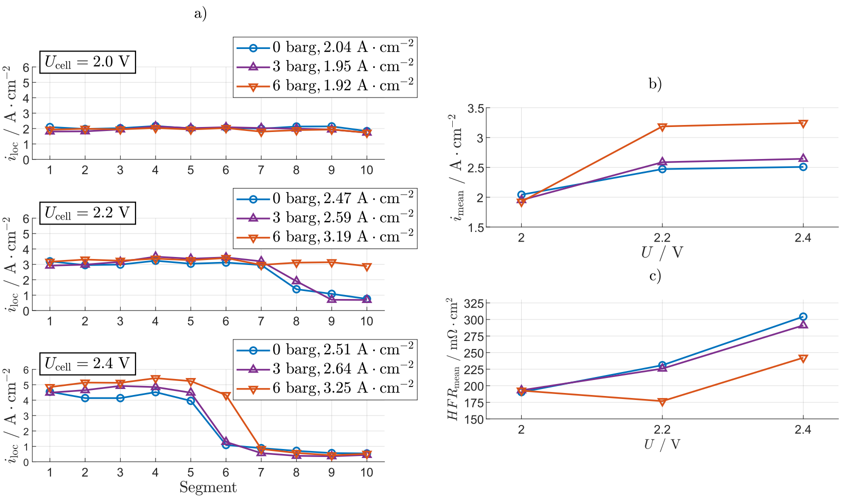

Figure 6.5: Current density distribution at 2.0 V, 2.2 V and 2.4 V cell voltage for $0\ \mathrm{bar_g}$, $3\ \mathrm{bar_g}$ and $6\ \mathrm{bar_g}$ balanced cell pressure, b) mean current density and c) mean HFR over cell voltage. The measurements are done at 60 °C (inlet water temperature) a water flow rate of $54\ \mu\mathrm{l} \cdot \mathrm{min}^{-1} \cdot \mathrm{cm}^{-2}$. Figure reformatted and taken from [6].

Figure 6.5 a) depicts the current density profiles with a water flow rate of $54\ \mu\mathrm{l} \cdot \mathrm{min}^{-1} \cdot \mathrm{cm}^{-2}$ at 2.0 V, 2.2 V and 2.4 V, respectively, and the different pressures applied. At 2.0 V, inactive segments are not observable at all, as all graphs show equal current density distribution, for even lower voltages as well no inactive segments are expected, see Figure 6.1. The mean cell current densities for each cell voltage are provided in the legend and in Figure 6.5 b). A slightly lower performance with increased pressure is observed at a given cell voltage of 2.0 V which is attributed to increased Nernst potential [67] and setup depending increased HFR, as shown in Figure 6.5 c). The HFR slightly increases with pressure since the contact between PTL and flow field decreases, as previously discussed for differential pressure operation with a comparable setup as used in Chapter 5. It is assumed that a similar phenomenon occurs as well with balanced pressure operation and might be even more pronounced due to the anode pressure, leading to further detachment of the PTL from the flow field lands.

At $2.2\ \mathrm{V}$ and at $0\ \mathrm{bar_g}$ and $3\ \mathrm{bar_g}$ pressure, a drop in current density is observed at segment 8 to 10, which is not detected under $6\ \mathrm{bar_g}$ pressure. Additionally, the mean cell current densities and HFR values change, with the highest pressure showing the best cell performance. The change in HFR at these low water flow rates is associated with local membrane dry-out. At $2.4\ \mathrm{V}$, all pressure conditions result in a drop in local current density towards the cell outlet. However, the current density profiles, mean cell current densities and the HFR suggest that pressure operation leads to less critical dry-out effects.

6.4 Conclusion

This work discusses the behavior of a PEM water electrolysis cell at high current densities up to $5\ \mathrm{A \cdot cm^{-2}}$ under water starvation with water stoichiometries of < 10. Water flow rates between $54\ \mu\mathrm{l \cdot min^{-1} \cdot cm^{-2}}$ and $161\ \mu\mathrm{l \cdot min^{-1} \cdot cm^{-2}}$ were applied to an along the channel test cell with an active area of $56\ \mathrm{cm^2}$ and compared with a standard flow rate of $10.7\ \mathrm{ml \cdot min^{-1} \cdot cm^{-2}}$. Water stoichiometries above 5 do not show significant mass transport-related limitations, even at high current densities of $5\ \mathrm{A \cdot cm^{-2}}$, which is in good agreement with the literature [35, 38]. When operating at stoichiometries of 3, significant increase of the HFR, which is associated with membrane dry-out, is observed, resulting in unstable cell voltages. An increase in mass transport resistance has been detected when operating close to the stoichiometric water level, superimposing low-frequency inductive features analyzed by electrochemical impedance spectroscopy.

Locally resolved impedance analysis showed that even when operating close to the stoichiometric level, inlet segments were still properly supplied with water, while segments towards the cell outlet showed local membrane drying and increased mass transport resistance. Segments at the cell outlet exhibited unstable behavior, which drastically affected the quality of impedance data. Under potentiostatic operation, it is demonstrated that there is a direct correlation between the current density distribution and the distribution of the inverse high frequency resistance, which is referred to as membrane conductivity. Comparison to experimental studies of membrane conductivity depending on the membrane's water content shows that severe membrane dry-out is present at the cell outlet. Theoretical calculations of the liquid-to-gas ratio show that at characteristic current density drops, no liquid water is present anymore and that the reaction might be covered by the humidity of the oxygen produced. The relative humidity of the gas is therefore decreasing along the channel, resulting in negative values, which are interpreted as back diffusion of water through the membrane, and are neglected in the calculation. A quantitative comparison of the missing stoichiometric water flux has the same order of magnitude as experimental analyses of the same membrane reported in the literature.

Varying the cell pressure revealed that increased gas pressure can reduce dry-out effects. This is attributed to the reduced volume demand of the gas transport from the catalyst layer through the PTL and subsequently the improved water transport to humidify the ionomer and membrane.

In summary, it can be stated that, for the herein used cell setup, the limiting factor of operation under water starvation is an increasing membrane resistance, due to dry-out. Increase of low-frequency capacitance in impedance data, which is attributed to mass transport processes, are observed simultaneously, indicating water transport limitations. The operation presented in this work may not be typical for PEM water electrolysis, which is usually conducted at water stoichiometries > 100, but it highlights the importance of proper water distribution. This is especially pressing for large industry stack designs. Given the severe impact on cell performance observed under these extreme conditions, further investigations into degradation under full or partial water supply are recommended. Moreover, electrochemical and fluidic modeling is suggested to better understand the limiting factors of water supply to the anode.

7 Summary and Outlook [1]

7.1 Summary

In this thesis, a segmented *Along the Channel* test cell in the field of PEM water electrolysis with industrially relevant channel length was designed and built. The key focus was to investigate yet untouched operation points of current densities up to $10\ \mathrm{A} \cdot \mathrm{cm}^{-2}$ to analyze harsh water-to-gas ratios along the flow field channels. The implementation of a printed circuit board, in combination with segmented bipolar plates and PTLs at the anode, enabled simultaneous analysis of current density, temperature, and impedance distribution across all 10 cell segments and the entire cell. The cell was designed to be able to employ PTLs with different heights and CCMs with different thicknesses. Also, different approaches in segmentation can be employed, such as operating the cell unsegmented or both electrodes segmented. The default configuration is to segment only the anode side. The cell can be operated up to $10\ \mathrm{bar}$ differential and balanced pressure, temperatures of $80\ ^\circ\mathrm{C}$, and water flow rates of $1200\ \mathrm{ml} \cdot \mathrm{min}^{-1} \cdot \mathrm{cm}^{-2}$. Since it was presumed that the voltage is identical in all cell segments, a study on voltage equality alongside the active area was conducted and the assumption proved. Impedance measurements of the cell segments showed severe inductive and capacitive artefacts at high frequencies. Therefore, a new method to properly analyze the HFR, circumventing these artefacts was presented. Furthermore, the implementation of reference electrodes at the inlet, the center, and the outlet of the cell, to separate anodic and cathodic contributions, was successfully done and discussed within this thesis. A detailed analysis of the cell performance and quality of the locally resolved measurements was performed under different operational conditions, see Chapter 4.

Parameter variations under industrially relevant operating conditions provided important insights for the future operation of PEM water electrolysis, particularly regarding heat management and inhomogeneous contact along the active cell area. The impedance data was analyzed using *Distribution of Relaxation Time* with subsequent *Equivalent Circuit Modeling* to understand the influence of Ohmic and polarization resistances. Additionally, voltage breakdown analysis using the Tafel model was performed.

---

[1] Parts of this chapter have been published in [1–6]

Next-generation CCMs with low iridium loadings have been employed and the catalyst and porous transport layer interface studied. Therefore, PTLs with different structural parameters (fiber and powder based) were used. Significant influence on charge transfer and low-frequency polarization resistances have been obtained by varying the cell compression. Surprisingly, the contact resistance was not significantly influenced, which seems to be only valid for low loading CCMs. These findings highlight the importance of proper interface engineering, such as employing micro porous layers, see Chapter 5.

Operating the AtC cell close to the stoichiometric level revealed significant findings regarding membrane and ionomer dry-out and mass transport. Using a state-of-the-art CCM with high catalyst loading showed that the increase of Ohmic resistance, which is related to the membrane resistance, is responsible for cell failure due to exponentially increasing cell voltage. Mass transport polarization processes were identified as significant capacitive impedance contributions increased with decreasing water amount along the channel. Increasing the gas pressure showed a positive influence on the cell stability, which is interpreted as improved gas removal due to decreased volume demand. In the literature, calculations of the membrane's water content have been reported, which were used to estimate the water amount present in these measurements. Furthermore, calculations of the liquid-to-gas ratio along the flow field channels were done. These analyses suggest the existence of tipping points between liquid and vapor-fed electrolysis operations, depending on the water amount applied to the cell, see Chapter 6.

In impedance spectra at high current densities, inductive processes were observed at low frequencies that have not yet been discussed in the PEMWE literature. With studies on laboratory-scale, the so-called *inductive loop* has been further investigated using operational and structural parameter variations, comparison to DC measurements and the use of reference electrodes. These studies suggest that the inductive features do not have their origin in the electrode but are associated with a membrane/ionomer effect due to slow water diffusion or thermal effects, see Chapter 2. These findings are essential to discuss low-frequency processes, such as mass transport, which were used for the analysis of the AtC cell measurements. Under industrial-relevant water flow rates the inductive loop is increasing along the channel once high temperature gradients between inlet and outlet are present. This is intepreted as higher temperature at the catalyst layer towards the cell outlet and therefore higher thermal flux which lowers membrane and ionomer resistance. Under operation close to the stoichiometric water level, inductive loops are present at the cell inlet, which is still properly humidified. Cell segments towards the cell outlet show severe mass transport processes, which are superimposing the inductive process.

Furthermore, studies on laboratory-scale regarding the optimal implementation of carbon-based PTLs at the cathode were performed within this thesis. Since carbon-based PTLs are often directly transferred from PEM fuel cells but not in detailed understood, studies on cell compression, contact to coated and uncoated flow fields, use of micro porous layers, and hydrophobic additives were conducted, see Chapter 3. These findings were used to properly design the cathode setup for the AtC cell. For the use of low-loading CCMs in combination with GDLs within the AtC cell inapprorpiate cell compression was observed, which led to increased high-frequency and charge transfer resistance. This was attributed to poor contact between anode CL and PTL due to GDL compression into the cathode flow field channels which worsened the contact at the anode over the flow field lands. With the use of stiff titanium PTLs at anode and cathode, this issue has been solved.

7.2 Outlook

The, within this thesis, developed AtC test cell provides, compared with segmented cells in the literature a proper compression of the cell segments, which enables locally-resolved measurements with high quality. However, a certain inhomogeneity remains, which might be further reduced, when equipping the cell with compression tools for each segment.

To mimic the cell behavior along the channel in the center of an industrial stack, isothermal conditions of the AtC cell to the surrounding is a prerequisite. Within this thesis, external heat pads are used to support the flow field temperature when operating at low water flow rates. However, perfectly isothermal conditions are not achieved. Therefore, improved external thermal management is mandatory to be implemented, e.g. by using a thermal box with equal temperature as the cell under operation.

Further work should focus the implementation of industrial-relevant cell designs, such as employing flow field replacement materials (expanded metals and multilayer PTLs) or embossed bipolar plates. For these investigations the discussion on contact distribution, pressure loss along the flow field channel and comparison with stack designs of identical materials are suggested. Since the cell is designed up to $30\ \mathrm{bar}$ gas pressure but not yet tested, high pressure operation should be performed to be even closer to many industrial PEMWE applications.

Other than that, water starvation analysis with the AtC cell has high potential to deeper understand transport processes and dry-out effects in industrial scale. Employing low-loading catalyst layers for these kind of studies are recommended to analyze the impact on membrane resistance, water transport, and ionomer dry-out, which might result in increased residual overpotentials (protonic in-plane electrolyte resistivity). A combination of experimental investigations, fluidic, and electrochemical modeling should be envisaged for deeper understanding. Possible scenarios should be identified with which cell design and under which operation conditions these phenomena might occur in industrial stack designs.

Regarding the investigations on the low-frequency inductive features in impedance spectra, an experimental validation of the model by Franz et al. [113] is suggested. The model includes inductive processes originated from transient heat flux in the catalyst layer, therefore, temperature monitoring close to the CCM is one possible option, which might be done by implementing Pt100 sensors on top of the anode PTL. Inductive processes occurring due to heat flux from PTL to the end plate and the surrounding might be validated by using a thermal box to realize fixed flow field temperatures.

The investigations on the usage of carbon-based GDLs should be enhanced with CCMs with low-loading anode catalyst layers. The micro-strucutral contact between PTL and anode catalyst layer is sensitive regarding catalyst utilization and in-plane conductivity and might be highly influenced by the GDL compression. Variations of the flow field channel width and the use of flow field replacement materials are suggested.

A more advanced voltage breakdown analysis of the residual overpotentials is necessary to analyze resistances and processes that occur especially with low-loading CCMs. Therefore, impedance spectroscopy underneath the water-splitting voltage may be a valuable method, as discussed in the literature. For low-frequency processes, measured by EIS, such as mass transport or inductive loops, equivalent circuit modeling using transmission line models is suggested to not only quantify polarization processes but describe the behavior of single processes.

Studies on durability are suggested with either solar and wind profiles or accelerated stress tests. With that, important findings might be identified on local degradation effects, e.g. by water-to-gas or temperature gradients along the channel.

A Appendix

A.1 Low-Frequency Inductive Feature in Impedance Spectra

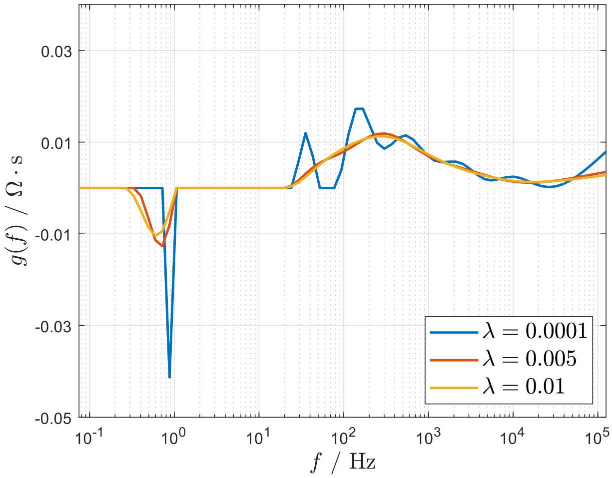

Figure A.1: Variation of the Tikhonov regularization parameter to determine the optimal value. Figure reformatted and taken from [2].

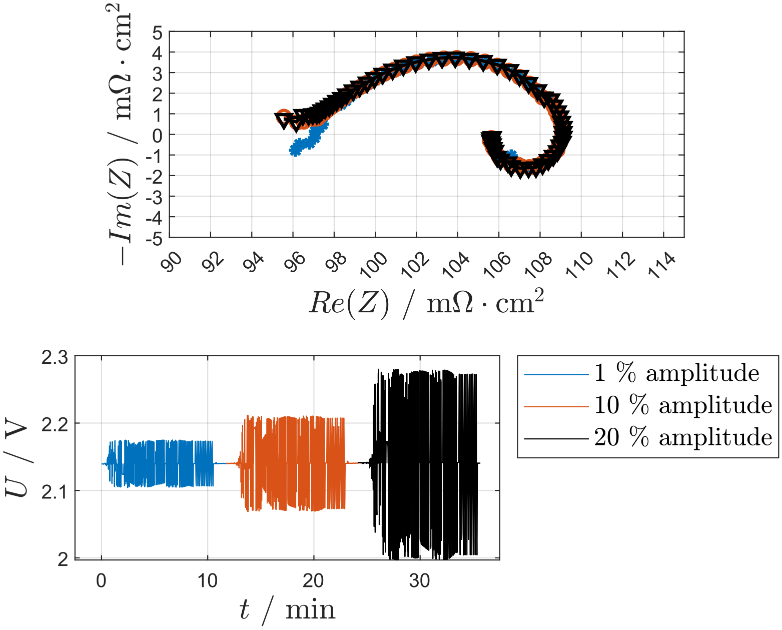

Figure A.2: Variation of the amplitude during EIS at the same bias current density. Figure reformatted and taken from [2].

A.2 Usage of Carbon-Based Porous Transport Layers

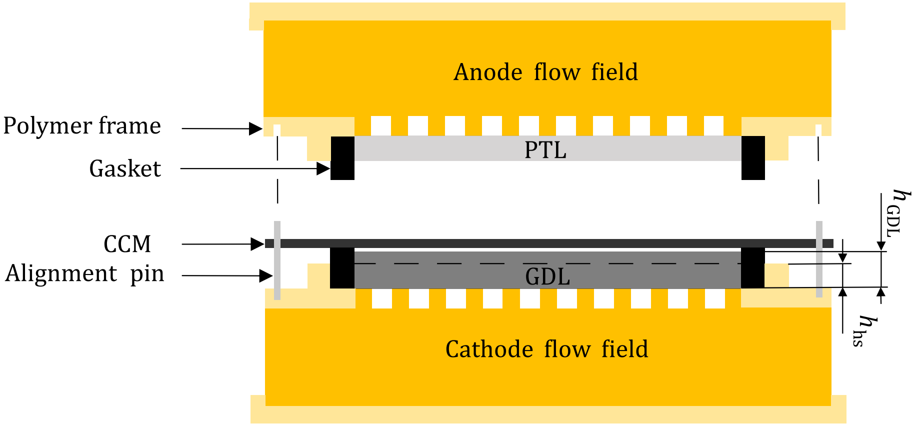

Figure A.3: Schematic diagram of the test cell setup using the “hard stop” approach to define nominal compression. Figure reformatted and taken from [4].

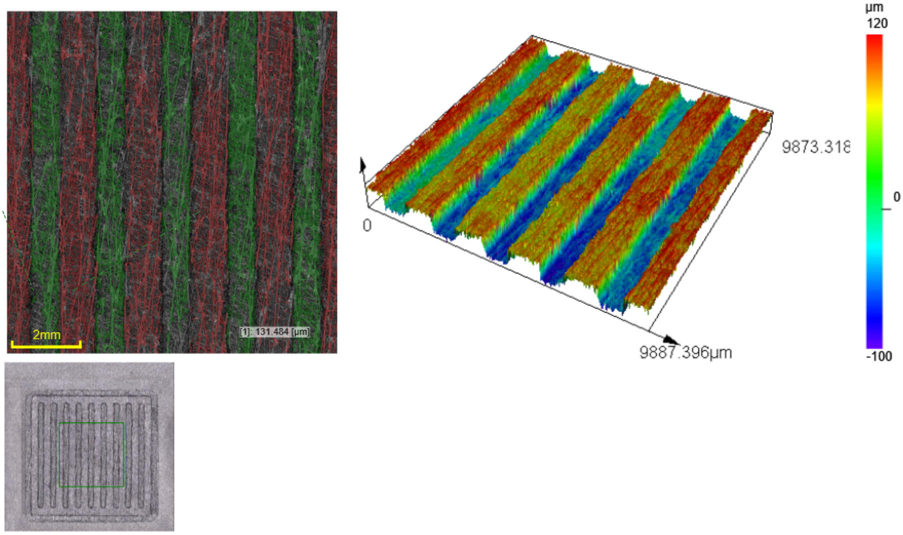

Figure A.4: Compression analysis of the top fiber layers of uncompressed (red) and compressed (green) carbon fibers using CLSM scans. Figure reformatted and taken from [4].

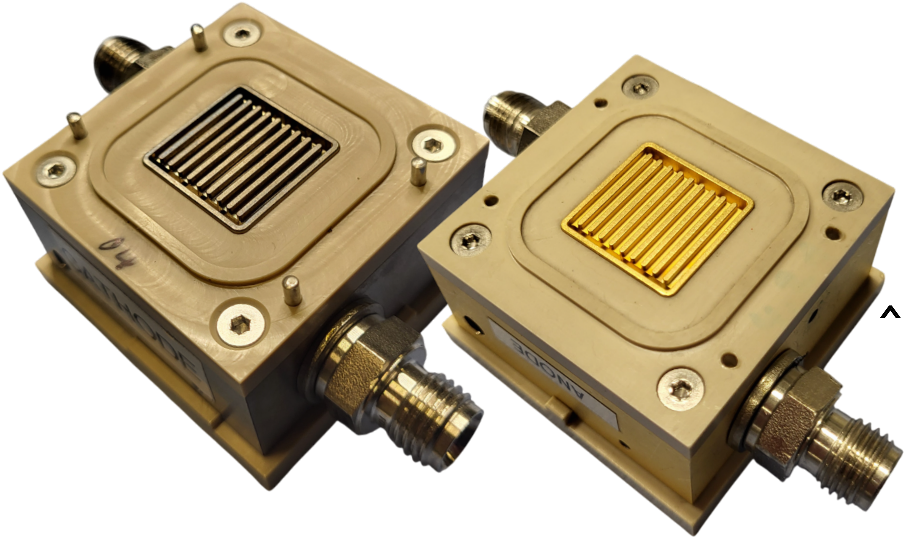

Figure A.5: Photos of the gold-coated and uncoated flow field referring to discussion on Figure 3.3. Figure reformatted and taken from [4].

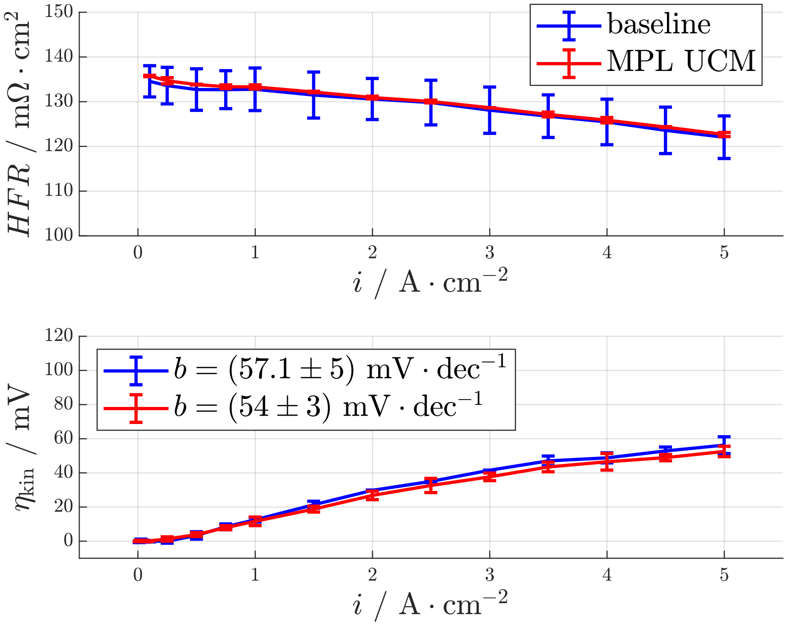

Figure A.6: HFR, Tafel slope and residual overpotentials of measurements with commercial CCM and baseline GDL (blue curve) and GDL with MPL UCM (red curve), corresponding to Figure 3.5. Figure reformatted and taken from [4].

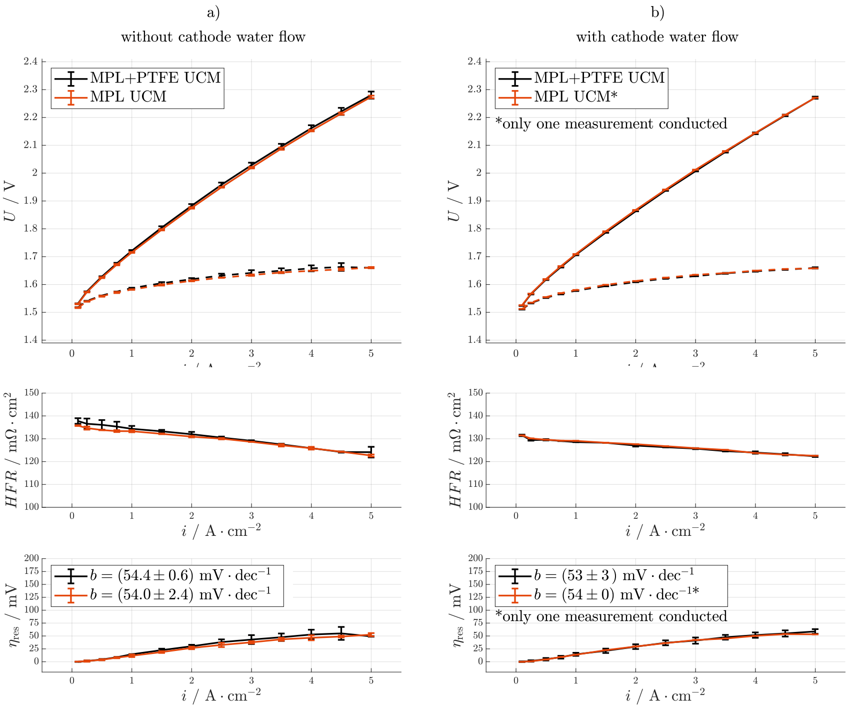

Figure A.7: Electrochemical analysis of the influence of hydrophobic treatment (PTFE) in the GDL at the cathode using the commercial CCM and comparing MPL UCM and MPL+PTFE UCM. Polarization curve, HFR-free polarization curve (dashed lines), HFR and residual overpotentials over current density at a) dry cathode and b) with water flow at the cathode, corresponding to Figure 3.6. Figure reformatted and taken from [4].

A.3 Along the Channel Test Cell

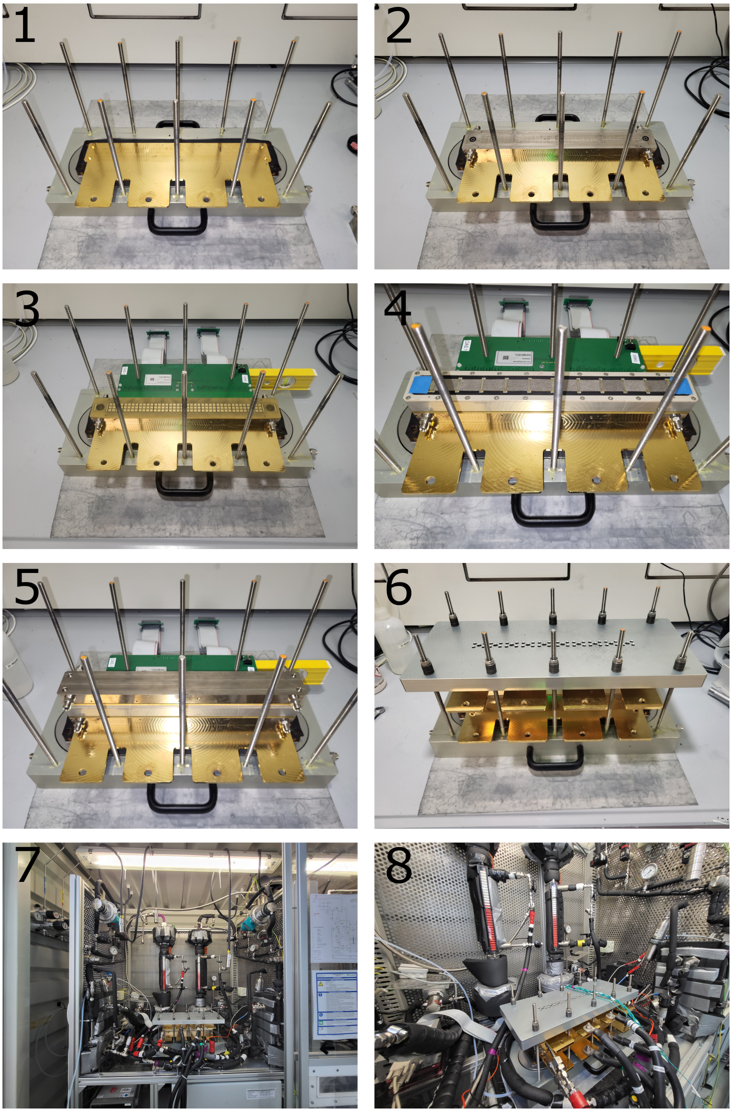

Figure A.8: Photos during the assembly of the Along the Channel test cell. Figure reformatted and taken from [3].

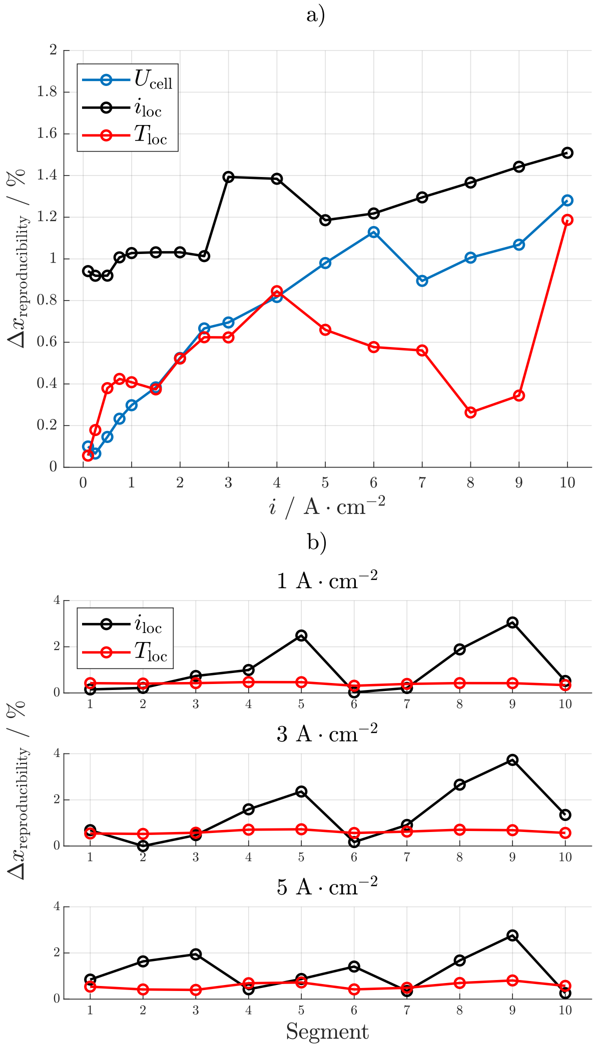

Figure A.9: Analysis of the reproducibility of the voltage, current density and temperature distribution measurement shown in Figure 4.9 at 80 °C and differential pressure of 10-1 bar. a) relative deviation of cell voltage and the mean values of current density and temperature distribution of all segments and b) deviation of each segment of current density and temperature distribution at 1 A · cm^{-2}, 3 A · cm^{-2} and 5 A · cm^{-2} exemplarily shown for all cell current densities. Figure reformatted and taken from [3].

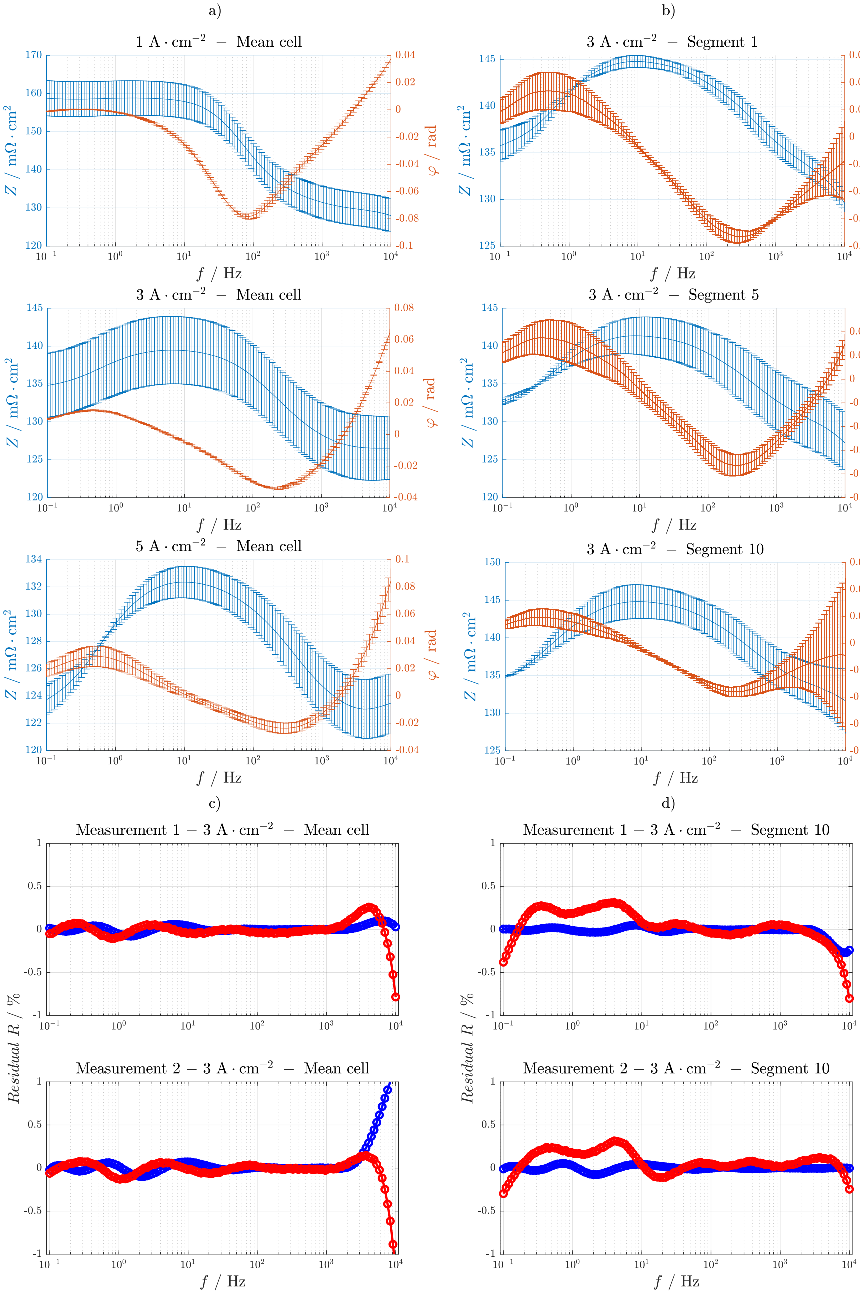

Figure A.10: Analysis of the reproducibility of the voltage, current density and temperature distribution measurement shown in Figure 4.9 at 80 °C and differential pressure of 10-1 bar. a) relative deviation of cell voltage and the mean values of current density and temperature distribution of all segments and b) deviation of each segment of current density and temperature distribution at 1 A · cm^{-2}, 3 A · cm^{-2} and 5 A · cm^{-2} exemplarily shown for all cell current densities. Figure reformatted and taken from [3].

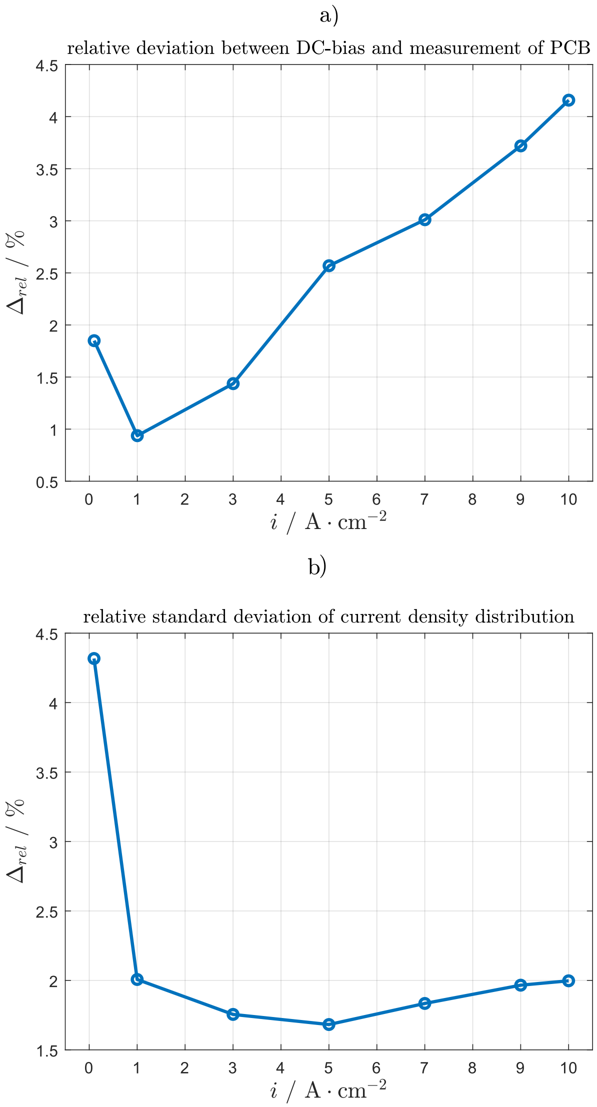

Figure A.11: Analysis of the relative deviation between potentiostat's output (DC-bias) and the measured mean current density of the PCB and b) analysis of the relative standard deviation of the current density distribution at different mean current densities during the measurement shown in Figure 4.9. Figure reformatted and taken from [3].

A.4 Performance-Based Along the Channel Analysis

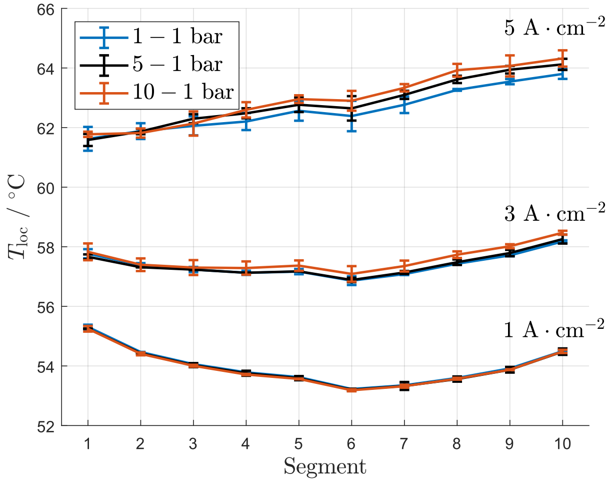

Figure A.12: Temperature distribution during differential pressure variation at mean current densities of $1\ \mathrm{A}\cdot\mathrm{cm}^{-2}$, $3\ \mathrm{A}\cdot\mathrm{cm}^{-2}$, and $5\ \mathrm{A}\cdot\mathrm{cm}^{-2}$. Figure reformatted and taken from [5].

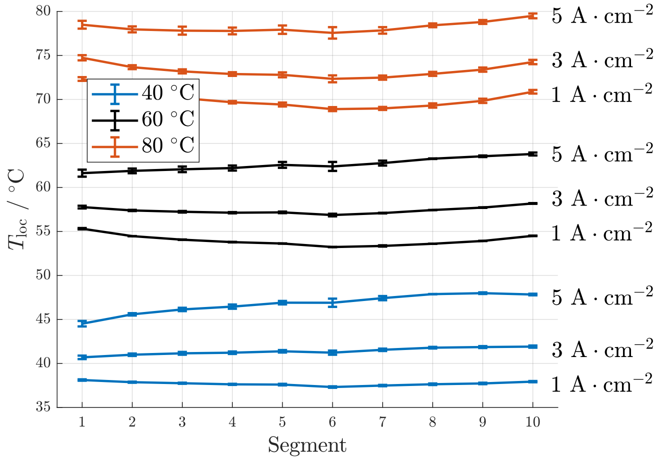

Figure A.13: Temperature distribution during mean cell temperature variation at mean current densities of $1\ \mathrm{A}\cdot\mathrm{cm}^{-2}$, $3\ \mathrm{A}\cdot\mathrm{cm}^{-2}$, and $5\ \mathrm{A}\cdot\mathrm{cm}^{-2}$. Figure reformatted and taken from [5].

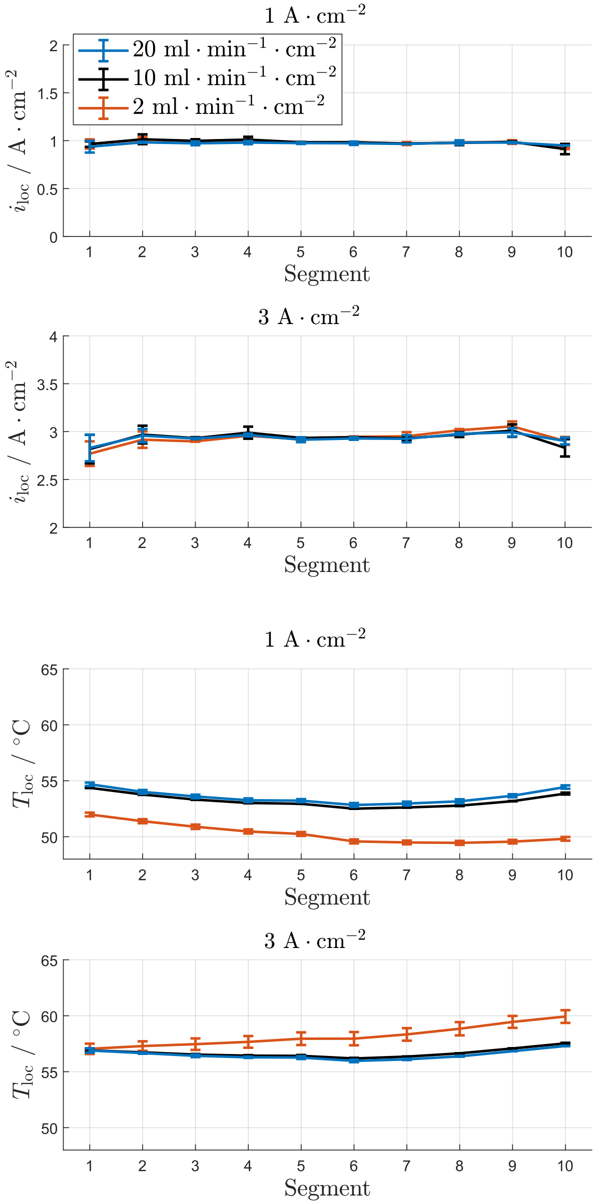

Figure A.14: Current density (top) and temperature (bottom) distribution during flow rate variation at mean current densities of $1\ \mathrm{A}\cdot\mathrm{cm}^{-2}$ and $3\ \mathrm{A}\cdot\mathrm{cm}^{-2}$. Figure reformatted and taken from [5].

Calculation of the theoretical heat loss and temperature difference along the channel shown in Figure 5.4 d):

ΔT_{exp}: Difference of measured temperature values in segment 1 and segment 10 using the 12 contacts per segment within the PCB.
$\Delta T_{\mathrm{theo,adiabtic}}$: Theoretical calculation assuming adiabatic conditions

$$\dot{Q}_{\text{water,in}} + \dot{Q}_{\text{reaction}} = \dot{Q}_{\text{water,out}} + \dot{Q}_{\text{diss}} \quad \text{with } \dot{Q}_{\text{diss}} = 0$$

$$\dot{Q}_{\text{reaction}} = i \cdot A \cdot (U_{\text{cell}} - U_{\text{th},60^\circ C}) \quad \text{with } U_{\text{th},60^\circ C} \text{ being the thermoneutral voltage at } 60^\circ C$$

$$\Delta T_{\text{theo, adiabatic}} = \frac{\dot{Q}_{\text{reaction}}}{\dot{m}_{\text{water}} \cdot c_{p,\text{water}}}$$

$$\text{with } \dot{m}_{\text{water,in}} \cdot c_{p,\text{water,in}} = \dot{m}_{\text{mix,out}} \cdot c_{p,\text{mix,out}} = \dot{m}_{\text{water}} \cdot c_{p,\text{water}}$$

$$\Delta T_{\text{theo, corrected}} = \frac{\dot{Q}_{\text{reaction}} - \dot{Q}_{\text{diss}}}{\dot{m}_{\text{water}} \cdot c_{p,\text{water}}} \quad \text{with } \dot{Q}_{\text{diss}} = \dot{Q}_{\text{PCB}} = 49.41\,\text{W}$$

$\dot{Q}_{\mathrm{PCB}}$ heat loss at $i = 0.01\ \mathrm{A \cdot cm^{-2}}$ and $\dot{q}_{\mathrm{water,in}} = 10\ \mathrm{ml \cdot min^{-1} \cdot cm^{-2}}$ at measured temperature difference between inlet and outlet

$$\Delta T_{\text{theo, fit}} = \frac{\dot{Q}_{\text{reaction}} - \dot{Q}_{\text{diss}}}{\dot{m}_{\text{water}} \cdot c_{p,\text{water}}} \quad \text{with } \dot{Q}_{\text{diss}} = \dot{Q}_{\text{PCB}} + \dot{Q}_{\text{loss, fit}} = 49.41\,\text{W} + 152\,\text{W}$$

Estimation of exchange surface area:

The total area (A_{total}) for heat exchange is determined of all sides of both flow field plates:

$$A_{\text{PCB}} = A_{\text{cathode, end plate}} = 185\,\text{cm}^2$$

$$A_{\text{flow field plate, outlet}} = A_{\text{flow field plate, outlet}} = 15\,\text{cm}^2$$

$$A_{\text{flow field plate, left}} = A_{\text{flow field plate, right}} = 111\,\text{cm}^2$$

$$A_{\text{total}} = A_{\text{PCB}} + A_{\text{cathode, end plate}} + A_{\text{flow field plate, left}} + A_{\text{flow field plate, right}} + A_{\text{flow field plate, inlet}} + A_{\text{flow field plate, outlet}} = 607\,\text{cm}^2$$

The heat loss through the PCB and the fitted heat loss term seems reasonable since the geometrical factors are comparable. Since the inlet and outlet water to and out of the cell flow through the anode endplate and therefore heat up the PCB from the bottom, $\dot{Q}_{\text{PCB}}$ might be underestimated which would fit even better with the geometrical factor.

$$\frac{A_{\text{PCB}}}{A_{\text{total}}} = 30.48\% \quad \text{and} \quad \frac{\dot{Q}_{\text{PCB}}}{\dot{Q}_{\text{PCB}} + \dot{Q}_{\text{loss, fit}}} = 24.53\%$$

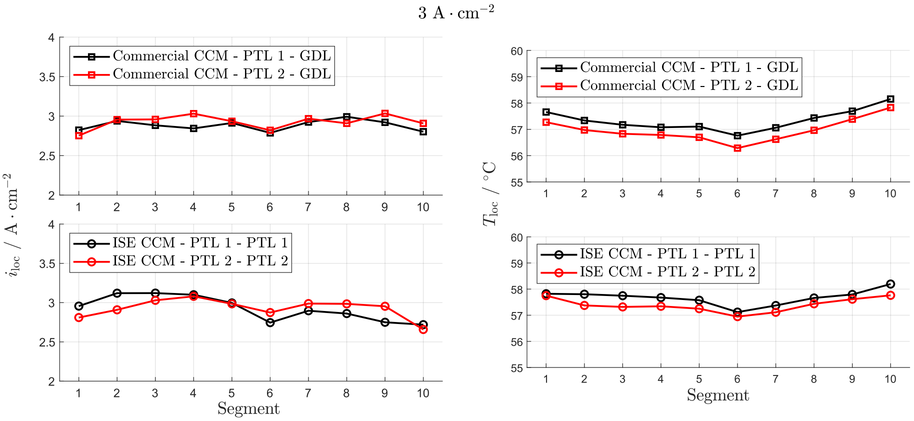

Figure A.15: Current density (left) and temperature (right) distribution during water flow rate variation at mean current densities of 3 $\text{A} \cdot \text{cm}^{-2}$ for commercial CCM (top) and ISE CCM (bottom). Figure reformatted and taken from [5].

A.5 Water Starvation Analysis Along the Channel

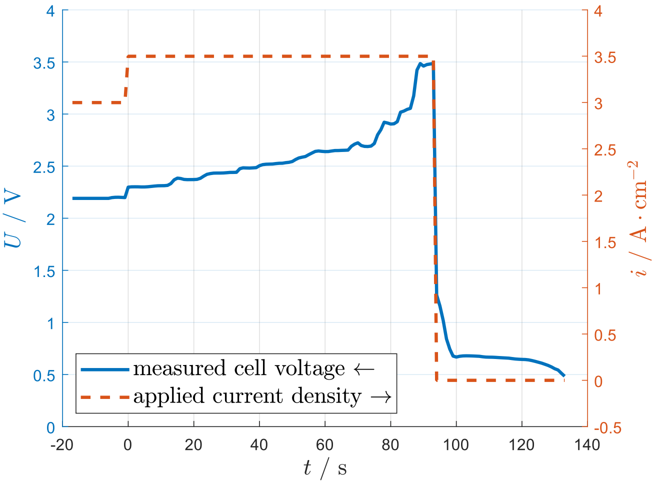

Figure A.16: Instable cell voltage over time when set $3.5\ \mathrm{A \cdot cm^{-2}}$ at $54\ \mu\mathrm{l \cdot min^{-1} \cdot cm^{-2}}$ anode water flow rate, referring to Figure 6.1. Figure reformatted and taken from [6].

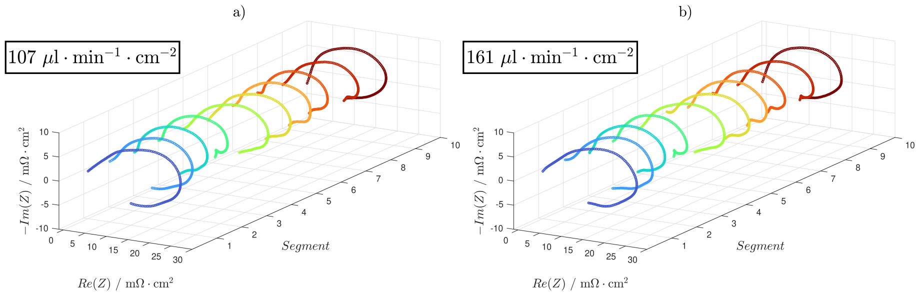

Figure A.17: Locally resolved impedance analysis under flow rate variation. HFR-free Nyquist presentation at a water flow rate of a) $107\ \mu\mathrm{l \cdot min^{-1} \cdot cm^{-2}}$ and b) $161\ \mu\mathrm{l \cdot min^{-1} \cdot cm^{-2}}$, corresponding to Figure 6.2. Figure reformatted and taken from [6].

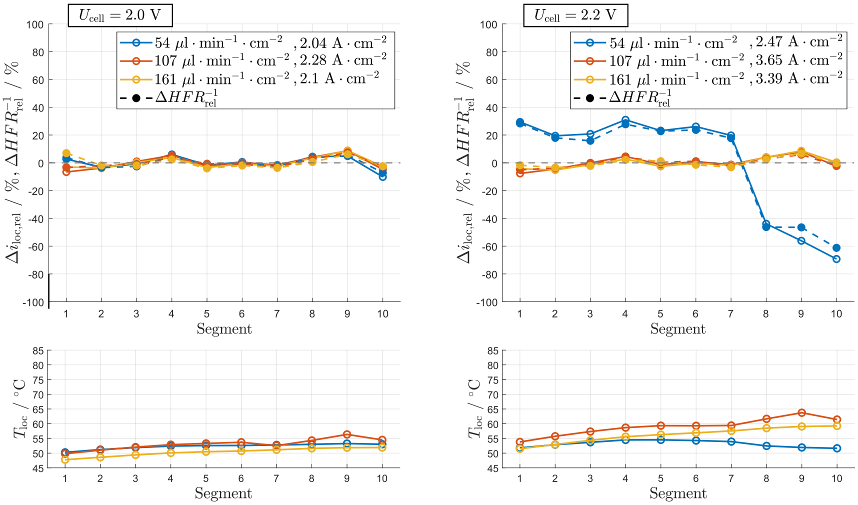

Figure A.18: Relative deviation of the mean current density at 2.0 V and 2.2 V and water flow rate variation at the top. The relative deviation of the inverse HFR is given in dashed lines and corresponding temperature profiles at the bottom, corresponding to Figure 6.4. Figure reformatted and taken from [6].

B Supervised Student Theses

- Uffelmann J. (2023). *Analyse der Zweiphasenströmung in PEM-Wasserelektrolysekomponenten mittels ex-situ Durchfluss-Testzellen.* Bachelor's thesis, Hochschule RheinMain

- Armbruster S. (2023). *Ex-Situ Visualisierung und Analyse der Zweiphasenströmung in PEM-Wasserelektrolyse-Zellen.* Bachelor's thesis, Hochschule Offenburg

- Andaluri U. A. (2024). *Investigation of Mass Transport Losses in Proton Exchange Membrane Water Electrolysis.* Masters's thesis, Albert Ludwigs Universität Freiburg

- Winterholler N. (2024). *Investigation of Loss Mechanisms in a Segmented Along-the-Channel PEM Water Electrolysis Cell.* Masters's thesis, Albert Ludwigs Universität Freiburg

- Hoffmann J. (2024). *Charakterisierung von Carbon-basierten Gasdiffusionsschichten in der PEM Wasserelektrolyse.* Project thesis, FH Münster

- Hoffmann J. (2025). *Untersuchung von Anodenkatalysatorschichten in einer segmentierten PEM-Wasserelektrolyse-Testzelle.* Bachelor's thesis, FH Münster

List of Publications

Journal articles

- Hensle, N., Brinker, D., Metz, S., Smolinka, T., & Weber, A. (2023). *On the role of inductive loops at low frequencies in PEM electrolysis*. Electrochemistry Communications, 155, 107585. [1]

- Brinker, D., Hensle, N., de la Viña, J. H., Franzetti, I., Bühre, L. V., Andaluri, U. A., Charlotte Menke, Tom Smolinka & Weber, A. (2024). *Inductive loops in impedance spectra of PEM water electrolyzers*. Journal of Power Sources, 622, 235375. [2]

- Hensle, N., Metz, S., Weber, A., & Smolinka, T. (2024). *A Segmented Along the Channel Test Cell for Locally Resolved Analysis at High Current Densities in PEM Water Electrolysis*. Journal of The Electrochemical Society, 171(11), 114510. [3]

- Hensle, N., Hoffmann, J., Najafianashrafi, Z., Smolinka, T., Chuang, P.Y.A. & Weber A. (2024). *Understanding the use of carbon-based porous transport layers at the cathode in PEM water electrolysis*. Journal of Power Sources, 642, 236913. [4]

- Hensle, N., Horstmann de la Viña, J., Winterholler, N., Hoffmann, J., Armbruster, S., Lindner, A., Weber, A. & Smolinka, T. (2025). *Understanding the Cell Performance Along the Channel for Industrial PEM Water Electrolysis Operation.* ACS Applied Energy Materials. [5]

- Hensle N., Lickert T., Winterholler N., Smolinka T., Weber A. (2025). *Water Starvation Phenomena in a Segmented Along the Channel PEM Water Electrolysis Cell.* Journal of Power Sources. [6]

Conference contributions

- Hensle, N., Metz S. & Smolinka T. (2023, August). *A segmented along the channel PEM electrolysis cell for the operation at high current densities.* International Conference on Electrolysis 2023, Sun City, South Africa

- Hensle, N. & Smolinka T. (2024, May). *Locally-resolved investigations in an industrial-scaled along the channel PEM electrolysis test cell.* Aachen Hydrogen Colloquium 2024, Aachen, Germany

- Hensle, N. & Smolinka T. (2024, May). *Understanding Mass Transport at High Current Densities in an Industrial Scale PEM Electrolysis Test Cell - a Segmented Along-the-Channel Approach.* 245th Meeting of the Electrochemical Society, San Francisco, USA

- Hensle, N., Hoffmann J., Smolinka T., Chuang P. A. & Weber A. (2025, May). *Gas diffusion layers and their optimal usage in PEM water electrolysis.* Aachen Hydrogen Colloquium 2025, Aachen, Germany

- Hensle, N., Weber A. & Smolinka T. (2025, July). *Performance Analysis of a Segmented Along the Channel PEM Water Electrolysis Cell.* European Fuel Cell Forum 2025, Luzern, Switzerland

Acronyms and Symbols

Acronyms

AC	Alternating current
AEMWE	Anion exchange membrane water electrolysis
Ag/AgCl RE	Silver/silver chloride reference electrode
ASR	Area-specific resistance
AtC	Along the channel
BoT	Begin of test
CAPEX	Capital expenditure
CCM	Catalyst-coated membrane
CDD	Current density distribution
CL	Catalyst layer
CLSM	Confocal laser scanning microscopy
$\mathbf{CO_2}$	Carbon dioxide
CPE	Constant phase element
CT	Computer tomography
DC	Direct current
DME	Dimethylether
DRT	Distribution of relaxation time
ECM	Equivalent circuit modeling
EIS	Electrochemical impedance spectroscopy
EoT	End of test
FRA	Frequency response analyzer
GDL	Gas diffusion layer
$\mathbf{H_2}$	Hydrogen
HER	Hydrogen evolution reaction
HFR	High frequency resistance

IAM – ET	Institute for Applied Materials – Electrochemical Technologies
I/C	Ionomer-to-carbon
ICR	Internal contact resistance
IrO_x	Iridium oxide
I/S	Ionomer-to-solid
ISE	Institute for Solar Energy Systems
IWM	Institute for Mechanics of Materials
j	Imaginary unit
KIT	Karlsruhe Institute of Technology
LFR	Low frequency resistance
MEA	Membrane electrode assembly
MFR	Minimal frequency resistance
MIP	Mercury intrusion porosimetry
MPL	Micro porous layer
MTL	Mass transport losses
NaCl	Sodium chloride
OCV	Open circuit voltage
OER	Oxygen evolution reaction
PCB	Printed circuit board
PEEK	Polyether ether ketone
PEM	Proton exchange membrane, polymer electrolyte membrane
PEMFC	PEM fuel cell
PEMWE	Proton exchange membrane water electrolysis
PFSA	Perfluorosulfonic acids
PGM	Platinum group metals
Pt	Platinum

PTE	Porous transport electrode
PTFE	Polytetrafluoroethylene
PTL	Porous transport layer
RC	Parallel circuit of resistor and capacitor
RQ	Parallel circuit of resistor and constant phase element
SEM	Scanning electron microscope
sin	Sine function
t	Time
Ti	Titanium
TPB	Triple phase boundary
UCM	University of California, Merced
XRF	X-ray fluorescence spectroscopy
Z	Impedance

Constants

F	Faraday's constant
R	General gas constant
π	Circle number

Latin symbols and variables

$\mathbf{A}$	Active area
$\mathbf{G}$	Gibbs free energy
$\mathbf{H}$	Enthalpy
$\mathbf{M}$	Molar mass
$\mathbf{V}$	Volume
$\mathbf{U}$	Cell voltage
$\mathbf{a}$	Activity
$\mathbf{f}$	Frequency
$\mathbf{g}$	Distribution function
$\mathbf{n}$	Amount of substance
$\mathbf{p}$	Pressure
$\mathbf{S}$	Entropy
$\mathbf{T}$	Temperature
$\mathbf{z}$	Number of transferred electrons

Greek symbols and variables

α	Symmetry factor
η	Overpotential
ζ	Electro-osmotic drag coefficient
λ	Tikhonov regularization parameter, stoichiometry, water content
$\boldsymbol{\Omega}$	Ohmic
$\boldsymbol{\Psi}$	Ratio
ρ	Density
τ	Time constant
φ	Potential, relative humidity, phase shift
ω	Circuit frequency

General deep indexes

an	Anode
app	Applied
bulk	Bulk material
ca	Cathode
cap	Capacitive
e	Electrical
FF	Flow field
g	Gauge
hs	Hard stop
In	Inlet
ind	Inductive
kin	Kinetic
l/g	Liquid-to-gas ratio
loc	Local
nom	Nominal
Out	Outlet
pol	Polarization
p	Protonic
rel	Relative
res	Residual
rev	Reversible
s	Saturated
Series	Series resistance, HFR
0	Standard condition
stoich	Stoichiometric
th	Thermal neutral
w	Water

List of Figures

List of Tables

Bibliography

[1] Niklas Hensle, Debora Brinker, Sebastian Metz, Tom Smolinka, and André Weber. On the role of inductive loops at low frequencies in pem electrolysis. *Electrochemistry Communications*, 155:107585, 2023. ISSN 1388-2481. doi: 10.1016/j.elecom.2023.107585.

[2] Debora Brinker, Niklas Hensle, La Horstmann de Viña, Irene Franzetti, Jerónimo, Lena Viviane Bühre, Umesh Anirudh Andaluri, Charlotte Menke, Tom Smolinka, and André Weber. *Inductive Loops in Impedance Spectra of PEM Water Electrolyzers*. 2024. doi: 10.1016/j.jpowsour.2024.235375.

[3] Niklas Hensle, Sebastian Metz, André Weber, and Tom Smolinka. A segmented along the channel test cell for locally resolved analysis at high current densities in pem water electrolysis. *Journal of The Electrochemical Society*, 171(11):114510, 2024. ISSN 0013-4651. doi: 10.1149/1945-7111/ad9064.

[4] Niklas Hensle, Justin Hoffmann, Zabihollah Najafianashrafi, Tom Smolinka, Po-Ya Abel Chuang, and André Weber. *Understanding the Use of Carbon-Based Porous Transport Layers at the Cathode in Pem Water Electrolysis*. Elsevier BV, 2025. doi: 10.1016/j.jpowsour.2025.236913.

[5] Niklas Hensle, Jerónimo La Horstmann de Viña, Nico Winterholler, Justin Hoffmann, Stephan Armbruster, Adrian Lindner, André Weber, and Tom Smolinka. Understanding the cell performance along the channel for industrial pem water electrolysis operation. *ACS Applied Energy Materials*, 8(11):7107–7124, 2025. ISSN 2574-0962. doi: 10.1021/acsaem.5c00505.

[6] Niklas Hensle, Thomas Lickert, Nico Winterholler, Tom Smolinka, and André Weber. Water starvation phenomena in a segmented along the channel pem water electrolysis cell. *Journal of Power Sources*, 654:237865, 2025. ISSN 0378-7753. doi: 10.1016/j.jpowsour.2025.237865.

[7] *The copenhagen diagnosis*. 2009. ISBN 978-0-9807316-1-3]. URL `https://www.ccrc.unsw.edu.au/sites/default/files/copenhagen_diagnosis_low.pdf`.

[8] Hoesung Lee, Katherine Calvin, Dipak Dasgupta, Gerhard Krinmer, Aditi Mukherji, Peter Thorne, Christopher Trisos, Jose Romero, Paulina Aldunce, Ko Barret, Gabriel Blanco, William W.L. Cheung, Sarah L. Connors, Fatima Denton, Aïda Diongue-Niang, David Dodman, Matthias Garschagen, Oliver Geden, Bronwyn Hayward, Christopher Jones, Frank Jotzo, Thelma Krug, Rodel Lasco, June-Yi Lee, Valerie Masson-Delmotte, Malte Meinshausen, Katja Mintenbeck, Abdalah Mokssit, Friederike E. L. Otto, Minal Pathak, Anna Pirani, Elvira Poloczanska, Hans-Otto Pörtner, Aromar Revi, Debra C. Roberts, Joyashree Roy, Alex C. Ruane, Jim Skea, Priyadarshi R. Shukla, Raphael Slade, Aimée Slangen, Youba Sokona, Anna A. Sörensson, Melinda Tignor, Detlef van Vuuren, Yi-Ming Wei, Harald Winkler, Panmao Zhai, and Zinta Zommers. *Synthesis report of the IPCC Sixth Assessment Report (AR6), Longer report. IPCC.* Intergovernmental Panel on Climate Change (IPCC), 2023. URL `https://mural.maynoothuniversity.ie/17733/`.

[9] Bundesministerium für Wirtschaft und Klimaschutz. Ausbau erneuerbarer energien 2024, 2025. URL `https://www.bundesnetzagentur.de/1043738`.

[10] Bruno Burger. Stromerzeugung in deutschland im jahr 2024, 01.01.2025. URL `https://energy-charts.info/presentations/2025-03-27_Stromerzeugung_Deutschland_2024.pdf`.

[11] Bundesministerium für Wirtschaft und Klimaschutz. Klimaschutzplan 2050, 2022. URL `https://www.bundeswirtschaftsministerium.de/Redaktion/DE/Artikel/Industrie/klimaschutz-klimaschutzplan-2050.html`.

[12] Peter Kurzweil and Otto Dietlmeier. *Elektrochemische Speicher: Superkondensatoren, Batterien, Elektrolyse-Wasserstoff, Rechtliche Rahmenbedingungen.* Springer Vieweg, Wiesbaden, 2., aktualisierte und erweiterte auflage edition, 2018. ISBN 9783658218294.

[13] P. Galindo Cifre and O. Badr. Renewable hydrogen utilisation for the production of methanol. *Energy Conversion and Management*, 48(2):519–527, 2007. ISSN 0196-8904. doi: 10.1016/j.enconman.2006.06.011.

[14] Masashi Hattori, Shinya Iijima, Takuya Nakao, Hideo Hosono, and Michikazu Hara. Solid solution for catalytic ammonia synthesis from nitrogen and hydrogen gases at 50 °c. *Nature Communications*, 11(1):2001, 2020. ISSN 2041-1723. doi: 10.1038/s41467-020-15868-8.

[15] Joydev Manna, Prakash Jha, Rudranath Sarkhel, Chandan Banerjee, A. K. Tripathi, and M. R. Nouni. Opportunities for green hydrogen production in petroleum refining and ammonia synthesis industries in india. *International Journal of Hydrogen Energy*, 46(77): 38212–38231, 2021. ISSN 0360-3199. doi: 10.1016/j.ijhydene.2021.09.064.

[16] Oliver Martin, Antonio J. Martín, Cecilia Mondelli, Sharon Mitchell, Takuya F. Segawa, Roland Hauert, Charlotte Drouilly, Daniel Curulla-Ferré, and Javier Pérez-Ramírez. Indium oxide as a superior catalyst for methanol synthesis by co 2 hydrogenation. *Angewandte Chemie*, 128(21):6369–6373, 2016. ISSN 1521-3757. doi: 10.1002/ange.201600943.

[17] Davide Ripepi, Riccardo Zaffaroni, Herman Schreuders, Bart Boshuizen, and Fokko M. Mulder. Ammonia synthesis at ambient conditions via electrochemical atomic hydrogen permeation. *ACS Energy Letters*, 6(11):3817–3823, 2021. doi: 10.1021/acsenergylett.1c01568.

[18] Ogawa, T., Inoue, N., Shikada, T., & Ohno, Y. *Direct dimethyl ether synthesis*, volume 12. 2003. URL `https://citeseerx.ist.psu.edu/document?repid=rep1&type=pdf&doi=02ec0d4308b5537b424ba572b3cda761f5ec871c`.

[19] *Wasserstoff-Farbenlehre*. 2020. URL `https://www.ikem.de/wp-content/uploads/2021/03/ikem_kurzstudie_wasserstoff_farbenlehre.pdf`.

[20] Tuananh Bui, Dongkeun Lee, Kook Young Ahn, and Young Sang Kim. Techno-economic analysis of high-power solid oxide electrolysis cell system. *Energy Conversion and Management*, 278:116704, 2023. ISSN 0196-8904. doi: 10.1016/j.enconman.2023.116704.

[21] Tonghui Cui, Jianzhong Zhu, Zewei Lyu, Minfang Han, Kaihua Sun, Yang Liu, and Meng Ni. Efficiency analysis and operating condition optimization of solid oxide electrolysis system coupled with different external heat sources. *Energy Conversion and Management*, 279:116727, 2023. ISSN 0196-8904. doi: 10.1016/j.enconman.2023.116727.

[22] Jörn Brauns and Thomas Turek. Experimental evaluation of dynamic operating concepts for alkaline water electrolyzers powered by renewable energy. *Electrochimica Acta*, 404: 139715, 2022. ISSN 0013-4686. doi: 10.1016/j.electacta.2021.139715.

[23] Alejandra Tello, Francisco A. Cataño, Arulraj Arunachalam, Diego Oyarzún, Rodrigo Henriquez, Patricio Valdivia, Mangalaraja Ramalinga Viswanathan, and Humberto Gómez. Green hydrogen production by photovoltaic-assisted alkaline water electrolysis: A review on the conceptualization and advancements. *International Journal of Hydrogen Energy*, 2024. ISSN 0360-3199. doi: 10.1016/j.ijhydene.2024.04.333.

[24] Alfredo Ursúa, Ernesto L. Barrios, Julio Pascual, Idoia San Martín, and Pablo Sanchis. Integration of commercial alkaline water electrolysers with renewable energies: Limitations and improvements. *International Journal of Hydrogen Energy*, 41(30):12852–12861, 2016. ISSN 0360-3199. doi: 10.1016/j.ijhydene.2016.06.071.

[25] Pengzuo Chen and Xile Hu. High–efficiency anion exchange membrane water electrolysis employing non–noble metal catalysts. *Advanced Energy Materials*, 10(39):2002285, 2020. ISSN 1614-6840. doi: 10.1002/aenm.202002285.

[26] Immanuel Vincent and Dmitri Bessarabov. Low cost hydrogen production by anion exchange membrane electrolysis: A review. *Renewable and Sustainable Energy Reviews*, 81: 1690–1704, 2018. ISSN 1364-0321. doi: 10.1016/j.rser.2017.05.258.

[27] Immanuel Vincent, Andries Kruger, and Dmitri Bessarabov. Hydrogen production by water electrolysis with an ultrathin anion-exchange membrane (aem). *International Journal of Electrochemical Science*, 13(12):11347–11358, 2018. ISSN 1452-3981. doi: 10.20964/2018.12.84.

[28] Khaja Wahab Ahmed, Saeed Habibpour, Zhongwei Chen, and Michael Fowler. Investigation of nicoox catalysts for anion exchange membrane water electrolysis: Performance, durability, and efficiency analysis. *Journal of Energy Storage*, 79:110149, 2024. ISSN 2352-152X. doi: 10.1016/j.est.2023.110149.

[29] S. Campagna Zignani, M. Lo Faro, A. Carbone, C. Italiano, S. Trocino, G. Monforte, and A. S. Aricò. Performance and stability of a critical raw materials-free anion exchange membrane electrolysis cell. *Electrochimica Acta*, 413:140078, 2022. ISSN 0013-4686. doi: 10.1016/j.electacta.2022.140078.

[30] Sun Young Kang, Ji Eun Park, Ga Young Jang, Ok-Hee Kim, Oh Joong Kwon, Yong-Hun Cho, and Yung-Eun Sung. High-performance and durable water electrolysis using a highly conductive and stable anion-exchange membrane. *International Journal of Hydrogen Energy*, 47(15):9115–9126, 2022. ISSN 0360-3199. doi: 10.1016/j.ijhydene.2022.01.002.

[31] Tobias Schuler, Carl Cesar Weber, Jacob A. Wrubel, Lorenz Gubler, Bryan Pivovar, Felix N. Büchi, and Guido Bender. Ultrathin microporous transport layers: Implications for low catalyst loadings, thin membranes, and high current density operation for proton exchange membrane electrolysis. *Advanced Energy Materials*, 14(7):2302786, 2024. ISSN 1614-6840. doi: 10.1002/aenm.202302786.

[32] Dawei Wang, Fangxu Lin, Heng Luo, Jinhui Zhou, Wenshu Zhang, Lu Li, Yi Wei, Qinghua Zhang, Lin Gu, Yanfei Wang, Mingchuan Luo, Fan Lv, and Shaojun Guo. Ir-o-mn embedded in porous nanosheets enhances charge transfer in low-iridium pem electrolyzers. *Nature Communications*, 16(1):181, 2025. ISSN 2041-1723. doi: 10.1038/s41467-024-54646-8.

[33] Tom Smolinka. What do we need in pem water electrolysis to achieve our 2030 targets: A review of key challenges, 06.12.2023.

[34] Daniel Siegmund, Sebastian Metz, Volker Peinecke, Terence E. Warner, Carsten Cremers, Anna Grevé, Tom Smolinka, Doris Segets, and Ulf-Peter Apfel. Crossing the valley of death: From fundamental to applied research in electrolysis. *JACS Au*, 1(5):527–535, 2021. doi: 10.1021/jacsau.1c00092.

[35] C. Immerz, B. Bensmann, P. Trinke, M. Suermann, and R. Hanke-Rauschenbach. Local current density and electrochemical impedance measurements within 50 cm single-channel pem electrolysis cell. *Journal of The Electrochemical Society*, 165(16):F1292–F1299, 2018. ISSN 0013-4651. doi: 10.1149/2.0411816jes.

[36] C. Immerz, M. Schweins, P. Trinke, B. Bensmann, M. Paidar, T. Bystroň, K. Bouzek, and R. Hanke-Rauschenbach. Experimental characterization of inhomogeneity in current density and temperature distribution along a single-channel pem water electrolysis cell. *Electrochimica Acta*, 260:582–588, 2018. ISSN 0013-4686. doi: 10.1016/j.electacta.2017.12.087.

[37] Ishanka Dedigama, Pangiota Angeli, Nicholas van Dijk, Jason Millichamp, Dimitrios Tsaoulidis, Paul R. Shearing, and Daniel J.L. Brett. Current density mapping and optical flow visualisation of a polymer electrolyte membrane water electrolyser. *Journal of Power Sources*, 265:97–103, 2014. ISSN 0378-7753. doi: 10.1016/j.jpowsour.2014.04.120.

[38] Shucheng Sun, Yu Xiao, Dong Liang, Zhigang Shao, Hongmei Yu, Ming Hou, and Baolian Yi. Behaviors of a proton exchange membrane electrolyzer under water starvation. *RSC Advances*, 5(19):14506–14513, 2015. doi: 10.1039/C4RA14104K.

[39] U.S. Department of Energy. Technical targets for proton exchange membrane electrolysis | department of energy, 2025. URL `https://www.energy.gov/eere/fuelcells/technical-targets-proton-exchange-membrane-electrolysis`.

[40] Clean Hydrogen Partnership. *Strategic research and innovation agenda 2021–2027*. 2022. URL `https://www.horizon-europe.gouv.fr/sites/default/files/2022-03/programme-strat-gique-de-recherche-et-d-innovation-de-clean-hydrogen-5867.pdf`.

[41] Frederick C. Strong. Faraday's laws in one equation. *Journal of Chemical Education*, 38 (2):98, 1961. ISSN 0021-9584. doi: 10.1021/ed038p98.

[42] Burin Yodwong, Damien Guilbert, Matheepot Phattanasak, Wattana Kaewmanee, Melika Hinaje, and Gianpaolo Vitale. Faraday's efficiency modeling of a proton exchange membrane electrolyzer based on experimental data. *Energies*, 13(18):4792, 2020. ISSN 1996-1073. doi: 10.3390/en13184792.

[43] Carolin Klose, Torben Saatkamp, Andreas Münchinger, Luca Bohn, Giorgi Titvinidze, Matthias Breitwieser, Klaus-Dieter Kreuer, and Severin Vierrath. All–hydrocarbon mea for pem water electrolysis combining low hydrogen crossover and high efficiency. *Advanced Energy Materials*, 10(14):1903995, 2020. ISSN 1614-6840. doi: 10.1002/aenm.201903995.

[44] Carolin Klose. *Novel polymer electrolyte membrane compositions for electrolysis and fuel cell systems*. 2020. URL `https://www.researchgate.net/profile/Carolin-Klose/publication/340540880_Novel_polymer_electrolyte_membrane_compositions_for_electrolysis_and_fuel_cell_systems/links/5f1ffd3992851cd5fa4e38b0/Novel-polymer-electrolyte-membrane-compositions-for-electrolysis-and-fuel-cell-systems.pdf`.

[45] Torsten Berning. On the nature of electro-osmotic drag. *Energies*, 13(18):4726, 2020. ISSN 1996-1073. doi: 10.3390/en13184726.

[46] Dmitri Bessarabov, Andries Kruger, Sean M. Luopa, Jiyoung Park, Attila A. Molnar, and Krzysztof A. Lewinski. Gas crossover mitigation in pem water electrolysis: Hydrogen crossover benchmark study of 3m's ir-nstf based electrolysis catalyst-coated membranes. *ECS Transactions*, 75(14):1165–1173, 2016. ISSN 1938-5862. doi: 10.1149/07514.1165ecst.

[47] Agate Martin, Patrick Trinke, Markus Stähler, Andrea Stähler, Fabian Scheepers, Boris Bensmann, Marcelo Carmo, Werner Lehnert, and Richard Hanke-Rauschenbach. The effect of cell compression and cathode pressure on hydrogen crossover in pem water electrolysis. *Journal of The Electrochemical Society*, 169(1):014502, 2022. ISSN 0013-4651. doi: 10.1149/1945-7111/ac4459.

[48] Xiaohui Yan, Jiazhen Li, Shu Yuan, Congfan Zhao, Cehuang Fu, Shuiyun Shen, Jiewei Yin, and Junliang Zhang. Influence and improvement of membrane electrode assembly fabrication methods for proton exchange membrane water electrolysis. *Journal of The Electrochemical Society*, 171(6):064504, 2024. ISSN 0013-4651. doi: 10.1149/1945-7111/ad4f20.

[49] Matthias F. Ernst, Vivian Meier, Matthias Kornherr, and Hubert A. Gasteiger. Preparation and performance evaluation of microporous transport layers for proton exchange membrane (pem) water electrolyzer anodes. *Journal of The Electrochemical Society*, 171(7):074511, 2024. ISSN 0013-4651. doi: 10.1149/1945-7111/ad63cf.

[50] A.-S. Feiner and A. J. McEvoy. The nernst equation. *Journal of Chemical Education*, 71 (6):493, 1994. ISSN 0021-9584. doi: 10.1021/ed071p493.

[51] Maximilian Bernt and Hubert A. Gasteiger. Influence of ionomer content in iro 2 /tio 2 electrodes on pem water electrolyzer performance. *Journal of The Electrochemical Society*, 163(11):F3179–F3189, 2016. ISSN 0013-4651. doi: 10.1149/2.0231611jes.

[52] Elliot Padgett, Guido Bender, Andrew Haug, Krzysztof Lewinski, Fuxia Sun, Haoran Yu, David A. Cullen, Andrew J. Steinbach, and Shaun M. Alia. Catalyst layer resistance and utilization in pem electrolysis. *Journal of The Electrochemical Society*, 170(8):084512, 2023. ISSN 0013-4651. doi: 10.1149/1945-7111/acee25.

[53] Tobias Schuler, Ruben de Bruycker, Thomas J. Schmidt, and Felix N. Büchi. Polymer electrolyte water electrolysis: Correlating porous transport layer structural properties and performance: Part i. tomographic analysis of morphology and topology. *Journal of The Electrochemical Society*, 166(4):F270–F281, 2019. ISSN 0013-4651. doi: 10.1149/2.0561904jes.

[54] Tobias Schuler, Thomas J. Schmidt, and Felix N. Büchi. Polymer electrolyte water electrolysis: Correlating performance and porous transport layer structure: Part ii. electrochemical performance analysis. *Journal of The Electrochemical Society*, 166(10):F555–F565, 2019. ISSN 0013-4651. doi: 10.1149/2.1241908jes.

[55] Gergely Schmidt, Michel Suermann, Boris Bensmann, Richard Hanke-Rauschenbach, and Insa Neuweiler. Modeling overpotentials related to mass transport through porous transport layers of pem water electrolysis cells. *Journal of The Electrochemical Society*, 167(11):114511, 2020. ISSN 0013-4651. doi: 10.1149/1945-7111/aba5d4.

[56] Tobias Schuler. *Towards a Generic Understanding of Porous Transport Layers in Polymer Electrolyte Water Electrolysis*. 2020. URL `https://www.research-collection.ethz.ch/bitstream/handle/20.500.11850/438165/4/Abstract_26835.pdf`.

[57] GFS Fuel Cells GmbH. Gfs fuel cells - brennstoffzellen prototypen. URL `https://www.gfs-fuelcells.de/`.

[58] Jacob Wrubel, Samantha Ware, Corey Schaffer, Matt Allen, Ellis Klein, Robin Rice, Chaiwat Engtrakul, and Guido Bender. Nrel 25-cm2 high-pressure low-temperature electrolysis cell hardware (open source). URL `https://data.nrel.gov/submissions/223#:~:text=Log%20in-,NREL%2025%2Dcm2%20High%2DPressure%20Low%2DTemperature%20Electrolysis%20Cell,it%20comes%20to%20R%26D%20testing`.

[59] Thomas Lickert, Stefanie Fischer, James L. Young, Selina Klose, Irene Franzetti, Daniel Hahn, Zhenye Kang, Meital Shviro, Fabian Scheepers, Marcelo Carmo, Tom Smolinka, Guido Bender, and Sebastian Metz. Advances in benchmarking and round robin testing for

pem water electrolysis: Reference protocol and hardware. *Applied Energy*, 352:121898, 2023. ISSN 0306-2619. doi: 10.1016/j.apenergy.2023.121898.

[60] Marius Holst, Stefan Aschbrenner, Tom Smolinka, Christopher Voglstätter. Cost forecast for low temperature electrolysis - technology driven bottom-up prognosis for pem and alkaline water electrolysis systems, 2021. URL `https://www.ise.fraunhofer.de/en/publications/studies/catf.html`.

[61] Tao Liu, Youkun Tao, Yanli Wang, Meiqi Hu, Zhen Zhang, and Jing Shao. Towards cost-effective and durable bipolar plates for proton exchange membrane electrolyzers: A review. *Fuel*, 368:131610, 2024. ISSN 0016-2361. doi: 10.1016/j.fuel.2024.131610.

[62] Xiao-Zi Yuan, Nima Shaigan, Chaojie Song, Mantaj Aujla, Vladimir Neburchilov, Jason Tai Hong Kwan, David P. Wilkinson, Aimy Bazylak, and Khalid Fatih. The porous transport layer in proton exchange membrane water electrolysis: perspectives on a complex component. *Sustainable Energy & Fuels*, 6(8):1824–1853, 2022. doi: 10.1039/D2SE00260D.

[63] Alex Badgett, Joe Brauch, Amogh Thatte, Rachel Rubin, Christopher Skangos, Xiaohua Wang, Rajesh Ahluwalia, Bryan Pivovar, and Mark Ruth. Updated manufactured cost analysis for proton exchange membrane water electrolyzers. (NREL/TP-6A20-87625), 2024. doi: 10.2172/2311140.

[64] Hartmut Krause. *Power-to-Gas Grundlagen - Konzepte - Lösungen.* Edition gwf Gas/Erdgas. Deutscher Industrieverlag, München, 1. aufl. edition, 2015. ISBN 9783835672536.

[65] Carl Cesar Weber, Tobias Schuler, Ruben de Bruycker, Lorenz Gubler, Felix N. Büchi, and Salvatore de Angelis. On the role of porous transport layer thickness in polymer electrolyte water electrolysis. *Journal of Power Sources Advances*, 15:100095, 2022. ISSN 2666-2485. doi: 10.1016/j.powera.2022.100095.

[66] Maximilian Bernt, Armin Siebel, and Hubert A. Gasteiger. Analysis of voltage losses in pem water electrolyzers with low platinum group metal loadings. *Journal of The Electrochemical Society*, 165(5):F305–F314, 2018. ISSN 0013-4651. doi: 10.1149/2.0641805jes.

[67] Pierre Millet. Pem water electrolysis. In *Hydrogen Production*, pages 63–116. John Wiley & Sons, Ltd, 2015. doi: 10.1002/9783527676507.ch3.

[68] Stefania Siracusano, Stefano Trocino, Nicola Briguglio, Vincenzo Baglio, and Antonino S. Aricò. Electrochemical impedance spectroscopy as a diagnostic tool in polymer electrolyte membrane electrolysis. *Materials*, 11(8):1368, 2018. ISSN 1996-1944. doi: 10.3390/ma11081368.

[69] N. Wagner, W. Schnurnberger, B. Müller, and M. Lang. Electrochemical impedance spectra of solid-oxide fuel cells and polymer membrane fuel cells. *Electrochimica Acta*, 43(24): 3785–3793, 1998. ISSN 0013-4686. doi: 10.1016/S0013-4686(98)00138-8.

[70] Woosung Choi, Heon-Cheol Shin, Ji Man Kim, Jae-Young Choi, and Won-Sub Yoon. Modeling and applications of electrochemical impedance spectroscopy (eis) for lithium-ion batteries. *Journal of Electrochemical Science and Technology*, 11(1):1–13, 2020. ISSN 2093-8551. doi: 10.33961/jecst.2019.00528.

[71] Xiao-Zi Yuan, Chaojie Song, Haijiang Wang, Jiujun Zhang. *Electrochemical impedance spectroscopy in PEM fuel cells: fundamentals and applications*. 2010. ISBN 978-1-84882-846-9.

[72] Jun Huang, Zhe Li, Bor Yann Liaw, and Jianbo Zhang. Graphical analysis of electrochemical impedance spectroscopy data in bode and nyquist representations. *Journal of Power Sources*, 309:82–98, 2016. ISSN 0378-7753. doi: 10.1016/j.jpowsour.2016.01.073.

[73] Alexandros Ch Lazanas and Mamas I. Prodromidis. Electrochemical impedance spectroscopy-a tutorial. *ACS Measurement Science Au*, 3(3):162–193, 2023. doi: 10.1021/acsmeasuresciau.2c00070.

[74] Bernard A. Boukamp. A linear kronig–kramers transform test for immittance data validation. *Journal of The Electrochemical Society*, 142(6):1885–1894, 1995. ISSN 0013-4651. doi: 10.1149/1.2044210.

[75] M. Schönleber, D. Klotz, and E. Ivers-Tiffée. A method for improving the robustness of linear kramers-kronig validity tests. *Electrochimica Acta*, 131:20–27, 2014. ISSN 0013-4686. doi: 10.1016/j.electacta.2014.01.034.

[76] H. Schichlein, A. C. Müller, M. Voigts, A. Krügel, and E. Ivers-Tiffée. Deconvolution of electrochemical impedance spectra for the identification of electrode reaction mechanisms in solid oxide fuel cells. *Journal of Applied Electrochemistry*, 32(8):875–882, 2002. ISSN 1572-8838. doi: 10.1023/A:1020599525160.

[77] Andrej N. Tikhonov, A. Gončarskij, V. V. Stepanov, and A. G. Jagola. Numerical methods for the solution of ill-posed problems. 328, 1995. doi: 10.1007/978-94-015-8480-7.

[78] IVERS-TIFF&Eacute, Ellen E, and Andr&eacute WEBER. Evaluation of electrochemical impedance spectra by the distribution of relaxation times. *Journal of the Ceramic Society of Japan*, 125(4):193–201, 2017. ISSN 1882-0743. doi: 10.2109/jcersj2.16267.

[79] Marcel Heinzmann, André Weber, and Ellen Ivers-Tiffée. Advanced impedance study of polymer electrolyte membrane single cells by means of distribution of relaxation times.

Journal of Power Sources, 402:24–33, 2018. ISSN 0378-7753. doi: 10.1016/j.jpowsour.2018.09.004.

[80] Mohamed Khalid Ratib, Kashem M. Muttaqi, Md Rabiul Islam, Danny Sutanto, and Ashish P. Agalgaonkar. Electrical circuit modeling of proton exchange membrane electrolyzer: The state-of-the-art, current challenges, and recommendations. *International Journal of Hydrogen Energy*, 49:625–645, 2024. ISSN 0360-3199. doi: 10.1016/j.ijhydene.2023.08.319.

[81] Irene Franzetti, Artem Pushkarev, Ai-Lin Chan, and Tom Smolinka. Parasitic effects in impedance spectrum of pem water electrolysis cells: Case study of high–frequency inductive effects. *Energy Technology*, 11(12), 2023. ISSN 2194-4288. doi: 10.1002/ente.202300375.

[82] Jeawoo Jung, Young-Hoon Chung, Hee-Young Park, Jonghee Han, Hyoung-Juhn Kim, Dirk Henkensmeier, Sung Jong Yoo, Jin Young Kim, So Young Lee, Kwang Ho Song, Hyun S. Park, and Jong Hyun Jang. Electrochemical impedance analysis with transmission line model for accelerated carbon corrosion in polymer electrolyte membrane fuel cells. *International Journal of Hydrogen Energy*, 43(32):15457–15465, 2018. ISSN 0360-3199. doi: 10.1016/j.ijhydene.2018.06.093.

[83] Jae-Hoon Kim, Chang-Yeol Oh, Ki-Ryong Kim, Jong-Pil Lee, and Tae-Jin Kim. Parameter identification of electrical equivalent circuits including mass transfer parameters for the selection of the operating frequencies of pulsed pem water electrolysis. *Energies*, 15(24): 9303, 2022. ISSN 1996-1073. doi: 10.3390/en15249303.

[84] N. Wagner and M. Schulze. Change of electrochemical impedance spectra during co poisoning of the pt and pt–ru anodes in a membrane fuel cell (pefc). *Electrochimica Acta*, 48(25-26):3899–3907, 2003. ISSN 0013-4686. doi: 10.1016/s0013-4686(03)00528-0.

[85] A. Schiefer, M. Heinzmann, and A.Weber. Inductive low-frequency processes in pemfc-impedance spectra. *Fuel Cells*, 2020. ISSN 1615-6854. doi: 10.1002/fuce.201900212.

[86] Debora Brinker. *Electrochemical Characterization and Modelling of incremental PEM Water Electrolysis Cells: Work in Progress*.

[87] Q-C.. Zhuang, Xiang-Yun Qiu, Shou-Dong Xu, Ying-Huai Qiang, and S-G. Sun. Diagnosis of electrochemical impedance spectroscopy in lithium ion batteries. *Lithium Ion Batteries – New Developments 8*, 2010. doi: 10.5772/26749.

[88] Harald Brandstätter, Ilie Hanzu, and Martin Wilkening. Myth and reality about the origin of inductive loops in impedance spectra of lithium-ion electrodes — a critical experimental

approach. *Electrochimica Acta*, 207:218–223, 2016. ISSN 0013-4686. doi: 10.1016/j.electacta.2016.03.126.

[89] J. S. Gnanaraj, R. W. Thompson, S. N. Iaconatti, J. F. DiCarlo, and K. M. Abraham. Formation and growth of surface films on graphitic anode materials for li-ion batteries. *Electrochemical and Solid-State Letters*, 8(2):A128, 2005. ISSN 1944-8775. doi: 10.1149/1.1850390.

[90] Hirofumi Sumi, Hiroyuki Shimada, Konosuke Watanabe, Yuki Yamaguchi, Katsuhiro Nomura, Yasunobu Mizutani, and Yuji Okuyama. External current dependence of polarization resistances for reversible solid oxide and protonic ceramic cells with current leakage. *ACS Applied Energy Materials*, 6(3):1853–1861, 2023. ISSN 2574-0962. doi: 10.1021/acsaem.2c03733.

[91] D. Montinaro, A. R. Contino, A. Dellai, and M. Rolland. Determination of the impedance contributions in anode supported solid oxide fuel cells with (la,sr)(co,fe)o 3−d cathode. *International Journal of Hydrogen Energy*, 39(36):21638–21646, 2014. ISSN 0360-3199. doi: 10.1016/j.ijhydene.2014.09.081.

[92] K. Kreka, K. V. Hansen, M. B. Mogensen, K. Norrman, C. Chatzichristodoulou, and T. Jacobsen. The impact of strong cathodic polarization on ni|ysz microelectrodes. *Journal of The Electrochemical Society*, 165(5):F253–F263, 2018. ISSN 0013-4651. doi: 10.1149/2.0141805jes.

[93] Kongfa Chen, Na Ai, and San Ping Jiang. Origin of low frequency inductive impedance loops of o 2 reduction reaction of solid oxide fuel cells. *Solid State Ionics*, 291:33–41, 2016. ISSN 0167-2738. doi: 10.1016/j.ssi.2016.04.021.

[94] A. Barbucci, R. Bozzo, G. Cerisola, and P. Costamagna. Characterisation of composite sofc cathodes using electrochemical impedance spectroscopy. analysis of pt/ysz and lsm/ysz electrodes. *Electrochimica Acta*, 47(13-14):2183–2188, 2002. ISSN 0013-4686. doi: 10.1016/S0013-4686(99)00134-6.

[95] Quentin Meyer and Chuan Zhao. Air perturbation-induced low-frequency inductive electrochemical impedance arc in proton exchange membrane fuel cells. *Journal of Power Sources*, 488:229245, 2021. ISSN 0378-7753. doi: 10.1016/j.jpowsour.2020.229245.

[96] Sunil K. Roy, Mark E. Orazem, and Bernard Tribollet. Interpretation of low-frequency inductive loops in pem fuel cells. *Journal of The Electrochemical Society*, 154(12):B1378, 2007. ISSN 0013-4651. doi: 10.1149/1.2789377.

[97] Sunil K. Roy and Mark E. Orazem. Error analysis of the impedance response of pem fuel cells. *Journal of The Electrochemical Society*, 154(8):B883, 2007. ISSN 0013-4651. doi: 10.1149/1.2747533.

[98] Ivan Pivac and Frano Barbir. Inductive phenomena at low frequencies in impedance spectra of proton exchange membrane fuel cells – a review. *Journal of Power Sources*, 326: 112–119, 2016. ISSN 0378-7753. doi: 10.1016/j.jpowsour.2016.06.119.

[99] Brian P. Setzler and Thomas F. Fuller. A physics-based impedance model of proton exchange membrane fuel cells exhibiting low-frequency inductive loops. *Journal of The Electrochemical Society*, 162(6):F519–F530, 2015. ISSN 0013-4651. doi: 10.1149/2.0361506jes.

[100] Dino Klotz. Negative capacitance or inductive loop? – a general assessment of a common low frequency impedance feature. *Electrochemistry Communications*, 98:58–62, 2019. ISSN 1388-2481. doi: 10.1016/j.elecom.2018.11.017.

[101] Christophe Gerling, Matthias Hanauer, Ulrich Berner, and K. Andreas Friedrich. Experimental and numerical investigation of the low-frequency inductive features in differential pemfcs: Ionomer humidification and platinum oxide effects. *Journal of The Electrochemical Society*, 170(1):014504, 2023. ISSN 0013-4651. doi: 10.1149/1945-7111/acb3ff.

[102] Samuel Cruz-Manzo, Rui Chen, and Pratap Rama. Inductive effect on the fuel cell cathode impedance spectrum at high frequencies. *Journal of Fuel Cell Science and Technology*, 9 (5), 2012. ISSN 1550-624X. doi: 10.1115/1.4007115.

[103] Olivier Antoine, Yann Bultel, and Robert Durand. Oxygen reduction reaction kinetics and mechanism on platinum nanoparticles inside nafion®. *Journal of Electroanalytical Chemistry*, 499(1):85–94, 2001. ISSN 1572-6657. doi: 10.1016/S0022-0728(00)00492-7.

[104] H. Kuhn, A. Wokaun, and G. G. Scherer. Exploring single electrode reactions in polymer electrolyte fuel cells. *Electrochimica Acta*, 52(6):2322–2327, 2007. ISSN 0013-4686. doi: 10.1016/j.electacta.2006.03.108.

[105] C. A. Schiller and H. Goehr. Faraday-impedanz als verknüpfung von impedanzelementen. *Zeitschrift für Physikalische Chemie*, (1):105–124, 1986. ISSN 2196-7156. doi: 10.1524/zpch.1986.148.1.105.

[106] C. A. Schiller, F. Richter, E. Gülzow, and N. Wagner. Relaxation impedance as a model for the deactivation mechanism of fuel cells due to carbon monoxide poisoning. *Physical Chemistry Chemical Physics*, 3(11):2113–2116, 2001. ISSN 14639076. doi: 10.1039/B007674K.

[107] N. Wagner and E. Gülzow. Change of electrochemical impedance spectra (eis) with time during co-poisoning of the pt-anode in a membrane fuel cell. *Journal of Power Sources*, 127(1-2):341–347, 2004. ISSN 0378-7753. doi: 10.1016/j.jpowsour.2003.09.031.

[108] Jan van der Merwe, Kenny Uren, George van Schoor, and Dmitri Bessarabov. Characterisation tools development for pem electrolysers. *International Journal of Hydrogen Energy*, 39(26):14212–14221, 2014. ISSN 0360-3199. doi: 10.1016/j.ijhydene.2014.02.096.

[109] Michel Suermann, Alexandra Pătru, Thomas J. Schmidt, and Felix N. Büchi. High pressure polymer electrolyte water electrolysis: Test bench development and electrochemical analysis. *International Journal of Hydrogen Energy*, 42(17):12076–12086, 2017. ISSN 0360-3199. doi: 10.1016/j.ijhydene.2017.01.224.

[110] J. C. Garcia-Navarro, M. Schulze, and K. A. Friedrich. Measuring and modeling mass transport losses in proton exchange membrane water electrolyzers using electrochemical impedance spectroscopy. *Journal of Power Sources*, 431:189–204, 2019. ISSN 0378-7753. doi: 10.1016/j.jpowsour.2019.05.027.

[111] T. Ferriday and P. H. Middleton. Experimental analysis of materials in proton exchange membrane electrolysis cells. *International Journal of Hydrogen Energy*, 44(51):27656–27663, 2019. ISSN 0360-3199. doi: 10.1016/j.ijhydene.2019.09.020.

[112] Jian Zuo, Nadia Yousfi Steiner, Zhongliang Li, and Daniel Hissel. Interpreting full-frequency impedance spectrum for pem electrolyzers: Distribution of relaxation times-based modeling. *Applied Energy*, 394:126185, 2025. ISSN 0306-2619. doi: 10.1016/j.apenergy.2025.126185.

[113] Tobias Franz, Tamara Miličić, Georgios Papakonstantinou, Tanja Vidaković-Koch, and Kai Sundmacher. On the origin of low-frequency inductive loops in the impedance spectra of proton exchange membrane water electrolyzers. *Journal of Power Sources*, 655:237981, 2025. ISSN 0378-7753. doi: 10.1016/j.jpowsour.2025.237981.

[114] S. Adler. Reference electrode placement and seals in electrochemical oxygen generators. *Solid State Ionics*, 134(1-2):35–42, 2000. ISSN 0167-2738. doi: 10.1016/S0167-2738(00)00711-6.

[115] Zyun Siroma, Ryou Kakitsubo, Naoko Fujiwara, Tsutomu Ioroi, Shin-Ichi Yamazaki, and Kazuaki Yasuda. Compact dynamic hydrogen electrode unit as a reference electrode for pemfcs. *Journal of Power Sources*, 156(2):284–287, 2006. ISSN 0378-7753. doi: 10.1016/j.jpowsour.2005.05.045.

[116] Olli Sorsa, Jussi Nieminen, Pertti Kauranen, and Tanja Kallio. Stable reference electrode in polymer electrolyte membrane electrolyser for three-electrode measurements. *Journal of The Electrochemical Society*, 166(16):F1326–F1336, 2019. ISSN 0013-4651. doi: 10.1149/2.0461916jes.

[117] Dietmar Gerteisen. Realising a reference electrode in a polymer electrolyte fuel cell by laser ablation. *Journal of Applied Electrochemistry*, 37(12):1447–1454, 2007. ISSN 1572-8838. doi: 10.1007/s10800-007-9352-y.

[118] Dietmar Gerteisen. *Investigation of dominant loss mechanisms in low-temperature polymer electrolyte membrane fuel cells*. 2009. URL `https://kops.uni-konstanz.de/entities/publication/b41ebc59-29ad-4faa-be42-62e504b7bfbd`.

[119] S. B. Adler. Reference electrode placement in thin solid electrolytes. *Journal of The Electrochemical Society*, 149(5):E166, 2002. ISSN 0013-4651. doi: 10.1149/1.1467368.

[120] Lena V. Bühre, Sven Bullerdiek, Patrick Trinke, Boris Bensmann, Anna-Lena E. R. Deutsch, Peter Behrens, and Richard Hanke-Rauschenbach. Application and analysis of a salt bridge reference electrode setup for pem water electrolysis: Towards an extended voltage loss break down. *Journal of The Electrochemical Society*, 169(12):124513, 2022. ISSN 0013-4651. doi: 10.1149/1945-7111/ac9ee1.

[121] Jason K. Lee, ChungHyuk Lee, Kieran F. Fahy, Benzhong Zhao, Jacob M. LaManna, Elias Baltic, David L. Jacobson, Daniel S. Hussey, and Aimy Bazylak. Critical current density as a performance indicator for gas-evolving electrochemical devices. *Cell Reports Physical Science*, 2(5):100440, 2021. ISSN 2666-3864. doi: 10.1016/j.xcrp.2020.100147.

[122] Thomas Lickert, Maximilian L. Kiermaier, Kolja Bromberger, Jagdishkumar Ghinaiya, Sebastian Metz, Arne Fallisch, and Tom Smolinka. On the influence of the anodic porous transport layer on pem electrolysis performance at high current densities. *International Journal of Hydrogen Energy*, 45(11):6047–6058, 2020. ISSN 0360-3199. doi: 10.1016/j.ijhydene.2019.12.204.

[123] Irina V. Pushkareva, Maksim A. Solovyev, Sergey I. Butrim, Margarita V. Kozlova, Dmitri A. Simkin, and Artem S. Pushkarev. On the operational conditions' effect on the performance of an anion exchange membrane water electrolyzer: Electrochemical impedance spectroscopy study. *Membranes*, 13(2):192, 2023. doi: 10.3390/membranes13020192.

[124] Andrei Kulikovsky. Effect of proton conductivity transients on pem fuel cell impedance: Formation of a low–frequency inductive loop. *Electrochemistry Communications*, 140: 107340, 2022. ISSN 1388-2481. doi: 10.1016/j.elecom.2022.107340.

[125] Paul Greenwood Samuel Cruz-Manzo. Low frequency inductive loop in eis measurements of an open-cathode polymer electrolyte fuel cell stack. impedance of water vapour diffusion in the cathode catalyst . . .. *Journal of Electroanalytical Chemistry*, 2021. ISSN 1572-6657. doi: 10.1016/j.jelechem.2021.115733.

[126] Tomáš Hrbek, Peter Kúš, Miquel Gamón Rodríguez, Vladimír Matolín, and Iva Matolínová. Operando x-ray photoelectron spectroscopy cell for water electrolysis: A complete picture of iridium electronic structure during oxygen evolution reaction. *International Journal of Hydrogen Energy*, 57:187–197, 2024. ISSN 0360-3199. doi: 10.1016/j.ijhydene.2023.12.216.

[127] Johanna Hemauer, Sebastian Rehfeldt, Harald Klein, and Andreas Peschel. Performance and cost modelling taking into account the uncertainties and sensitivities of current and next-generation pem water electrolysis technology. *International Journal of Hydrogen Energy*, 48(66):25619–25634, 2023. ISSN 0360-3199. doi: 10.1016/j.ijhydene.2023.03.050.

[128] Daniela Lorena Canelas Montaño, Pablo Ruiz García, Andrés Jerez Navarro, Modesto Aguirre Gomez, and José Javier López Cascales. Effect of the cathodic gas diffusion layer on the performance of a proton exchange membrane electrolyzer. *Energies*, 17(21):5298, 2024. ISSN 1996-1073. doi: 10.3390/en17215298.

[129] J. C. Cruz, R. Barbosa, B. Escobar, Z. Zarhri, D. L. Trejo-Arroyo, B. Pamplona, and L. Gómez-Barba. Electrochemical and microstructural analysis of a modified gas diffusion layer for a pem water electrolyzer. *International Journal of Electrochemical Science*, 15 (6):5571–5584, 2020. ISSN 1452-3981. doi: 10.20964/2020.06.12.

[130] F. Madadi, A. Rezaeian, H. Edris, and M. Zhiani. Improving performance in pemfc by applying different coatings to metallic bipolar plates. *Materials Chemistry and Physics*, 238:121911, 2019. ISSN 0254-0584. doi: 10.1016/j.matchemphys.2019.121911.

[131] Tabbi Wilberforce, O. Ijaodola, Emmanuel Ogungbemi, F. N. Khatib, T. Leslie, Zaki El-Hassan, J. Thomposon, and A. G. Olabi. Technical evaluation of proton exchange membrane (pem) fuel cell performance – a review of the effects of bipolar plates coating. *Renewable and Sustainable Energy Reviews*, 113:109286, 2019. ISSN 1364-0321. doi: 10.1016/j.rser.2019.109286.

[132] Jiabin Ge, Andrew Higier, and Hongtan Liu. Effect of gas diffusion layer compression on pem fuel cell performance. *Journal of Power Sources*, 159(2):922–927, 2006. ISSN 0378-7753. doi: 10.1016/j.jpowsour.2005.11.069.

[133] A. H. Mahmoudi, A. Ramiar, and Q. Esmaili. Effect of inhomogeneous compression of gas diffusion layer on the performance of pemfc with interdigitated flow field. *Energy Conversion and Management*, 110:78–89, 2016. ISSN 0196-8904. doi: 10.1016/j.enconman.2015.12.012.

[134] Qitong Shi, Cong Feng, Pingwen Ming, Fumin Tang, and Cunman Zhang. Compressive stress and its impact on the gas diffusion layer: A review. *International Journal of Hydrogen Energy*, 47(6):3994–4009, 2022. ISSN 0360-3199. doi: 10.1016/j.ijhydene.2021.10.058.

[135] Hao-Ming Chang, Chien-Wei Lin, Min-Hsing Chang, Huan-Ruei Shiu, Wen-Chen Chang, and Fang-Hei Tsau. Optimization of polytetrafluoroethylene content in cathode gas diffusion layer by the evaluation of compression effect on the performance of a proton exchange membrane fuel cell. *Journal of Power Sources*, 196(8):3773–3780, 2011. ISSN 0378-7753. doi: 10.1016/j.jpowsour.2010.12.090.

[136] Mrittunjoy Sarker, Md Azimur Rahman, Felipe Mojica, Shirin Mehrazi, Wilton J.M. Kort-Kamp, and Po-Ya Abel Chuang. Experimental and computational study of the microporous layer and hydrophobic treatment in the gas diffusion layer of a proton exchange membrane fuel cell. *Journal of Power Sources*, 509:230350, 2021. ISSN 0378-7753. doi: 10.1016/j.jpowsour.2021.230350.

[137] Shirin Mehrazi, Mrittunjoy Sarker, and Po-Ya Abel Chuang. Effect of high aspect ratio additives on microstructural and mass transport properties of the microporous layer in a proton exchange membrane fuel cell. *Journal of Power Sources*, 580:233361, 2023. ISSN 0378-7753. doi: 10.1016/j.jpowsour.2023.233361.

[138] Sehkyu Park, Jong-Won Lee, and Branko N. Popov. A review of gas diffusion layer in pem fuel cells: Materials and designs. *International Journal of Hydrogen Energy*, 37(7): 5850–5865, 2012. ISSN 0360-3199. doi: 10.1016/j.ijhydene.2011.12.148.

[139] Michel Suermann, Thomas Gimpel, Lena V. Bühre, Wolfgang Schade, Boris Bensmann, and Richard Hanke-Rauschenbach. Femtosecond laser-induced surface structuring of the porous transport layers in proton exchange membrane water electrolysis. *Journal of Materials Chemistry A*, 8(9):4898–4910, 2020. ISSN 2050-7488. doi: 10.1039/C9TA12127G.

[140] Manas Mandal and Marc Secanell. Improved polymer electrolyte membrane water electrolyzer performance by using carbon black as a pore former in the anode catalyst layer. *Journal of Power Sources*, 541:231629, 2022. ISSN 0378-7753. doi: 10.1016/j.jpowsour.2022.231629.

[141] P. J. Kim, CH. Lee, J. K. Lee, K. F. Fahy, and A. Bazylak. In-plane transport in water electrolyzer porous transport layers with through pores. *Journal of The Electrochemical Society*, 167(12):124522, 2020. ISSN 0013-4651. doi: 10.1149/1945-7111/abb173.

[142] Holger Janßen, Sebastian Holtwerth, Walter Zwaygardt, Andrea Stähler, Wilfried Behr, Dirk Federmann, Marcelo Carmo, Werner Lehnert, and Martin Müller. A facile and economical approach to fabricate a single-piece bipolar plate for pem electrolyzers. *International Journal of Hydrogen Energy*, 49:816–828, 2024. ISSN 0360-3199. doi: 10.1016/j.ijhydene.2023.09.175.

[143] Zhixuan Fan, Hongmei Yu, Guang Jiang, Dewei Yao, Shucheng Sun, Jun Chi, Bowen Qin, and Zhigang Shao. Low precious metal loading porous transport layer coating and anode catalyst layer for proton exchange membrane water electrolysis. *International Journal of Hydrogen Energy*, 47(44):18963–18971, 2022. ISSN 0360-3199. doi: 10.1016/j.ijhydene.2022.04.114.

[144] Maximilian Cieluch, Dennis Düerkop, Norbert Kazamer, Florian Wirkert, Pit Podleschny, Ulrich Rost, Achim Schmiemann, and Michael Brodmann. Manufacturing and investigation of meas for pemwe based on glass fibre reinforced pfsa/ssps composite membranes and catalyst-coated substrates prepared via catalyst electrodeposition. *International Journal of Hydrogen Energy*, 52:521–533, 2024. ISSN 0360-3199. doi: 10.1016/j.ijhydene.2023.07.310.

[145] Edgar Cruz Ortiz, Niklas van Treel, Susanne Koch, Severin Vierrath, and Melanie Bühler. The effect of compression on pem electrolyzer membrane electrode assemblies. *Journal of Power Sources*, 614:235018, 2024. ISSN 0378-7753. doi: 10.1016/j.jpowsour.2024.235018.

[146] Markus Stähler, Andrea Stähler, Fabian Scheepers, Marcelo Carmo, Werner Lehnert, and Detlef Stolten. Impact of porous transport layer compression on hydrogen permeation in pem water electrolysis. *International Journal of Hydrogen Energy*, 45(7):4008–4014, 2020. ISSN 0360-3199. doi: 10.1016/j.ijhydene.2019.12.016.

[147] Zhenye Kang, Shaun M. Alia, James L. Young, and Guido Bender. Effects of various parameters of different porous transport layers in proton exchange membrane water electrolysis. *Electrochimica Acta*, 354:136641, 2020. ISSN 0013-4686. doi: 10.1016/j.electacta.2020.136641.

[148] Tobias Kennerknecht. Fatigue of micro molded materials - aluminum bronze and yttria stabilized zirconia. doi: 10.5445/KSP/1000043832.

[149] Thomas Straub. Experimental investigation of crack initiation in face-centered cubic materials in the high and very high cycle fatigue regime. doi: 10.5445/KSP/1000051515.

[150] Thomas Straub, Jonas Fell, Simon Zabler, Tobias Gustmann, Hannes Korn, and Sarah C. L. Fischer. Characterization of filigree additively manufactured niti structures using micro tomography and micromechanical testing for metamaterial material models. *Materials*, 16 (2):676, 2023. ISSN 1996-1944. doi: 10.3390/ma16020676.

[151] S. A. Slaby, O. Kraft, and C. Eberl. Fatigue properties of conventionally manufactured and micro–powder–injection–moulded 17–4ph micro–components. *Fatigue & Fracture of Engineering Materials & Structures*, 39(6):780–789, 2016. ISSN 8756-758X. doi: 10.1111/ffe.12416.

[152] Stefania Siracusano, Vincenzo Baglio, Nicholas van Dijk, Luca Merlo, and Antonino Salvatore Aricò. Enhanced performance and durability of low catalyst loading pem water electrolyser based on a short-side chain perfluorosulfonic ionomer. *0306-2619*, 192:477–489, 2017. ISSN 0306-2619. doi: 10.1016/j.apenergy.2016.09.011.

[153] Ibrahim Alaefour, G. Karimi, Kui Jiao, and X. Li. Measurement of current distribution in a proton exchange membrane fuel cell with various flow arrangements – a parametric study. *Applied Energy*, 93:80–89, 2012. ISSN 0306-2619. doi: 10.1016/j.apenergy.2011.05.033.

[154] Daniel J.L Brett, Stephen Atkins, Nigel P. Brandon, Velisa Vesovic, Nikos Vasileiadis, and Anthony R. Kucernak. Measurement of the current distribution along a single flow channel of a solid polymer fuel cell. *Electrochemistry Communications*, 3(11):628–632, 2001. ISSN 1388-2481. doi: 10.1016/S1388-2481(01)00234-X.

[155] S. J. C. Cleghorn, C. R. Derouin, M. S. Wilson, and S. Gottesfeld. A printed circuit board approach to measuring current distribution in a fuel cell. *Journal of Applied Electrochemistry*, 28(7):663–672, 1998. ISSN 1572-8838. doi: 10.1023/A:1003206513954.

[156] Dietmar Gerteisen, Nada Zamel, Christian Sadeler, Florian Geiger, Victor Ludwig, and Christopher Hebling. Effect of operating conditions on current density distribution and high frequency resistance in a segmented pem fuel cell. *International Journal of Hydrogen Energy*, 37(9):7736–7744, 2012. ISSN 0360-3199. doi: 10.1016/j.ijhydene.2012.02.024.

[157] Martin Geske, Maik Heuer, Günter Heideck, and Zbigniew A. Styczynski. Current density distribution mapping in pem fuel cells as an instrument for operational measurements. *Energies*, 3(4):770–783, 2010. ISSN 1996-1073. doi: 10.3390/en3040770.

[158] O. Lottin, J. Dillet, G. Maranzana, S. Abbou, S. Didierjean, A. Lamibrac, R. L. Borup, R. Mukundan, and D. Spernjak. Experimental results with fuel cell start-up and shutdown. impact of type of carbon for cathode catalyst support. *ECS Transactions*, 69(17): 1065–1074, 2015. ISSN 1938-5862. doi: 10.1149/06917.1065ecst.

[159] A. Phillips, M. Ulsh, J. Porter, and G. Bender. Utilizing a segmented fuel cell to study the effects of electrode coating irregularities on pem fuel cell initial performance. *Fuel Cells*, 17(3):288–298, 2017. ISSN 1615-6854. doi: 10.1002/fuce.201600214.

[160] A. Lamibrac, G. Maranzana, O. Lottin, J. Dillet, J. Mainka, S. Didierjean, A. Thomas, and C. Moyne. Experimental characterization of internal currents during the start-up of a proton exchange membrane fuel cell. *Journal of Power Sources*, 196(22):9451–9458, 2011. ISSN 0378-7753. doi: 10.1016/j.jpowsour.2011.07.013.

[161] Tobias Schmitt, Rémi Bligny, Gaël Maranzana, Jerome Dillet, and Ulrich Sauter. An experimental study of humidity distribution dynamics in a segmented pem fuel cell. *Journal of The Electrochemical Society*, 169(12):124505, 2022. ISSN 0013-4651. doi: 10.1149/1945-7111/aca720.

[162] Tobias Schmitt, Rémi Bligny, Gaël Maranzana, and Ulrich Sauter. Rapid and local eis on a segmented fuel cell: A new method for spatial and temporal resolution. *Journal of The Electrochemical Society*, 169(9):094504, 2022. ISSN 0013-4651. doi: 10.1149/1945-7111/ac9089.

[163] B. Verdin, F. Fouda-Onana, S. Germe, G. Serre, P. A. Jacques, and P. Millet. Operando current mapping on pem water electrolysis cells. influence of mechanical stress. *International Journal of Hydrogen Energy*, 42(41):25848–25859, 2017. ISSN 0360-3199. doi: 10.1016/j.ijhydene.2017.08.189.

[164] Saher Al Shakhshir, Fan Zhou, and Søren Knudsen Kær. On the effect of clamping pressure and methods on the current distribution of a proton exchange membrane water electrolyzer. *ECS Transactions*, 85(13):995–1004, 2018. ISSN 1938-5862. doi: 10.1149/08513.0995ecst.

[165] Julian Parra-Restrepo, Rémi Bligny, Jérôme Dillet, Sophie Didierjean, Didier Stemmelen, Christian Moyne, Alain Degiovanni, and Gaël Maranzana. Influence of the porous transport layer properties on the mass and charge transfer in a segmented pem electrolyzer. *International Journal of Hydrogen Energy*, 45(15):8094–8106, 2020. ISSN 0360-3199. doi: 10.1016/j.ijhydene.2020.01.100.

[166] Shuaihao Ma, Kaichen Wang, Feng Xiao, Tianying Zhang, Feng Ye, Chao Xu, and Jianguo Liu. In-plane performance analysis of pem electrolyzer cell under multiple operating

conditions based on anode segmented visualization design. *Applied Energy*, 381:125167, 2025. ISSN 0306-2619. doi: 10.1016/j.apenergy.2024.125167.

[167] Zahner-Elektrik GmbH & Co. KG. *Electronic Load EL1002 (Operation Manual)*. 2024. URL `https://zahner.de/products-details/electronic-loads/el1002`.

[168] B. Savova-Stoynov and Z. B. Stoynov. Analysis of the inductance influence on the measured electrochemical impedance. *Journal of Applied Electrochemistry*, 17(6):1150–1158, 1987. ISSN 1572-8838. doi: 10.1007/BF01023598.

[169] Rasmus Rode Mosbæk. *Solid Oxide Fuel Cell Stack Diagnostics*. Department of Energy Conversion and Storage, Technical University of Denmark, 2014. ISBN 978-87-92986-20-7.

[170] Michel Suermann, Thomas J. Schmidt, and Felix N. Büchi. Cell performance determining parameters in high pressure water electrolysis. *Electrochimica Acta*, 211:989–997, 2016. ISSN 0013-4686. doi: 10.1016/j.electacta.2016.06.120.

[171] Amin Nouri-Khorasani, Emile Tabu Ojong, Tom Smolinka, and David P. Wilkinson. Model of oxygen bubbles and performance impact in the porous transport layer of pem water electrolysis cells. *International Journal of Hydrogen Energy*, 42(48):28665–28680, 2017. ISSN 0360-3199. doi: 10.1016/j.ijhydene.2017.09.167.

[172] Alessandra Pellegrino and Niklas Hensle. Measurement data - reference electrodes in a segmented along the channel pem water electrolysis cell. doi: 10.24406/FORDATIS/376.

[173] J. Costard, M. Ender, M. Weiss, and E. Ivers-Tiffée. Three-electrode setups for lithium-ion batteries. *Journal of The Electrochemical Society*, 164(2):A80–A87, 2017. ISSN 0013-4651. doi: 10.1149/2.0241702jes.

[174] Moses Ender, André Weber, and Ivers-Tiffée Ellen. Analysis of three-electrode setups for ac-impedance measurements on lithium-ion cells by fem simulations. *Journal of The Electrochemical Society*, 159(2):A128–A136, 2011. ISSN 0013-4651. doi: 10.1149/2.100202jes.

[175] Muthumeenal Arunachalam and Dong Suk Han. Efficient solar-powered pem electrolysis for sustainable hydrogen production: an integrated approach. *Emergent Materials*, 7(4): 1401–1415, 2024. ISSN 2522-574X. doi: 10.1007/s42247-024-00697-y.

[176] Philipp Lettenmeier, Rainey Wang, Rami Abouatallah, Fabian Burggraf, Aldo Saul Gago, and K. Andreas Friedrich. Proton exchange membrane electrolyzer systems operating dynamically at high current densities. *ECS Transactions*, 72(23):11–21, 2016. ISSN 1938-5862. doi: 10.1149/07223.0011ecst.

[177] V. A. Martinez Lopez, H. Ziar, J. W. Haverkort, M. Zeman, and O. Isabella. Dynamic operation of water electrolyzers: A review for applications in photovoltaic systems integration. *Renewable and Sustainable Energy Reviews*, 182:113407, 2023. ISSN 1364-0321. doi: 10.1016/j.rser.2023.113407.

[178] Amin Mohammadi and Mehdi Mehrpooya. A comprehensive review on coupling different types of electrolyzer to renewable energy sources. *Energy*, 158:632–655, 2018. ISSN 0360-5442. doi: 10.1016/j.energy.2018.06.073.

[179] Hyunjun Lee, Boreum Lee, Manhee Byun, and Hankwon Lim. Economic and environmental analysis for pem water electrolysis based on replacement moment and renewable electricity resources. *Energy Conversion and Management*, 224:113477, 2020. ISSN 0196-8904. doi: 10.1016/j.enconman.2020.113477.

[180] A. Villagra and P. Millet. An analysis of pem water electrolysis cells operating at elevated current densities. *International Journal of Hydrogen Energy*, 44(20):9708–9717, 2019. ISSN 0360-3199. doi: 10.1016/j.ijhydene.2018.11.179.

[181] Agate Martin, Patrick Trinke, Boris Bensmann, and Richard Hanke-Rauschenbach. Hydrogen crossover in pem water electrolysis at current densities up to 10 a cm -2. *Journal of The Electrochemical Society*, 169(9):094507, 2022. ISSN 0013-4651. doi: 10.1149/1945-7111/ac908c.

[182] Anders Christian Olesen, Steffen Henrik Frensch, and Søren Knudsen Kær. Towards uniformly distributed heat, mass and charge: A flow field design study for high pressure and high current density operation of pem electrolysis cells. *Electrochimica Acta*, 293: 476–495, 2019. ISSN 0013-4686. doi: 10.1016/j.electacta.2018.10.008.

[183] Krzysztof A. Lewinski, Dennis van der Vliet, and Sean M. Luopa. Nstf advances for pem electrolysis - the effect of alloying on activity of nstf electrolyzer catalysts and performance of nstf based pem electrolyzers. *ECS Transactions*, 69(17):893–917, 2015. ISSN 1938-5862. doi: 10.1149/06917.0893ecst.

[184] Gudrun Reichenauer, Christian Balzer, Rafael Meinusch, and Bernd M. Smarsly. Determining mechanical moduli of disordered materials with hierarchical porosity on different structural levels. *Langmuir*, 38(31):9631–9639, 2022. doi: 10.1021/acs.langmuir.2c01139.

[185] Ta Yang Goh, Shafriza Nisha Basah, Haniza Yazid, Muhammad Juhairi Aziz Safar, and Fathinul Syahir Ahmad Saad. Performance analysis of image thresholding: Otsu technique. *Measurement*, 114:298–307, 2018. ISSN 0263-2241. doi: 10.1016/j.measurement.2017.09.052.

[186] Olha Panchenko, Lennard Giesenberg, Elena Borgardt, Walter Zwaygardt, Nikolay Kardjilov, Henning Markötter, Tobias Arlt, Ingo Manke, Martin Müller, Detlef Stolten, and Werner Lehnert. Influence of stoichiometry on the two-phase flow behavior of proton exchange membrane electrolyzers. *Energies*, 12(3):350, 2019. ISSN 1996-1073. doi: 10.3390/en12030350.

[187] Katherine E. Ayers, Everett B. Anderson, Christopher Capuano, Blake Carter, Luke Dalton, Greg Hanlon, Judith Manco, and Michael Niedzwiecki. Research advances towards low cost, high efficiency pem electrolysis. *ECS Transactions*, 33(1):3–15, 2010. ISSN 1938-5862. doi: 10.1149/1.3484496.

[188] Ahmad Mayyas, Mark Ruth, Bryan Pivovar, Guido Bender, and Keith Wipke. Manufacturing cost analysis for proton exchange membrane water electrolyzers. (NREL/TP-6A20-72740), 2019. doi: 10.2172/1557965.

[189] Martin Müller, Marcelo Carmo, Andreas Glüsen, Michael Hehemann, Sayed Saba, Walter Zwaygardt, and Detlef Stolten. Water management in membrane electrolysis and options for advanced plants. *International Journal of Hydrogen Energy*, 44(21):10147–10155, 2019. ISSN 0360-3199. doi: 10.1016/j.ijhydene.2019.02.139.

[190] Xiaoping Guan, Jinhao Bai, Jingchang Zhang, and Ning Yang. Multiphase flow in pem water electrolyzers: a mini-review. *Current Opinion in Chemical Engineering*, 43:100988, 2024. ISSN 2211-3398. doi: 10.1016/j.coche.2023.100988.

[191] Thomassen et al. Method for producing hydrogen in a pem water electrolyser system, pem water electrolyser cell, stack and system, 2022.

[192] Michael R. Gerhardt, Jenny S. Østenstad, Alejandro O. Barnett, and Magnus S. Thomassen. Modeling contact resistance and water transport within a cathode liquid-fed proton exchange membrane electrolyzer. *Journal of The Electrochemical Society*, 170(12):124516, 2023. ISSN 0013-4651. doi: 10.1149/1945-7111/ad129d.

[193] Alexandre Tugirumubano, Hee-Jae Shin, Sun-Ho Go, Min-Sang Lee, Lee Ku Kwac, and Hong-Gun Kim. Electrochemical performance analysis of a pem water electrolysis with cathode feed mode based on flow passage shape of titanium plates. *International Journal of Precision Engineering and Manufacturing*, 17(8):1073–1078, 2016. ISSN 2005-4602. doi: 10.1007/s12541-016-0130-9.

[194] S. Toghyani, E. Afshari, E. Baniasadi, S. A. Atyabi, and G. F. Naterer. Thermal and electrochemical performance assessment of a high temperature pem electrolyzer. *Energy*, 152:237–246, 2018. ISSN 0360-5442. doi: 10.1016/j.energy.2018.03.140.

[195] E. A. Norman, V. M. Maestre, A. Ortiz, and I. Ortiz. Steam electrolysis for green hydrogen generation. state of the art and research perspective. *Renewable and Sustainable Energy Reviews*, 202:114725, 2024. ISSN 1364-0321. doi: 10.1016/j.rser.2024.114725.

[196] Scott D. Greenway, Elise B. Fox, and Amy A. Ekechukwu. Proton exchange membrane (pem) electrolyzer operation under anode liquid and cathode vapor feed configurations. *International Journal of Hydrogen Energy*, 34(16):6603–6608, 2009. ISSN 0360-3199. doi: 10.1016/j.ijhydene.2009.06.048.

[197] Anirban Roy, Frida H. Roenning, Douglas S. Aaron, Feng-Yuan Zhang, and Matthew M. Mench. Combining distributed electrochemical measurements with a semi-empirical model to identify local variations in overpotentials for pem water electrolyzers. *Journal of The Electrochemical Society*, 172(1):014509, 2025. ISSN 0013-4651. doi: 10.1149/1945-7111/ada63d.

[198] Dzmitry Malevich, Ela Halliop, Brant A. Peppley, Jon G. Pharoah, and Kunal Karan. Investigation of charge-transfer and mass-transport resistances in pemfcs with microporous layer using electrochemical impedance spectroscopy. *Journal of The Electrochemical Society*, 156(2):B216, 2009. ISSN 0013-4651. doi: 10.1149/1.3033408.

[199] Thomas A. Zawodzinski, Charles Derouin, Susan Radzinski, Ruth J. Sherman, T. van Smith, Thomas E. Springer, and Shimshon Gottesfeld. Water uptake by and transport through nafion® 117 membranes. *Journal of The Electrochemical Society*, 140(4):1041–1047, 1993. ISSN 0013-4651. doi: 10.1149/1.2056194.

[200] T. E. Springer, T. A. Zawodzinski, and S. Gottesfeld. Polymer electrolyte fuel cell model. *Journal of The Electrochemical Society*, 138(8):2334–2342, 1991. ISSN 0013-4651. doi: 10.1149/1.2085971.

[201] Di Zhong, Rui Lin, Zhenghua Jiang, Yike Zhu, Dengchen Liu, Xin Cai, and Liang Chen. Low temperature durability and consistency analysis of proton exchange membrane fuel cell stack based on comprehensive characterizations. *Applied Energy*, 264:114626, 2020. ISSN 0306-2619. doi: 10.1016/j.apenergy.2020.114626.

[202] G. W. THOMSON. The antoine equation for vapor-pressure data. *Chemical Reviews*, 38 (1):1–39, 1946. ISSN 0009-2665. doi: 10.1021/cr60119a001.

[203] Hee-Sun Shin and Byeong Soo Oh. Water transport according to temperature and current in pem water electrolyzer. *International Journal of Hydrogen Energy*, 45(1):56–63, 2020. ISSN 0360-3199. doi: 10.1016/j.ijhydene.2019.10.209.

[204] Paul Majsztrik, Andrew Bocarsly, and Jay Benziger. Water permeation through nafion membranes: the role of water activity. *The journal of physical chemistry. B*, 112(51): 16280–16289, 2008. ISSN 1520-6106. doi: 10.1021/jp804197x.

[205] Motupally S.m Beker A. J., Weidner J. W. Diffusion of water in nafion 115 membranes. 2000. doi: 10.1149/1.1393879.